ASAPTERRA

ADVANCING SAR AND OPTICAL METHODS FOR RAPID MAPPING

Final Report

January 2017

Dossier Lead: **DLR**

Contributors: **SERTIT**

Project duration: 11/2014 – 12/2016

Funded by: ESA/ESRIN (Contract No.: 4000112375/14/I-NB)

DLR

sertit

Project leader

Dr. Sandro Martinis (sandro.martinis@dlr.de)

Authors

Sandro Martinis[1], Stephen Clandillon[2], Simon Plank[1], André Twele[1], Claire Huber[2], Mathilde Caspard[2], Jérôme Maxant[2], Wenxi Cao[1], Sadri Haouet[2], Eva-Maria Fuchs[1]

[1]German Aerospace Center (DLR), German Remote Sensing Data Center (DFD), Oberpfaffenhofen, 82234 Wessling, Germany

[2]Service Régional de Traitement d'Image et de la Télédétection (SERTIT), Illkirch Graffenstaden, France

Table of Contents

1 Introduction

1.1 Objectives

Optical and radar satellite remote sensing have proven to provide essential crisis information in case of natural disasters, humanitarian relief activities and civil security issues in a growing number of cases through mechanisms such as the Copernicus Emergency Management Service (EMS) of the European Commission or the International Charter 'Space and Major Disasters'.
The aforementioned programs and initiatives make use of satellite-based rapid mapping services aimed at delivering reliable and accurate crisis information after natural hazards.
Although these services are increasingly operational, they need to be continuously updated and improved through research and development (R&D) activities. The principal objective of ASAPTERRA (Advancing SAR and Optical Methods for Rapid Mapping), the ESA-funded R&D project being described here, is to improve, automate and, hence, speed-up geo-information extraction procedures in the context of natural hazards response. This is performed through the development, implementation, testing and validation of novel image processing methods using optical and Synthetic Aperture Radar (SAR) data. The methods are mainly developed based on data of the German radar satellites TerraSAR-X and TanDEM-X, the French satellite missions Pléiades-1A/1B as well as the ESA missions Sentinel-1/2 with the aim to better characterize the potential and limitations of these sensors and their synergy. The resulting algorithms and techniques are evaluated in real case applications during rapid mapping activities.
The project is focussed on three types of natural hazards: floods, landslides and fires.

1.2 ASAPTERRA publication list

The following studies have been published within the ESA-funded project ASAPTERRA and have been used as basis for the content in chapter 2:

1. Martinis, S., Caspard, M., Plank, S., Clandillon, S., Haouet, S., 2017 (submitted): Mapping burn scars, fire severity and soil erosion susceptibility in southern France using multisensoral satellite data. IGARSS 2017, Fort Worth, USA, 23.-28.07.2017.
2. Plank, S., Jüssi, M., Martinis, S., Twele, A., 2017 (submitted): A Combining polarimetric Sentinel-1 and ALOS-2/PALSAR-2 imagery for mapping of flooded vegetation. IGARSS 2017, Fort Worth, USA, 23.-28.07.2017.
3. Cao, W., Plank, S., Martinis, S., 2017 (submitted): Automatic SAR-based Flood detection using hierarchical tile-ranking thresholding and fuzzy logic. IGARSS 2017, Fort Worth, USA, 23.-28.07.2017.
4. Martinis, S., Brcic, R., Plank, S., Tavri, A., Rodriguez Gonzalez, F., 2017 (submitted): The use of the Sentinel-1 InSAR Browse service on ESA's Geohazards Exploitation Platform for improved disaster monitoring. Fringe 2017, Helsinki, Finland, 05.-09.06.2017.

5. Cao, W., Twele, A., Martinis, S., Plank, S., 2017 (submitted): A three-class change detection methodology for SAR-data based on hypothesis testing and Markov Random Field modelling. International Journal of Remote Sensing.
6. Plank, S., Jüssi, M., Martinis, S., Twele, A, 2017 (submitted): Mapping of flooded vegetation by means of polarimetric Sentinel-1 and ALOS-2/PALSAR-2 imagery. International Journal of Remote Sensing.
7. Martinis, S., Clandillon, S., Twele, A., Huber, C., Plank, S., Maxant, J., Cao, W., Caspard, M., May, S., 2016: Improving the extraction of crisis information in the context of flood, landslide, and fire rapid mapping using SAR and optical remote sensing data. EGU 2016, Vienna, Austria, 17-22 April 2016.
8. Plank, S., Martinis, S., Twele, A., 2016: Combining pre-event optical and post-event polarimetric SAR data for rapid landslide mapping. TerraSAR-X/TanDEM-X Science Team Meeting 2016, Oberpfaffenhofen, Germany, 17-20 October 2016.
9. Huber, C., Clandillon, S., Martinis, S., Twele, A., Plank, S., Maxant, J., Cao, W., Haouet, S., Yésou, H., May, S., 2016: Improving the extraction of crisis information in the context of flood, fire, and landslide rapid mapping using SAR and optical remote sensing data. IGARSS 2016, Beijing, China, 10-15 July 2016.
10. Chow, C., Twele, A., Martinis, S., 2016: An assessment of the 'Height Above Nearest Drainage' terrain descriptor for the thematic enhancement of automatic SAR-based flood monitoring services. In: Proceedings of SPIE, SPIE Remote Sensing 2016, 26-29 September 2016, Edinburgh, United Kingdom.
11. Tavri, A. 2016: Flood monitoring based on multi-temporal Sentinel-1 data - a synergistic approach of amplitude data with interferometric coherence. Mater thesis, Technical University of Munich, 69 pages.
12. Twele, A., Cao, S., Plank, S., Martinis, S., 2016a: Sentinel-1 based flood mapping: a fully-automated processing chain. International Journal of Remote Sensing, 37:13, 2990-3004.
13. Plank, S., Twele, A., Martinis, S., 2016: Landslide mapping in vegetated areas using change detection based on optical and polarimetric SAR data. Remote Sensing, 8, 307, doi:10.3390/rs8040307.
14. Clandillon, S.; Bouillot, L.; Caspard, M.; Haouet, S.; May, S., 2016: Developing improved optical rapid mapping methods by combining Orfeo Tool Box and recent satellite data in the fire mapping domain, ESA Living Planet Symposium 2016, Prague, Czech Republic, 09-13 May 2016.
15. Plank, S., Martinis, S., Twele, A., 2016: Rapid landslide mapping by means of post-event polarimetric SAR imagery, ESA Living Planet Symposium 2016, Prague, Czech Republic, 09-13 May 2016.
16. Twele, A., Martinis, S., Cao, W., Plank, S., 2016b: Automated flood mapping and monitoring using Sentinel-1 data. ESA Living Planet Symposium, Prague, Czech Republic, 09-13 May, 2016.

17. Martinis, S., Rieke, C., Fissmer, B., 2015: Time series analysis of multi-frequency SAR backscatter and bistatic coherence in the context of flood mapping. Multitemp 2015, Annecy, 22-24 July 2015.
18. Plank, S., Hölbling, D., Eisank, C., Friedl, B., Martinis, S. and Twele, A., 2015: Comparing object-based landslide detection methods based on polarimetric SAR and optical satellite imagery – a case study in Taiwan. 7th International Workshop on Science and Applications of SAR Polarimetry and Polarimetric Interferometry, POLInSAR 2015, Frascati, Italy, 27.-30. Jan. 2015.
19. Fissmer, B., 2015: Multitemporal analysis andstatistical evaluation of radar backscatter and bi-Static coherence of flood affected areas. Mater thesis, University of Bochum, 73 pages.
20. Twele, A., Martinis, S. Cao, W., Plank, S., 2015: Inundation mapping using C- and X-band SAR data: From algorithms to fully-automated flood services. ESA Mapping Water Bodies from Space conference, Frascati, 18-19 March 2015.
21. Caspard, M., Haouet, S., Clandillon, S. (submitted): BURNOUT: a rapid mapping burnt area extraction tool. 14th International Wildland Fire Summit, 31 January 2017, Barcelona, Spain.

2 ASAPTERRA Research and Development Activities

2.1 Technical note on flood detection in rural areas

2.1.1 State-of-the-art

Introduction

Every year flood disasters occur in many regions of the globe and cause great losses. Flood extent maps derived from optical or Synthetic Aperture Radar (SAR)-based earth observation (EO) data can be a crucial information source for an effective flood disaster management by supporting humanitarian relief organisations and decision makers in their activities during the time-critical crisis response phase (Voigt et al. 2007). In addition they need a precise monitoring because over- and underestimations can have hard consequences, particularly on people. Besides disaster relief operations, such maps can serve as valuable distributed calibration and validation data for hydraulic models of river flow processes (e.g. Bates et al. 1997, Horritt 2000, Aronica et al. 2002, Hunter 2005, Horritt 2006, Pappenberger et al. 2007, Schumann et al. 2009, Hostache et al. 2009, Matgen et al. 2010) and improve the derivation of spatially accurate hazard maps utilised for spatial planning, flood prevention activities, and insurance risk management (e.g. De Moel et al. 2009).

Flood mapping based on optical data

In case of favourable weather conditions, optical EO data are the preferred information source for flood mapping due to their straightforward interpretability and rich information content. Examples for a successful utilisation of optical satellite data for flood mapping can be found in e.g. Blasco et al. (1992), Smith (1997), Wang et al. (2002), Peinado et al. (2003), Van der Sande (2003), Ahtonen et al. (2004), Brakenridge and Anderson (2005), and Ottinger et al. (2013). A detailed review of optical-based flood mapping is provided by Marcus and Fonstad (2008). However, as flood events often occur during long-lasting periods of persistent cloud cover, a systematic monitoring by optical imaging instruments is rarely feasible.

Visible spectral bands, but particularly near and short-wave infrared wavelengths are the most adapted for water detection. Water reflectance is generally low in the red and infrared spectrum, while higher in the blue and green wavelengths. But this theoretical behaviour of course varies according a water body`s texture (wind), its turbidity and water depth.

Since the 90s', many studies focused on the potential of the infrared domain and more particularly on the SWIR band for water and soil moisture detection. All concluded that EO satellite data with a SWIR band has an increased sensitivity to water and moisture. This leads to a better mapping of flooded and flood affected areas, even when draw off has started. On a colour composition using a SWIR band, the contrast between water bodies and the other landscape elements is far greater (fig. 2.1.1) (Yésou et al. 2003).

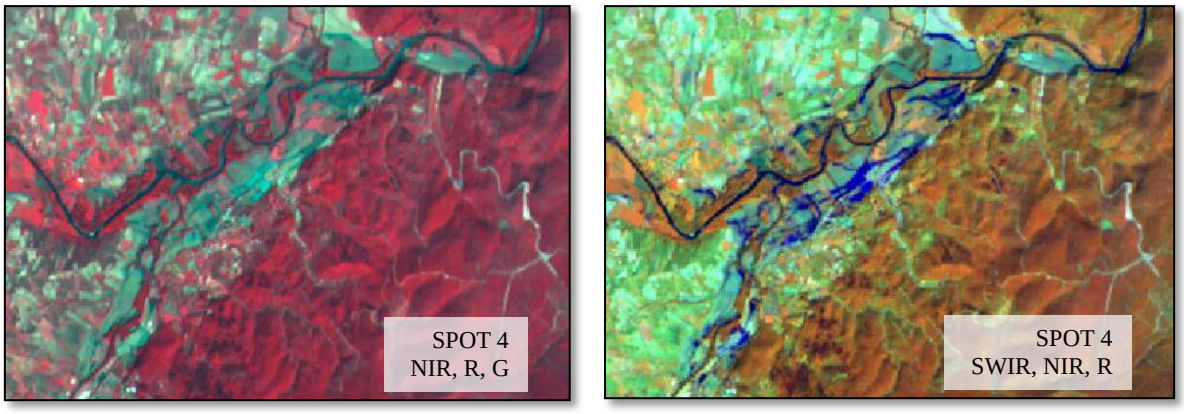

Figure 2.1.1: Contribution of SWIR band in flood detection – Gard Flood, September 2002 (Yésou et al. 2003).

The comparison between water extractions over the Central Alsace flood plain (France) on the same image (SPOT-4) but using two different band combinations - with and without SWIR - has shown that the classification accuracy of the final water surface increased by 7.0% with the SWIR (Clandillon et al. 1999).

Significant achievements have been made in water detection but despite those advancements only few algorithms offer a sufficient reliability for general practical use. Common water classification methods could be organised into few categories: Thematic classification including unsupervised classification (Jenny and McCarthy 2003), Euclidian classifiers, Support Vector Machines (SVM) (Gidudu Anthony 2007), Bayesian classifiers (Alecu Corina 2006, Young-Joon Jeon 2004), Decision Trees (Hu Zhuowei 2007), linear un-mixing, thresholding based on single bands (Leen-Kiat Soh 2005, Yuanzhi Zhang 2003) and two band spectral indices (Zhang Quiwen 2007) as well as visual interpretation. Also combinations of various methods are being used to improve accuracies of water extractions. Techniques based on single bands and indices are commonly used due to their simplicity and time-efficiency.

The spectral characteristics of water can change considerably depending on particle charge (turbidity) plus meteorological conditions (clouds, cloud shadows, wind), landcover/terrain (high vegetation, shadowing) and acquisition factors (sun-glint). To improve mapping potential more complex classification procedures need to be tested and applied. R&D for classification improvement is still an important issue (Brakenridge and Anderson 2006, Michael 2007). The greatest challenge is to achieve sufficient robustness and accuracy for producing reliable results independent from the imagery used.

Flood mapping based on SAR-data

For the purposes of systematic flood mapping and monitoring, the use of the microwave region of the electromagnetic spectrum offers some clear advantages compared to sensors operating in the visible, infrared or thermal range. Being an active monostatic instrument and therefore providing its

own source of illumination in the microwave range, SAR is characterised by nearly all-weather/day-night imaging capabilities as the emitted radar signal is able to penetrate clouds and the imaging process is independent from solar radiation. Over the last decades, spaceborne SAR systems have increasingly been used for flood extent mapping. While past and current SAR satellite and space shuttle radar missions with spatial resolutions of the categories HR2 to MR1 have a proven track-record for large-scale flood and inundation mapping in the X- (SIR-C/X-SAR, SRTM), C- (ERS-1/2 AMI, ENVISAT ASAR, RADARSAT-1, RISAT-1, SIR-C/X-SAR), and L-band domain (SEASAT-1, JERS-1, ALOS PALSAR-1/2, SIR-A/B/C/X-SAR), their capability for deriving flood parameters in complex and small-scale scenarios is limited. Since 2007, the successful launch of the European platforms TerraSAR-X/TanDEM-X and the COSMO-SkyMed constellation (CSK) consisting of four satellites marks a new generation of civil X-band SAR systems suitable for flood mapping purposes. These satellites provide data up to the 0.24 m spatial resolution (TerraSAR-X Staring SpotLight mode), permitting an operational derivation of detailed hydrological parameters from space during rapid mapping activities. The potential of these data has been demonstrated by several studies to support flood emergency situations (e.g. Giustarini et al. 2012, Kuenzer et al. 2013a, Kuenzer et al. 2013b, Martinis et al. 2009, 2011, 2013 and 2014, Martinis and Twele 2010, Mason et al. 2012, Matgen et al. 2011, Pulvirenti et al. 2011 and 2012, Pierdicca et al. 2013, Schumann et al. 2010). The Sentinel-1 satellite mission, operated by the European Space Agency (ESA) in the frame of the European Union Copernicus Programme, a constellation of two polar orbiting C-Band SAR sensors, will enable a systematic large-scale flood monitoring with a spatial resolution of 5 x 20 m in the standard Interferometric Wide (IW) Swath mode and a high temporal resolution of up to six days (Sentinel-1A and 1B) over large parts of the land surface. Sentinel-1 is designed to operate in a pre-programmed conflict-free mode which ensures a consistent long-term data archive for flood mapping purposes (Torres et al. 2012) enabling the implementation of fully-automated flood services (Twele et al. 2015, 2016a and 2106b).

Fully-automated flood services

The number of automatic flood mapping algorithms has significantly increased within the last years, particularly in the SAR domain (e.g. Martinis et al. 2009, Pulvirenti et al. 2011, Matgen et al. 2011), and in most cases a certain amount of user interaction is needed for data pre-processing, the collection and adaptation of auxiliary data as well as the preparation and dissemination of the crisis information to end users. Further, the utility of medium-resolution optical data, such as MODIS, for inundation mapping and monitoring, has been demonstrated in numerous flood events by the Dartmouth Flood Observatory (DFO, http://floodobservatory.colorado.edu/). Building upon this work, NASA's Goddard's Office of Applied Science proposes an automated global daily flood and surface water mapping service (http://oas.gsfc.nasa.gov/floodmap/). As one of the first SAR-based services, the Fast Access to Imagery for Rapid Exploitation (FAIRE) service hosted on the ESA's Grid Processing on Demand system (G-POD, http://gpod.eo.esa.int/) provides automatic SAR pre-processing and change detection capabilities which can be triggered on demand by a user via a web-

interface. The application has been extended with flood mapping capabilities which are based on a comparison of the SAR crisis image with corresponding archive/reference data acquired during normal water level conditions. A prototype automated processing algorithm for medium resolution surface water mapping based on systematic and global-scale ENVISAT ASAR Wide Swath acquisitions has been presented by Westerhoff et al. (2013). A further example is the Fully Automatic Aqua Processing Service (FAAPS) which aims to develop a future operational service delivering NRT flood extent maps generated from ESA satellite data (Schlaffer et al. 2012). A fully automated TerraSAR-X based flood service is presented by Martinis et al. (2015). The processing chain which is automatically triggered after satellite data delivery is comprised of SAR data pre-processing, computation and adaption of global auxiliary data, unsupervised initialisation of the classification as well as post-classification refinement by using a fuzzy logic-based approach.
The dissemination of flood maps resulting from this service is performed through an online service (see figure 2.1.2) which can be activated on-demand for emergency response purposes (i.e., when a flood situation evolves). During the course of the project, the processing chain of the TerraSAR-X Flood Service (TFS) has been adapted to Sentinel-1 data (Twele et al. 2015, 2016a and 2016b), which enables a systematic disaster monitoring with high spatial and temporal resolutions. In contrast to the TerraSAR-X Flood Service, this is a major advantage as the time-consuming step of tasking new satellite data can be omitted.

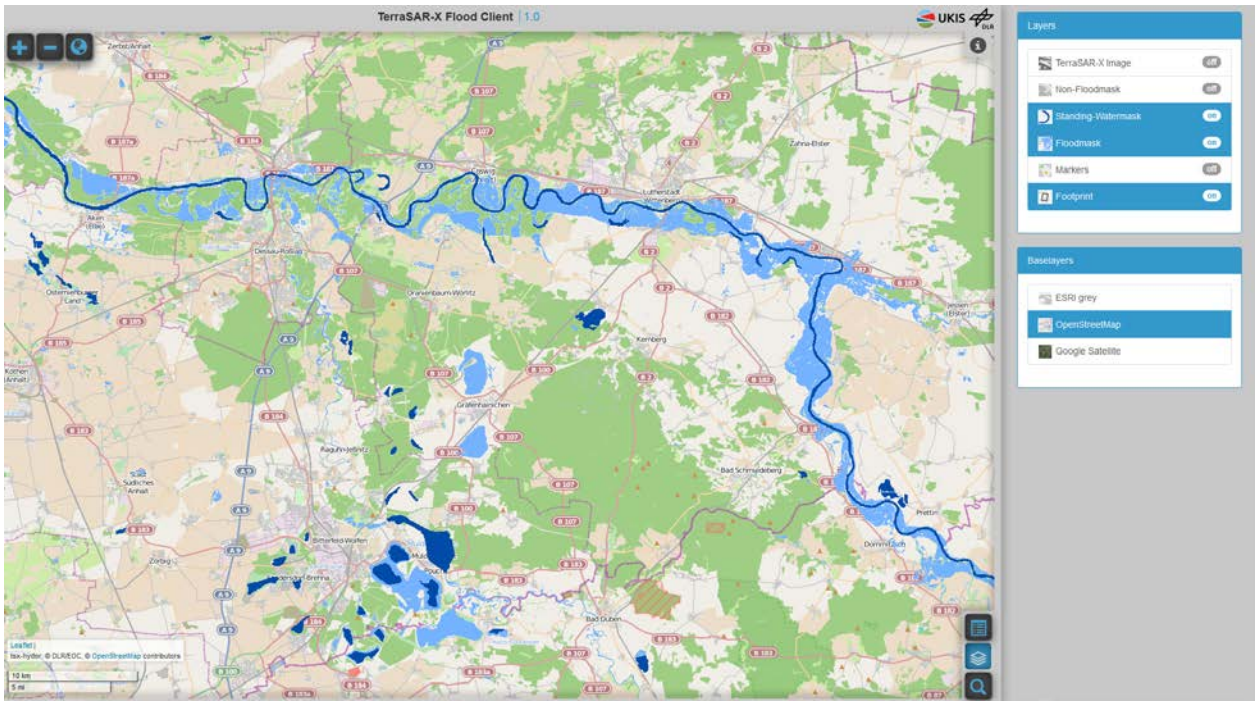

Figure 2.1.2: Web client of DLR's TerraSAR-X Flood Service (TFS).

Flood mapping in rural areas

The accuracy of SAR-based flood mapping can vary drastically in dependence of the land cover prevalent in a given scene. For instance, flood detection in urban areas is usually very challenging

due to shadowing effects from buildings as a result of the side-looking viewing geometry of SAR satellite systems. Also floods beneath vegetation layers are difficult to detect due to double bounce scattering resulting in a drastic increase of radar backscatter in such areas.

Some of these challenges demand for very specific solutions with respect to classification methodologies. For this reason, separate work packages are dedicated to flood detection in areas of partially submerged vegetation (see chapter 2.3) and flood detection in urban areas (see chapter 2.4). Nevertheless, also when disregarding these two specific cases, the detection of open flood surfaces in rural areas can be difficult since a number of factors (see tab. 2.1.1) can lead to either an over- or underestimation of the actual flood extent. Although shadowing effects from anthropogenic structures (e.g. buildings) are less dominant in rural areas, also vertical natural features, such as individual trees or forests, can cast shadows which can easily be misclassified as floods. While a skilled image interpreter might be able to use contextual information to separate such features from the flood surface, a semi- or fully-automated algorithm which mainly relies on the grey level of a given pixel is usually unable to differentiate between two features with similar backscattering characteristics. The utilisation of ancillary data (e.g. land cover or digital elevation data) to reduce misclassifications is thus mandatory. In case the shadow effects only affect a small group of pixels (e.g. the radar shadow from individual trees), the implementation of a minimum mapping unit (MMU) as a post-classification step can further help to reduce the number of overestimations in the classification.

Table 2.1.1: Factors leading to misclassification of flooding in SAR data as well as their occurrence and impact on the flood classification result (feature range: high +++, medium ++, low +) (Martinis et al. 2015, modified).

Flood overestimation		**Flood underestimation**	
Factor	**Occurrence/ Impact**	**Factor**	**Occurrence/ Impact**
Shadowing effects behind vertical objects (e.g. vegetation, topography, anthropogenic structures)	+++	Volume scattering of partially submerged vegetation and water surfaces completely covered by vegetation	+++
Smooth natural surface features (e.g. sand dunes, salt and clay pans, bare ground)	+++	Double bounce scattering of partially submerged vegetation	++
Smooth anthropogenic features (e.g. streets, airstrips)	++	Anthropogenic features on the water surface (e.g. ships, debris)	+
Heavy rain cells	+	Roughening of the water surface by wind, heavy rain or high flow velocity	+
		Layover effects on vertical objects (e.g. topography urban structures, vegetation)	+

Apart from radar shadowing, also certain unshaded natural surfaces such as sand dunes, salt clay pans or agricultural fields can exhibit backscatter levels similar to open water surfaces and may lead to an overestimation of the flood extent. Factors which usually occur less frequently are heavy rain cells leading to an overestimation particularly in short-wavelength SAR data (X-band). Although less frequently observed in inland water compared to oceans, strong wind conditions can roughen the water surface, leading to an increased backscatter level in dependence of SAR-polarisation, resulting in an underestimation in the flood extent.

Concerning the accuracy of optical-based flood mapping, a number of factors can lead to the under or over-estimation of flood water surfaces. Meteorological factors such as clouds can reduce the visibility of floods and cloud shadowing can lead to extra erroneous 'flood' surfaces. Wind can also perturb the spectral characteristics of water/flood surfaces. Floodwater spectral characteristics can change substantially due to: quantity of suspended particles and particle colour (turbidity), landcover/terrain can affect flood water visibility through high vegetation, terrain or building shadowing, submerged vegetation, and acquisition factors (sun-glint). Furthermore, the delineation of water surfaces can be complex due to confusion with water saturated soils (see tab. 2.1.2).

Table 2.1.2: Factors leading to misclassification of flooding in optical data as well as their occurrence and impact on the classification result (feature range: high +++, medium ++, low +).

Flood overestimation		**Flood underestimation**	
Factor	**Occurrence/ Impact**	**Factor**	**Occurrence/ Impact**
Shadowing effects of building, forest areas or trees	+++	Water turbidity	+++
Confusion between water and soil moisture	++	Partially submerged vegetation	++
Similar spectral signature of water with artificial surfaces	+	Sun glint and/or strong wind effects on water surfaces	+

References

1. Ahtonen, P., Euro, M., Hallikainen, M., Solbø, S., Johansen, B., Solheim, I., 2004: SAR and optical based algorithms for estimation of water bodies. Technical Report, FloodMan Project, Helsinki University of Technology, Helsinki, Finland.
2. Alecu Corina, O.S., 2006: Multi-resolution analysis of MODIS and ASTER satellite data for water classification. In Proceedings of the SPIE, the International Society for Optical Engineering.
3. Aronica, G., Bates, P. D., Horritt, M. S., 2002: Assessing the uncertainty in distributed model predictions using observed binary pattern information within GLUE. Hydrol Process, 16, 2001–2016.
4. Bates, P. D., Horritt, M. S., Smith, C. N., Mason, D. C., 1997: Integrating remote sensing observations of flood hydrology and hydraulic modelling. Hydrol Process, 11, 1777–1795.
5. Blasco F., Bellan, M. F., Chaudury, M. U., 1992: Estimating the extent of floods in Bangladesh using SPOT data. Remote Sens Environ, 39, 167–178.

6. Brakenridge, G. R., and Anderson, E., 2005: MODIS-based flood detection, mapping, and measurement: the potential for operational hydrological applications. Proceedings of the NATO Advanced Research Workshop, Baile Felix – Oradea, Romania.
7. Brakenridge, G. R., and Anderson, E., 2006: MODIS-based flood detection, mapping and measurement: the potential for operational hydrological applications. Transboundary Floods: Reducing Risks Through Flood Management, pp. 1-12.
8. Clandillon, S., Meyer, C., Bestault, C., Yesou, H., de Fraipont, P., 1999: SPOT 4 MIR: Evaluation thématique hydrologie/milieux humides. Validation des résultats obtenus sur la plaine d'Alsace au cours des projets pilotes SPOT 4 MIR: Décision d'aide à la Recherche No794/98/CNES/7378 - Rapport final SERTIT - CNES, 57p.
9. De Moel, H., Van Alphen, J., Aerts, J., 2009: Flood maps in Europe, methods, availability and use. Nat Hazard Earth Sys, 9, 289-301.
10. Gidudu Anthony, H.G., 2007: Classification of images using support vector machines. Cornell University, arXiv: 0709.3967v1, Library.
11. Giustarini, L., Hostache, R., Matgen, P., Schumann, G., Bates, P. D., Mason, D. C., 2012: A change detection approach to flood mapping in urban areas using TerraSAR-X. IEEE T Geosci Remote 51, 2417-2430.
12. Horritt, M. S., 2000: Calibration of a two-dimensional finite element flood flow model using satellite radar imagery. Water Resour Res, 36, 3279-3291.
13. Horritt, M. S., 2006: A methodology for the validation of uncertain flood inundation models. J Hydrol 326, 153-165.
14. Hostache, R., Matgen, P., Schumann, G., Puech, C., Hoffmann, L., Pfister, L., 2009: Water level estimation and reduction of hydraulic model calibration uncertainties using satellite SAR images of floods. IEEE T Geosci Remote, 47, 431.441.
15. Hu Zhuowei, G. H., 2007: Fast flooding information extraction in emergency response or flood disaster. ISPRS Workshop on Updating Geo-spatial Databases with Imagery & The 5th ISPRS Workshop on DMGISs. Urumchi, Xingjiang.
16. Hunter, N. M., Bates, P. D., Horritt, M. S., De Roo, P. J., Werner, M., 2005: Utility of different data types for flood inundation models within a GLUE framework. Hydrol Earth Syst Sc, 9, 412-430.
17. Jenny, M., McCarthy, T. G., 2003: Flooding patterns of the Okavango wetland in Botswana between 1972 and 2000. AMBIO: A journal of the Human Environment.
18. Kuenzer, C., Huadong, G., Huth, J., Leinenkugel, P., Xinwu, L., Dech, S., 2013b: Flood mapping and flood dynamics of the Mekong Delta: ENVISAT-ASAR-WSM based time series analyses. Remote Sensing 5, 687–715.
19. Kuenzer, C., Guo, H., Schlegel, I., Tuan, V. Q., Li, X., Dech, S., 2013a: Varying scale and capability of Envisat ASAR-WSM, TerraSAR-X Scansar and TerraSAR-X Stripmap data to assess urban flood situations: A case study of the Mekong delta in Can Tho province. Remote Sensing, 5, 5122-5142.
20. Leen-Kiat Soh, C.T., 2005: Segmentation of satellite imagery of natural scenes using data mining. IEEE Transactin On Geoscience and Remote Sensing, p. vol. 37(2) 10861099.
21. Marcus, W. A., Fonstad, M. A., 2008: Optical remote mapping of rivers at sub-meter resolution and watershed extents. Earth Surf. Processes Landforms, 33, 4-24.
22. Martinis, S., Twele, A., Voigt, S., 2009: Towards operational near real-time flood detection using a split-based automatic thresholding procedure on high resolution TerraSAR-X data. Nat Hazard Earth Syst, 9, 303-314.

23. Martinis, S., Twele, A., Voigt, S., 2011: Unsupervised extraction of flood-induced backscatter changes in SAR data using Markov image modeling on irregular graphs. IEEE T Geosci Remote, 49, 251-263.
24. Martinis, S., Twele, A., Strobl, C., Kersten, J., Stein, E., 2013: A multi-scale flood monitoring system based on fully automatic MODIS and TerraSAR-X processing chains. Remote Sensing, 5, 5598-5619.
25. Martinis, S., Twele, A., 2010: A hierarchical spatio-temporal Markov model for improved flood mapping using multi-temporal X-band SAR data. Remote Sensing, 2, 2240-2258.
26. Martinis, S., Kersten, J., Twele, A., 2015: A fully automated TerraSAR-X based flood service. ISPRS J Photogramm.
27. Martinis, S., Kuenzer, C., Twele, A., 2015: Flood studies using Synthetic Aperture Radar data. Remote Sensing of Water Resources, Disasters and Urban Studies, Taylor & Francis, submitted.
28. Mason, D., Davenport, I., Neal, J., Schumann, G., Bates, P., 2012: Near real-time flood detection in urban areas and rural areas using high resolution synthetic aperture radar images. IEEE Trans. Geosci. Remote Sensing, 50, 3041-3052.
29. Matgen, P., Hostache, R., Schumann, G., Pfister, L., Hoffman, L., Svanije, H. H. G., 2011: Towards an automated SAR based flood monitoring system: Lessons learned from two case studies. Phys Chem Earth 36, 241-252.
30. Matgen, P., Montanari, M., Hostache, R., Pfister, L., Hoffmann, L., Plaza, D., Pauwels, V. R. N., De Lannoy, G. J. M., De Keyser, R., Savenije, H. H. G., 2010: Towards the sequential assimilation of SAR-derived water stages into hydraulic models using the particle filter: proof of concept. Hydrol Earth Syst Sc, 14, 1773-1785.
31. Michael, 2007: Multitemporal Remote Sensing for mapping and monitoring Floods an approach involves validation of the KAFRIBA. Master Thesis.
32. Ottinger, M., Kuenzer, C., Liu, G., Wang, S., Dech, S., 2013: Monitoring land cover dynamics in the Yellow River Delta from 1995 to 2010 based on Landsat 5 TM. Appl Geogr, 44, 53-68.
33. Pappenberger, F., Frodsham, K., Beven, K., Romanowicz, R., Matgen, P., 2007: Fuzzy set approach to calibrating distributed flood inundation models using remote sensing observations. Hydrol Earth Syst Sc, 11, 739-752.
34. Peinado, O., Kuenzer, C., Voigt, S., Reinartz, P., Mehl, H., 2003: Fernerkundung und GIS im Katastrophenmangement – die Elbe Flut 2003: Angewandte Geographische Informationsverarbeitung XV. Beitraege zum AGIT-Symposium Salzburg 2003, Heidelberg, Wichmann, 342-348.
35. Pierdicca, N., Pulvirenti, L., Chini, M., Guerriero, L., Candela, L., 2013: Observing floods from space: Experience gained from COSMO-SkyMed observations. Acta Astronaut, 84, 122-133.
36. Pulvirenti, L., Chini, M., Marzano, F. S., Pierdicca, N., Mori, S., Guerriero, L., Boni, G., Candela, L., 2012: Detection of floods and heavy rain using Cosmo-SkyMed data: The event in Northwestern Italy of November 2011. Proc. of IEEE International Geoscience and Remote Sensing Symposium (IGARSS 2012), Munich, Germany, 22-27 July 2012, 3026-3029.
37. Pulvirenti, L., Pierdicca, N., Chini, M., Guerriero, L., 2011: An algorithm for operational flood mapping from Synthetic Aperture Radar (SAR) data using fuzzy logic. Nat Hazard Earth Sys, 11, 529-540.
38. Pulvirenti, L., Pierdicca, N., Chini, M., Guerriero, L., 2013: Monitoring flood evolution in vegetated areas using COSMO-SkyMed data: The Tuscany 2009 case study. IEEE J Sel Top Appl, 99, 1-10.
39. Schlaffer, S., Hollaus, M., Wagner, W., Matgen, P., 2012: Flood delineation from synthetic aperture radar data with the help of a priori knowledge from historical acquisitions and digital elevation models in support of near-real-time flood mapping. In: Proceedings of SPIE, Earth

Resources and Environmental Remote Sensing/GIS Applications III, Edinburgh, 853813-1 - 853813-9.
40. Schumann, G., di Baldassarre, G. D., Paul, P. D., 2009: The utility of spaceborne radar to render flood inundation maps based on multialgorithm ensembles. IEEE T Geosci Remote, 47, 2801-2807.
41. Schumann, G., di Baldassarre, G. D., Alsdorf, D., Bates, P. D., 2010: Near real-time flood wave approximation on large rivers from space: Application to the River Po, Italy. Water Resour Res, 46, 1–8.
42. Smith, L. C., 1997: Satellite remote sensing of river inundation area, stage, and discharge: A review. Hydrol Process, 11, 1427-1439.
43. Torres, R., Snoeij, P., Geudtner, D., Bibby, D., Davidson, M., Attema, E., Potin, P., Rommen, B., Floury, N., et al., 2012: GMES Sentinel-1 mission, Remote Sens Environ, 120, 9-24.
44. Twele, A., Martinis, S., Cao, W., Plank, S., 2015: Inundation mapping using C- and X-band SAR data: From algorithms to fully-automated flood services. Mapping Water Bodies from Space (MWBS 2015), 18-19 March 2015, Frascati, Italy, 46-47.
45. Twele, A., Cao, S., Plank, S., Martinis, S., 2016a: Sentinel-1 based flood mapping: a fully-automated processing chain. International Journal of Remote Sensing, 37:13, 2990-3004.
46. Twele, A., Martinis, S., Cao, W., Plank, S., 2016b: Automated flood mapping and monitoring using Sentinel-1 data. ESA Living Planet Symposium, Prague, Czech Republic, 09-13 May, 2016.
47. Van der Sande, C. J., de Jong, S. M., De Roo, A. P. J., 2003: A segmentation and classification approach of IKONOS-2 imagery for land cover mapping to assist flood risk and flood damage assessment. Int J Appl Earth Obs, 4, 217-229.
48. Voigt, S., Kemper, T., Riedlinger, T., Kiefl, R., Scholte, K., Mehl, H., 2007: Satellite image analysis for disaster and crisis-management support. IEEE T Geosci Remote, 45, 1520-1528.
49. Wang, Y., Colby, J. D., Mulcahy, K. A., 2002: An efficient method for mapping flood extent in a coastal flood plain using Landsat TM and DEM data. Int J Remote Sens, 23, 3681-3696.
50. Westerhoff, R. S., Kleuskens, M. P. H., Winsemius, H. C., Huizinga, H. J., Brakenridge, G. R., Bishop, C., 2013: Automated global water mapping based on wide-swath orbital synthetic-aperture radar. Hydrol Earth Syst Sc, 17, 651-663.
51. Yesou, H., Clandillon, S., Allenbach, B., Bestault, C., de Fraipont, P., 2003: Exploitation de données SPOT 5, SPOT 4 et SPOT 2 pour la cartographie des zones affectées par les inondations de type Cévenols les 9-10 septembre 2002 dans le département du Gard, SIRNAT, Les Journées pour la Prévention des Risques, 29-30 January 2003, BRGM, Orléans, 6 p.
52. Young-Joon Jeon, J. G. C. I., 2004: A study on supervised classification of remote sensing satellite image by bayesian algorithm using average fuzzy intracluster distance. IWCIA, pp. 597-606.
53. Yuanzhi Zhang, J. T., 2003: Water quality retrievals from combined Landsat TM data and ERS-2 SAR data in the Gulf of Finland. IEEE Transacrtion on GEOSCIENCE AND REMOTE SENSING, pp. 0196-2892.
54. Zhang Quiwen, W. C., 2007: Automatic extraction of water body based on EOS/MODIS remotely sensed imagery. In Proceedings of the SPIE, pp. Volume 6786, 678642.

2.1.2 SAR-based flood detection in rural areas

2.1.2.1 Single temporal flood detection

Since the establishment of DLR's ZKI (Center for Satellite-Based Crisis Information), the development of EO-based methodologies for the rapid mapping of flood situations in rural areas has been of major concern. This is can be especially contributed to the fact that inundations constitute the majority of all ZKI-activations as well as activations of the International Charter 'Space and Major Disasters'.

These requirements have led to the development of dedicated SAR-based flood mapping tools ("AFD" and "RaMaFlood") which have been utilised within numerous rapid mapping activities of flood situations since 2008. The core of these tools is an automatic tile-based thresholding approach (Martinis et al. 2009, Martinis and Twele 2010, Martinis et al. 2011) which allows separating inundated areas from land-areas without any user interaction.

Since 2012, the SAR-based flood detection algorithm has been substantially extended and refined in robustness and transferability to guarantee high classification accuracy under different environmental conditions and sensor configurations with the ultimate goal to allow its implementation in an automatic processing chain for TerraSAR-X data (Martinis et al. 2015). The processing chain including TerraSAR-X data pre-processing, computation and adaption of global auxiliary data, unsupervised initialisation of the classification as well as post-classification refinement by using a fuzzy logic-based approach is automatically triggered after new TerraSAR-X data is available on the delivery server. The dissemination of flood maps resulting from the service is performed through a dedicated web client (see fig. 2.1.2). With respect to accuracy and computational effort, experiments performed on a data set of ~400 different TerraSAR-X scenes acquired during flooding all over the world with different sensor configurations confirmed the robustness and effectiveness of the flood mapping service. Currently, the flood mapping service is activated on-demand in case of emergencies (e.g. in the framework of the 'International Charter Space and Major Disasters') by tasking suitable TerraSAR-X new acquisitions

The processing chain of the TerraSAR-X flood service (Martinis et al. 2015) has recently been adapted to the new ESA's C-band SAR mission Sentinel-1 (Twele et al. 2015, 2016b). In the frame of ASAPTERRA, the current prototype has further being improved in robustness and its accuracy has been assessed based on several test sites (Twele at al. 2016a). Both thematic processors (TerraSAR-X and Sentinel-1 based) have further been enhanced through the integration of the "Height above nearest drainage" (HAND) index (Rennó et al. 2008) which helps to reduce water look-alikes depending on the hydrologic-topographic setting. The HAND index will be calculated near-globally based on elevation and drainage direction information provided by the Hydrosheds mapping product (see chapter 2.2.4).

The processing steps of the Sentinel-1 processing chain can be divided into six main parts (see fig. 2.1.3):

1) Data ingestion,
2) Data preprocessing including geometric correction and radiometric calibration,
3) Initial classification using automatic thresholding,
4) Fuzzy logic-based classification refinement,
5) Final classification including reference water masks and the HAND-index,
6) and the dissemination of the results.

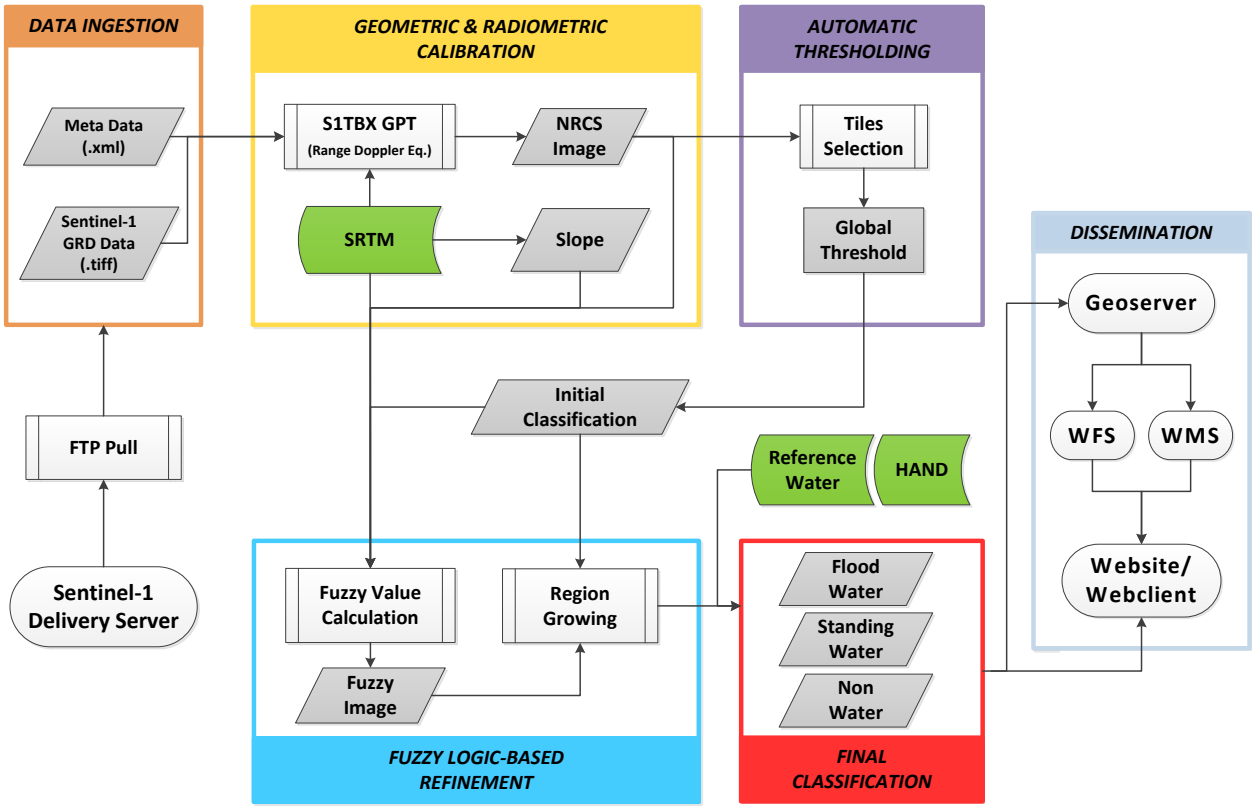

Figure 1.1.3: Processing chain of the Sentinel-1 based flood service (prototype).

The processing chain is activated through a Python script which routinely polls the data delivery server (e.g. FTP-site) for new data. In order to allow an immediate processing, data streams from the Collaborative Ground Segment and ESA Sentinel Data Hub can directly be ingested into the processing chain. In an experimental study, a near real-time (NRT) data access to Sentinel-1 data through DFD's ground station in Neustrelitz is currently being implemented to allow an even faster data access for scenes acquired over European territories. Once new data are found, the data are downloaded to the local file system and the thematic processor is executed. After unzipping the data, the folder structure is searched for files relevant for the further processing, namely Sentinel-1 data in GeoTIFF-format and XML metadata used for radiometric calibration. During the preprocessing step, a range doppler terrain correction of Sentinel-1 data and radiometric calibration

to sigma naught (dB) is performed using the graph processing tool (GPT) of the ESA Sentinel-1 Toolbox (S1TBX), which allows an execution of this processing step within a fully automated processing chain. The SRTM-tiles corresponding to a given Sentinel-1 scene are automatically downloaded by the S1TBX and transformed from sensor coordinate system (Ground Range Detected - GRD) to geographical coordinates (lat/lon, WGS84). After data pre-processing using the S1TBX, the calibrated data is filtered to reduce the SAR-inherent speckle noise. The result of the pre-processing is a reprojected, radiometrically calibrated and rescaled normalised radar cross section (NRCS) image.

The subsequent classification step can be subdivided into three parts: a) a tile-based initial classification using an automatic thresholding algorithm, b) a fuzzy-logic based post-classification, and c) the final classification including reference water masks and the exclude layer derived from the HAND-index. The tile-based initial classification divides the SAR image into a set of tiles, from which a maximum of five tiles are selected to derive the global optimal threshold for flood detection. This result is then improved through a fuzzy-logic based post-classification according to fuzzy values calculated from backscatter, DEM, slope and the size of individual flood objects. The elements of the fuzzy set are defined by standard *S* and *Z* membership functions (Pal and Rosenfeld 1988), which express the degree of an element's membership $\boldsymbol{m_f}$ to the class water. The fuzzy threshold values of each element are either determined according to statistical computations or are set empirically. The average of the individual membership degrees is computed for each pixel to combine all fuzzy elements into one composite fuzzy set. Subsequently, the flood mask is derived through a threshold defuzzification step, which transforms each image element with a membership degree > 0.6 into a discrete thematic class. Subsequently, the exclusion mask based on the HAND-index (see chapter 2.2.4) is applied to mask out potential misclassifications in all areas situated ≥15 m above the drainage network. With the aid of the reference water mask (see chapter 2.2.2), it is then possible to classify the SAR image into three types of pixels: a) flood, b) non-flood, and c) standing water.

The output is stored in the local file system and the results can be automatically disseminated via a web-based user interface. While this user interface still needs to be developed for Sentinel-1 data, a comparable interface already exists for the MODIS and TerraSAR-X flood processing chains.

In the following sections, first results based on a prototype of the Sentinel-1 based processing chain, including a cross-comparison to the TerraSAR-X flood service, are presented.

Test site: Floods in Malawi/Mozambique, January 2015

The first test site comprises a flood situation which occurred in the border region between Southern Malawi and Northern Mozambique at the end of January 2015. The flood situation was captured by a Sentinel-1 scene acquired on 28 January 2015 in IW mode and VV-polarisation. A subset of the respective scene is shown in figure 2.1.4.

The main flood surface in the center of the scene is easily discernible through its relatively dark backscatter pattern. As a result of differing environmental conditions (e.g. wind and flow velocity)

there is certain variability in the flood surface with a backscatter coefficient ranging from -25 dB up to -15 dB. Potential sources for misclassifications include fairly bare soils at the borders of the main flood plain (backscatter coefficient ranging from -10 dB up to -16dB) and a small number of areas with topographically-induced shadow. The scene was automatically classified with the prototypic Sentinel-1 flood processing chain in less than 27 minutes on an Intel Xeon CPU with 3.4 GHz and 32 GB of RAM running Windows 7 (64 bit). The fuzzy threshold was automatically derived between a = -19 dB and b = -15.34 dB. The classification result is shown in figure 2.1.5, including a visualisation of the HAND-based exclude layer in green color.

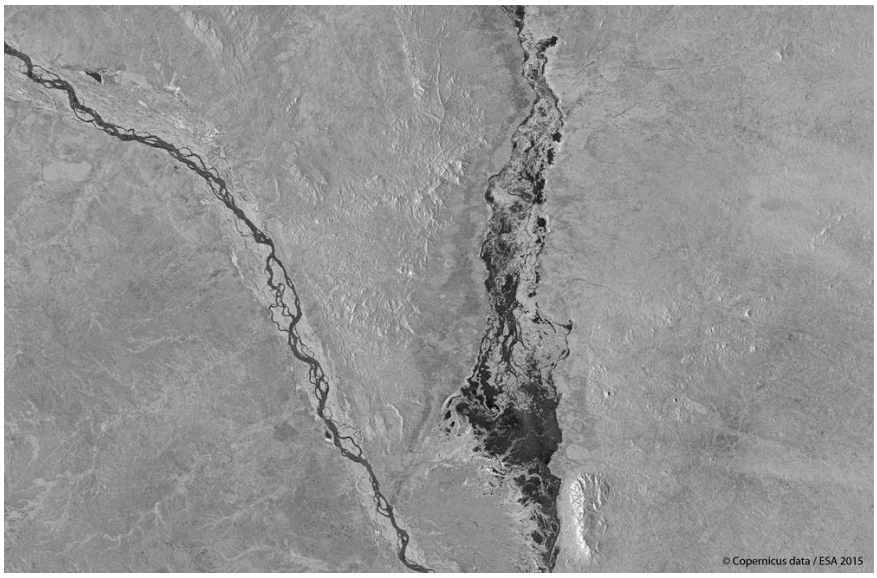

Figure 2.1.4: Sentinel-1 scene subset of the Malawi/Mozambique 2015 floods, mode: IW, acquisition date: 2015-01-18, polarisation: VV.

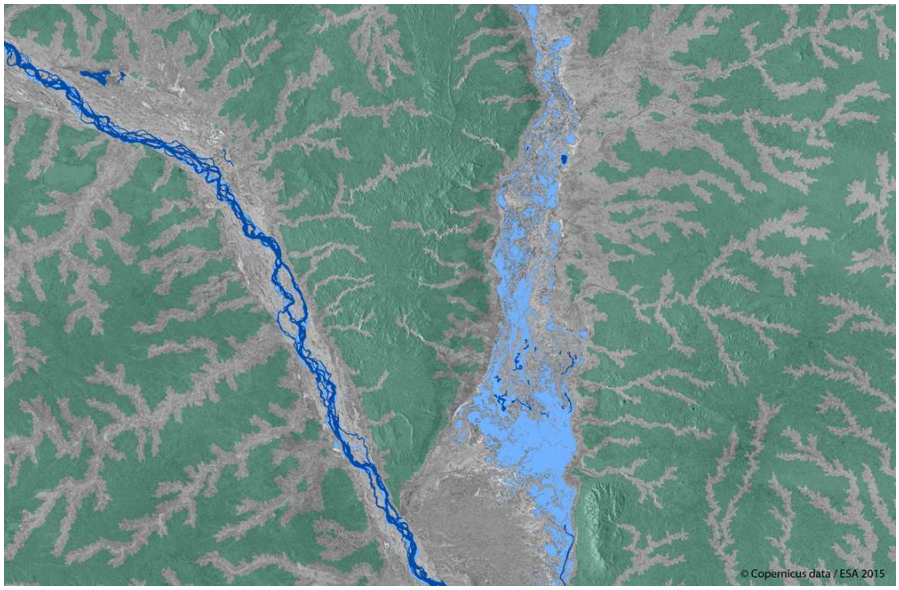

Figure 2.1.5: Classification result of the automatic Sentinel-1 based processing chain. Reference water mask: blue, flood extent: light blue, HAND-based exclude layer: green.

A qualitative analysis including a comparison of the original SAR-scene with the derived classification indicates a very satisfying accuracy of the flood extent, with only a low number of misclassifications. A majority of potential misclassifications have been effectively reduced through a combination of different fuzzy sets and the HAND-based exclude layer.

Test site: Floods in the Balkans, May 2014

In order to cross-compare the performance and classification accuracy of the Sentinel-1 flood processor prototype to the existing TerraSAR-X based processing chain, a test site located in the Balkans at the border region between Serbia and Bosnia Herzegovina has been selected. Located at the confluence between the Sava and Drina River, the terrain is relatively flat with elevations ranging from 74 up to 90m. The land cover is dominated by agriculture and a forested area is located in the north-western part of the test site. On 14 May 2014, a heavy rainfall event caused torrential floods across the region, destroying bridges and infrastructure, and leading to numerous landslides.

The satellite data analysed for this flood event comprise a TerraSAR-X Stripmap scene acquired on 21 May 2015 in HH-polarisation and a Sentinel-1 Stripmap (S3-beam) scene acquired on 24 May 2015 in dual-polarisation (HH/HV). Due to the superiority of HH- over HV-polarisation for flood mapping and better comparability to the TerraSAR-X scene, the Sentinel-1 analysis was based on the HH-polarised channel. Although the time-difference between both scenes is three days, the flood conditions remained very stable during this time frame (see upper row of fig. 2.1.6 for a visual comparison). Due to HH-polarisation, which is less sensitive to wind-induced roughening of the water surface, the flooded areas can easily be discerned from non-flooded regions in both X- and C-band data due to their low backscatter signature and further show a relatively low variability of backscatter levels. Major differences in the backscatter levels between X- and C-band data can be observed in agricultural areas, where the backscatter level of Sentinel-1 data is significantly lower. Such differences are potentially caused by the higher penetration depth of C-band data with respect to vegetation and soils and a higher amount of volume scattering in vegetated areas compared to a stronger canopy scattering of X-band data. As an additional factor and when presuming wet soil conditions due to strong rainfall events, the amplitude between the differing penetration depths of both radar wavelengths is higher than in soils with a lower moisture content (Behari 2005).

Figure 2.1.6 (lower row) shows a comparison of the classification results calculated by the TerraSAR-X and Sentinel-1 flood processors for scenes acquired during the Balkans floods in May 2014. A first qualitative analysis including a cross-comparison between Sentinel-1 and TerraSAR-X and a comparison of the original SAR-scene with derived classification indicates a very satisfying accuracy of the flood extent. Although the backscatter level of agricultural areas is relatively low in Sentinel-1 data and less impact of DEM-based classification refinement due to comparably flat terrain characteristics, no major misclassifications (i.e. “false alarms”) can be observed.

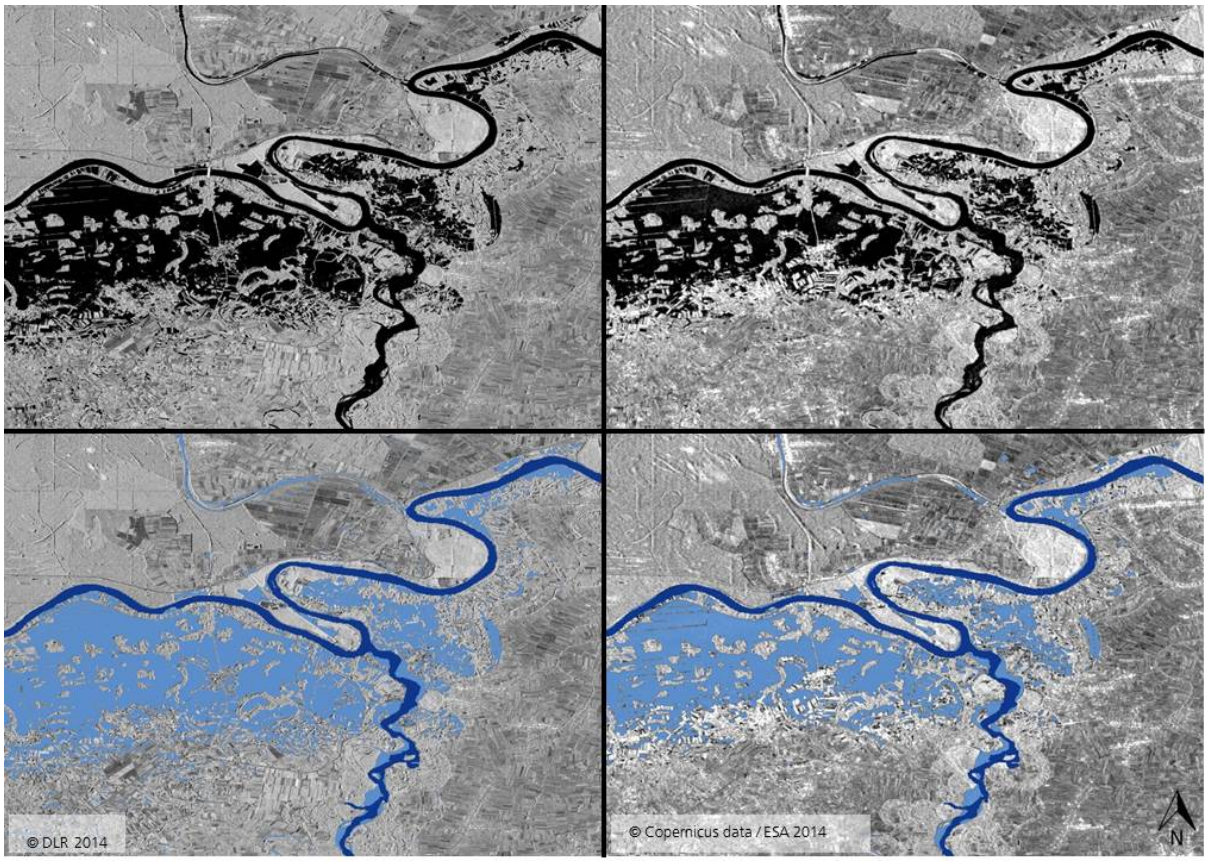

Figure 2.1.6: Floods in the Balkans 2014. Upper row (left to right): TerraSAR-X Stripmap scene (21/05/2014), Sentinel-1 Stripmap S3 (24/05/2014); lower row: Automatic classification results from the TerraSAR-X (left) and Sentinel-1 (right) flood processors.

Validation site: Floods in Greece/Turkey, March 2015

Introduction

For a quantitative accuracy assessment of the Sentinel-1 based flood processor, a validation site at the border between Greece and Turkey was chosen. The validation data consists of two subsets of a Sentinel-1 GRD VV/VH scene (ascending, relative orbit: 29) acquired on 12 March 2015. Each subset comprises an area of approx. 5000 x 3800m at River Evros, where a long-lasting flood situation which started in February 2015 caused widespread flooding of farmland (fig. 2.17).
The thematic accuracy has been assessed separately for both standard polarisation configurations (VV and VH) which are available using routinely acquired IW mode Sentinel-1 data. A reference water mask was generated by visual interpretation and manual digitalisation of a pan-sharpened WorldView-2 scene of 0.5m spatial resolution which was acquired on 11 March 2015 (see fig. 2.1.10a and 2.1.11a). Due to a time difference of ~31 hours between the Sentinel-1 and WorldView-2 data set, stable flood conditions have been ascertained using consecutive SAR and optical satellite acquisitions. No significant change in water levels could be observed.

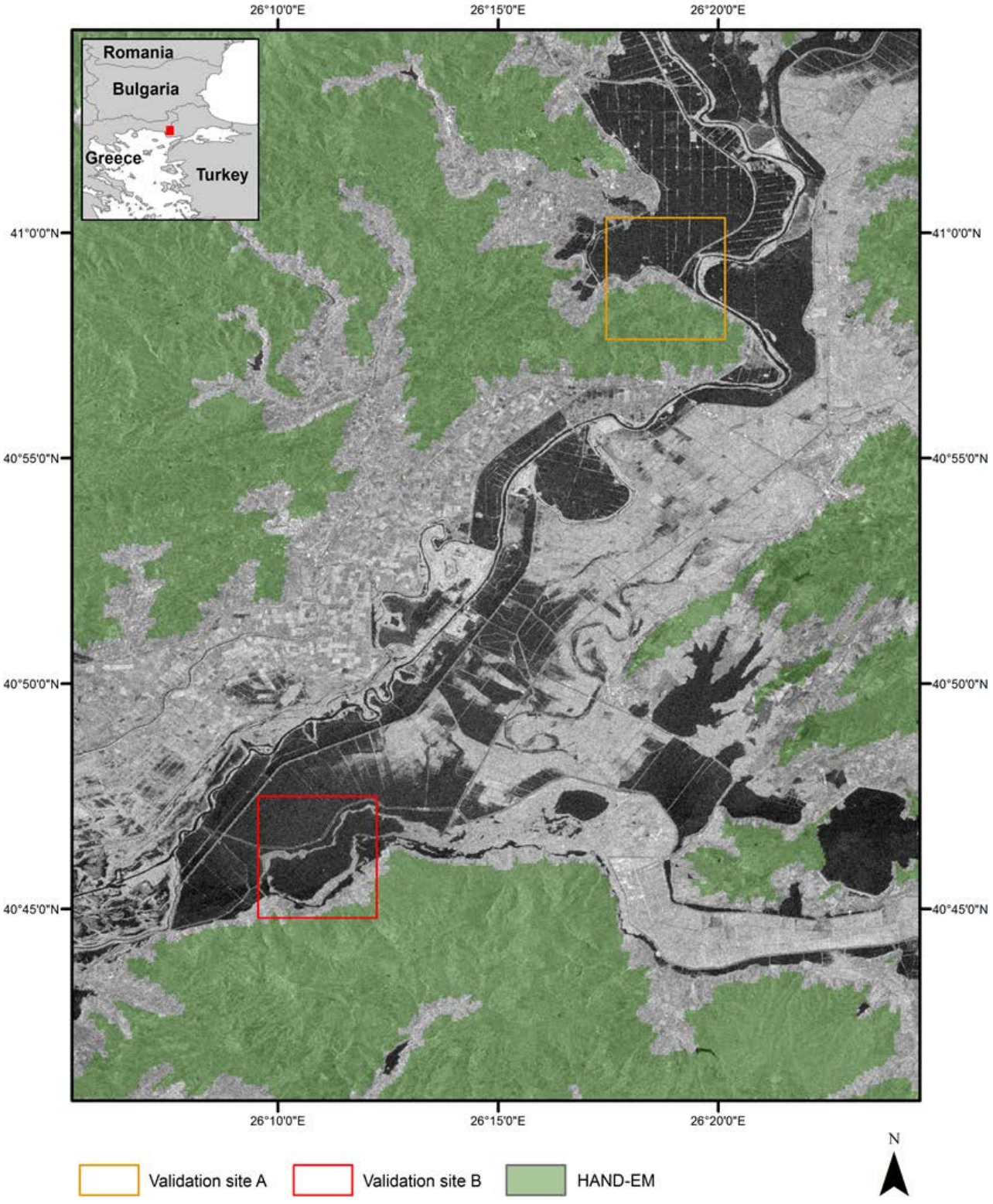

Figure 2.1.7: Overview of validation site locations. Background: Sentinel-1 scene acquired 12 March 2015, VV polarisation. HAND-EM: Exclusion mask derived from the "Height above nearest drainage" (HAND) index (Source: Twele et al. 2016b).

Accuracy assessment

The performance of the proposed algorithm is evaluated by comparing the classification results of the automatic Sentinel-1 based processing chain to the manually derived water extent of the WorldView-2 data set. Producer's (PA), user's (UA) and overall (OA) accuracy as well as the KHAT coefficient have been calculated for the classes "open water" and "other".
In table 2.1.3 and figure 2.1.8, the classification accuracies for the first validation site ("A") are listed. While no major differences between the classification accuracy of VV and VH polarisation can be observed, VV-polarised data consistently reached higher user's, producer's and overall accuracies. The KHAT coefficient of 0.91 for VV in contrast to 0.88 for VH polarisation confirms this observation.

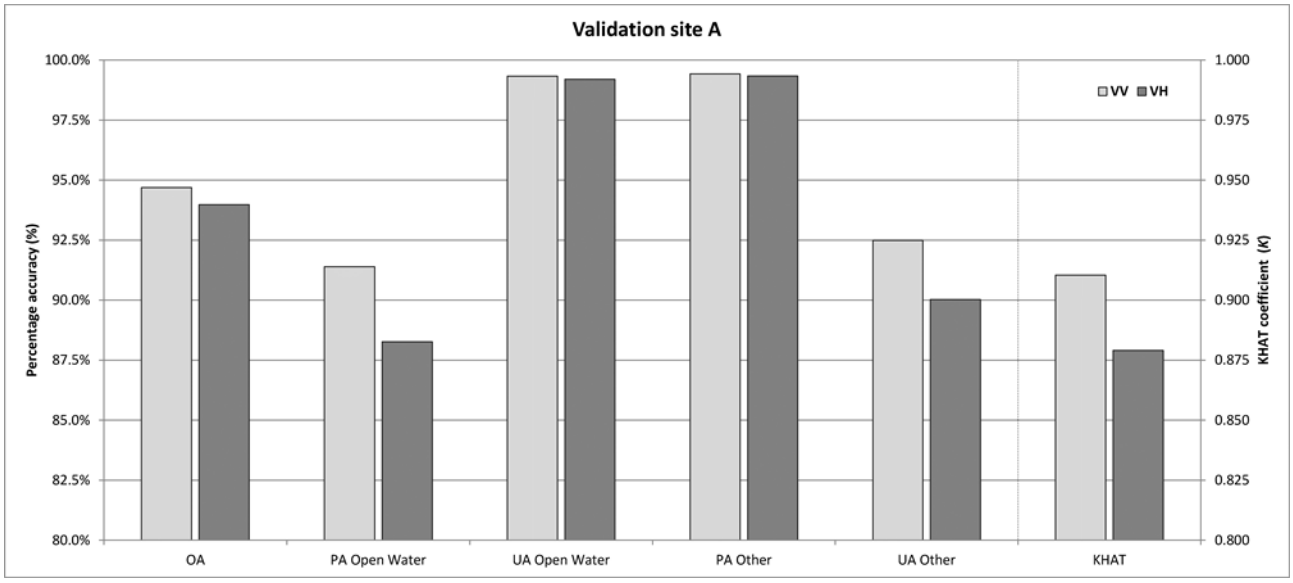

Figure 2.1.8: Classification accuracies for validation site A.

Table 2.1.3: Classification accuracies for validation site A (Source: Twele et al. 2016b).

Polarisation	OA	PA Open Water	UA Open Water	PA Other	UA Other	KHAT
VV	94.69%	91.39%	99.33%	99.43%	92.49%	0.91
VH	93.98%	88.26%	99.20%	99.34%	90.03%	0.88

With respect to OAs and KHAT coefficients, the results obtained for validation site B (see tab. 2.1.4 and fig. 2.1.9) are fairly consistent to validation site A with VV polarisation performing slightly better than VH polarisation. However, UAs and PAs obtained for the individual classes ("open water" and "other") show a larger variability. While VH polarisation offers the highest PA and VV polarisation the highest UA for the open water class, the PA for the remaining class ("other") is over 10.0% higher for VV compared to VH polarisation. In contrast, the UA of VH is over 6.0% higher than that of VV polarisation.

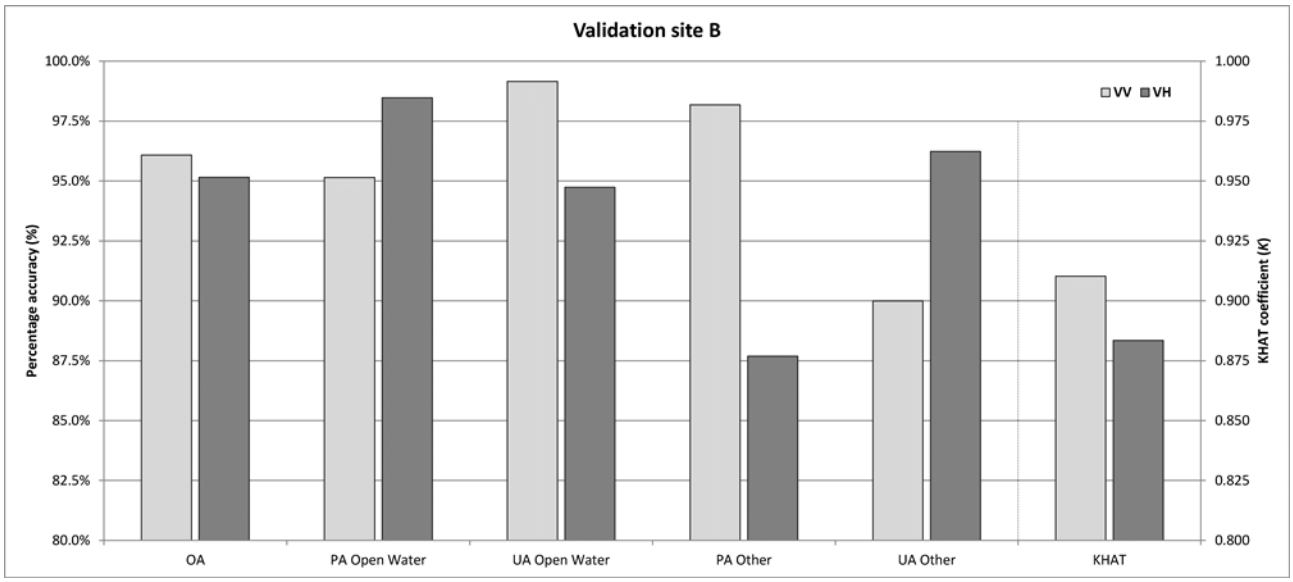

Figure 2.1.9: Classification accuracies for validation site B.

Table 2.1.4: Classification accuracies for validation site B (Source: Twele et al. 2016b).

Polarisation	OA	PA Open Water	UA Open Water	PA Other	UA Other	KHAT
VV	96.08%	95.15%	99.16%	98.18%	89.99%	0.91
VH	95.16%	98.47%	94.74%	87.69%	96.24%	0.88

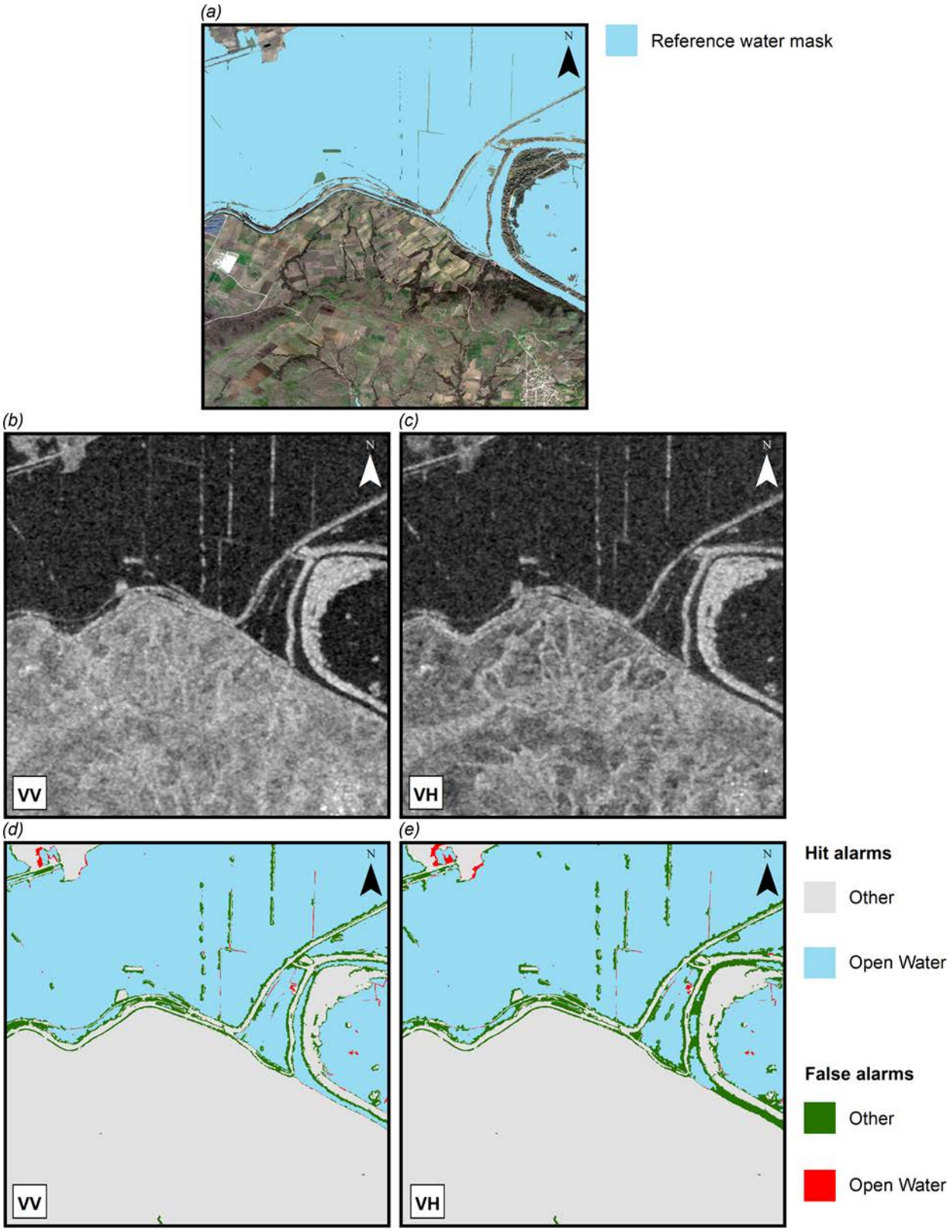

Figure 2.1.10: Subsets for validation site A: a) WorldView-2 scene acquired on 11 March 2015, band combination 5-3-2 (natural colour). Overlay: reference water mask b) Sentinel-1 scene acquired on 12 March 2015 in VV polarisation and c) in VH polarisation d) classification results for VV-polarised and e) for VH-polarised data (Source: Twele et al. 2016b).

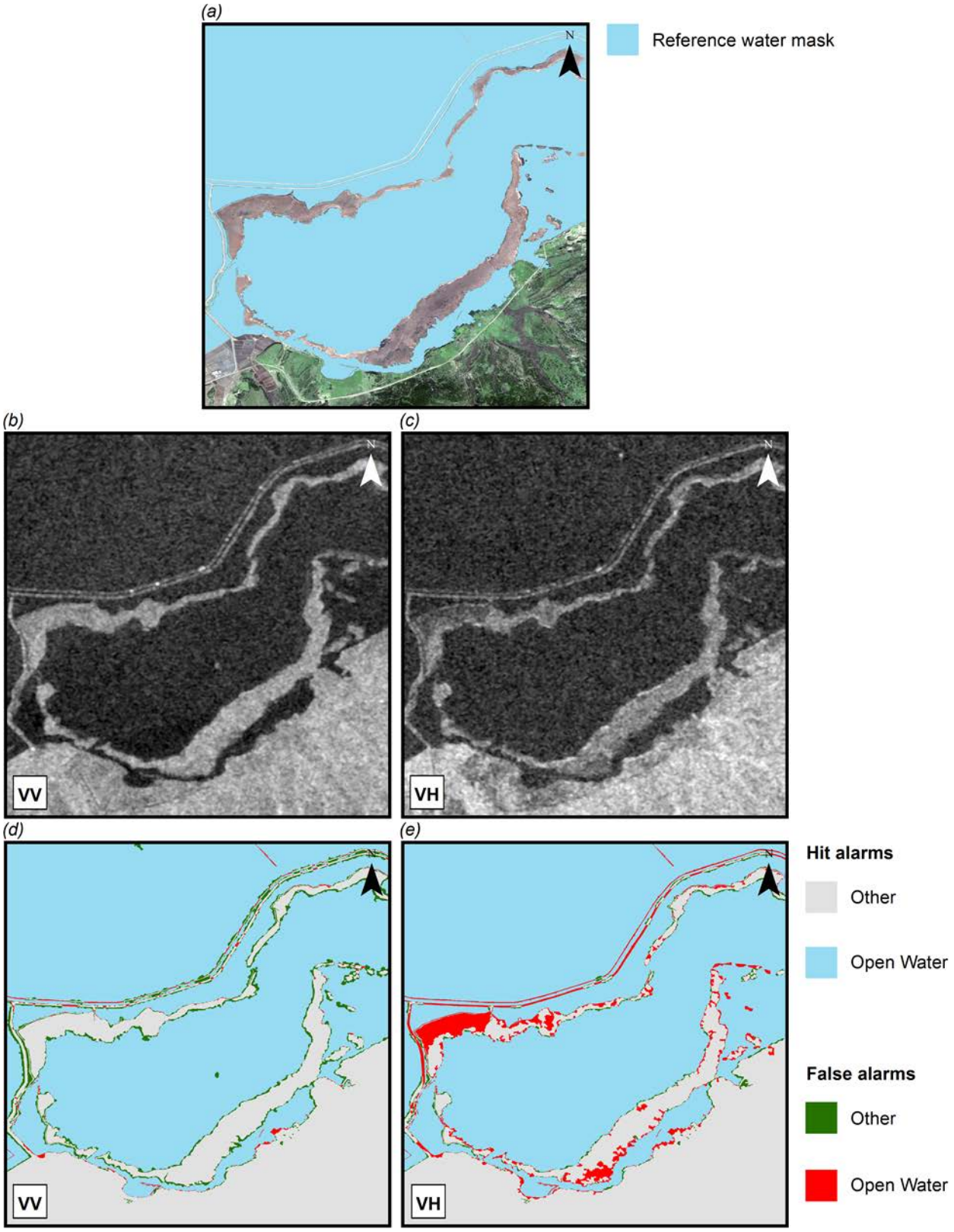

Figure 2.1.11: Subsets for validation site B: a) WorldView-2 scene acquired 11 March 2015, band combination 5-3-2 (natural colour). Overlay: reference water mask b) Sentinel-1 scene acquired 12 March 2015 in VV polarisation and c) in VH polarisation d) classification results for VV-polarised and e) for VH-polarised data (Source: Twele et al. 2016b).

Discussion

Regardless of validation site and polarisation configuration, the results obtained can be regarded as very satisfying with overall accuracies between 93.98% and 96.08% and KHAT coefficients between 0.88 and 0.91. Sources of misclassifications can be best identified when comparing the backscatter behaviour of both polarisations (fig. 2.1.10b/c and 2.1.11b/c with the corresponding classification results (fig. 2.1.10d/e and 2.1.11d/e).

In the upper right part of figure 2.1.10, thin lines of vegetation within open water areas can be perceived. However, these lines are much wider in the SAR image compared to the optical WorldView-2 scene. Due to geometric distortions such as foreshortening and layover resulting from the side-looking geometry of the sensor, the SAR-derived flood extent is commonly underestimated in these areas. In addition, when comparing the VV and VH polarisation images, a higher contrast between open water areas and the thin lines of vegetation can be observed for VV polarisation. This is due to double bounce effects, i.e. strong signal return of SAR waves, scattered at the water surface towards e.g. partially submerged tree trunks and then directly back to the SAR sensor. Within this scattering mechanism, a great percentage of the backscattered waves show preserved polarisation (i.e., V-polarised wave transmitted returns as V-polarised signal). Therefore, VV shows a higher signal response in double bounce conditions than VH.

The channel at the peninsula (right part of fig. 2.1.10) shows a higher rate of false alarms in VH polarisation (fig. 2.1.10 e) compared to VV polarisation (fig. 2.1.10d). Also when comparing the two corresponding SAR intensity images (fig. 2.1.10b/c), it is much easier to visually separate the channel from surrounding vegetation using VV polarisation instead of VH polarisation. According to Lee and Pottier (2009), VH polarisation is induced by volume scattering. Therefore, VH polarisation shows a higher signal return at the tree crowns which are flipped towards the channel due to the side-looking SAR geometry. In contrast to this, VV polarisation is characterised by a higher penetration depth into the tree crowns, i.e. VV is mainly influenced by double bouncing between tree trunks and the water surface and not by multiple scattering inside the tree crown as VH polarisation.

A further observation is the larger backscatter variability of VH-polarised data in vegetated areas. Within the land areas of figure 2.1.10, forest areas are much more highlighted in VH- compared to VV-polarised data. Contrarily, agricultural farmland shows comparably low backscatter in VH polarisation. The higher sensitivity of VH polarisation to volume scattering (an indication for vegetated areas) is the reason for its higher contrast within the land part compared to VV. The stronger contrast between forested areas and farmland in VH polarisation increases the risk of water lookalike areas. Due to the application of the HAND-EM (see fig. 2.1.7), lookalike areas situated in higher altitudes do not constitute a source of misclassification in VH-polarised data. In lower altitude areas however, certain more sparsely vegetated land cover types can exhibit similar backscatter profiles like open water surfaces. An example of such misclassifications is visible in figure 2.1.11c/e where a relatively high false alarm rate for open water can be observed.

When comparing the backscatter behaviour of VV and VH polarisation, it is further important to note that the Sentinel-1 scene used for the underlying study has been recorded under calm wind conditions of approx. 1.5m/s. Therefore, open water areas are mainly characterised by specular reflection of the SAR signal which results in relatively low backscatter values. The amount of specular reflection decreases when the water surface is roughened by wind, leading to an increased backscatter level and lower contrast to land areas. In a study to compare quad-polarised C-band SAR data for wind speed retrieval, Zhang et al. (2011) have shown that in contrast to co-polarised data, the NRCS of cross-polarised data does not saturate under strong wind conditions and is further not sensitive to incidence angles or wind directions. This finding suggests that under high winds speeds, the elevated and non-saturated backscatter signature of VH-polarised data might lead to a very low land-water contrast, potentially resulting in a higher amount of misclassifications. In the same manner, VV polarised data might suffer from a high backscatter variability of open water surfaces when wind directions vary across a given satellite scene. While HH polarisation is generally considered as superior to VV or VH polarisation for flood mapping purposes (Henry et al. 2008) since it yields the highest contrast between open water and land areas, this polarisation is usually not available for systematically acquired Sentinel-1 data of land surfaces.
The computational effort of the complete workflow was approx. 45 min. for a Sentinel-1 IW mode GRD scene using an Intel Xeon E5-4650 CPU (8 cores) with 2.7 GHz and 16 GB of RAM on a Linux-based 64-bit operating system.

Outlook and further development

In a few critical situations the global threshold derived from the tile-based automatic thresholding algorithm may not be optimal due to following considerations:

- The SAR signal from C-band, the working frequency of Sentinel-1 SAR sensor, strongly attenuates vegetated areas, which also results in a dominant contrast similar to that generated by surface water.
- The quality of selected tiles and their derived thresholds are not evaluated in the current implementation. Due to that overestimations might occur in rare cases.

In order to solve the abovementioned problems, a hierarchical version of KI algorithm was implemented, inspired and adapted from Chini et al. (2016). The original idea of Chini et al. (2016) is to transform a SAR image into a quad-tree of small regular split tiles, and then check the bimodality of the histogram for each tile using a curve fitting technique, later those tiles with a bimodal histogram will be collected and merged. This procedure starts from the root of the quad-tree (coarsest resolution) and repeats to its bottom (finest resolution). Finally all collected tiles at the finest resolution level (30^2 pixel) will be merged as a bimodal subset image, which is used to derive a global threshold by KI. The advantage of this implementation is that every selected tile has been checked for the bimodality of its histogram, so the final merged subset image is also supposed to have a bimodal histogram. However, in order to get a merged bimodal subset, this procedure have to iterate in the quad-tree from top to bottom and check bimodality for each split tile one by one.

This can impair the efficiency of the program. One difference between our current implementation to that by Chini et al. (2016) is that we do not try to collect and use all tiles with bimodal histograms to form a global subset image. Instead, at first we rank and sort all split tiles according to a contrast measure and save the result as a list. In this way we know that the most appropriate representatives for threshold estimation lie at the top of the list. The bimodality of each tile in that list is checked from top to bottom until enough representatives (current number is 5 or 7) are received. In this way we reduce the amount of data to be processed but still attain a robust result.

During the procedure of tile selection and threshold estimation, the program starts with tiles that have a strong contrast and a large size. In figure 2.1.12, a candidate tile is presented which is about 532 x 362 pixel in dimension and has the strongest contrast, its histogram is illustrated on the right hand side which shows an ambiguous bimodal curve. The derived threshold is -15.9 dB which is overestimated and rejected due to a relative low Ashman's separability of the histogram (about 3.38).

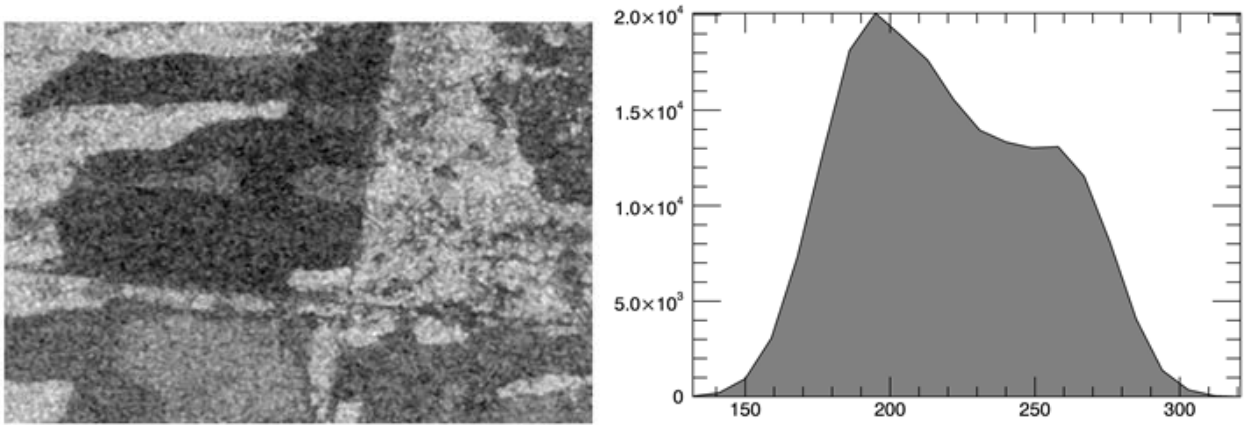

Figure 2.1.12: A rejected tile with a strong contrast but a poor bimodal histogram.

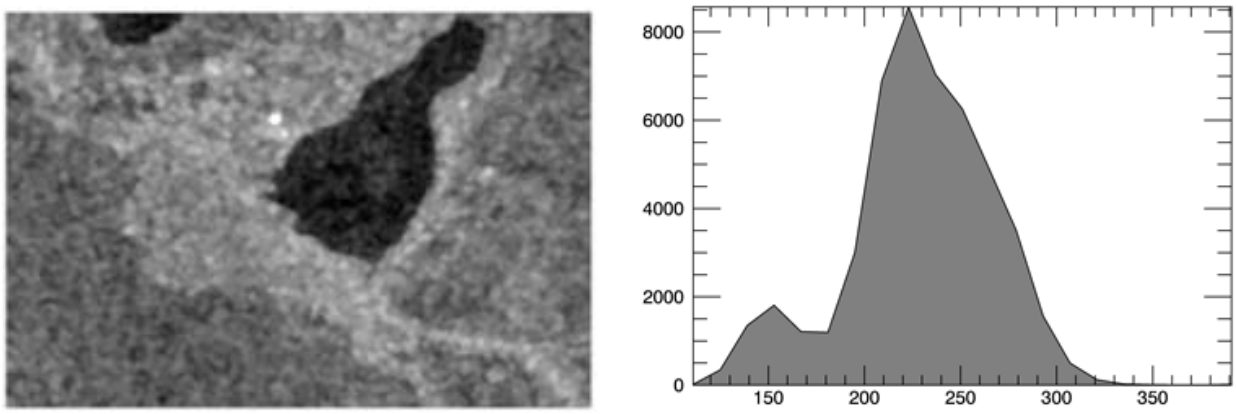

Figure 2.1.13: An accepted tile with a strong contrast and a pronounced bimodal histogram.

An accepted tile is illustrated in figure 2.1.13 which size is 266 x180 pixels. The Ashman's separability of the histogram is about 3.98 which demonstrates a clear bimodality. The result of threshold estimation is -22.7 dB, which is an improved threshold value to separate dark surface water from vegetated background areas with higher backscatter.

2.1.2.2 Change detection

Change detection is the process of identifying differences in the state of an object or phenomenon by observing it at different times (Lu et al., 2004). From the viewpoint of crisis monitoring these changes observed from remote sensing data may be significantly related to natural disaster events and are therefore of huge concern for civil security. Along with SAR which enables all-weather data acquisition change detection provides an effective framework to detect NRT changes caused by natural disaster and extract relevant crisis information. In the following, change detection methodologies geared towards a) the visualisation of changes based on RGB composites as well as b) the classification of changes will be analysed and discussed.

Change visualisation based on RGB colour composites

Besides change detection methodologies used to classify areas of change, which is subject of a separate sub-chapter, it is often desirable to only visualise changes for dissemination purposes or to facilitate thematic analysis by an image interpreter. For the purpose of visualising backscatter changes due to flood situations, a relatively simple but effective methodology has been developed. The technique is based on the combination of pre- and post-flood SAR imagery into a RGB composite which is intuitively interpretable. Backscatter changes between two given image dates are scaled and colour-coded in a way to highlight flooded areas in blueish tones, positive backscatter changes (e.g. due to land cover transition) in reddish tones, areas with open water surfaces on both image dates in black colour and relatively unchanged areas in greyish tones (fig. 2.1.14). In the following, the methodology for SAR-based RGB-visualisation of flood-related changes is outlined and demonstrated.

Blue channel: The blue channel principally controls the colour coding of negative backscatter changes to blueish tones in the change RGB. This is performed through the following steps:

- Calculation of the normalised change index (NCI) between pre- and post-flood scenes.
- Condition A: Use of the NCI-layer in case a) its pixel value is below the mean of the NCI-layer minus its standard deviation and if b) the corresponding pixel value of the pre-disaster image is above a user-defined upper backscatter threshold for open water areas.
- Condition B: If condition A is not fulfilled, the average pixel value of pre- and post-disaster scenes is employed for the blue channel.

Green channel: The backscatter information of the pre-disaster scene is utilised.
Red channel: The backscatter information of the post-disaster scene is utilised.

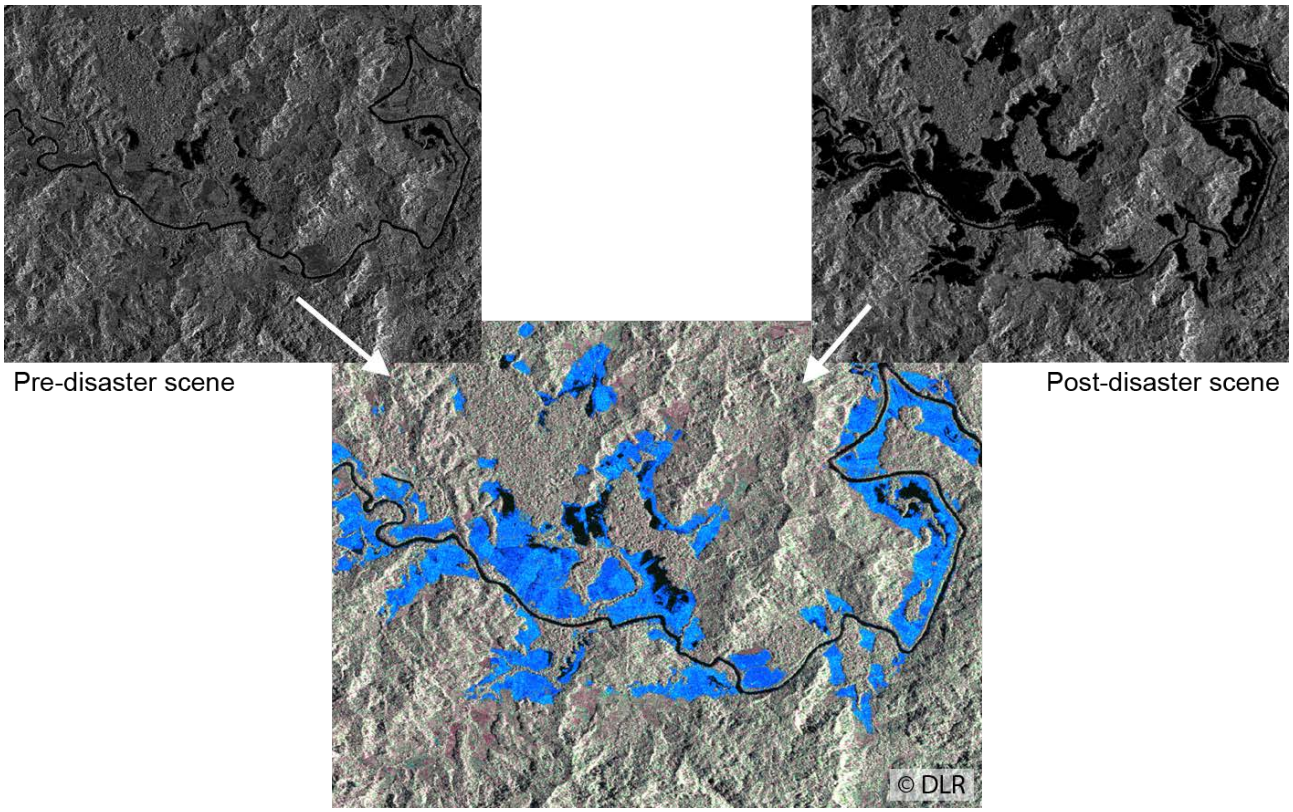

Figure 2.1.14: RGB colour composite based on pre- and post-flood TerraSAR-X data. Blue: areas of negative backscatter changes related to floods, Red/magenta: Positive backscatter changes, e.g. related to land cover transition, black: areas with open water surfaces on both image dates, grey: land surfaces with no or minor backscatter changes. Pre-disaster scene: TerraSAR-X SM, HH, 28-12-2010, Post-disaster scene: TerraSAR-X SM, HH, 2011-01-08.

The methodology is principally applicable to all SAR data. In order to minimise changes due to other factors than flood events (e.g. seasonal changes or land cover transition), the time-span between pre- and post-flood acquisition should be kept as short as possible.

In figure 2.1.15, the results for two Sentinel-1 scenes of the 2015 flood event in Malawi (see chapter 2.1.2) are shown. While the flood extent is still very well perceptible in blueish tones, also many changes unrelated to the flood event can be observed which can be attributed to the longer time-span between pre- and post-flood acquisitions (24 days) and the land cover types prevalent in this test site. In direct vicinity to the flood extent, areas with strong reddish tones are visible, indicating a strong backscatter increase. This backscatter increase can potentially be attributed to double bounce effects from partly submerged vegetation.

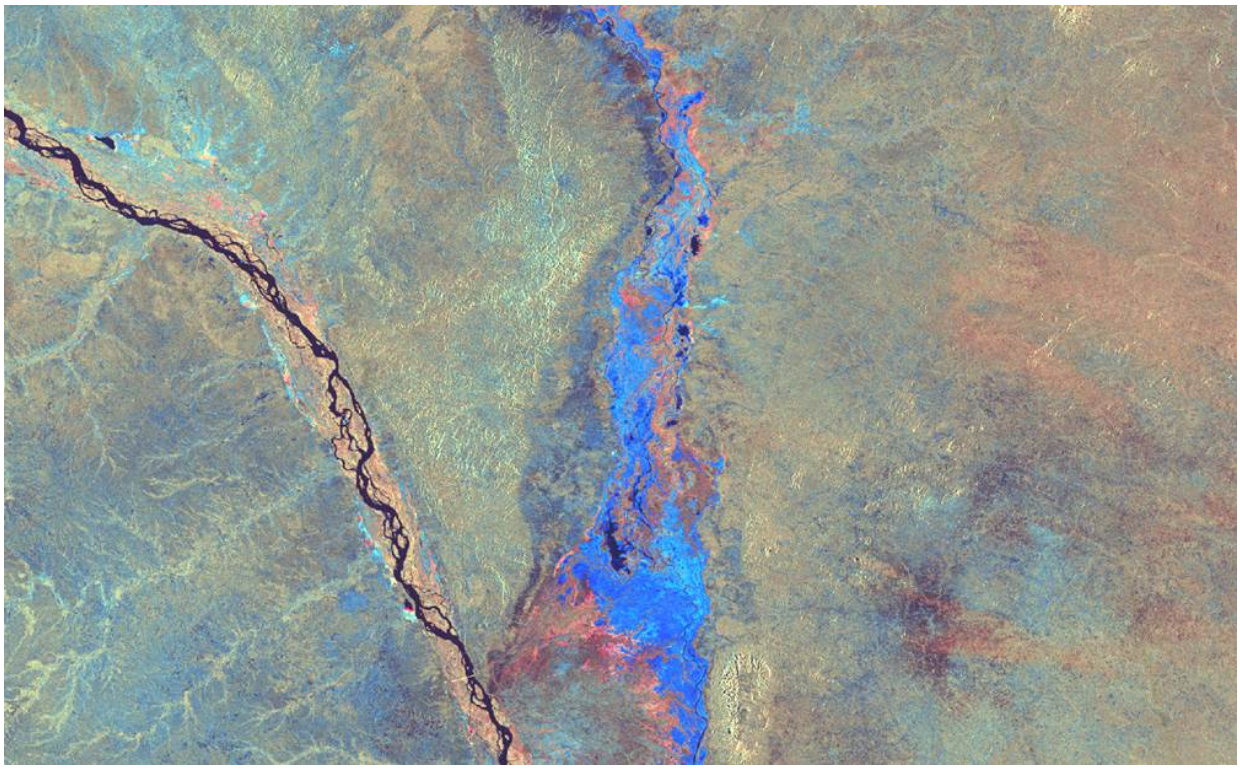

Figure 2.1.15: RGB colour composite based on pre- and post-flood Sentinel-1 data. Blue: areas of negative backscatter changes related to floods, Red/magenta: Positive backscatter changes, e.g. related to double bounce effects from partially submerged vegetation, black: areas with open water surfaces on both image dates. Pre-disaster scene: Sentinel-1 IW, VV, 2015-01-04; post-disaster scene: Sentinel-1 IW, VV, 2015-01-28.

Change detection based on automatic thresholding and graph cut algorithms

Related works in the area of change detection can be found in reviews given by Lu et al. (2004) and Radke et al. (2005). According to their description change detection techniques can be divided into following groups:

1. Algebraic methods such as image differencing, rationing and index differencing.
2. Transformation methods like principal component analysis (PCA).
3. Classification methods for multi-spectral images such as spectral-temporal combined hybrid change detection and artificial neural network (ANN).
4. Advanced models, for example a biophysical model related to the scattering process of vegetation to find changed areas.

In order to provide NRT results only time-efficient methods should be taken into account, therefore methods from the first group are preferred. At the same time an additional post-processing method is always necessary due to the speckle noise of SAR data. In this way we decide to apply a hybrid method that combines an efficient thresholding method with a post-processing algorithm from computer vision. Our method is designed as follows:

1. Based on the statistics of the ratio image the optimal thresholds for negative- and positive-change classes are derived automatically. This step provides at first an initial image classification.
2. The initial classification is typically noisy. This noise signal on SAR images can be modelled as a Markov Random Field (MRF) (Li 1995) which can be optimised using the graph-cut method by Boykov et al. (2011) and Kolmogorov et al. (2004).

In the next paragraphs we describe an automatic workflow of the proposed SAR-based automatic three-class change detection processor shown in figure 2.1.16, which consists of three sub-chains: a) a pre-processing step for radiometric and geometrical calibration of input Sentinel-1 GRD SAR data, b) an initial classification based on a threshold derived by hypotheses test, and c) a post classification using a graph-cut solver for a general MRF model. More details of each sub-chain are given in the following subsections.

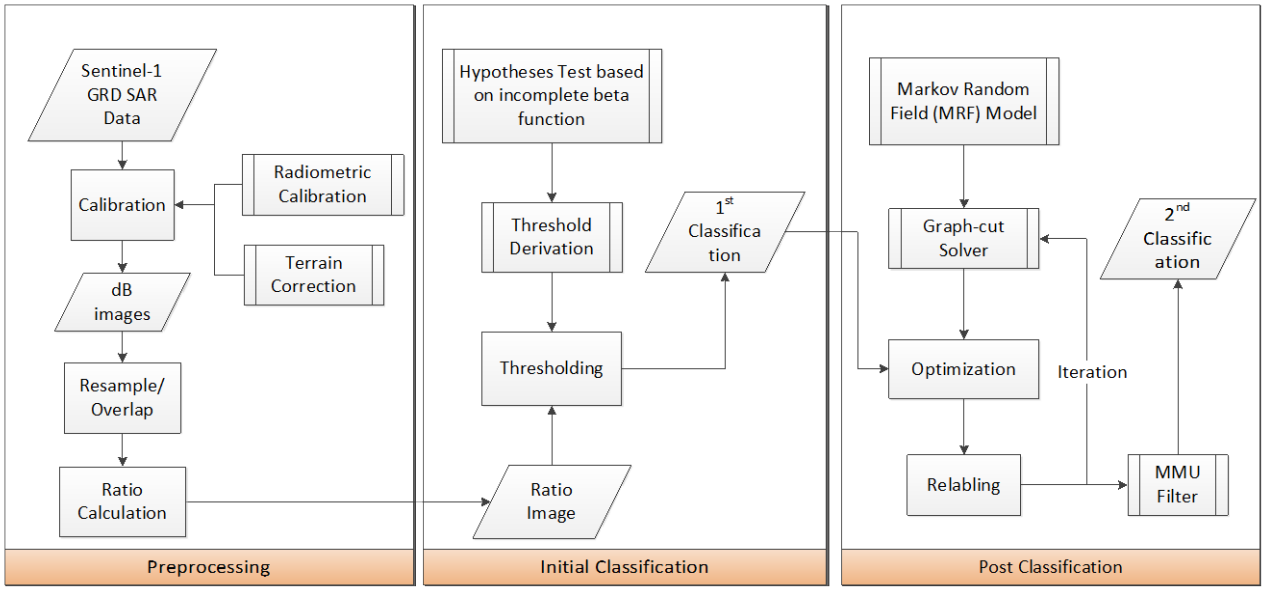

Figure 2.1.16: Workflow of the proposed SAR based automatic three-class change detection processor.

Geometric and radiometric calibration

The two input Sentinel-1 GRD SAR data sets are at first radiometrically calibrated to sigma naught (dB) using an included calibration Look Up Table (LUT), followed by a geocoding to GCS84. A Range-Doppler terrain correction is additionally integrated to correct geometric distortions of GRD products due to terrain effects. The whole calibration is implemented using the Graph Processing Tool (GPT) of ESA Sentinel-1 Toolbox (S1TBX), which is a command-line interface easily reusable in other programming languages, such as IDL used in this study. In addition, Shuttle Radar Topography Mission (SRTM) 1 arc second tiles corresponding to the given Sentinel-1 scenes are automatically downloaded by S1TBX for terrain correction. Subsequently, one of the two calibrated Sentinel-1 GRD SAR scenes is clipped and resampled in IDL to ensure the same image extent and

resolution. Then, an intensity ratio image is calculated for the next sub-chain. The output of the pre-processing is a reprojected, calibrated and terrain-corrected SAR intensity ratio image.

Image thresholding

In this process step, we rewrite the constant false alarm rate (CFAR) edge detector (Touzi et al., 1988), which was discussed by Oliver and Shaun (2004) for two-class SAR change detection, in a compact formula using the incomplete beta function (IBETA). To cope with a three-class change detection problem, the corresponding hypotheses are formulated as follows:

$$\alpha_L = P(r < q_L)$$
$$\alpha_U = P(r > q_U)$$

Both of them can be derived in terms of IBETA functions as follows:

$$\alpha_U = 1 - IBETA\left(\frac{q_U}{q_U + \frac{N_1 L_1}{N_2 L_2}}; N_2 L_2, N_1 L_1\right)$$
$$\alpha_L = IBETA\left(\frac{q_L}{q_L + \frac{N_1 L_1}{N_2 L_2}}; N_2 L_2, N_1 L_1\right),$$

where α_U and α_L are two given constant false alarm rates. These parameters are set to 5% for our current change detection processor. N_1 and N_2 are the numbers of pixels to be processed for change detection. In the case of pixel-based change detection, they are equal to 1. L_1 and L_2 correspond to the equivalent number of looks (ENL); they are set to 10 in our current change detection processor. δ_U and δ_L can then be calculated and used to threshold the ratio-image to perform a three-class change detection (see table 2.1.5).

Table 2.1.5: Decision rules for three-class change detection.

Class	Condition
Positive-Change	$r > q_{\mathrm{U}}$
Negative-Change	$r < q_{\mathrm{L}}$
No-Change	Otherwise

Post-processing by MRF and Graph-cuts

Our initial image classification mask can be considered as a noisy image with each pixel related to a class ID. The post-processing process can be seen as restoration of this noisy class mask by modifying the class IDs on these pixels. According to the description of the MRF, this optimisation problem can be generally formulated as follows:

$$E(l) = \sum_{p \in V_0} D_p(l_p) + \sum_{(p,q) \in N} V_{pq}(l_p, l_q)$$

where l is an arbitrary image class mask, on which all pixels form a field with each pixel as a vertex and neighboring pixels as an edge. For each vertex p on this MRF a function called data energy D_p is defined to evaluate the quality of the current classification at this vertex p, this term is denoted as $D_p(l_p)$ in the formula. At the same time a function called smoothness energy $V_{pq}(l_p, l_q)$ is defined to evaluate the spatial proximity of each pair of neighboring vertices (p, q) on the MRF, so that the noisy pixels can be removed by optimising this function. For our task of three-class change detection we defined these energy functions as follows:

$$D_p(l_p) = -\ln(pdf(x_p;\ \theta(l_p)$$
$$V_{pq}(l_p, l_q) = 1 - \delta(l_p, l_q)$$

where $D_p(l_p)$ is defined as the logarithmic likelihood of the pixel value x_p, the parameters $\theta(l_p)$ are estimated from the previous initialised classification. $V_{pq}(l_p, l_q)$ is equal to 0 if the neighboring pixels are classified to the same class, otherwise it is equal to 1. The pdf model used in the currently implemented processor is the logarithmic Gamma distribution function described as follows:

$$p_z(z; q, L) = \frac{\Gamma(2L)}{\Gamma^2(L)} \frac{q^L \exp zL}{q + \exp z^{2L}}$$

where $p_Z(z)$ is the distribution function of log-ratio variable $Z = \ln R$, $\Gamma(\cdot)$ is the Gamma function, q and L are parameters estimated in this study by the method of logarithmic cumulants (MoLC) suggested by (Moser, 2006) and (Nicolas, 2002). MoLC equations for parameter estimation are given as:

$$m_{Z(1)} = \int_{-\infty}^{+\infty} z p_Z(z) dz$$

$$m_{Z(2)} = \int_{-\infty}^{+\infty} \left(z - m_{Z(1)}\right)^2 p_Z(z) dz$$

where $mZ(n)$ is the n-th order centered moment of log-ratio $Z = \ln R$. The MoLC equations for Gamma log-ratio are described in nonlinear trigamma functions as follows:

$$m_{Z(1)} = \ln q$$

$$m_{Z(2)} = 2\Psi(1, L).$$

In order to adjust this method to change detection with respect to flood events, we additionally employ a MMU filtering step before and after the post-processing step. Considering that water regions on SAR ratio images have a stronger signal than other objects, we filter out all detected changed areas on the classification mask that are smaller than 100 pixels. In this way we get an improved initial and final mask with most of the classified pixels being highly related to water.

Test Area

The complete automatic change detection processor was tested using a pair of radiometrically calibrated SAR data. For a flood event of March 2015 at the border between Greece and Turkey, two Sentinel-1 GRD scenes were acquired on 12/03/2015 and 31/10/2014. A subset region of this scene and the corresponding classification result are visualised in figure 2.1.17.

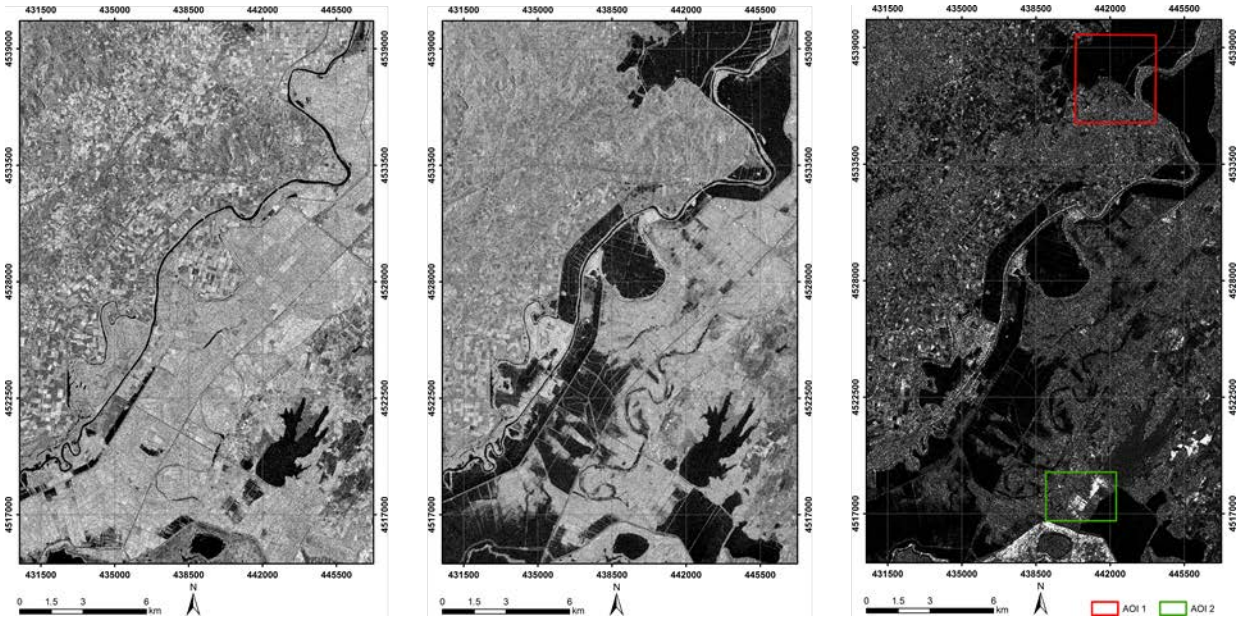

(*a*) (*b*) (*c*)

Figure 2.1.17: Study area of Greece/Turkey. Subsets of Sentinel-1 NRCS data of (*a*) 31/10/2014 and (*b*) 12/03/2015, (*c*) intensity ratio image between (*b*) and (*a*) with two AOI polygons defined for accuracy assessment. The green AOI polygon is selected for accuracy assessment of the negative-change class, whereas another smaller red AOI polygon is defined for accuracy assessment of positive changes. Both AOIs are displayed in details in figure 2.1.18 (red polygon) and 2.1.19 (green polygon) with the corresponding classification results.

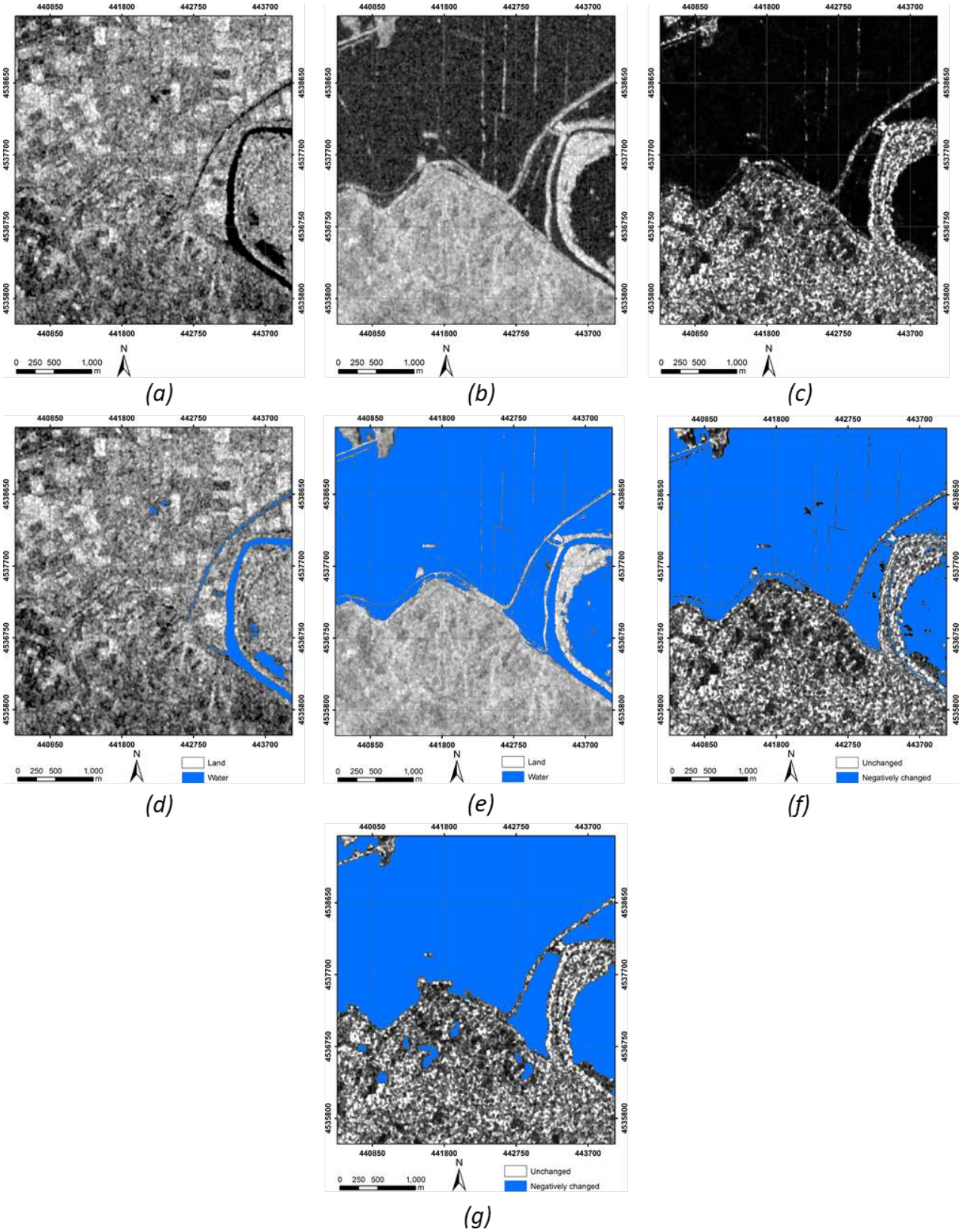

Figure 2.1.18: The first AOI subset of the study area of the Evros River. Subsets of Sentinel-1 calibrated NRCS data acquired on (*a*) 31/10/2014 and (*b*) 12/03/2015, (*c*) intensity ratio image between (*b*) and (*a*). The water mask shown in figure (*d*) is directly digitized from the corresponding NRCS image. In (*e*) the reference water mask was visually digitized based on a pan-

sharpened WorldView-2 scene acquired on 12/03/2015. The difference mask calculated from (*d*) and (*e*) is shown in (*f*) with the intensity ratio image as background. The blue mask in (*g*) is the classification result derived by the proposed method along with the same background as figure (*f*).

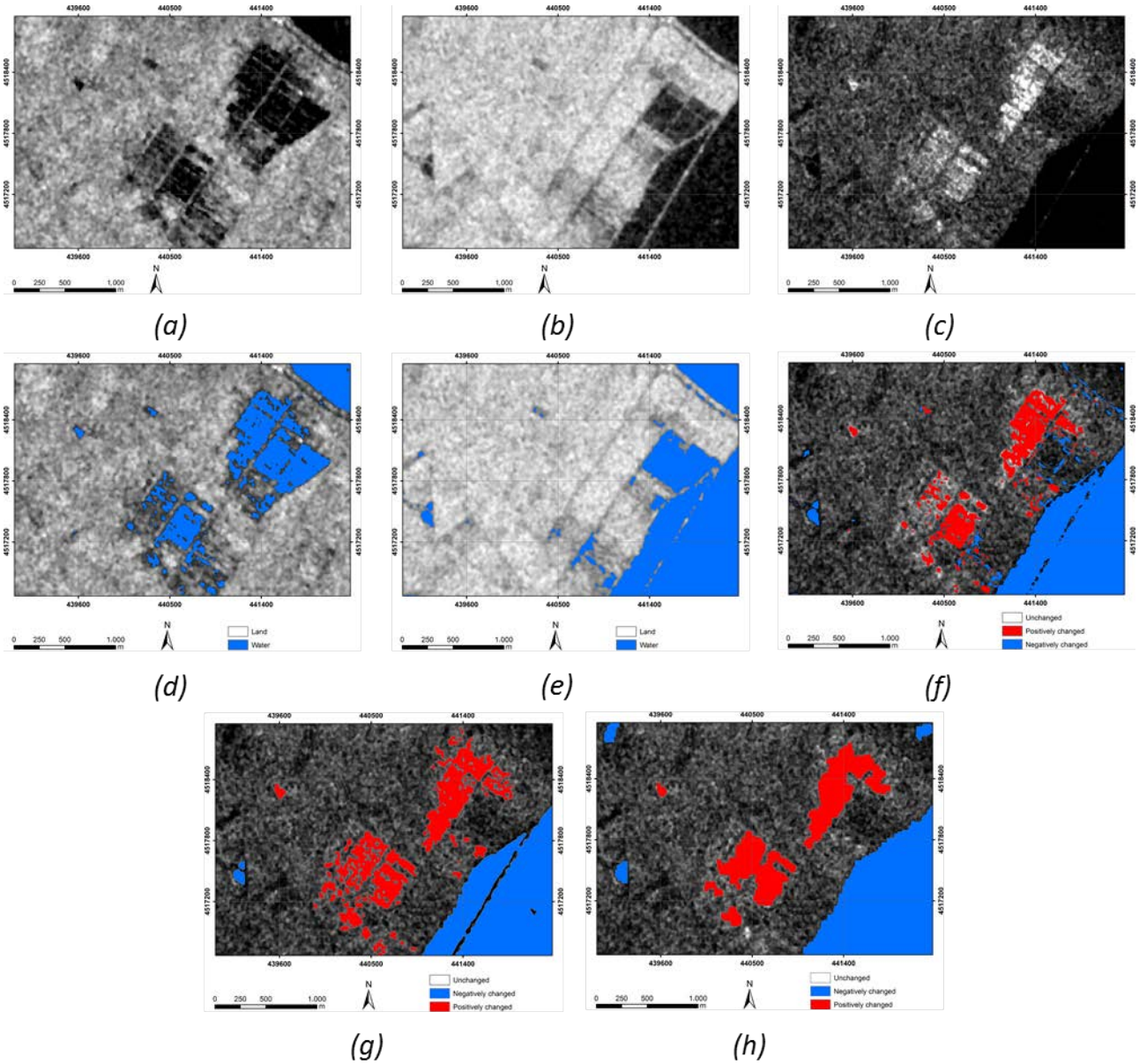

Figure 2.1.19: The second AOI subset of study area of the Evros River. Subsets of Sentinel-1 calibrated NRCS data acquired on (*a*) 31/10/2014 and (*b*) 12/03/2015, (*c*) intensity ratio image between (*b*) and (*a*). Water masks in (*d*) and (*e*) are obtained by the minimum error thresholding method. Figure (*f*) is the intensity ratio image overlapped with a classification result generated based on the difference of two water masks in figure (*d*) and (*e*), with positive changes presented in red, negative changes in blue and unchanged areas in transparent. This difference mask is compared with the classification result obtained by the proposed method shown in (*h*). A reference change mask in (*g*) was generated based on direct visual digitalization of the intensity ratio image with the same colour representation.

Table 2.1.6: Classification accuracy of the proposed algorithm evaluated on two AOIs of the study area. Sign (0) refers to the unchanged class, sign (-) represents negative change and (+) indicates positive change.

AOI	**AOI 1**		**AOI 2**					
Figure	2.1.16 (g)		2.1.17 (f)			2.1.17 (h)		
Class	(-)	(0)	(-)	(0)	(+)	(-)	(0)	(+)
UA [%]	95.8	96.1	89.1	94.6	82.6	89.1	97.4	84.7
PA [%]	96.8	94.8	98.6	96.6	53.3	99.6	96.2	77.7
OA [%]	95.9		93.1			95.1		
Kappa	0.92		0.81			0.87		

Discussion

In table 2.1.6, OA > 95% and Kappa > 0.87 achieved by the proposed method can be seen as a successful classification result. The source of misclassification can be examined by comparing the classification results to the corresponding references carefully. A few thin lines and small holes within open water areas classified in figures 2.1.18 (*g*) and 2.1.19 (*h*) are completely missing in the classification results shown in figures 2.1.18 (*f*) and 2.1.19 (*g*). These results come from the smoothing effect of the GCO algorithm with a relative large smoothing coefficient in the smoothness energy function. Abrupt edges and corners in the classification result are strongly penalized and are related to noise under a certain probability. Additionally, the MMU filter in the post-processing step can also contribute to smoothing if the size of clusters is too small (removed if less than 100 pixels in this study). The setting for this larger smoothing effect is due to the consideration of a subsequent cartographic usage of the classified result. Nevertheless, we can notice that larger line structures and boundaries in figure 2.1.19 (*g*) and (*h*) are still well retained.

On the contrary, the largest part of the misclassification lies in some extra negatively classified changes in the lower part of figure 2.1.18 (*g*) and around the left corner of the figure 2.1.19 (*h*). After comparing these misclassified regions to the corresponding SAR intensity data, we can identify that they are slightly bright before the flood event and appear slightly dark as water lookalike areas during the flood event. Therefore these misclassified regions appear darker in the ratio images, which indicate a strong change in intensity value. This behaviour of change is highly associated to vegetated areas that are submerged before the flood event and beneath water level during the flood event.

Another noticeable part of misclassification lies in the right corner of the figure 2.1.19 (*h*) where a small area in open water is classified as negative changes. Comparing the corresponding SAR data, we can observe that it indicates the change in the roughness of water surface during the flood event. Dependent on the wind speed the incidence angle of radar beam on the water surface can change and result in different intensity values in SAR images. This change is correctly classified from the ratio image in figure 2.1.19 (*h*), but in the context of flood classification it should be interpreted

with consideration of the original SAR intensity values to identify if they are flood relevant information.

In table 2.1.6, it can also be observed that the UA and PA of positive changes derived with respect to figure 2.1.19 (*f*) are both relatively low due to the very conservative water masks in figure 2.1.19 (*a*) and (*b*). Many dark pixels near the boundaries of the water masks are not included in figure 2.1.19 (*a*) and (*b*) so that their difference image in figure 2.1.19 (*c*) is also underestimated. We can still observe many uncovered bright pixels in figure 2.1.19 (*c*), which represent underestimated significant positive changes. Compared against figure 2.1.19 (*c*), the positively classified mask in figure 2.1.19 (*h*) covers the most significant changed areas and reaches higher UA and PA values.

2.1.2.3 Geohazard Exploitation Platform – analysis of the InSAR Browse Service results

This chapter describes the suitability analysis of the Sentinel-1 InSAR Browse Service results for flood mapping. This processor is part of ESA's Geohazards Exploitation Platform (GEP). The suitability analysis was performed for two test sites at River Evros at the border between Greece/Turkey and at Shannon River in Ireland for which a series of Sentinel-1 acquisitions and corresponding coherence data with a temporal resolution of 12 days computed from consecutive VV polarized Sentinel-1A data pairs was available. The spatial resolution of the data is 50 m.
The focus of the work was on embedding the proposed workflow as an optional processing step in the Sentinel-1 Flood Service presented in chapter 2.1.2.1 to be able to integrate beside the SAR amplitude data also coherence information into the classification process. Details can be found in Tavri (2016).

Evros – Greece/Turkey
Evros is the longest river (540 km) that runs through the Balcanian region, with origin in the Rila Mountains in Wester Bulgaria. River's average discharge rate is estimated to 1610 m³/s.

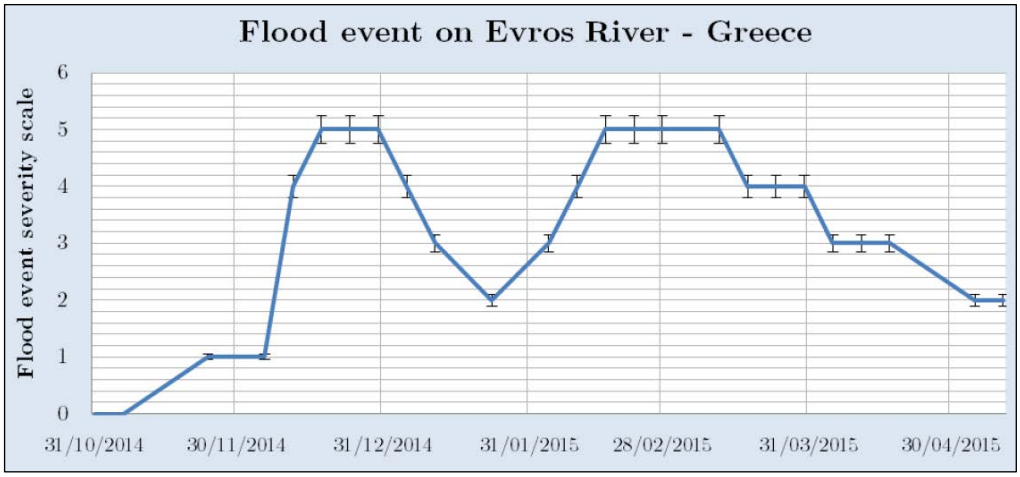

Fig. 2.1.20: Time series of the collected SAR data for the flood event at River Evros, Greece, Turkey. A flood severity scale from 0 to 5 is given to indicate the extent of the detected flood in this region. Error bars related to the percentage of each observation (5%) are shown.

The area around the river is mostly exploited for agriculture. The lower part at the border between Greece and Turkey is highly vulnerable to flooding. The flood event studied in this work peaked in December 2014, retreated in mid-January 2015 and peaked again in February 2014 due to intensive precipitation (see fig. 2.1.20).
14 SAR images were acquired from October 2014 until May 2016 and analysed to delineate the inundated areas. Subsequently, 13 interferometric coherence maps where produced.

Shannon River – Ireland

The Shannon River is the longest river in Ireland with a length of 360.5 km and divides the western part of Ireland from the east and south. The river mouth is located in Limerick and the average basin discharge can be up to 280.1 m^3/s. A severe flood event occurred from December 2015 until January 2016. Seven Sentinel-1A data were acquired from November 2015 until January 2016 (fig. 2.1.21). Subsequently, 6 interferometric coherence maps of consecutive image pairs were produced with a temporal distance of 12 days.

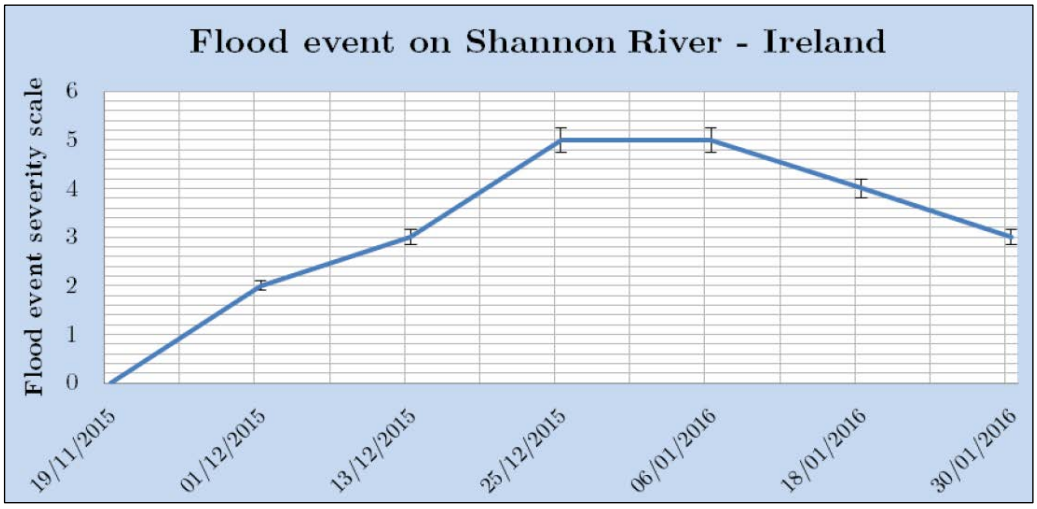

Fig. 2.1.21: Time series of the collected SAR data for the flood event at Shannon River, Ireland. A flood severity scale from 0 to 5 is given to indicate the extent of the detected flood in this region. Error bars related to the percentage of each observation (5%) are shown.

Pre-processing

The collected SLC data were processed based on the method of Yague-Martinez et al. (2016), following a three-level hierarchical structure. The lowest processing level is the burst-level, where signal interpolation and spectral shift filtering is applied. On the next level, the mosaics of the bursts are generated and at the highest processing level, the three different sub-swath mosaics are producing a final image. The selected SLC product pairs are coupled and a master-slave image choice is selected at burst-level sub-swath. The de-ramping function is calculated to account for the Doppler centroid frequency. Subsequently, interferometric processing for every burst is applied based on the Enhanced Spectral Diversity (ESD) technique to receive a range shift. In the first iteration, a geometric co-registration is performed to ensure negligible coherence loss for

interferogram formation. Exernal DEM and precise orbit information is used for this coarse co-registration. Interpolation of the slave bursts is performed with a six-point cubic convolution kernel along with spectral shift filtering to increase the resulting coherence. The master and slave bursts are filtered to a common range and azimuth bandwidth. Regarding the range direction, cross-correlation is applied to patches distributed over the master and slave SLC data and a linear correction of the shifts is performed as well as the ESD technique to obtain the fine azimuth accuracy (Yague-Martinez et al. 2016). By filtering master and slave bursts, de-correlation related to the acquisition geometry could be avoided. Based on the calculation of the common Doppler Bandwidth for each pixel due to possible Doppler centroid difference, the de-ramping and re-ramping operators were arranged. As a final stage the interferograms is formatted and the coherence information is retrieved.

Analysis

The produced coherence information was integrated into the existing processing chain of the S-1FS using a fuzzy logic classifier (fig. 2.1.22). An initial classification is applied on the SAR data based on the amplitude information and different auxiliary data (DEM, slope, HAND-EM). Image statistics are computed in order to determine the coherence distribution in the AOI and to define which type of function will be implemented.

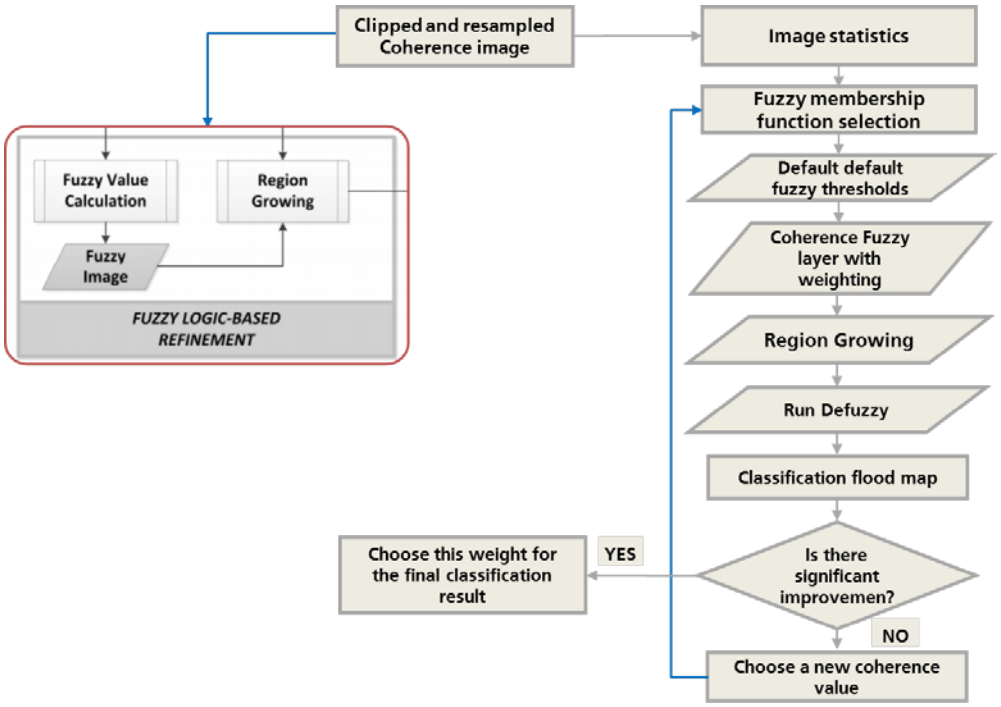

Fig. 2.1.22: The processing chain for interferometric coherence integration in the S-1FS.

Due to the randomness of the interferometric phase over water surfaces the interferometric coherence values are relatively low compared to surrounding land areas. Therefore, the standard Z fuzzy membership function was used to define the coherence information, where values smaller than a specific threshold x_1 belong definitively to the flood area (membership of 1), and values

above a threshold x_2 can be excluded from water classification. The degree of each pixel memberhip to the class flood was calculated and averaged in order to create a fuzzy set. Based on the Z membership function, different fuzzy thresholds were tested and default thresholds of 0.5 (x_1) and 0.55 (x_2) were obtained. Subsequently, the coherence fuzzy membership layer is obtained. Different weighting were determined for each fuzzy layer in order to be characterized as more or less significant. In order to examine the contribution level of the interferometric coherence addition, different scenarios where examined with weighting variation from 0 to 1, where 1 indicated the greatest importance given to the coherence complementary layer.
The final flood mask is derived through a defuzzification step, where each pixel with a membership degree >0.6 is transformed into a discrete thematic class. A region growing algorithm based on dilatation of the water bodies is applied, in order to increase spatial homogeneity and pixel connectivity. On a final step, the inundation maps area stored and visually inspected for improvements, in order to estimate the degree of improvement after the selected weight.

Results River Evros

The results at River Evros are exemplarily visualized on a Sentinel-1 scene acquired on 30/12/2014 (fig. 2.1.23). The Sentinel-1 image shows the presence of strong winds over the southern part of the river area which increases the intensity values of the water areas while the coherence is uniformly low over water bodies. Due to the fact that the loss of coherence is also located in areas not covered by water this information layer cannot be used for the mapping of water underestimated by the amplitude information. However, high coherence values can be used in the classification process to remove water look alike areas detected only using the amplitude information (e.g. bare soil, sand areas, streets, concrete areas, agricultural areas of high soil moisture, etc.) (fig. 2.1.24, left). Integrating the coherence and applying an average weighting w=0.6, satisfying results were obtained where a lot of misclassified areas are excluded from the final flood classification map.

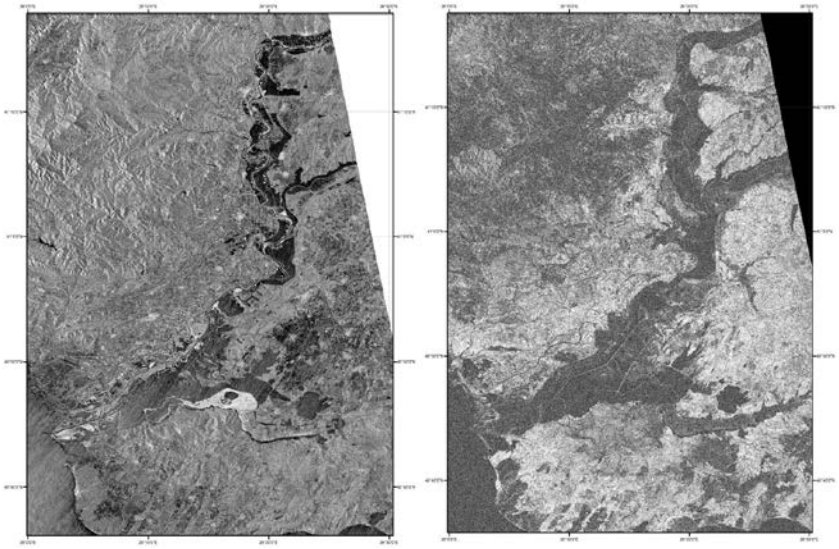

Fig. 2.1.23: Sentinel-1 amplitude (left) and coherence (right) data at River Evros, Greece/Turkey, on 30/12/2014.

Regarding the difference of the two maps (fig. 2.1.24, right), it becomes apparent that many variations between the two approaches and variations on classification where met on pixels along the river. Strong differences are apparent over crop fields and urban areas, where interferometric coherence maintain high compared to the amplitude information. By comparing the classification result derived from Sentinel-1 data of 20/04/2015 in two test areas with a reference classification based on Wordlview-2 data of 17/04/2015 an overall accuracy of 88.0% and 91.16%, respectively, could be reached (KHAT coefficient: 0.76 and 0.83).

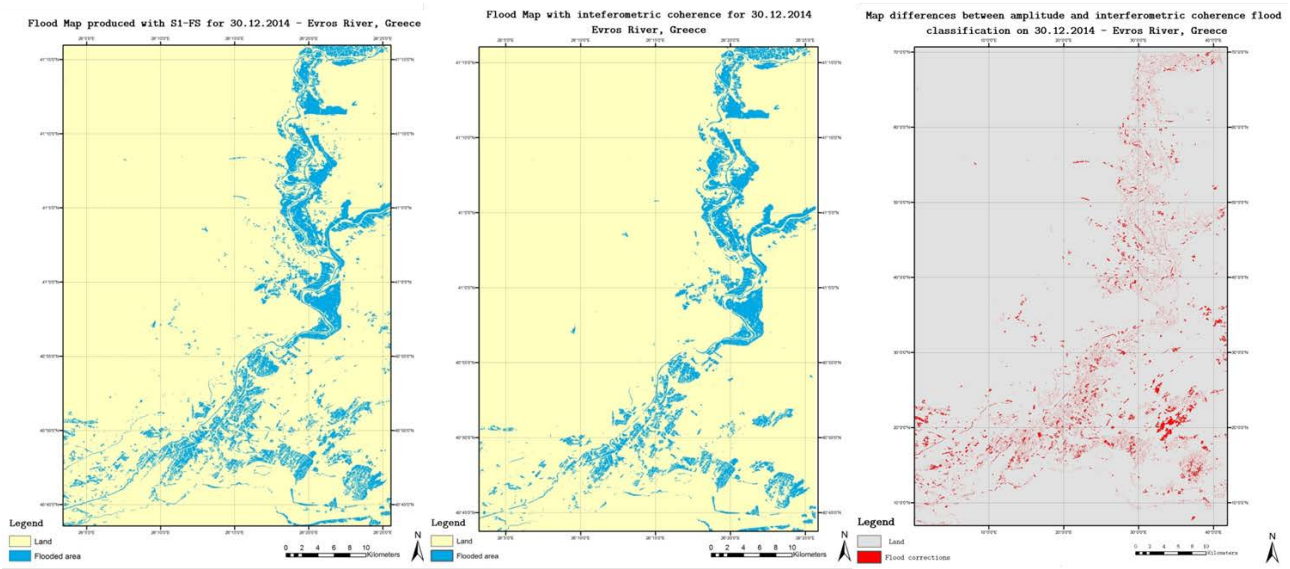

Fig. 2.1.24: Flood classification results of Sentinel-1 data (30/12/2014) based on the amplitude information (left) and on the amplitude information in combination with coherence (middle), and the difference between the two classification maps (right).

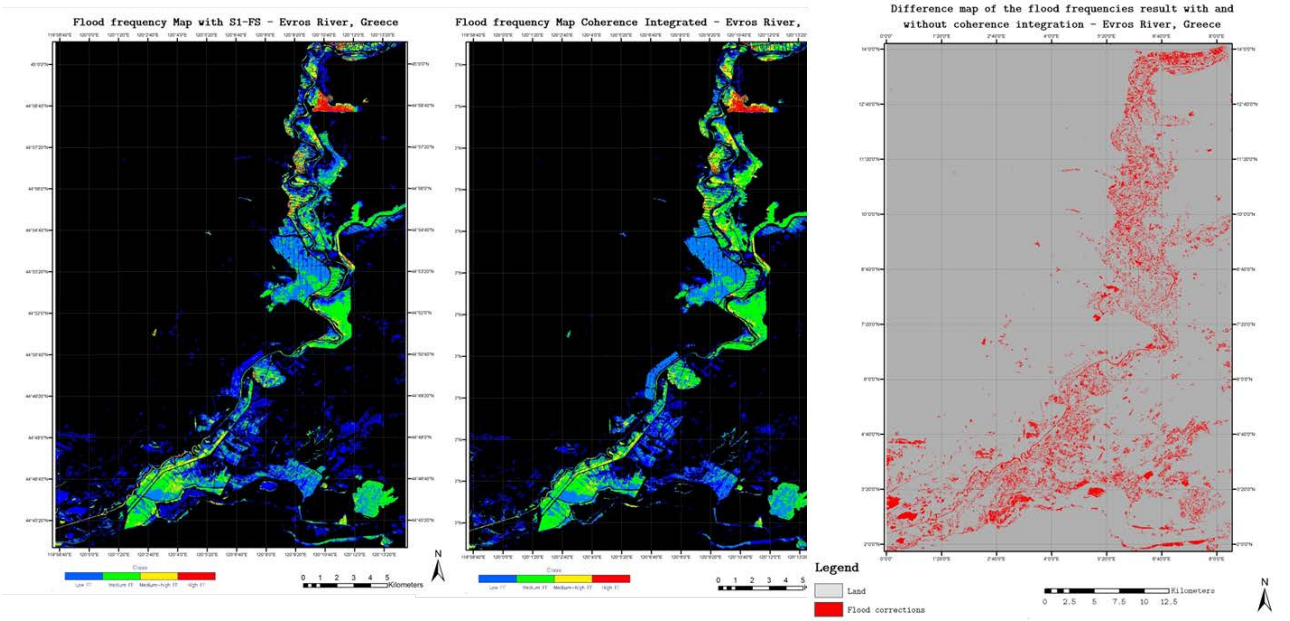

Fig. 2.1.25: Flood frequency maps obtained by the flood classification results without (left) and with coherence integration (middle) over the time series at River Evros, and the difference between the two frequency maps (right).

The classification results of all 14 Sentinel-1 data sets are visualized in a flood frequency map figure 2.1.25. Comparing the frequency maps based only on the amplitude information as well as based on the combination of amplitude and coherence information misclassified areas around the main river are significant less after the coherence layer integration.

Results Shannon River

The results for Shannon River are exemplarily visualized on a Sentinel-1 scene of 25/12/2015 (fig. 2.1.26). The amplitude shows a much better contrast than the coherence. Due to temporal decorrelation the coherence can only be used for the elimination of amplitude water look alike areas. The coherence based classification map in figure 2.1.27 shows a reduction of misclassifications along the river.

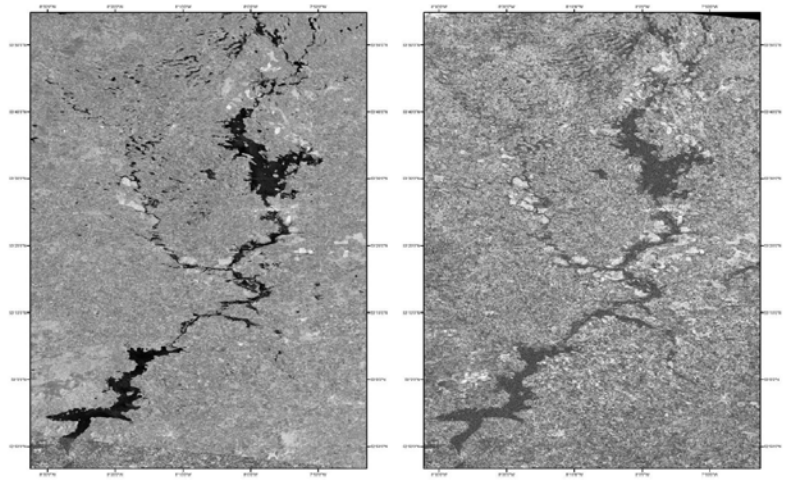

Fig. 2.1.26: Sentinel-1 amplitude (left) and coherence (right) data at Shannon River, Ireland, on 25/12/2015.

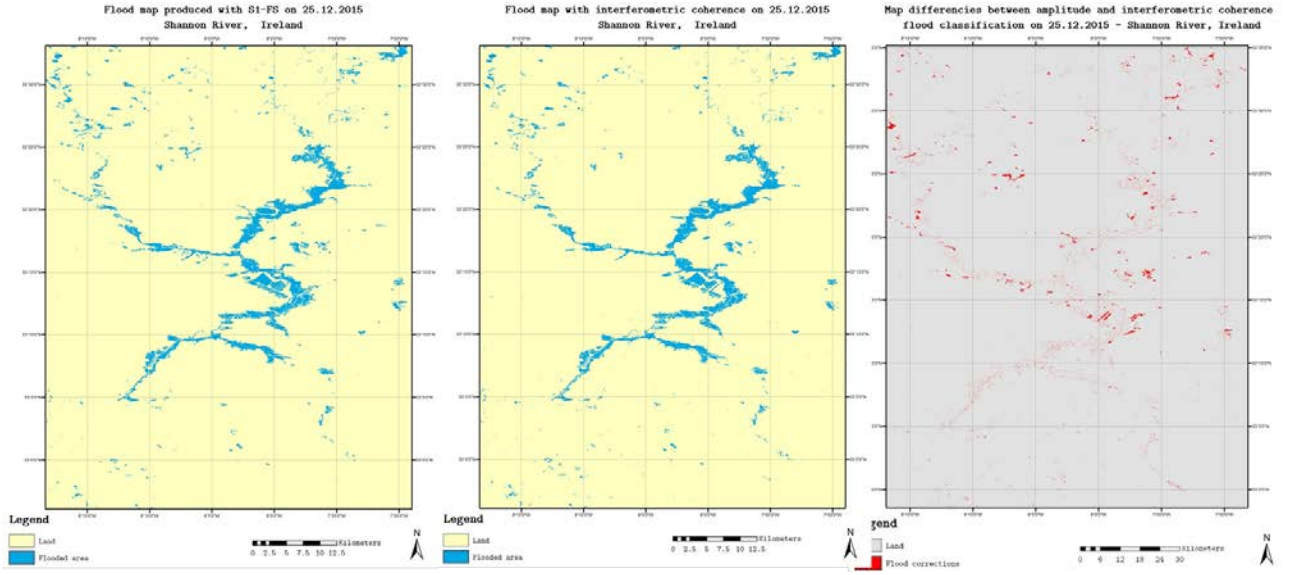

Fig. 2.1.27: Flood classification results of Sentinel-1 data (25/12/2015) based on the amplitude information (left) and on the amplitude information in combination with coherence (middle), and the difference between the two classification maps (right).

The classification results of all 7 Sentinel-1 data sets of Shannon River are visualized in a flood frequency map in figure 2.1.28. Comparing the frequency maps based only on the amplitude information as well as based on the combination of amplitude and coherence information misclassified areas along the main river are fewer after the coherence layer integration, however not as significant as at the River Evros test site.

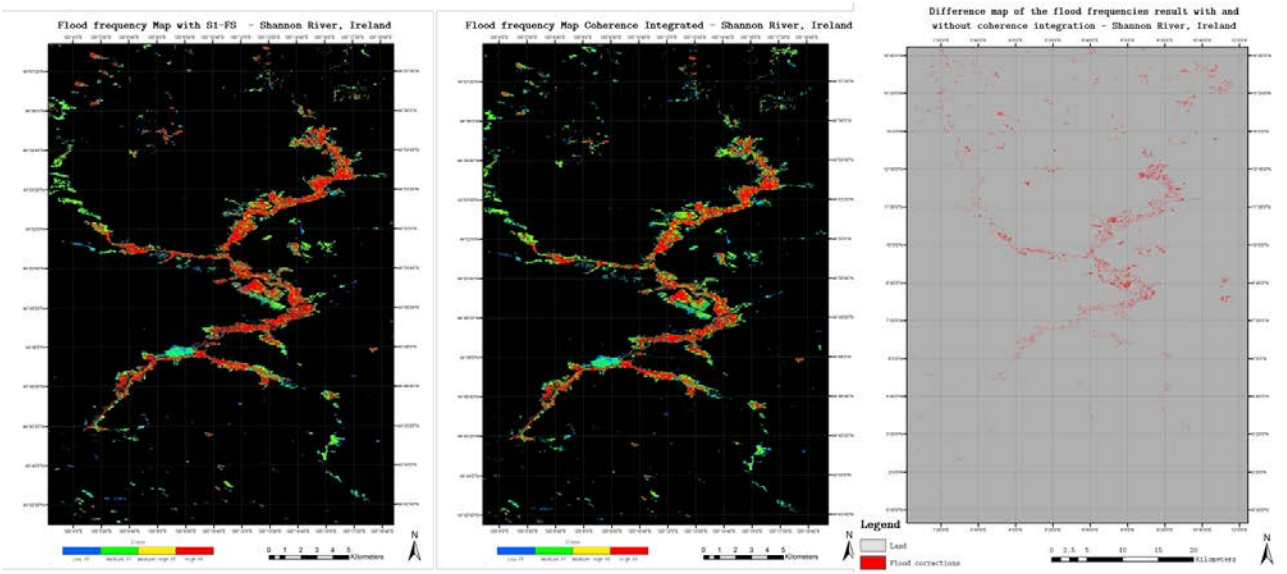

Fig. 2.1.28: Flood frequency maps obtained by the flood classification results without (left) and with coherence integration (middle) over the time series at Shannon River, and the difference between the two frequency maps (right).

Conclusion

In conclusion, the S-1 InSAR Browse Service of ESA's GEP shows some potential for flood mapping in combination with amplitude information. Due to the fact that the loss of coherence is also located in areas not covered by water this information layer cannot be used for the mapping of water bodies not detected by the amplitude information (e.g. rough water areas of high backscatter). However, high coherence values can be used in the classification process to remove water look alike areas detected using the amplitude information. The data analysed in this study has a spatial resolution of 50 m. The original resolution of Sentinel-1 data is 20 m. It is assumed that this higher spatial resolution would enable a better use of the SAR amplitude. It is assumed that temporal decorrelation effects could be reduced when the Sentinel-1A and B constellation regularly provides SAR imagery at a 6 days repeat cycle. This will increase the value of the interferometric coherence in water and flood mapping.

References

1. Behari, J., 2005: Microwave Dielectric Behavior of Wet Soils, 8, Springer.
2. Boykov, Y., Veksler, O., Zabih, R., 2011: Fast approximate energy minimization via graph cuts. IEEE Trans. Pattern Analysis and Machine Intelligence, 23(11), 1222–1239.
3. Chini, M., Giustarini, L., Hostache, R., Matgen, P., 2016: An Automatic SAR-based flood mapping algorithm combining hierarchical Tiling and change detection. ESA Living Planet Symposium, Prague, 9-13 May 2016.

4. Kolmogorov, V., Zabin, R., 2004: What energy functions can be minimized via graph cuts? IEEE Trans. Pattern Analysis and Machine Intelligence, 26(2), 147-159.
5. Lee, J.-S., Pottier, E., 2009: Polarimetric Radar Imaging - From Basics to Applications. Boca Raton, CRC Press.
6. Li, S. Z., 1995: Markov random field modeling in computer vision. New York, Springer.
7. Lu, D., Mausel, P., Brondizio, E., Moran, E., 2004: Change detection techniques. International Journal of Remote Sensing, 25(12), 2365-2401.
8. Martinis, S., Twele, A., Voigt, S., 2009: Towards operational near real-time flood detection using a split-based automatic thresholding procedure on high resolution TerraSAR-X data. Nat Hazard Earth Syst, 9, 303-314.
9. Martinis, S., Twele, A., 2010: A hierarchical spatio-temporal Markov model for improved flood mapping using multi-temporal X-band SAR data. Remote Sensing, 2, 2240-2258.
10. Martinis, S., Twele, A., Voigt, S., 2011: Unsupervised extraction of flood-induced backscatter changes in SAR data using Markov image modeling on irregular graphs. IEEE T Geosci Remote, 49, 251-263.
11. Martinis, S., Kersten, J., Twele, A., 2015: A fully automated TerraSAR-X based flood service. ISPRS J Photogramm., 104, 203-212.
12. Oliver, C. and Shaun, Q., 2004: Understanding Synthetic Aperture Radar Images. SciTech Publishing.
13. Radke, R. J., Andra, S., Al-Kofahi, O., Roysam, B., 2005: Image change detection algorithms: a systematic survey. IEEE Trans. Image Processing, 14(3), 294-307.
14. Rennó, C. D., Nobre, A. D., Cuartas, L. A., Soares, J. V., Hodnett, M. G., Tomasella, J., Waterloo, M. J., 2008: HAND, a new terrain descriptor using SRTM-DEM: Mapping terra-firme rainforest environments in Amazonia. Remote Sens Environ, 112, 3469-3481.
15. Tavri, A. 2016: Flood monitoring based on multi-temporal Sentinel-1 data - a synergistic approach of amplitude data with interferometric coherence. Mater thesis, Technical University of Munich, 69 pages.
16. Touzi, R., Lopes, A., Bousquet, P., 1988 : A statistical and geometrical edge detector for SAR images. IEEE Trans. Geoscience and Remote Sensing, 26(6), 764-773.
17. Twele, A., Martinis, S., Cao, W., Plank, S., 2015: Inundation mapping using C- and X-band SAR data: From algorithms to fully-automated flood services. Mapping Water Bodies from Space (MWBS 2015), 18-19 March 2015, Frascati, Italy, 46-47.
18. Twele, A., Cao, S., Plank, S., Martinis, S., 2016a: Sentinel-1 based flood mapping: a fully-automated processing chain. International Journal of Remote Sensing, 37:13, 2990-3004.
19. Twele, A., Martinis, S., Cao, W., Plank, S., 2016b: Automated flood mapping and monitoring using Sentinel-1 data. ESA Living Planet Symposium, Prague, Czech Republic, 09-13 May, 2016.
20. Yague-Martinez, N., Prats-Israola, P., Rodriguez Gonzalez, F., Brcic, R., Shau, R., Geudtner, D., Eineder, M., Bamler, R., 2016: Interferometric processing of Sentinel-1 TOPS data. IEEE Trans. Geoscience and Remote Sensing, 54 (4).
21. Zhang, B., Perrie, W., He, Y., 2011: Wind speed retrieval from RADARSAT-2 quad-polarization images using a new polarization ratio model. Journal of Geophysical Research 116.

2.1.3 Optical-based flood detection in rural areas

This section is sub-divided into a large part dedicated to very high resolution (VHR) optical data-based flood mapping and to flood mapping using Sentinel-2 data.

2.1.3.1 Very high resolution optical flood mapping

Much of the work performed relies on specific extraction techniques, including pixel-based, region-based and knowledge-based methods (Xiong 2001, Nevatia and Babu 1980, Mingjun and Daniel 2004).
Pixel-based methods are the most common and use spectral information to classify remote sensing imagery. In complex situations it is sometimes difficult to extract water bodies on a pixel by pixel basis because the algorithm does not bring the necessary spatial information to interpret the image (Boggess 1993, Roberts et al. 2001). Furthermore, in the past few decades, object-based algorithms have been developed exploiting spatial information in the procedure but the results are not always very promising. Most of these methods used alone do not provide reliable accuracy in flood situations. Thus, some researchers gathered spectral and spatial information from HR images and published promising results (Baatz and Schape 2000, Sande et al. 2003). Other researchers have found that SVM and Artificial Neural Networks (ANN) perform better than traditional methods (Mingjun and Daniel 2004, Karunanithi et al. 1994).

Support Vector Machines is a powerful machine learning procedure being created by Vapnik (Vapnik 1995) and are useful because of applicability in a large range of applications (Vapnik 1998, Cherkassky and Mulier 1998). The power of SVMs relies on the kernel function which can adapt its dimension function compared to the mapping input (Cortes and Vapnik 1995). In addition the kernel can adapt itself into a matrix kernel instead of high dimensional space if the classes are not separable in the input space. SVMs include three kernels that will be tested in this project: Linear, polynomial and the recommended Radial Basis Functions (RBF) (Lu et al. 2007).

Artificial Neural Networks are another widely used technique in the field of machine learning. ANNs are inspired by human's biological neural systems. It is an interconnected group of neurons that use mathematical or computational models for information processing. ANNs are mainly an adaptive function for nonlinear system. Like in nature, the network is determined by the connections between neurons. The training of ANNs is done by adjusting the connection (weight) between elements. Theoretically the neural network is adjusted to lead to a particular output with a specified input. When the ANN parameters are fixed the system can be deployed to solve a classification problem (Haykin 1994). The advantage of ANNs is that within nonlinear systems the network neurons provide an infinite flexibility that can perform any response. The most frequently used neural networks are Multi-layer Perceptrons (MLPs) (Marchant and Onyango 2003).

Optical data are often affected by clouds and shadows and it is important to take these into account to reduce misclassification, especially in the case of HR or VHR images. Furthermore, the appearance of water areas also relies on the sensitivity of the sensor and its spatial resolution. For this reason, it is strongly recommended to choose wisely the data set on which you work to develop a tool. Our aim is to extract water and also eliminate non-water features which have similar spectral values. Such misclassification can be reduced by choosing smartly and precisely a large and adequate number of samples for the training of the classifiers.

From all these assessments, in this project it is intended to consider a combination of pixel-based, region-based and knowledge based classification for the extraction of flood water. SVM and ANN algorithms will be tested and compared to classify the spectral information from an image and separate water pixels from non-water pixels. The commission and omission errors made by the classifiers, with similar spectral reflectance causing commission errors, can be decreased through region based and knowledge based techniques. Finally, to enable an objective assessment of the algorithm results ground truth data or reference layers will be employed.

References

1. Baatz, M., Schape, A., 2000: Multi-resolution Segmentation: an optimisation approach for high quality multi-scale image segmentation. In: Strobl, J. et al. (eds.): Angewandte Geographische Informationsverarbeitung XII. Wichmann, Heidelberg, 12-23.
2. Boggess, J. E., 1993: Identification of roads in satellite imagery using artificial neural networks: A contextual approach. Technical Report: MSU-930815, Mississippi State University.
3. Cherkassky, V., Mulier, F. M., 1998: Learning from Data: Concepts, Theory, and Method. John Wiley & Sons.
4. Cortes, C., Vapnik, V., 1995: Support-vector networks. Machine Learning 20, 273-297.
5. Haykin, S., 1994: Neural Networks – A Comprehensive Foundation. Macmillan College, New York.
6. Karunanithi, N., Greeney, W. J., Whitley, D., Bovee, K., 1994: Neural networks for river flow prediction. Journal of Computing in Civil Engineering, 8(2), 201–220.
7. Lu, C., Li, X.-w., Pan, H-b., 2007: Application of SVM and Fuzzy Set Theory for Classifying with Incomplete Survey Data. International Conference on Service Systems and Service Management, Chengdu, 1-4.
8. Marchant, J. A., Onyango, C. M., 2003: Comparison of a Bayesian classifier with a multilayer feed-forward neural network using the example of plant/weed/soil discrimination. Computers and Electronics in Agriculture, 39, 3-22.
9. Mingjun, S., Daniel, C., 2004: Road extraction using SVM and image segmentation. Photogrammetric Engineering & Remote Sensing, 70, 1365-1371.
10. Nevatia, R., Babu, K. R., 1980: Linear feature extraction and description. Computer Graphics and Image Processing. Computer Graphics and Image Processing, 13, 257-269.
11. Roberts, D., Gardner, M., Funk, C., Noronha, V., 2001: Road extraction using mixture and Q-tree filter techniques. National Center for Geographical Information & Analysis, University of California at Santa Barbara, http://www.ncgia.ucsb.edu/ncrst/research/reports/1Q3supplement-p.pdf.
12. Van der Sande, C. J., de Jong, S. M., de Roo, A. P. J., 2003: A segmentation and classification approach of IKONOS-2 imagery for land cover mapping to assist flood risk and flood damage

assessment. International Journal of Applied Earth Observation and Geoinformation, 4, 217-229.
13. Vapnik, V. N., 1995: The Nature of Statistical Learning Theory. Springer-Verlag.
14. Vapnik, V. N., 1998: Statistical Learning Theory. Wiley.
15. Xiong, D., 2001: Automated Road Network Extraction from High Resolution Images. National Consortia on Remote Sensing in Transportation, Technical Notes, 3.

Test sites

The test sites were chosen over areas SERTIT has already worked in rapid mapping and other frameworks, namely:

- Poyang, China
- Morombe, Madagascar

Poyang Lake, PR China

The first study site is located in the Popular Republic of China to the northeast of Jiangxi Province. Poyang Lake is one of the largest freshwater lake in China. Its watershed covers about 162,000km² and collects water from 5 main rivers in Jiangxi (Xiushui, Gan, Fuhe, Xin and Raohe). The Poyang system is complex with its outlet being into the Yangtze River north of the lake. The lake is a major hydrological subsystem that regulates river waters converging on the lake. Poyang Lake is an example of a monsoon lake with its water load varying greatly from season to season as in the dry season it covers around 1,000km² expanding to almost 3500km² in the rainy season. Therefore, we have the opportunity at a single site to test the algorithms at different flood levels, using images with mixed pixels and various pixel spatial and spectral characteristics.

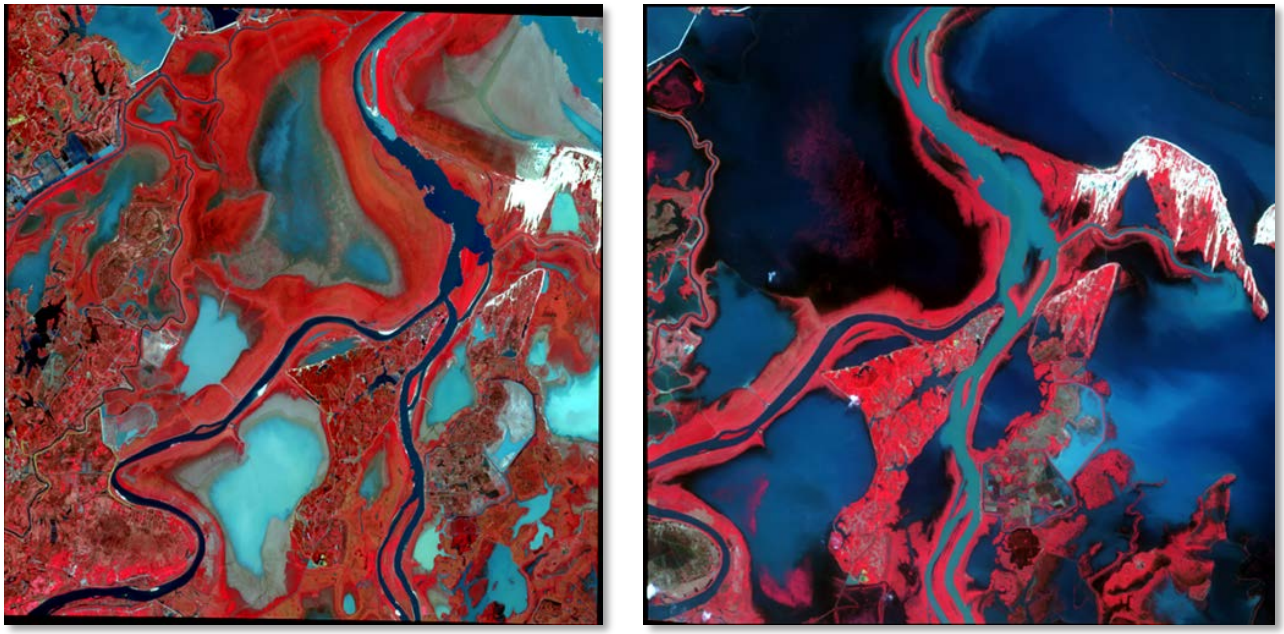

Figure 2.1.29: Left: Poyang Lake during dry season (05/03/2013); Right: Poyang Lake during wet season (22/05/2013)

SERTIT is involved in the DRAGON project since 2004. The aim of SERTIT's work within this project is to monitor the Poyang Lake (P.R. of China). A multi-temporal, multi-resolution and multi-sensor (radar and optical) database is established over this region, with some SPOT-4 data acquired in the framework of the TAKE 5 program plus Landsat-8 data. Poyang Lake is chosen as an ASAPTERRA test site because of the existing database and reference data to test a set of algorithms on their potential for semi-automatic water body/flood mapping.
The Pléiades HR images over Poyang Lake were acquired during the dry season (03/05/13) and during the wet season (22/05/13). They have a size of 20 by 20km and hence 10,000 x 10,000 pixels (fig. 2.1.29).

Morombe, Madagascar

The island of Madagascar is a country located in the western part of the Indian Ocean near the African coast. The island is subject to many climate events especially cyclones that form in the tropics. These depressions then cause, through their strong winds and raised sea levels, much damage as was the case for the Haruna cyclone 22 February 2013. A Pléiades image was acquired on the 26/02/2013 over the city of Morombe and its outlying rural areas (fig. 2.1.30). The water mapping difficulties lie in the small water bodies in urban areas and the extremely similar spectral reflectance of rural flooded and non-flooded areas due to presence of mud and flood residues.

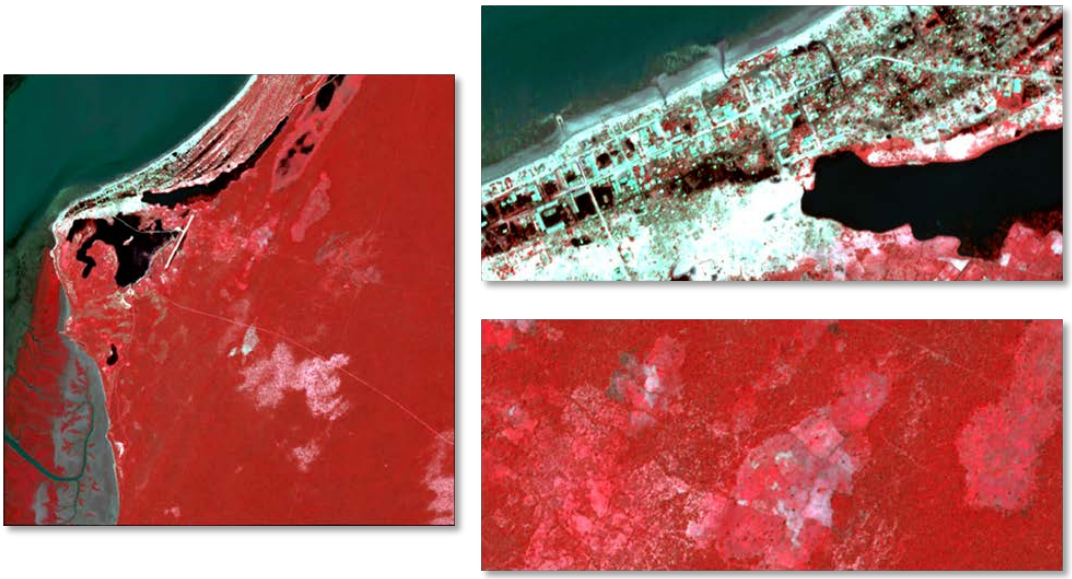

Figure 2.1.30: Pléiades data acquired on 26/02/2013. Left: City of Morombe, Madagascar: Upper right; small flood water bodies in urban area; Lower right: flood residues and mud in rural areas.

Development results

The supervised classification by the ANN and SVM used in this study were performed in the ORFEO Tool Box (OTB). A script was written in batch language for running OTB tools. We chose to classify the data with binary methods, water or non-water, using the same training samples with the two classifiers. The non-water class is composed of urban construction, transportation, land

cover and wetlands especially in Poyang images. The water class regroups all water pixels including water traces in the Morombe urban area. The training samples selected for each class were digitised through prior knowledge and visual interpretation. Training samples are digitized directly on the image that will be classified. According to (Foody and Arora, 1997) the best size of pixels per class is around 30 to 50 for ANN. On the contrary SVM has the advantage to perform well with samples of a small size. 50 samples per class were chosen. The spectral response variability within the water and non-water classes was represented in the set of training samples. Each site had its own sample set built.

Concerning the architecture of the ANN, the number of input and output neurons generally depends on the complexity of the problem. In this way the number of input neurons corresponds to the number of image bands and for the hidden level it corresponds to the number of input bands. The output neurons correspond to the number of classes. Unfortunately, a given architecture can give good results for an application over a given area but not assure the same performance for another. According to Bendiktsson (1990) a three level architecture can guarantee interesting results from different remote sensing sources. It was decided to keep the same architecture for all tests. However, two different training models were build, one for each test site. Most of the ANN parameters were fixed: momentum, termination criteria and update value. Dynamics' parameters selected for ANN are the method type, Beta and Alpha parameter and the identity function. It is noticed that OTB does not offer a large choice of identity functions, in a majority of cases the "sigmoid" function represents to be the most stable function. In terms of the SVM different kernels were selected associated with a selection of models and parameters linked to the model.

In a first step, the quantification of the impact of internal algorithm parameters were studied (tab. 2.1.6 and 2.1.7). It was decided to test these parameters on the Morombe data which is a crisis data coming from a rapid mapping action. Afterwards the two best configurations were tested over Poyang Lake because of their increased difficulties concerning water class detection and boundaries.

ANN	Method Type	Beta parameter	Alpha parameter	Identity function
Configuration 1	regression method	0,4	1	Sigmoïd
Configuration 2	regression method	0,8	0,8	Sigmoïd
Configuration 3	regression method	0,3	0,7	Gaussian
Configuration 4	regression method	0,2	0,9	Sigmoïd
Configuration 5	backpropagation method	1	1	Sigmoïd
Configuration 6	backpropagation method	1	0,1	Sigmoïd
Configuration 7	backpropagation method	0,7	0,3	Sigmoïd
Configuration 8	backpropagation method	0,5	0,5	Sigmoïd
Configuration 9	backpropagation method	0,2	0,8	Sigmoïd

Table 2.1.6: Table representing the different Artificial Neural Network configurations tested.

SVM	Kernel	Model	Degree	Parameter c / nu
Configuration 1	linear	C	-	10
Configuration 2	linear	Nu	-	0,1
Configuration 3	Polynomial	C	2	10
Configuration 4	Polynomial	Nu	2	0,1
Configuration 5	RBF	C	-	10
Configuration 6	RBF	Nu	-	0,1

Table 2.1.7: Table representing the different SVM configurations tested.

Results over Morombe and Poyang were compared with a reference classification produced by visual interpretation at SERTIT during a rapid mapping activation. An advantage of the comparison over the Morombe region is to analyse two types of information extraction in “rush mode” using different methods (fig. 2.1.31). Results over Poyang were compared with a reference produced at SERTIT by a traditional extraction tool and corrected by photo-interpretation (fig. 2.1.32).

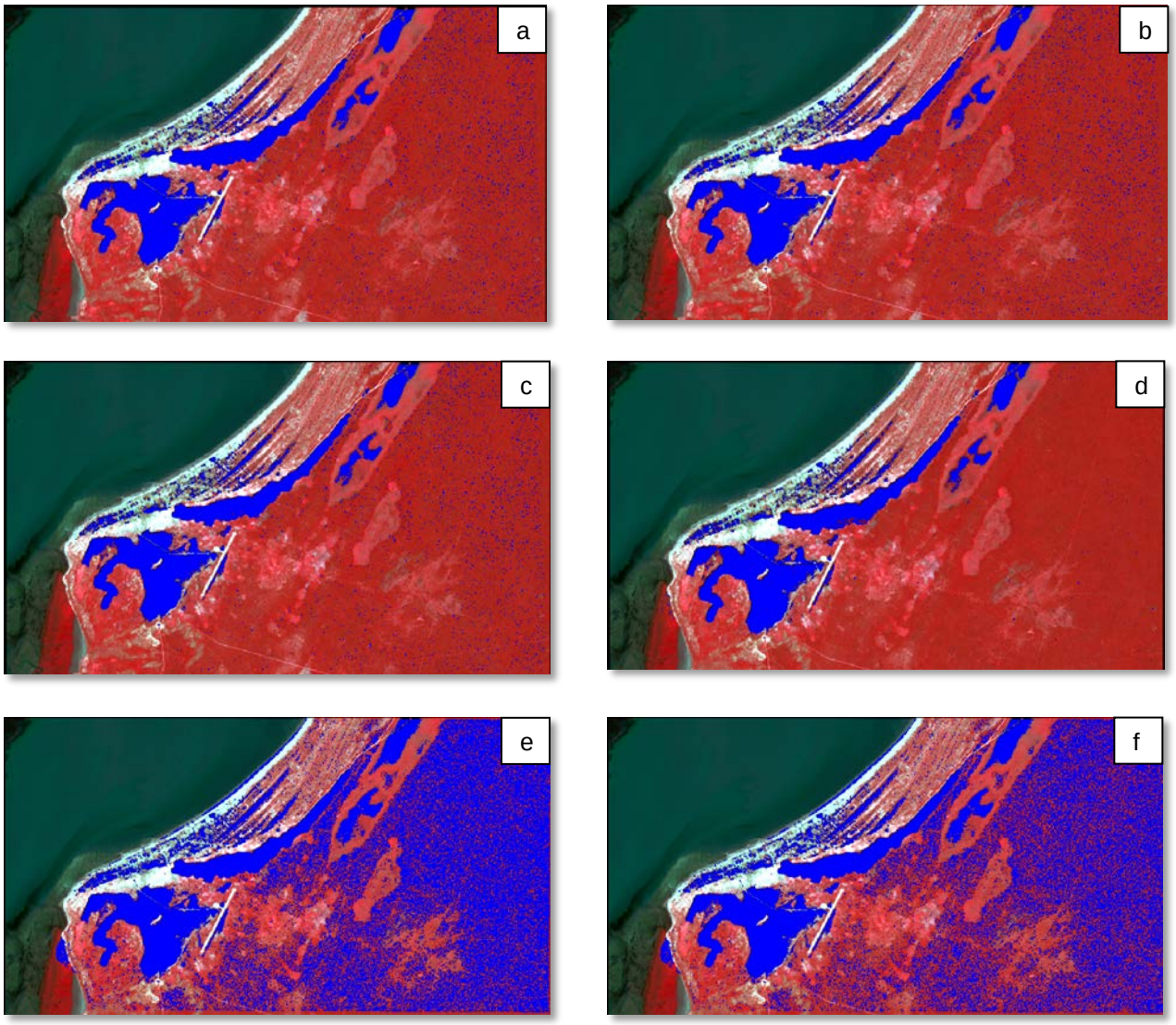

Figure 2.1.31: Results over Morombe: Upper left, upper right and middle left for SVM (configuration 1, 2, and 3, respectively) and middle right, lower left and right for ANN (configuration 1, 2, and 3, respectively).

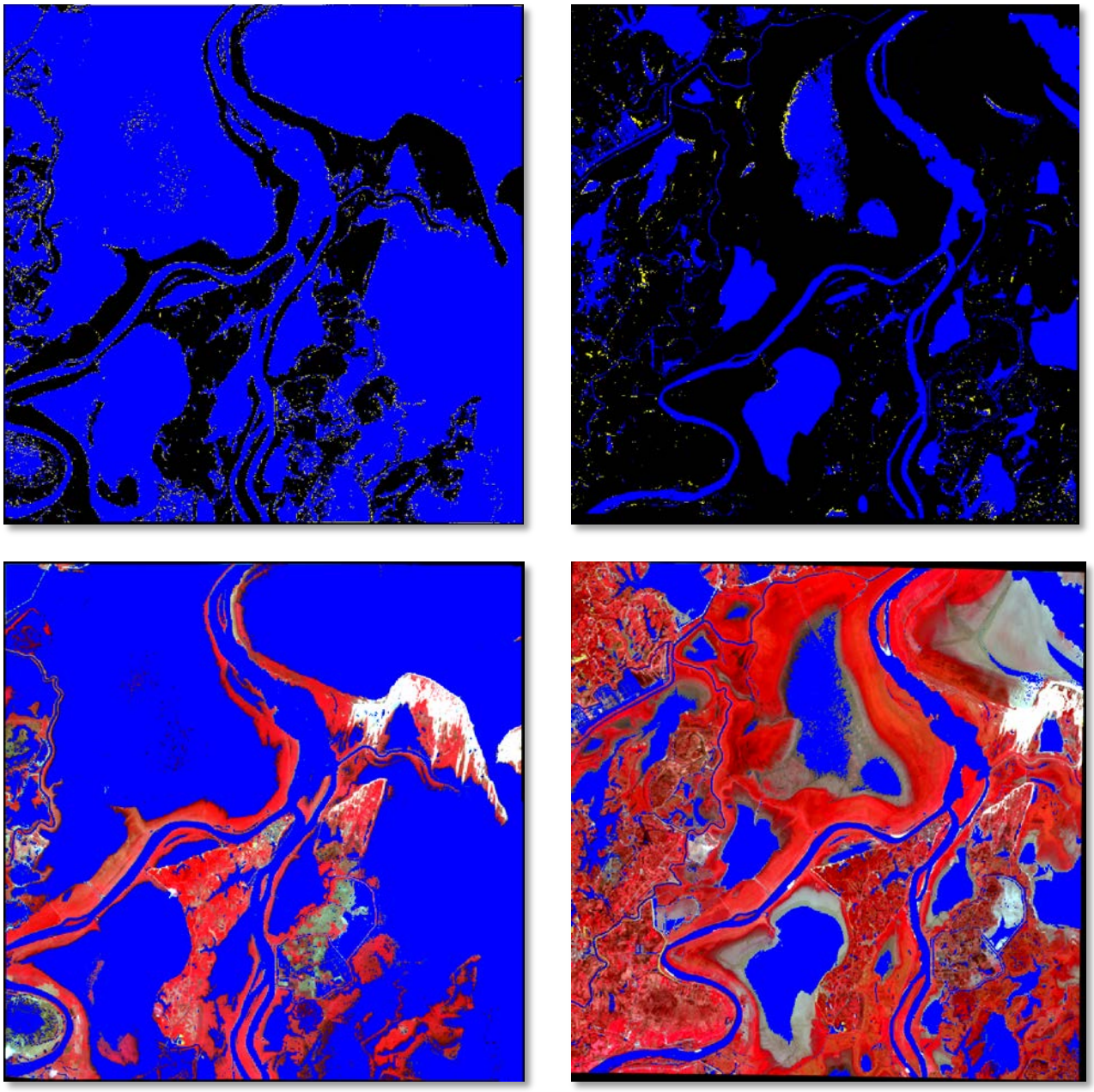

Figure 2.1.32: Extraction realised with the ANN algorithm (Configuration 1: Regression / beta = 0.4 / alpha = 1 / sigmoid) over the two Poyang images.

Figure 2.1.31 shows the impact of different parameters on the extraction of water in Morombe's region. Each configuration indicates a different pattern of water distribution in the city and rural area. By analysing those tests it was decided that one or two configurations are suitable to execute a correct water extraction on this image. Both ANN and SVM are observed to be similar using configuration 1 through visual interpretation. The statistics tables below demonstrate that ANN is in better agreement with visual interpretation and has the best accuracy among all.

The resulting classification accuracies obtained using the selected methods over Madagascar and using the best configuration for SVM and Artificial Neural Network over Poyang are shown in the tables below (tab. 2.1.8).

Table 2.1.8: Accuracies of the SVM and ANN methods and configurations over Poyang Lake

Artificial Neural Network Accuracy		Overall	Omission	Commission
Configuration number	Method	%	%	%
1	Regression / beta = 0,4 / alpha = 1 / sigmoïd	99,26	3,01	7,87
2	Regression / beta = 0,8 / alpha = 0,8 / sigmoïd	99,24	3,02	8,09
3	Regression / beta = 0,3 / alpha = 0,7 / Gaussian	31,03	74,22	90,71
4	Regression / beta = 0,2 / alpha = 0,9 / sigmoïd	99,24	3,91	7,37
5	Regression / beta = 1 / alpha = 1 / sigmoïd	99,22	2,65	8,64
6	Regression / beta = 1 / alpha = 0,1 / sigmoïd	67,66	34,91	82,09
7	Regression / beta =0,7 / alpha = 0,3 / sigmoïd	74,86	27,2	78,09
8	Regression / beta = 0,5 / alpha = 0,5 / sigmoïd	98,08	2,74	21,06
9	Regression / beta = 0,2 / alpha = 0,8 / sigmoïd	99,21	2,85	8,55

Support Vector Machine Accuracy		Overall	Omission	Commission
Configuration number	Method	%	%	%
1	Linear kernel / Model C / Parameter C=10	98,65	2,58	14,93
2	Linear kernel / Model Nu / Parameter Nu=0,1	97,76	3,29	23,16
3	Polynomial kernel / Degree 2 / Model C / Parameter C=10	97,47	3,5	25,43
4	Polynomial kernel / Degree 2 / Model Nu / Parameter Nu= 0,1	97,73	3,31	23,34
5	RBF kernel / Model C / Parameter C=10	92,62	8,26	50,18
6	RBF kernel / Model Nu / Parameter Nu=0,1	97,63	3,4	24,12

Accuracy over Poyang Images		Overall	Omission	Comission
Configuration number	Method	%	%	%
22/05/2013 Image	22/05/2013 Image			
1	SVM Linear kernel / Model C / Parameter C=10	98,12	2,98	5,62
1	ANN Regression / beta = 0,4 / alpha = 1 / sigmoïd	99,88	0,16	0,39
05/03/2013 Image	05/03/2013 Image			
1	SVM Linear kernel / Model C / Parameter C=10	98,73	4,66	2,7
1	ANN Regression / beta = 0,4 / alpha = 1 / sigmoïd	98,92	3,6	2,62

Above all, it is observed that generally the ANN performs better. The SVM is nearly as accurate over Poyang but has a lot more commission errors concerning Morombe's tests. The Morombe tests help in algorithm adjustment and in analysing core parameter impacts on machine learning. Consequently, among all the configurations, the ANN has the highest overall accuracy with 99.26%. This configuration omits a small percentage of the two classes (3.01%) but has a higher percentage of commission errors over Morombe even though over Poyang the ANN commission error reduces dramatically. The result over Poyang 22/05/2013 image is nearly perfect. As a reminder the image over Poyang is a Pléiades HR image (20 x 20 km) and with difficulties over this region being extremely hard to overcome especially for water extraction. The ANN results are very encouraging for crisis images with difficult spectral characteristics and mixed pixels but we would prefer to use SVM because of the ease of configuration, the smaller size of samples required, the shorter calculation speed, which is an important parameter during rapid mapping activations, and the capabilities to use the same configuration for all types of images. With respect to the Neural Network despite the results a new model (with different weights) over Poyang is being used but a

generalization has not been tested yet. It must be considered that it will be difficult to find a unique trained model for all images due to the difficulties to create a precise and generalizable architecture. This will be worked on in the near future.
Otherwise, the processing time for each test site is different. This parameter is important in a rapid mapping context and therefore has to be taken into account. A batch language OTB workflow was outlined which calculates statistics of the images, creates a model for each algorithm, produces the image classification and then performs post-classification routines to improve the extraction. The SVM takes around 23 min whereas the ANN takes around 29 min for the Poyang image. Over Morombe the calculation times were much lower: 15 sec for SVM and 20 sec for ANN.
Results achieved by SVM and ANN show high accuracy but with a better performance for ANN. More tests are required to confirm the use of the algorithm during rapid mapping actions. Uncertainty is a major factor affecting remotely sensed classifications quality. A lot of parameters have influence on the classifications including training samples for machine learning and the absolute accuracy of the reference used. The algorithms are based on spectral characteristics of the images and neglect relationship between adjacent pixels and this can be a source of misclassification. Of course, misclassification can also be linked to atmospheric phenomena or mixed pixels in the AOI.

VHR flood mapping results summary

Examination of results over simple test cases (e.g. City of Morombe, Madagascar) and more complex (e.g. Poyang, China) test sites using Pléiades imagery in terms of thematic accuracy has led to contrasting conclusions in terms of thematic accuracy. Over Poyang Lake Pléiades flood/ water body mapping accuracies are 98% (SVM) and 99% (ANN). User's accuracies are 94% (SVM) and 99% (ANN). Producer's accuracies are 97% (SVM) and 99% (ANN). An evaluation of results in the context of rapid mapping with a focus on simplicity, robustness, and speed of procedure execution, leads to the SVM being preferred in spite of its results being slightly worse. This algorithm is preferred in a rapid mapping context for its easier and faster implementation. Furthermore, SVM execution is slightly faster too.
Over a very complex case in St-Louis (Senegal) the work has led to unsatisfactory results. SVM gave accuracies of 11% to 45%. As an added procedure on this very difficult image (wind, waves, sun-glint, fog, haze) Random Forest algorithms were explored. These algorithms gave even lower accuracies of 4% to 39%. The accuracy variations depend on the input scenario parameters to the algorithm. In this case it would still be better to digitise the water bodies manually.

2.1.3.2 High resolution optical flood mapping (Sentinel-2)

As a last flood mapping challenge in ASAPTERRA it was decided to develop a Sentinel-2 flood mapping chain. The objective of this processing chain at the start was to produce a sophisticated chain which involved human interaction. In the last 6 months of ASAPTERRA SERTIT re-focussed

its efforts to produce a fully automatic flood mapping chain adapted to producing flood delineation maps in 3 hours within the Copernicus EMS Rapid Mapping context. The objective is that the chain produces a robust result that will be validated by an operator in a second phase for final products (Charter, EMS).

Taking into account the requirement to process Sentinel-2 data and the fact Sentinel-2 has not existed for a long time there were not many flood situations to choose from. SERTIT searched for flood mapping on the internet that had already been mapped using Sentinel-2 finding the Somalia, 2015, and Louisiana (USA), 2016 flood events. The methodological research leading to the choice of the indexes mentioned below was carried out within an internal research project.

Methodology

Overall, SERTIT has produced an automatic processing chain to extract water bodies/floodwaters from Sentinel-2 and Landsat 8 images that have already been accessed as or pre-processed to Top Of Atmosphere reflectance values. The workflow below highlights the following steps (fig. 2.1.33):

- Digital elevation model smoothing to reduce local DEM anomalies, which affect slopes, with the production of slope and hill-shade layers using sun azimuth and elevation information the date in question,
- Four water extraction indexes are then produced (tab. 2.1.9 and references 3-5) :

Table 2.1.9: Water extraction indexes: the 4 retained

Indice	Source	Formule
$NDWI_{McFeeters}$	(McFeeters, 1996)	(GREEN - NIR)/((GREEN + NIR)
$NDWI_{Xu}$ = MNDWI	(Xu, 2007)	(GREEN – SWIR1)/(GREEN + SWIR1)
$AWEI_{no\ shadow}$	(Feyisa, Meilby, Fensholt, & Proud, 2013)	➔
$AWEI_{shadow}$	(Feyisa, Meilby, Fensholt, & Proud, 2013)	➔

$$AWEI_{nsh} = 4 * (G - SWIR1) - (0.25 * NIR + 2.75 * SWIR2)$$

$$AWEI_{sh} = B + 2.5 * G - 1.5 * (NIR + SWIR1) - 0.25 * SWIR2$$

- The indexes are thresholded,
- The area of interest is reduced to relatively flat lying zones using a slope threshold,
- A cloud free water mask is generated along with a secondary class of flood affected vegetation,
- The final water layer is exported.

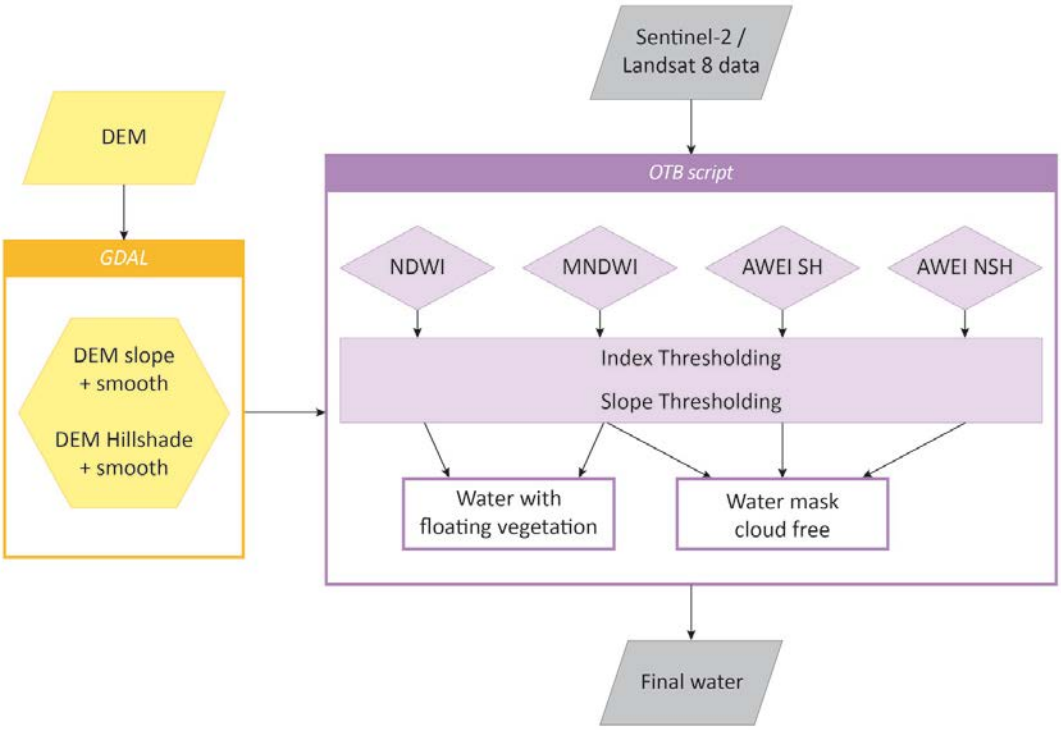

Figure 2.1.33: Workflow diagram of automatic Sentinel-2 water body/flood extraction method

Pre-demonstrator Sentinel-2 flood mapping case studies

Taking into account the requirement to process Sentinel-2 data and the fact it has not existed for a long time there were not many flood situations to choose from. SERTIT researched flood mapping on the internet and found Somalia, 2015, and Louisiana, 2016.

Somalia

According to ReliefWeb heavy rains in parts of Somalia and Ethiopian highlands led to flooding in Somalia, which is often the case around this period of the year, but more severe than average. As is often the case, Belet Weyne town and District were affected with over 70,000 people being displaced at the time. Of these, 36,000 people are in Ceel Jaale settlement alone, while others moved to other neighbouring villages. (OCHA, 7 June 2016) from http://reliefweb.int/disaster/fl-2016-000046-som

These floods were captured by Sentinel-2 on 25 May 2016 with the floods located in the Belet Weyne District. The map in figure 2.1.3420 is sourced from the ReliefWeb site and was produced by the Somalia Water and Land Information Management Project (SWALIM). SWALIM is implemented by the United Nation's Food &

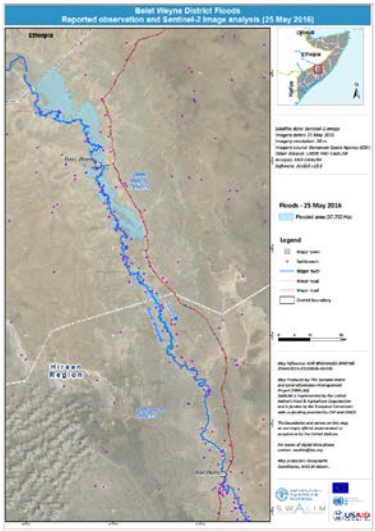

Figure 2.1.34: Map of 25/05/2016 flooding along the River Shabelle in the Belet Weyne District derived from Sentinel-2 data. Map

Agriculture Organization and is funded by the European Commision with co-funding provided by CHF (Common Humanitarian Fund) and USAID.

production: FAO-SWALIM; Data: ESA 2016; Other datasets UNDP, FAO-SWALIM Analysis: FAO-SWALIM.

In the Somalia example Sentinel-2 data are used (fig. 3.8), those acquired the 25 May 2016, along with a SRTM 1sec DEM. The Sentinel-2's bands (1-12) are resampled to 10 m to homogenise band resolutions and the DEM is smoothed. The resulting cloud free water mask is quite convincing and requires no photo-interpretation to render the results useable in rapid mapping (fig. 3.8) especially the Copernicus EMS First Activation Map phase (3 hours). The time to produce the flood without major errors is dramatically reduced with the end result taking 7.5 min involving no human intervention. The method needs to be applied to more flood situations to increase its Technological Readiness Level and to be demonstrated and used during real activations to become operational.

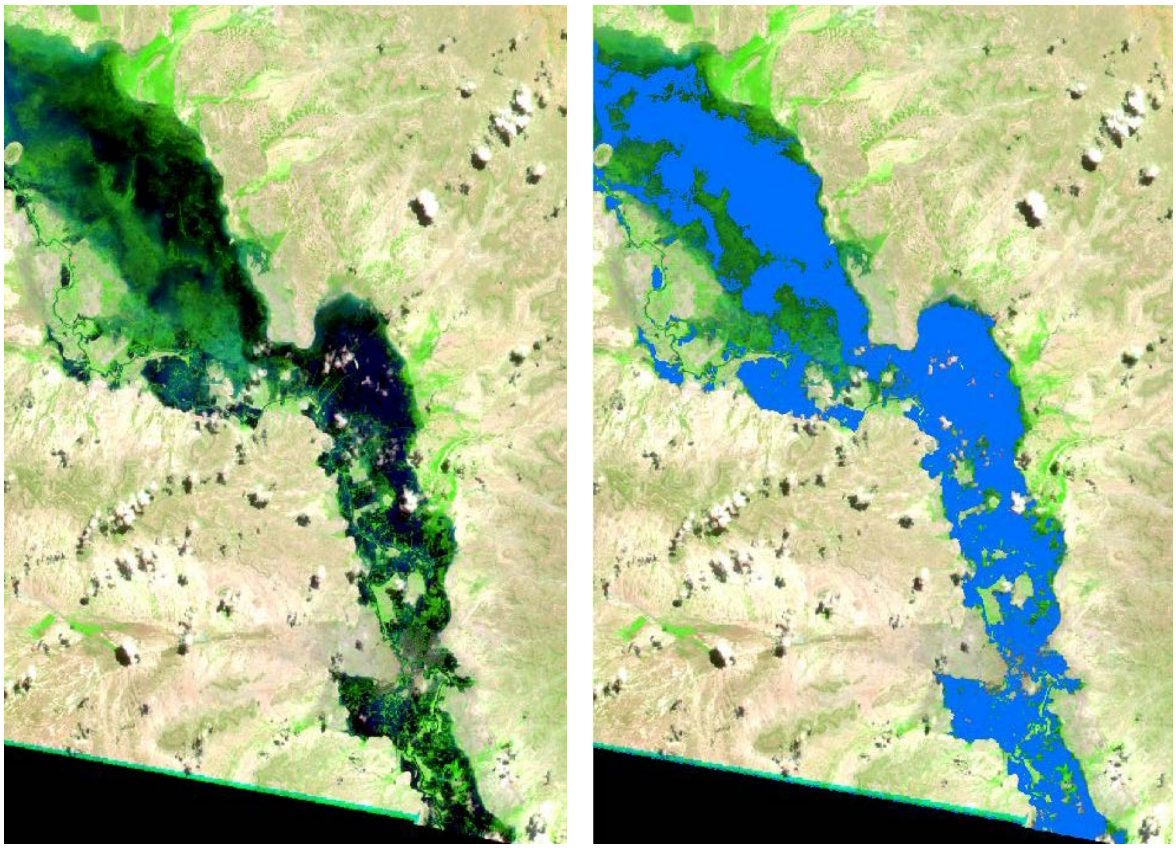

Figure 2.1.35: The Sentinel-2 imagery acquired the 25 May 2016 over the Belet Weyne District (left) and the same image overlaid by the final automatically derived flood mask (right).

Louisiana, USA

In May 2016, both the International Charter and Copernicus EMS were triggered to cover the Louisiana flooding. The Charter was triggered by the USGS on behalf of the State of Louisiana, USA, whereas Swedish AU triggered Copernicus EMS on the 14/08/2016 on behalf of American agencies. The activation reason is given as: "More than 20,000 people have needed rescue following massive floods that swept across the state of Louisiana. The flooding has killed at least

four people and residents are being warned it's going to get worse before the flood waters recede. President Barack Obama declared a major disaster in the hard-hit parishes of East Baton Rouge, Livingston, St. Helena and Tangipahoa, freeing up federal funding for flood-related assistance. The heavy rainfall started on Friday, where some areas received more than 17 inches (43cm) of rain. The neighbouring states of Alabama and Mississippi are also experiencing severe weather. Louisiana Governor John Bel Edwards declared a state of emergency on Friday" (https://www.disasterscharter.org/web/guest/activations/-/article/flood-in-united-stat-3).

In the Louisiana example both the Charter and EMS concentrated their mapping effort on derived flood extents from SAR data from the 15/08/2016 onwards.

SERTIT found a fairly cloudy Sentinel-2 image acquired the 14/08/2016 and has applied its pre-operational automatic flood extraction algorithm to produce a flood extent that has very little overlap with cloud shadows and other landuse/landcovers. The area covered is in and around Baton Rouge. The time taken to produce this layer is extremely fast (approx. 7.5 min) and is deemed acceptable thematically for a First Activation Map in the Copernicus EMS context. To produce a Charter or the final Copernicus EMS map the flood extent layer has to be manually validated.

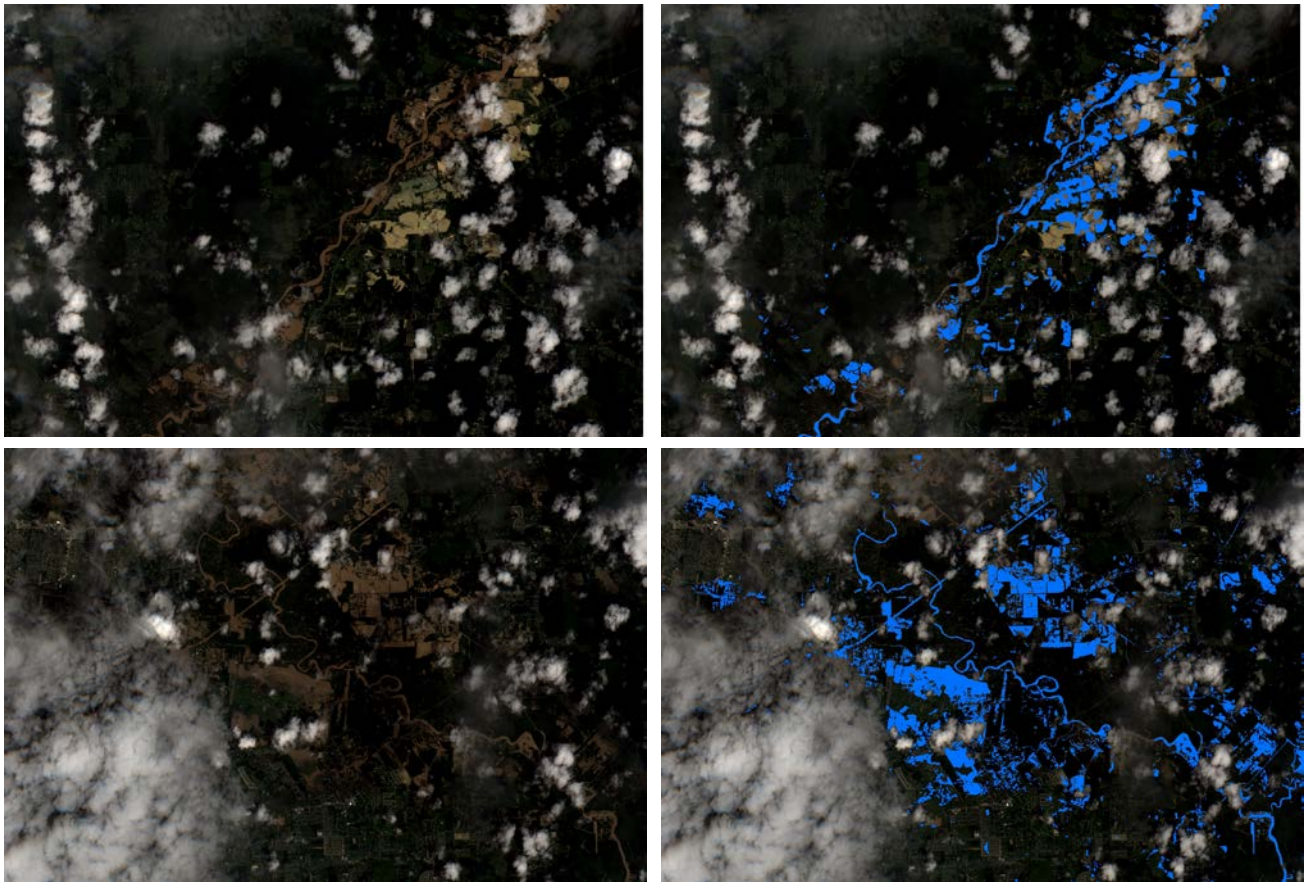

Figure 2.1.36: Two examples of automatic flood extraction obtained from processing the 14/08/2016 Sentinel-2 image in a cloudy and shadow strewn image. Data provided by ESA, 2016.

Whereas SAR data guarantee acquisitions of flood extents in relatively bad weather optical are much less reliable but when usable provide insight into flooding in slightly open areas of towns.

The automatic extraction from Sentinel-2 data, which has not been manually validated, shows flooding in the NE suburbs of Baton Rouge (blue in fig. 2.1.36). The Copernicus EMS flood delineation map extracted from TerraSAR-X data on the 17/08/2016 shows no such flooding (cyan). The Sentinel-2 derived flood extent is partial but definitely very interesting. Furthermore, by chance the acquisition occurred very early during the emergency.

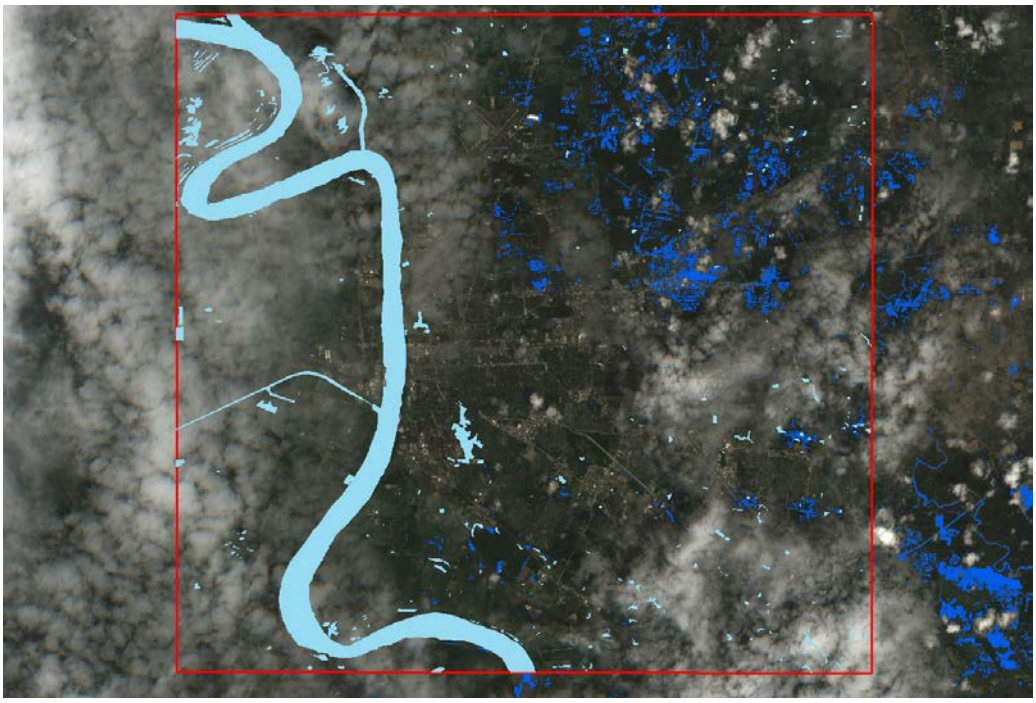

Figure 2.1.37: Comparison between a flood extent extracted from Sentinel-2 data acquired the 14/08/2016 (blue) and the flood delineation extracted from TerraSAR-X data acquired the 17/08/2016 within Copernicus EMS. Common areas are masked by Copernicus EMS mapping in cyan. The Copernicus EMS AOI is shown in red.

References

1. Bendiktsson, J., 1990. Neural Network approaches versus statistical methods in classification of multisource remote sensing data. IEEE Transactions on Geoscience and Remote Sensing, 28, 540-552.
2. Foody, G.M., Arora, M.K., 1997. An Evaluation of some factors affecting the accuracy of classification by an Artificial Neural Network. International Journal of Remote Sensing, 18, 799-810.
3. McFeeters, S., 1996: The use of normalized difference water index (NDWI) in the delineation of open water features. International Journal of Remote Sensing, 1425-1432.
4. Xu, H.,2007: Modification of normalised difference water index (NDWI) to enhance open water features in remotely sensed imagery. International Journal of Remote Sensing.
5. Feyisa, G., Meilby, H., Fensholt, R., Proud, S., 2013: Automated Water Extraction Index: A new technique for surface water using Landsat imagery. Remote Sensing of Environment.

2.2 Report on auxiliary data

2.2.1 Introduction

The aim of this section is to introduce and evaluate existing ancillary data sets with respect to their applicability within automatic SAR-based flood processing chains. Ancillary data sets are required in different steps, i.e.:

- Digital Elevation Models (DEMs):
  - terrain-correction of SAR-data
  - radiometric calibration of SAR-data to sigma naught (dB)
  - calculation of terrain characteristics for post-classification improvement (e.g. layover areas, slope, height above nearest drainage)
- Reference water mask to separate between normal water levels from flooded areas

2.2.2 Reference Water Masks

SWBD and MOD44W

A global reference water mask is required for separating the Sentinel-1 detected open surface water extent into areas of standing water (i.e. normal water levels) and inundation areas. In order to achieve global coverage, the reference water mask is a combination of three data sources:

- SRTM Water Body Data (SWBD) which covers the Earth's surface between 56° southern latitude and 60° northern latitude at a resolution of approx. 30m at the equator
- The MODIS 250m land-water mask (MOD44W) which is used for all northern and southern latitudes not covered by SWBD data.
- A water layer extracted from the Base DLM is used for Germany – see below.

In addition, so called “dummy-tiles” have been created for all land surfaces where no reference water mask is available due to the absence of water surfaces. All data sources have been combined to a consistent global data set, which is available as one by one degree lat/lon (WGS84) projected GeoTIFF-tiles (see fig. 2.2.1).

During processing, the tiles corresponding to a given SAR scene are extracted and resampled using nearest neighbour resampling. The global reference water mask can be regarded as a “best-of” database – for the future, it is foreseen to further improve the database using up-to-date continental- or country-scale reference water layers of higher spatial resolution.

Base DLM

The Base DLM (“Basis DLM” in German) is a digital landscape model of Germany that is provided at a scale of 1:25.000 by the Federal Agency for Cartography and Geodesy (BKG). From the Base DLM, all water bodies and drainage areas have been extracted in order to compile a reference water mask with a comparably high accuracy. For the integration of the layers into the global reference

water mask, the vector data has been rasterized to a spatial resolution of 15 meters. For harmonization purposes, particularly in the transition areas, the rasterized Base DLM water layer was subsequently merged with the SWBD-based water bodies.

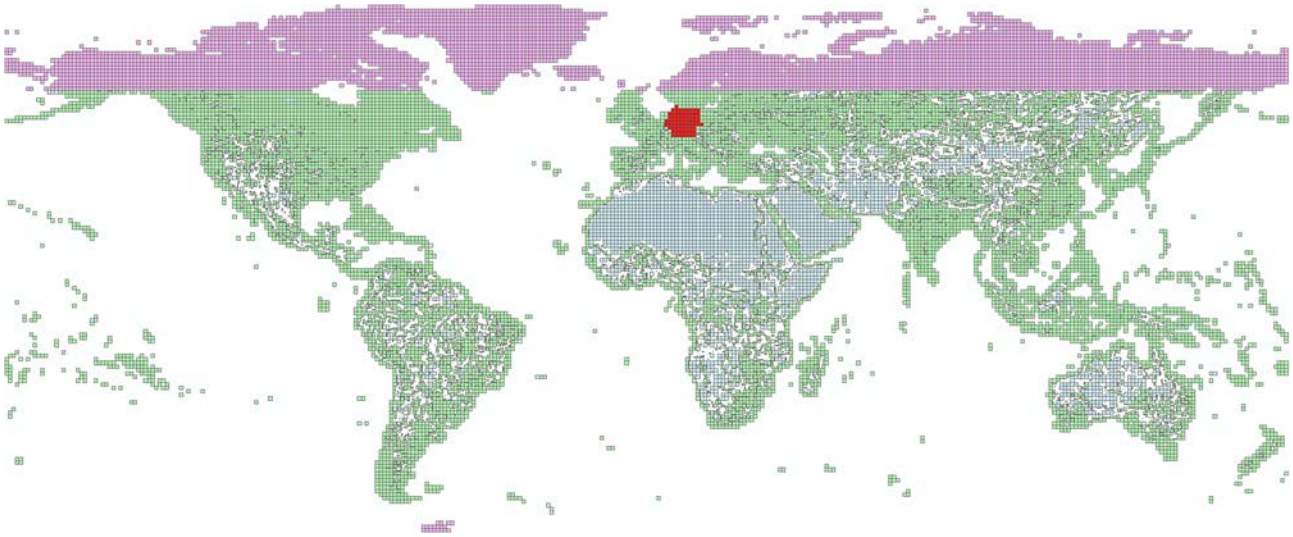

Figure 2.2.1: Coverage of global reference water mask (green: SWBD, purple: MOD44W, blue: dummy-tiles, red: Base DLM water bodies).

2.2.3 Digital Elevation Data

Aster GDEM V2

The ASTER Global Digital Elevation Model Version 2 (GDEM V2) with a pixel size of one arc second is used for a refinement of the flood mask. The same terrain information is used for the optional computation of a GIM in the pre-processing step of the TerraSAR-X flood service. While the reference water mask is resampled to the SAR pixel size during its extraction from the global dataset, resampling of the DEM is conducted after the slope and optional GIM computation. This is performed because the pixel size of TerraSAR-X and scenes is usually smaller than that of the DEM (~30m) leading to slope values of zero in the resampled DEM for all target pixels covering the same source DEM pixel.

While the ASTER GDEM V2 has certain advantages over SRTM in areas of strong relief, DEM artifacts can sometimes be observed in rather flat areas which cause artificially high slope values. Since the fuzzy-logic based post-classification includes terrain slope as a fuzzy set, this can lead to small gaps in derived flood surfaces because the membership value of these pixels to the class “flood” is drastically reduced. The recently released SRTM data with 1 arc second spatial resolution may provide a solution to this problem when finally available on a global scale and its incorporation in the TerraSAR-X flood processing chain is currently being considered.

SRTM

SRTM 3 arc second data is used for the range doppler terrain correction of Sentinel-1 data and the radiometric calibration to sigma naught (dB). This preprocessing step is performed using the graph

processing tool of the ESA Sentinel-1 Toolbox, which allows an execution of this processing step within a fully automated processing chain. The SRTM-tiles corresponding to a given Sentinel-1 scene are automatically downloaded by the Toolbox and stored in a user-defined directory.

HydroSHEDS

HydroSHEDS is a series of map products that provides near-global hydrological information for multiple scale applications (Lehner et al. 2008). The spatially consistent products are primarily derived from SRTM elevation data and currently available between 56°S and 84°N. Void-filled and conditioned DEMs, flow direction and accumulation products are produced globally per continent, and can be freely downloaded for non-commercial uses. HydroSHEDS hydrologically conditioned elevation (CON), void-filled elevation (DEM), and drainage direction (DIR) products are being used for the calculation of the height above nearest drainage index (see chapter 2.2.4).

2.2.4 DEM-derived indices and land surface characteristics

Slope

The slope information $sl_{(x,y)}$ in degrees for each pixel (x, y), i.e., the local steepness of the terrain, is used as input for the fuzzy-logic based post-classification and is computed from the ASTER GDEM V2 according to:

$$sl_{(x,y)} = arctan\left(\sqrt{\left(\frac{\Delta x_{(x,y)}}{n \cdot r_x}\right)^2 + \left(\frac{\Delta y_{(x,y)}}{n \cdot r_y}\right)^2}\right) \cdot \frac{180}{\pi}, \quad (1)$$

where Δx and Δy are the result of a standard Sobel edge filter applied on the DEM taking into account $n = 8$ pixel values, and r_x, r_y is the pixel resolution of the DEM in x and y direction.

Height above nearest drainage (HAND)

The height above nearest drainage (HAND) terrain descriptor expresses the height difference between a DEM cell and the closest cell of the drainage network along the actual flow path. As such, the index can be used to define flood-prone regions and consequently areas with a low probability of flood occurrence. Based on the index, areas above an empirically-derived threshold are excluded from the flood classification, thereby reducing potential misclassifications in non-flood-prone regions. For the purposes of the flood processing chains, the HAND index is currently being calculated on a near-global basis based on elevation and drainage direction information provided by the HydroSHEDS mapping product (Lehner et al. 2008).

The calculation of the HAND index is based on the treatment of the input DEM in three stages: data pre-processing, channel network delineation, and the normalisation of terrain elevations with respect to the defined drainage network (see fig. 2.2.2). After the source DEM data are imported, topographic irregularities (i.e. voids, sinks, pits and/or barriers) that may be present are identified and accordingly treated. Barriers are features that protrude from the surface, thereby restricting

continuous flow to the drainage network. Sinks (or conceptually comparable pits) are defined as the lowest points of a depression without an outlet, which may represent both natural aspects of the terrain or artifacts that are introduced during the preparation of the DEM datasets.

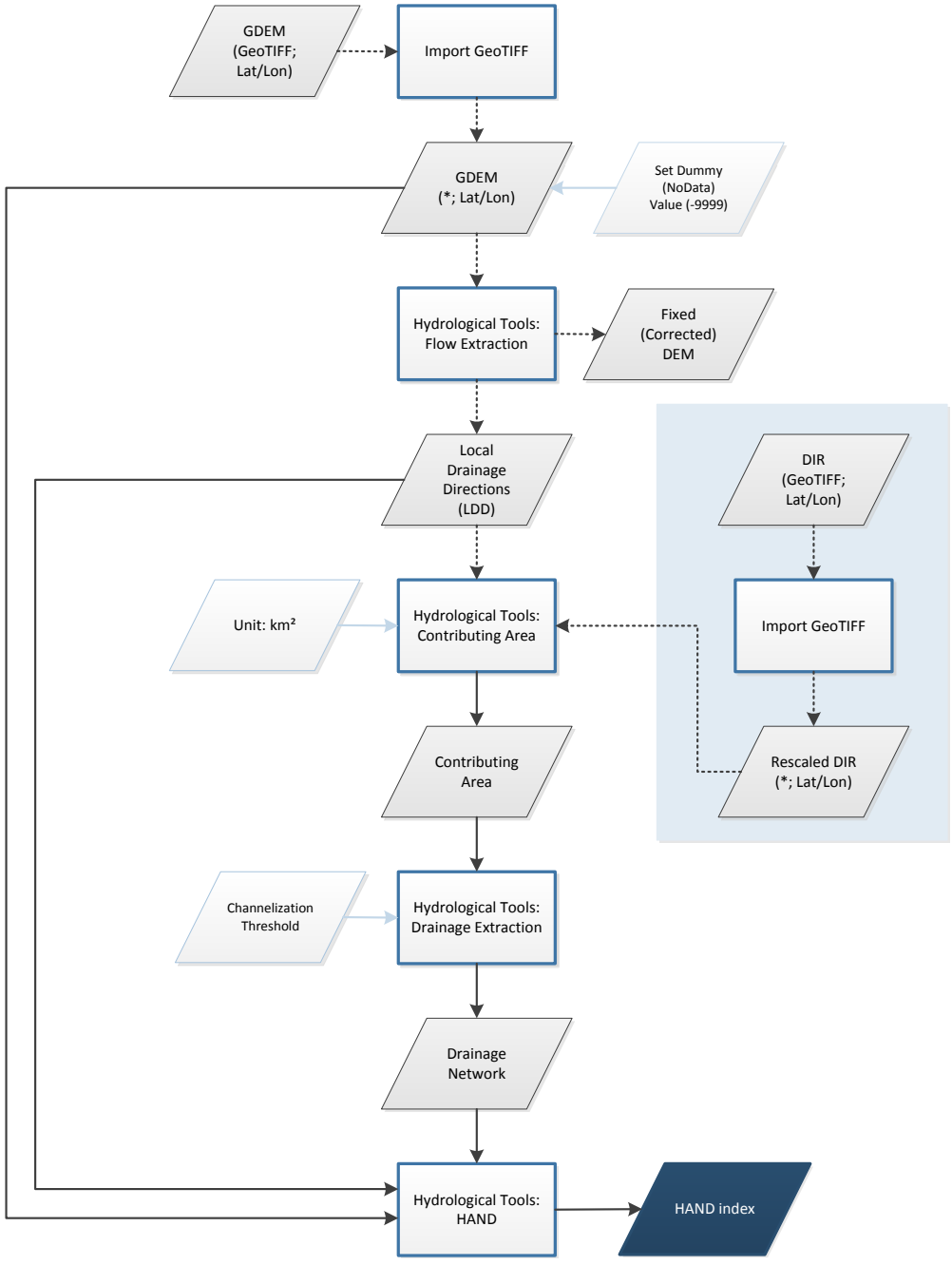

Figure 2.2.2: HAND calculation workflow using TerraView/TerraHidro.

Due to the utilisation of the HydroSHEDS drainage direction product (DIR) which has been generated from the HydroSHEDS hydrologically conditioned CON-product, the first and computationally very demanding processing steps can be avoided. The processing thus effectively starts with the delineation of the contributing area (i.e. catchment area) based on the local drainage directions (see shaded blue part of fig. 2.2.3). Subsequently, the drainage network is calculated

based on the derived catchment areas and the definition of a channelisation threshold value. The latter threshold value defines the number of pixels or area in km^2 contributing to a given drainage point and thereby determines the density of the resultant channel network. Based on empirical tests and comparison with a geodata base of rivers and lakes, a channelisation threshold of 10 km^2 was chosen to sufficiently resemble true drainage conditions.

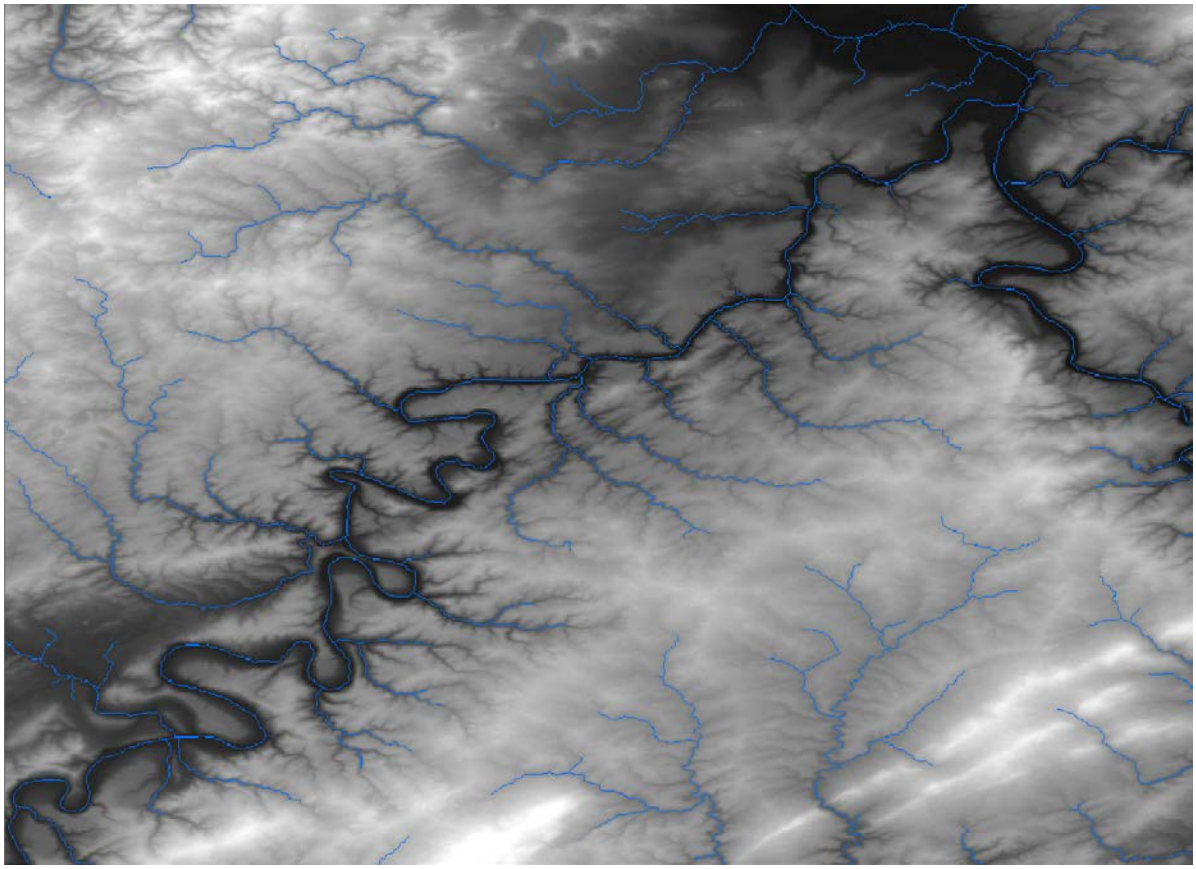

Figure 2.2.3: Example of the drainage network derived for an area near Koblenz/Germany at the confluence between Rhine and Mosel using a channelisation threshold of 10 km^2.

The final calculation of the HAND index is achieved using the HydroSHEDS void-free DEM product with two sets of procedures. First, each cell in the DEM is associated with the nearest drainage cell, with respect to the pre-identified flow directions. Here, it is important to distinguish between hydrological and Euclidean distances. This procedure is executed iteratively, based on the function described in Rennó et al. (2008). The HAND index values represent the vertical elevation difference between any non-drainage point <i, j> and the drainage point that it is hydrologically associated with based on flow directions. Therefore, if a point is a part of the channel network, it will have a value of 0. The HAND value can then be defined for any point <i, j>, with the assumption that flow paths are defined for all points, and that all flow paths are associated to respective drainage points.

Due to the aim of calculating the HAND index on a global scale, the primary focus was on choosing a stable environment that could produce consistent results. The TerraHidro software (INPE) was

favoured as it was developed in cooperation with a member of the research team that originally authored the HAND index. Furthermore, once contact was established, the ongoing correspondence was instrumental in clarifying key points of uncertainty.

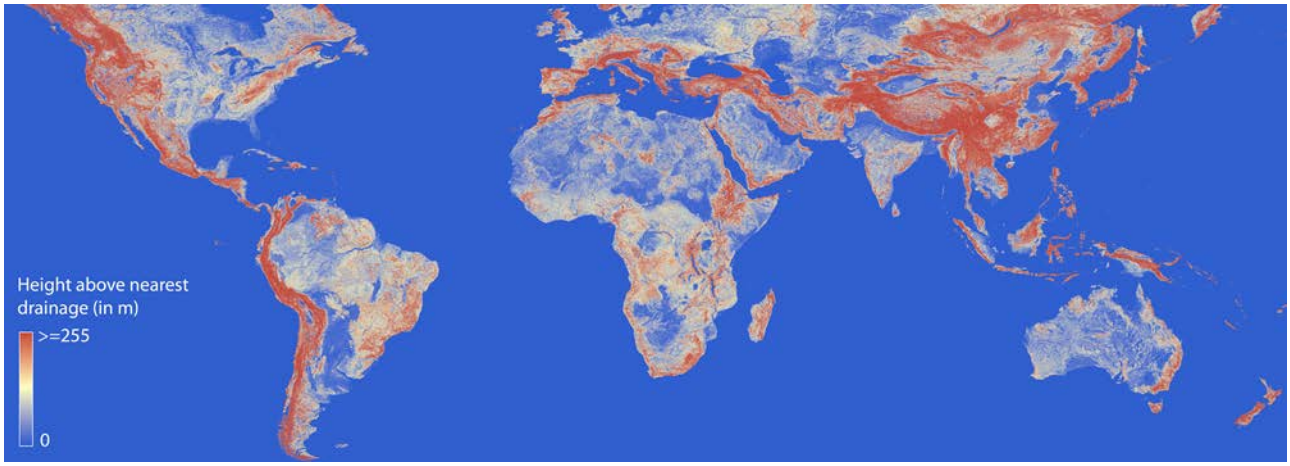

Figure 2.2.4: Near-globally calculated "Height above nearest drainage" index computed based on HydroSHEDS products, zoombox: Rhine valley near Freiburg/Germany.

Recently, the HAND-index was calculated near-globally (see figure 2.2.4). In order to utilise the derived HAND-index to mask out flood-lookalikes and misclassifications in areas with a defined positive height difference to the drainage network, a binary layer has been computed to separate flood-prone from non-flood-prone areas. Both binary classes are determined using an appropriate threshold value. Choosing the threshold value too high may lead to misclassifications (i.e. the inclusion of flood-lookalikes in areas much higher than the actual flood surface and drainage network) while a threshold value set too low would eliminate parts of the true flood surface. The choice of an appropriate threshold is thus critical, but could only be derived through a series of empirical tests (Chow et al. 2016). Due the global application scope of the flood processing chains, a rather conservative threshold value of ≥15 m was chosen to derive non-flood-prone areas. The mask has been further shrunk by one pixel in order to account for potential geometric errors between the exclude layer and SAR data. The derived binary layer was subsequently included in the Sentinel-1 and TerraSAR-X based flood processing chains as an "exclude layer" in the final classification. All areas with a HAND-index value ≥15 m are hence excluded from the flood extent (see fig. 2.2.5).

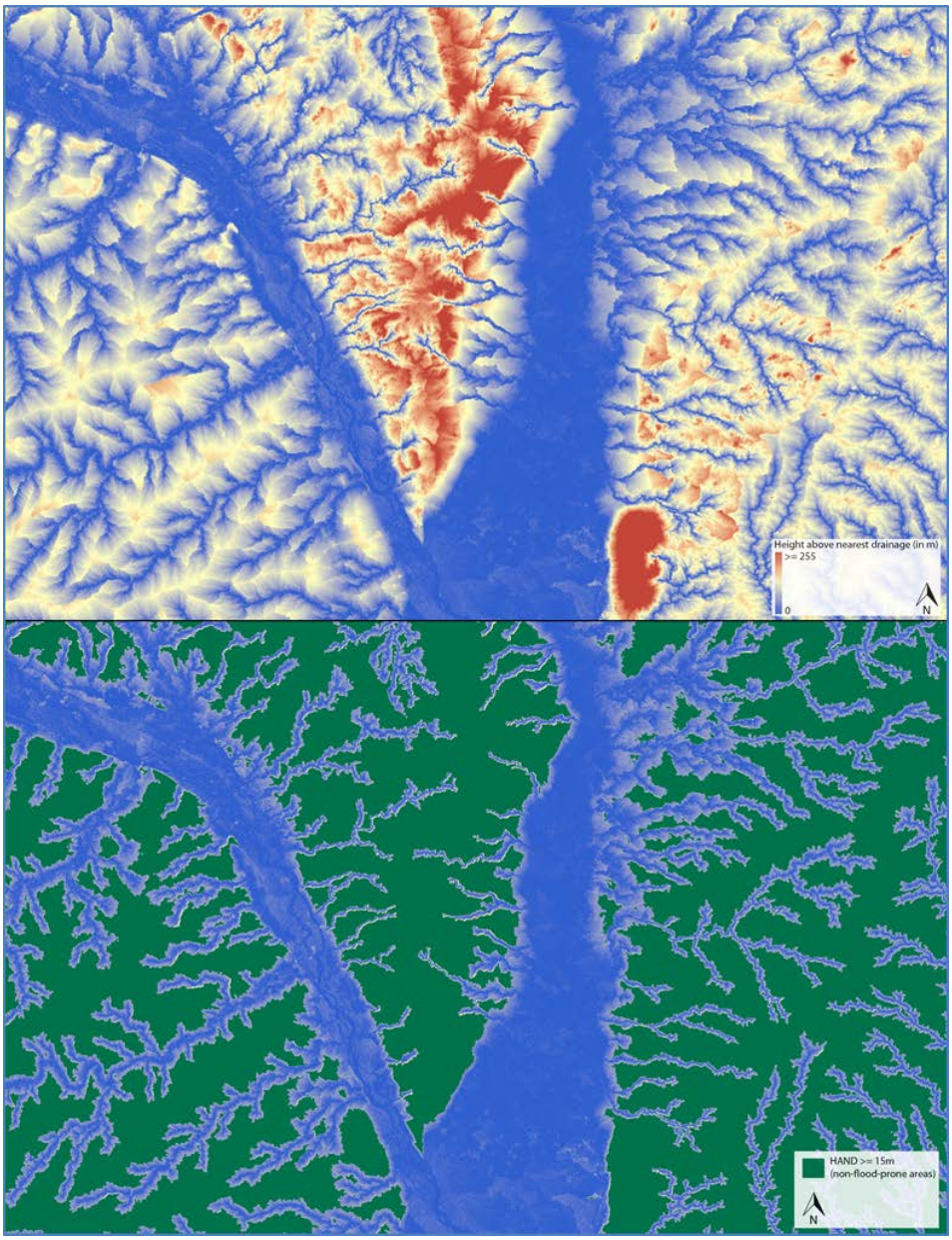

Figure 2.2.5: HAND-index for a test-site in Malawi (upper image) and derived binary exclusion mask (lower image) using a threshold value of 15m.

References

1. Chow, C., Twele, A., Martinis, S., 2016 (submitted): An assessment of the 'Height Above Nearest Drainage' terrain descriptor for the thematic enhancement of automatic SAR-based flood monitoring services. In: Proceedings of SPIE, SPIE Remote Sensing 2016, 26-29 September 2016, Edinburgh, United Kingdom.
2. Lehner, B., Verdin, K., Jarvis, A., 2008: New global hydrography derived from spaceborne elevation data. Eos, Transactions, AGU, 89, 93-94.
3. Rennó, C. D., Nobre, A. D., Cuartas, L. A., Soares, J. V., Hodnett, M. G., Tomasella, J., Waterloo, M. J., 2008: HAND, a new terrain descriptor using SRTM-DEM: Mapping terra-firme rainforest environments in Amazonia. Remote Sens Environ, 112, 3469-3481.

2.3 Technical note on flood detection in vegetation areas

2.3.1 State-of-the-art

SAR is the preferred tool for flood mapping from space due to the following reasons: On the one hand a SAR sensor provides its own source of illumination in the microwave range. Therefore, it is characterised by near all-weather/day-night imaging capabilities independent from atmospheric conditions. This guarantees a continuous observation of the Earth's surface. On the other hand smooth open water areas can be easily detected in SAR data due to the large contrast between water bodies and non-water areas. Further, in comparison to optical sensors, SAR offers the unique opportunity to detect – to a certain extent – standing water beneath vegetation.

The detectability of partially submerged vegetation is enabled by multiple-bounce effects: The penetrated radar signal is backscattered from the horizontal water surface and lower sections of the vegetation (e.g. branches and trunks). Compared to normal water level conditions, this leads to an increased backscatter return to the sensor (e.g. Richards et al. 1987, Townsend 2001, Hong et al. 2010), as diffuse scattering effects on the dry ground reduces the corner reflection effect.

The signal return from partially submerged vegetation is very complex and strongly depends on SAR system (e.g. wavelength, incidence angle and polarisation) and environmental parameters (canopy type, structure and density).

Generally, the capability of microwaves to penetrate into vegetation canopy increases with the system's wavelength. L-band SAR sensors have proven to be very effective to detect flooding in forests (e.g. Ormsby et al. 1985, Richards et al. 1987, Hess et al. 1990, Hess and Melack 1994, Hess et al. 1995, Townsend and Walsh 1998, Hess et al. 2003). In these wavelengths, the double-bounce trunk-ground signal interactions generate bright signatures in the data (Richards et al. 1987). In C-band and especially X-band, canopy attenuation, volume and surface scattering from the top layer of the forest canopy is usually higher (Richards et al. 1987). This is related to a decreased backscatter ratio between forests with dry and flooded conditions. Some studies state that also C-band SAR data can be used to map inundation beneath selected floodplain forest canopies (Townsend and Walsh 1998, Townsend 2001 and 2002, Lang et al. 2008). A decrease in leaf-area index (LAI) increases the transmissivity of the crown layer (Townsend 2001 and 2002) and therefore increases the amount of microwave energy reaching the ground (Lang et al. 2008). Therefore, higher classification accuracies can generally be derived during leaf-off conditions (Townsend 2001 and 2002).

Increasing backscatter using C-band SAR over floating aquatic macrophytes and emergent shrubs in floodplain lakes is reported by Alsdorf et al. (2000). Usually, high X-band double-bounce returns from flooded foliated forests only occur at the edges as the SAR signal is not able to the penetrate the vegetation canopy (Henderson 1995).

Double bouncing may also occur with decreasing wavelength at shorter or sparser vegetation with thin branches and small diameter trunks. Horritt et al. (2003) observed backscatter increases over marshlands in C-band rather than in L-band. The reason for this lies in the capability of the C-band

signal to penetrate the sparse canopy and to interact with the water surface and lower parts of the vegetation. This causes an enhanced signal return. Sparse vegetation may be very transparent for the SAR signal at L-band. In that case no interaction of the water body and the vegetation occurs. Results reported by Ormsby et al. (1985) and Ramsey (1995) indicate enhanced backscattering in marshland environments in C-Band and even in X-Band, respectively. During the no-foliage season Voormansik et al. (2014) used TerraSAR-X data to successfully map flooding in deciduous and coniferous forests of the temperate zone in Estonia. In this study an average backscatter increase of 3.2 dB could be stated over mixed forests. The difference in average backscatter during non-flood and flood situations offered values of Δ6.2 dB and Δ4.0 dB over deciduous and coniferous forests, respectively. Increased double bounce mechanisms could also be stated over water surfaces covered by olive groves and deciduous forests in Italy using Cosmo-SkyMed data (Pulvirenti et al. 2013) and covered by grassland and foliated shrubs in Caprivi/Namibia using TerraSAR-X data (Martinis and Twele 2010). Therefore, even in X-band there lies a certain potential to map flooding beneath vegetation.

Other properties that need to be considered for flood mapping beneath vegetation are incidence angle and polarisation. Several studies have shown that steep incidence angles are better suited for flood mapping in forests than shallow ones (e.g. Richards et al. 1987, Hess et al. 1990, Wang and Imhoff 1993, Wang et al. 1995, Bourgeau-Chavez et al. 2001, Lang et al 2008). This generalisation can be attributed to a shorter path length of the SAR signal through the canopy which increases the transmissivity in the crown layer. Thus more microwave energy is available for ground-trunk interactions. In contrast, shallower incidence angle signals interact more strongly with the canopy, resulting in increased volume scattering (Hess et al. 1990, Lang et al. 2008).

SAR systems with multiple polarisations provide more information on inundated vegetation areas than single-polarised SAR (Hess and Melack 2003, Horritt et al. 2003). Many studies employing multi-polarised data indicate advantages of like-polarisation (HH or VV) for separating flooded and non-flooded forests (e.g. Evans et al. 1986, Wu and Sader 1987). Backscattering is generally very low for cross-polarisation (HV or VH) as depolarisation does not occur for ideal corner reflectors (Leckie 1998). According to Wang et al. (1995) and Townsend (2002), the backscatter ratio between flooded and non-flooded forest is higher at HH polarisation than at VV polarisation.

The greatest challenge in classifying flooded vegetation areas is the definition of threshold values between the double bouncing vegetation and the diffuse backscattering non-water covered areas in the SAR data. Results in the literature are very heterogeneous and depend strongly on environmental and system parameters. Several approaches for the derivation of flooded vegetation exist: Townsend (2001) use a decision tree classifier for classifying forested wetlands in North Carolina based on RADARSAT C-band data in a supervised manner on a pixel basis. Hess and Melack (2003) use the same classifier for detecting flooded woody and herbaceous vegetation in North Australia using SIR-C data. In Martinis and Twele (2010), an automatic tile-based thresholding procedure is used to derive the threshold values separating open water surfaces, flooded vegetation areas covered by shrubs and grassland and non-water areas in TerraSAR-X data in Namibia/Caprivi. The derived

threshold values are used for the initialisation of a hybrid multi-contextual Markov model, which incorporates scale-dependent, as well as spatio-temporal contextual information into the object-based classification scheme. This is performed by combining hierarchical marginal posterior mode (HMPM) estimation on directed graphs with noncausal Markov image modeling related to planar Markov random fields (MRFs). In the same region of Namibia, Martinis et al. (2015) use a semi-automatic object-based approach combining supervised thresholding with region growing procedures to extract flooded vegetation areas in multi-temporal TerraSAR-X data.

An object-based fuzzy logic approach for detecting flooded olive groves and deciduous forests is presented by Pulvirenti et al. (2013) integrating theoretical electromagnetic scattering models, simplified hydrologic assumptions and context information. This method has been tested in Tuscany, Italy, based on COSMO-SkyMed data.

References

1. Alsdorf, D.E., Melack, J.M., Dunne, T., Mertes, L.A.K., Hess, L.L. and Smith, L. C., 2000: Interferometric radar measurements of water level changes on the Amazon flood plain. Nature, 404, 174-177.
2. Bourgeau-Chavez, L. L., Kasischke, E. S., Brunzell, S. M., Mudd, J. P., Smith, K. B., and Frick, A. L., 2001: Analysis of space-borne SAR data for wetland mapping in Virginia riparian ecosystems. International Journal of Remote Sensing, 22, 3665-3687.
3. Evans, D. C, T. Farr, G., Forf, J.P., Thompson, T.W., Werner, C.L., 1986: Multipolarisation radar images for geologic mapping and vegetation discrimination. IEEE Transactions on Geoscience and Remote Sensing, 24, 246-257.
4. Henderson, F. M., 1995: Environmental factors and the detection of open surface water using X-band radar imagery. International Journal of Remote Sensing, 16, 2423-2437.
5. Hess, L.L., Melack, J.M., Simonett, D.S., 1990: Radar detection of flooding beneath the forest canopy: a review. International Journal of Remote Sensing, 11, 1313-1325.
6. Hess, L.L., Melack, J.M., 1994: Mapping wetland hydrology and vegetation with synthetic aperture radar. International Journal of Ecology and Environmental Sciences, 20, 197-205.
7. Hess, L.L., J.M. Melack, E.M. Novo, C.C. Barbosa, and M. Gastil., 2003: Dual season mapping of wetland inundation and vegetation for the central Amazon basin. Remote Sensing of Environment, 87, 404-428.
8. Hess, L.L., Melack, J.M., 2003: Remote sensing of vegetation and flooding on Magela Creek floodplain (Northern Territory, Australia) with the SIR-C synthetic aperture radar. Hydrobiologia, 50, 65-82.
9. Hess, L.L., Melack, J.M., Filoso, S., Wang, Y., 1995: Delineation of inundated area and vegetation along the Amazon floodplain with the SIR-C synthetic aperture radar. IEEE Transactions on Geoscience and Remote Sensing, 33, 896-904.
10. Hong, S.-H., Wdowinski, S., Kim, S.-W., 2010: Evaluation of TerraSAR-X observations for wetland InSAR application. IEEE Transactions on Geoscience and Remote Sensing, 48, 864-873.
11. Horritt, M., 1999: A statistical active contour model for SAR image segmentation. Image Vision Computing, 213-224.
12. Lang, M.W., Townsend, P.A., Kasischke, E.S., 2008: Influence of incidence angle on detecting flooded forests using C-HH synthetic aperture radar data. Remote Sensing of Environment, 112, 3898-3907.

13. Leckie, D.G., 1998: Forestry applications using imaging radar. In Henderson, F.M., Lewis, A.J. (eds.): Manual of remote sensing: Principles and applications of imaging radar. Third edition, John Wiley and Sons, New York, USA.
14. Martinis, S., Twele, A., 2010: A hierarchical spatio-temporal Markov model for improved flood mapping using multi-temporal X-band SAR data. Remote Sensing, 2, 2240-2258.
15. Martinis, S., Kuenzer, C., Twele, A., 2015: Flood studies using Synthetic Aperture Radar data. Remote Sensing of Water Resources, Disasters and Urban Studies, Taylor & Francis, submitted.
16. Ormsby, J.P., Blanchard, B.J., Blanchard, A.J., 1985: Detection of lowland flooding using active microwave systems. Photogrammetric Engineering and Remote Sensing, 51, 317-328.
17. Ramsey, E. W., 1995: Monitoring flooding in coastal wetlands by using radar imagery and ground-based measurements. International Journal of Remote Sensing, 16, 2495-2502.
18. Richards, J. A., Woodgate, P.W., Skidmore., A.K., 1987: An explanation of enhanced radar backscattering from flooded forests. International Journal of Remote Sensing, 8, 1093-1100.
19. Townsend, P.A., Walsh, S.J., 1998: Modeling floodplain inundation using an integrated GIS with radar and optical remote sensing. Geomorphology, 21, 295-312.
20. Townsend, P.A., 2001: Mapping seasonal flooding in forested wetlands using multi-temporal RADARSAT SAR. Photogrammetric Engineering and Remote Sensing, 67, 857-864.
21. Townsend, P.A., 2002: Relationships between forest structure and the detection of flood inundation in forest wetlands using C-band SAR. International Journal of Remote Sensing, 23, 332-460.
22. Voormansik, K., Praks, J., Antropov, O., Jagomägi, J., Zalite, K., 2014: Flood mapping with TerraSAR-X in forested regions in Estonia. IEEE International Journal of Selected Topics in Applied Earth Observations, 7, 562-577.
23. Wang, Y., Hess, L.L., Filoso, S., Melack, J.M., 1995: Understanding the radar backscattering from flooded and non-flooded Amazonian forests: Results from canopy backscatter modeling. Remote Sensing of Environment, 54, 324-332.
24. Wang, Y., Imhoff, M.L. 1993: Simulated and observed L-HH radar backscatter from tropical mangrove forests. International Journal of Remote Sensing, 14, 2819-2828.
25. Wu, S.T., Sader, S.A., 1987: Multipolarisation SAR data for surface feature delineation and forest vegetation characterization. IEEE Transactions on Geoscience and Remote Sensing, 25, 67-76.

2.3.2 Time series analysis of multi-frequency SAR amplitude data in Saxony-Anhalt, Germany

Introduction

This chapter describes an analysis of multi-temporal and multi-frequency SAR data to investigate the backscatter behavior of various semantic classes in the context of flood mapping in central Europe. The focus is mainly on partially submerged vegetation such as forests and agricultural fields at different densities and plant phenological stages. The test area is located at River Saale, Saxony-Anhalt, Germany, which is covered by a time series of 39 TerraSAR-X scenes acquired within the time interval of December 2009 to June 2013. The data set is supplemented by ALOS PALSAR L-band and RADARSAT-2 C-band data. The time series covers two inundations in January 2011 and June 2013 which allows evaluating backscatter variations between flood periods and normal water level conditions using different radar wavelengths. The objective of this backscatter analysis is to provide essential preliminary work for improving existing flood mapping algorithms, especially by considering partially submerged vegetation at different plant phenological stages.

Study area

The study was conducted along the River Saale located in Saxony-Anhalt, Germany, which was recently affected by floods in January 2011 and June 2013.

The flood in January 2011 was caused by a particular sequence of events. Persistently heavy rainfall from August to December 2010 in central Germany led to a sharp rise in groundwater levels in the Saale catchment area. Unusually heavy snowfall in mid-December 2010, followed by several short melting periods and repeated rainfall events led to a strong rise of river levels and the subsequent flooding (LHW, 2011). Intensive large-scale and continuous rainfall in central Germany and the Czech Republic through May 2013 were responsible for flood occurrences in early June 2013. Despite the high seasonal water demand of developing vegetation, the soils were quickly saturated, which led to increased direct runoff (LHW, 2013).

Because of their high agricultural potential, soils in the study area are mainly used as arable land. Grassland areas are sporadically employed as pasturage and orchards. Furthermore, small areas of forestry can be found. The vegetation period (growing season) occurs between May and July. The tree vegetation in the regularly inundated areas of the flood plain is mainly composed of deciduous species typical of riparian woodlands, including English oak, field- and fluttering elm, and common ash (LAU, 2011).

Data set

The multi-temporal backscatter analysis is accomplished by using multi-frequency SAR data (see tab. 2.3.1): The largest time-series is based on 39 TerraSAR-X HH-polarised data (λ: 3.1cm) covering the time interval December 2009 to June 2013. All data sets are acquired in ascending orbit direction within the same incidence angle range (~31.7°–34.6°). The first 37 data takes are acquired in Stripmap mode (SM) (2009-12-17 to 2011-05-29) with a pixel spacing of 3.0m. This X-

band time series is supplemented by two TerraSAR-X ScanSAR (SC) data (pixel spacing: 8.25m) acquired in June 2013. As this time series covers two flood situations in January 2011 and June 2013 the data sets are predestined to analyse various semantic classes in dependence of seasonal effects – especially flooded vegetation areas during leaf-on and leaf-off conditions.
The X-band backscatter effects are compared to single temporal C-band (λ: 5.6cm) RADARSAT-2 Fine Beam (F, pixel spacing: 6.25m) and multi-temporal L-band (λ: 23.5cm) ALOS PALSAR data acquired in Fine Beam Single (FBS, pixel spacing: 6.25m) and Fine Beam Dual (FBD, pixel spacing: 12.5m) mode. Data of both sensor types cover the flood event in January 2011 during the leaf-off phase, but not the inundation event in June 2013.
Water level data of the gauging station Rischmuehle/Saale for the time interval 2009-07-01 to 2013-07-31 are used as validation purposes.
The SAR data sets were converted to sigma nought (σ_0) values (dB) to ensure that images obtained from different sensors and acquisition modes were statistically comparable. The calibrated values represent the normalised radar cross section and describe radar reflectance properties per pixel. The data calibration compensates for the radiometric influences of different incidence angles.

Table 2.3.1: SAR data analysed in this case study. Data sets acquired during flood events are marked in bold.

Sensor type	Mode	Polarisation	Acquisition date
TerraSAR-X	SM	HH	2009-12-17, 2009-12-28, 2010-01-08, 2010-01-19, 2010-01-30, 2010-02-10, 2010-03-15, 2010-03-26, 2010-04-06, 2010-05-20, 2010-06-11, 2010-06-22, 2010-07-03, 2010-07-14, 2010-07-25, 2010-08-05, 2010-08-16, 2010-08-27, 2010-09-07, 2010-09-18, 2010-09-29, 2010-10-10, 2010-11-01, 2010-11-12, 2010-12-15, 2010-12-26, **2011-01-17**, 2011-02-08, 2011-02-19, 2011-03-02, 2011-03-24, 2011-04-04, 2011-04-15, 2011-04-26, 2011-05-07, 2011-05-18, 2011-05-29
TerraSAR-X	SC	HH	**2013-06-04**, **2013-06-09**
ALOS PALSAR	FBS	HH	2010-03-22, 2010-12-23, **2011-01-21**
ALOS PALSAR	FBD	HH/VV	2009-12-03, 2010-05-07, 2010-06-05, 2010-07-21
RADARSAT-2	Fine	HH	**2011-01-16**

Statistical analysis of test areas

The statistical analysis of the time series data was performed for four vegetation classes, each consisting of several manually digitised test areas:

- Class 1: Deciduous dense occasionally flood affected forest (tree height: 20-25m)
- Class 2: Sparse deciduous forest consisting of 5 to 8m high orchard trees in 7-12m trunk distance with varying canopy sizes. Gaps of approx. 20-50m exist in between the tree communities
- Class 3: Non-flooded cropland
- Class 4: Flooded cornfield (maize)

For each test class several statistical parameters of σ_0 were calculated. Based on the test area polygons the mean, median, minimum, maximum value and standard deviation were derived.

Results

This section highlights significant trends and extreme values in the time course of the radar backscatter. Possible influences on the scattering processes of the X-, C- and L-band sensors by system and environmental parameters are considered. Furthermore, the ability of TerraSAR-X to detect flooding under vegetation will be compared with C- and L-band sensors. Figures 2.3.1 to 2.3.4 show mean and standard deviation of σ_0 (dB) for all test classes over the time course of the study period.

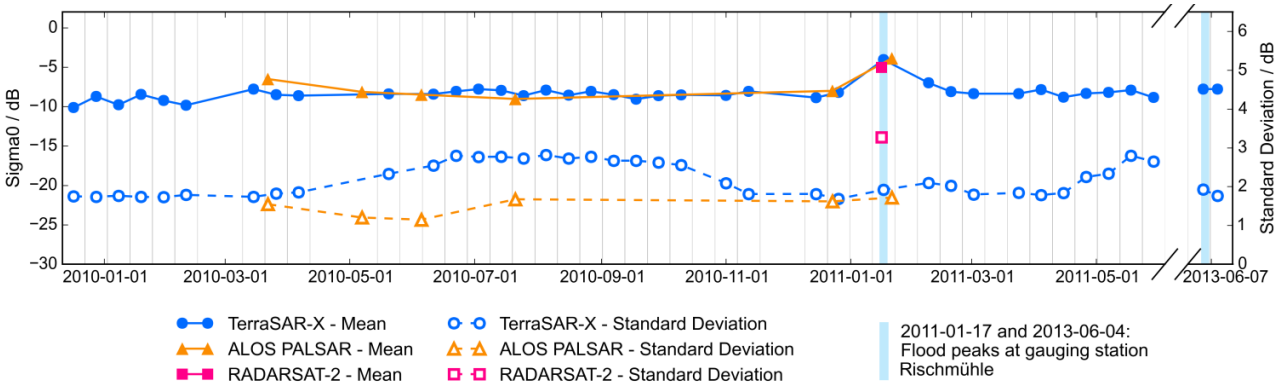

Figure 2.3.1: Time course of σ_0 (dB): Mean and standard deviation for test class 1 (Deciduous forest, dense, flooded).

Outside the flood periods, the backscatter characteristics of dense, deciduous forest (class 1) show a high degree of conformity in X-, C-, and L-Band (see fig. 2.3.1). The start of the vegetation period coincides with a rise of standard deviation in X-band. The developing canopy increases the amount of diffuse volume scattering. In contrast the standard deviation of PALSAR data is characterised by a much lower variability over the time series due to the reduced sensibility of L-band to surface scattering from the vegetation canopy.

During the flood event in January 2011, class 1 shows similar mean backscatter in X- (-4.06 dB), C- (-5.02 dB), and L-band (-3.87 dB) data. These values differ clearly from the homogenous backscatter profiles and their time course mean in X- (-8.48 dB) and L-Band (-8.10 dB) of class 1 during non-flood conditions (excluding January 2011). This corresponds to an increase in X-Band of Δ4.42 dB and in L-band of Δ4.11 dB caused by strong double bounce scattering under flood conditions. This confirms the findings of previous studies that flooded vegetation can - at least under leaf-off conditions of deciduous vegetation - be reliably detected with X-band sensors (e.g. Martinis and Twele 2010, Pulvirenti et al. 2013, Voormansik et al. 2014).

In contrast to the above described good separability in January 2011, the TerraSAR-X SC data of 4 June 2013 only shows a relatively small shift for class 2 of mean σ_0 to -7.78 dB. In direct

comparison to the time series mean of the TerraSAR-X SM data under non-flood conditions (-8.48 dB) the backscatter increases by only 0.7 dB. The limited ability of X-Band to penetrate the dense summer foliage leads to dominating diffuse volume scattering. Without a strong backscatter increase due to additional double-bounce interaction with the water surface, the separation of partially flooded and non-flooded areas of vegetation cover is nearly not possible.

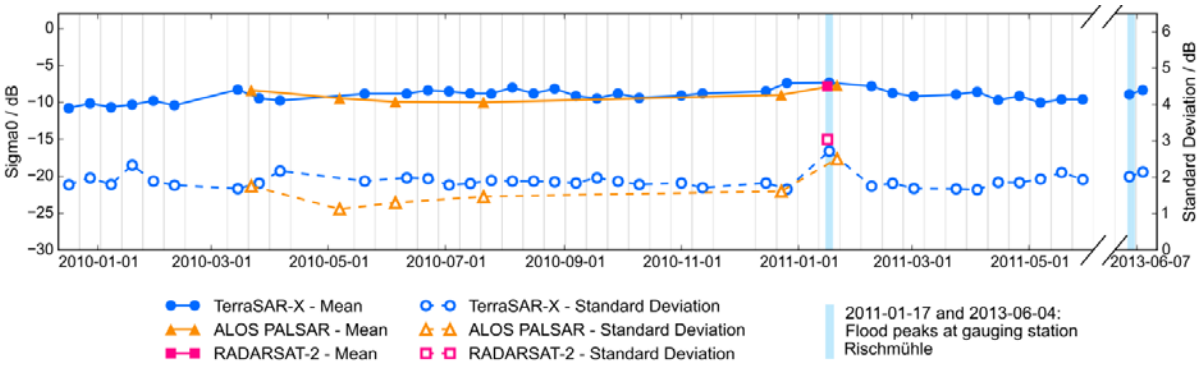

Figure 2.3.2: Time course of σ_0 (dB): Mean and standard deviation for test class 2 (Deciduous forest, sparse, flooded).

Despite different tree density and species composition, class 2 is showing very similar time series characteristics as class 1. During the flooding in January 2011 the absolute mean backscatter values are comparable among each other in X- (-7.33 dB), C- (-7.8 dB), and L-band (-7.69 dB) data. The increase in radar backscatter in comparison to the respective time course mean under non-flooded conditions (excluding January 2011) is not very distinct in X- (Δ1.81 dB) and L-band (Δ1.61 dB). The backscatter mean only slightly increases as class 2 consists of single trees partially interrupted from wide gaps of approx. 20 to 20 m. Bright backscattering due to double bouncing on the flooded vegetation is therefore nearly compensated by SAR shadowing effects as well as specular reflection on open water surfaces. However, these phenomena lead to a noticeable increase of the standard deviation of the backscatter within the test areas in X- and L-band data which can be used as an indicator for detecting partially submerged vegetation.

Both the mean backscatter and the standard deviation of non-flooded cropland (class 3) are very heterogeneous over the time series (fig. 2.3.3). This is related to several factors such as differences in soil moisture, plant phenological stages, and furrow orientation as well as variations of the crop type over time. The values of mean σ_0 are much higher and the backscatter variations are much more pronounced in X- (-17.19 to -6.08 dB) than in L-band (-16.49 to -13.63 dB). Cropland is one of the most difficult classes for detecting standing water beneath the vegetation as backscatter changes are often erroneously connected with strong backscatter effects of other classes. The high variability of this class requires very distinct backscatter changes over time and absolute backscatter values of > -5 dB in X- and > -10 dB in L-band.

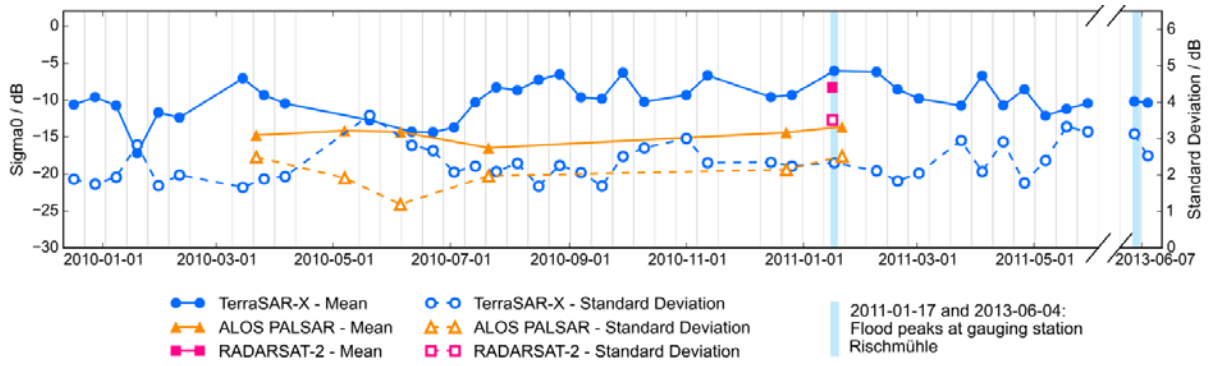

Figure 2.3.3: Time course of σ_0 (dB): Mean and standard deviation for test class 3 (cropland, non-flooded).

Fig. 2.3.4 shows the statistical characteristics of a maize field (class 4). The temporal backscattering over maize is highly variable in X-band data. This cannot be explained by the evolution of the crop biophysical parameters. Due to the structure of its canopy, maize is one of the most transparent crops to the SAR signal even at fully developed stages (O'Grady et al. 2014) and therefore, the SAR backscatter is strongly influenced by soil moisture properties (Engman et al. 2001). The test area is partially flooded in January 2011 and therefore gives a very bright backscatter signal in both X- and C-band of 1.17 dB and 0.92 dB, respectively. This corresponds to an X-band backscatter increase of 9.86 dB in comparison to the TerraSAR-X SM time course mean under non-flooded conditions (-8.69 dB). The backscatter in L-band also shows the influence of double bounce effects with an absolute backscatter change of Δ8.58 dB. However, compared to X-band the absolute signal return in L-band for January 2011 is much lower (-4.70 dB). The standard deviation is nearly constant over time in both TerraSAR-X SM (ca. 1.44 dB) and ALOS PALSAR data (ca. 1.17 dB). During the flooding in January this parameter increases to 2.02 dB in X-band, whereas there is no significant increase of the standard deviation in L-band.

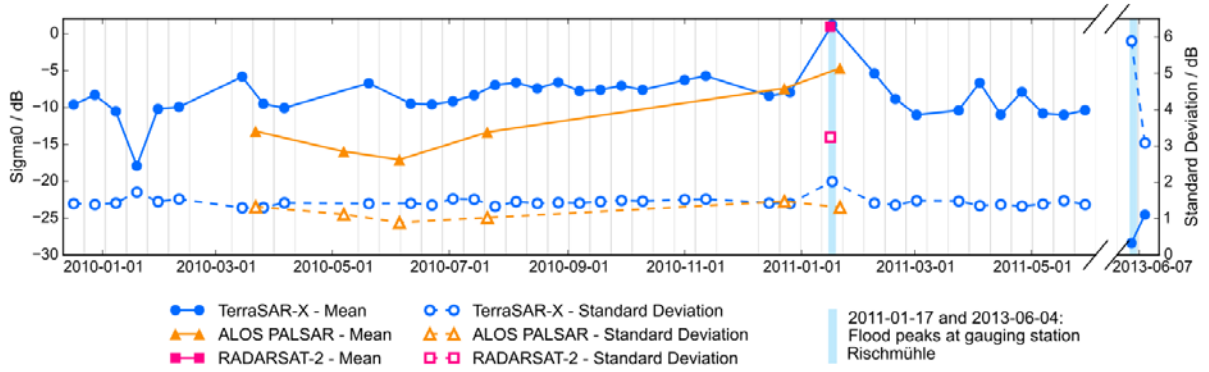

Figure 2.3.4: Time course of σ_0 (dB): Mean and standard deviation for test class 4 (flooded cornfield).

Due to the higher water level during the flooding in June 2013, this cornfield is completely inundated and is characterised by specular reflection. Therefore, the absolute backscatter is < -25 dB in both TerraSAR-X ScanSAR scenes.

Conclusion

According to the findings there is a great potential in detecting flooding beneath vegetation in all microwave wavelengths, even in X-band for sparse vegetation or leaf-off forests. However, the use of fixed empirical threshold values for automating the detection of partially submerged vegetation of various types is nearly impossible due to the dependency of the SAR signal return over partially flooded vegetation on various system and environmental parameters. Most straightforward seem to be approaches which consider various parameters. e.g., fuzzy logic-based algorithms could be used for combining different absolute backscatter thresholds for various semantic classes (e.g., forest during leaf-off and leaf-on phase, grassland, and cropland) and change detection information based on backscatter differences between single pre-flood or time series data and the crisis image. Further, SAR data of various wavelengths, incidence angles, and polarisations could be integrated to account for different backscatter mechanisms. Most critical is the selection of pre-flood data, especially for classes of high backscatter variability such as cropland. This requires the comparison of the data to mean backscatter values of corresponding time series data sets and the limitation of false-alarms by restricting the potential of flood occurrence by e.g. topographic information sources.

2.3.3 Time series analysis of SAR amplitude and bistatic coherence at Wabash River, USA

Introduction

The objective of this study is the analysis of multi-temporal SAR data to investigate the potential of using bistatic coherence as additional information source for the extraction of open water areas and flooded vegetation. The time series analysis is carried out at River Wabash, USA, based on 27 co-registered single look slant-range complex (CoSSC) data of the German single-pass across-track SAR interferometry mission TanDEM-X acquired between 2011 and 2014.

Study area

The study area is located at lower Wabash River, serving as the state boundary between Indiana and Illinois, USA. It is close to the outfall into Ohio River. The lowlands along the river are characterised by farmland and deciduous forests (tulip trees, maple, cottonwood, and shrubs). Wet prairie, swamps, sloughs, oxbows and marshes with reed are encompassed in the bottomland. While the Wabash River mostly remained its natural flow patterns, the changing land use of the surrounding area generally causes increased runoff rates.

Data set

The time-series for this study area consists of 27 HH-polarised CoSSC data (SM, pixel spacing 3m) of the TanDEM-X mission acquired between November 2011 and August 2014 (see tab. 2.3.2). Flooding occurs in the data of 2011-11-30, 2012-12-11, 2012-01-02, 2012-01-24, and 2012-03-08. All CoSSC data sets are pre-processed using the SARscape software.

Table 2.3.2: SAR data analysed in this case study. Data sets acquired during flood events are marked in bold.

Mission	Mode	Polarisation	Acquisition date
TanDEM-X	SM	HH	2011-11-08, **2011-11-30**, **2011-12-11**, 2011-12-22, **2012-01-02**, **2012-01-24**, 2012-02-15, **2012-03-08**, 201-20-330, 2012-05-13, 2012-06-04, 2012-06-26, 2012-07-18, 2012-10-14, 2012-11-05, 2012-12-19, 2013-01-10, 2013-02-01, 2013-02-23, 2013-03-17, 2013-03-28, 2013-04-19, 2013-06-02, 2013-07-16, 2014-06-22, 2014-08-05, 2014-08-27

Statistical analysis of test areas

The statistical analysis of the time series data was performed for the following three classes:

- Class 1: Permanent water bodies
- Class 2: Occasionally flood affected deciduous reeds and bushes
- Class 4: Perennial flood non-flood affected reeds and bushes

For each class one homogeneous polygon has been manually digitised. The study area and the selected polygons for each semantic class are visualised in figure 2.3.5.

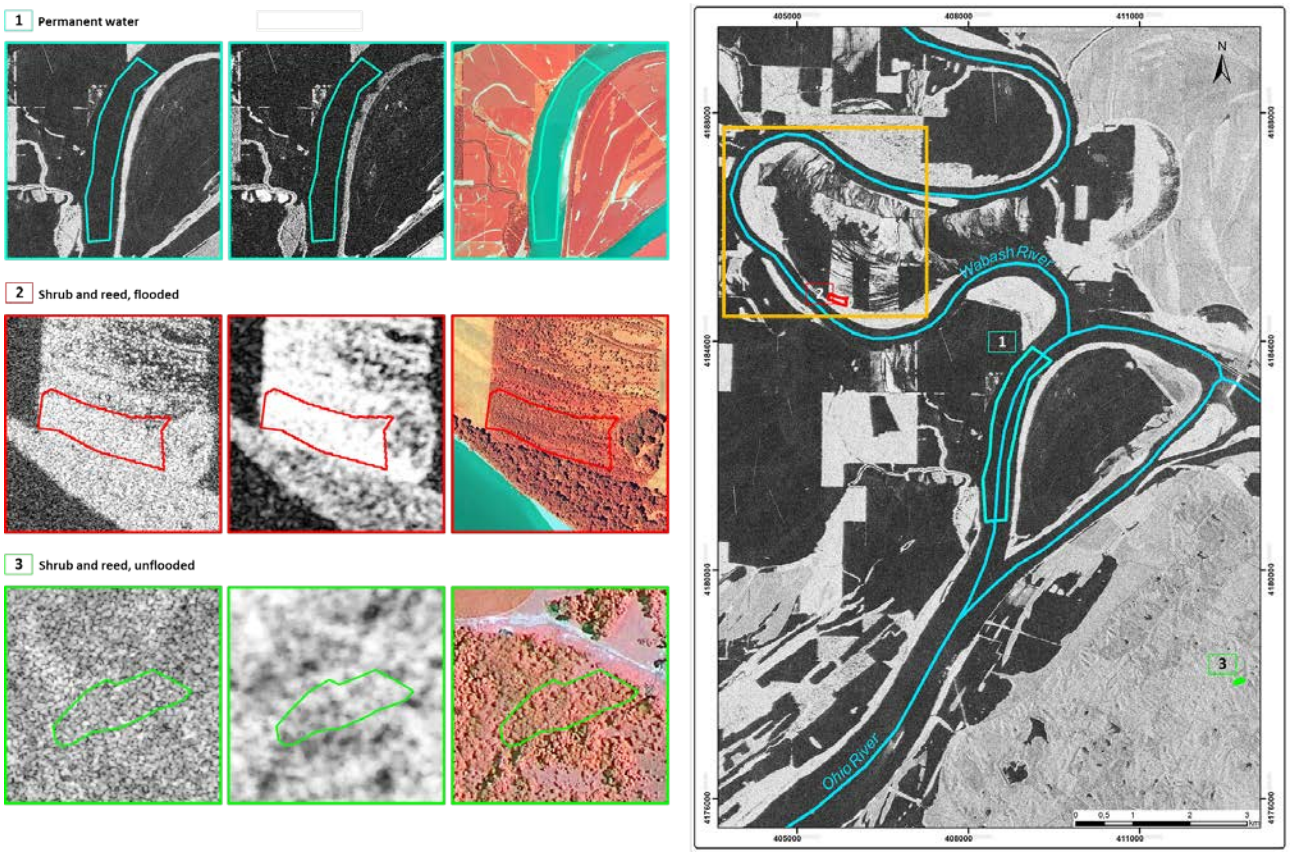

Figure 2.3.5: Study area at River Wabash and visualisation of test classes in data of the TanDEM-X mission (2011-12-11, © DLR 2014); left column: SAR amplitude; mid column: bistatic coherence; right column: aerial photographs (2011-08-12, 2010-06-23, © USDA-FSA-APFO) (Source: Martinis et al. 2015).

The polygons are used for the calculation of the amplitude and bistatic coherence over the whole time series (fig. 2.3.6).

Analysis

Permanent water (class 1, fig. 2.3.6a) is showing strong fluctuations of σ_0 in X-band through the entire time course (Δ6.3 dB). This fluctuation can be related to different surface roughness conditions due to wind effects. Over open water areas the bistatic coherence shows very low fluctuations over time (Δ0.04) due to a low sensitivity of this parameter to different roughness conditions of water. Therefore, this parameter can be well used in synergy with backscatter information for the optimised detection of open flood surfaces.

Occasionally flood affected deciduous reeds and bushes (class 2, fig. 2.3.6b) show a significant increase in σ_0 during flood events (mean σ_0 of -4.62 dB in comparison to the non-flooded time course mean of -10.14 dB). The magnitude of change during the flood events is significantly higher than during the non-flooded period. Alteration of coherence and σ_0 in the latter period may be caused by phenological phases. With rising water level the coherence increases over partially

flooded vegetation until the entire vegetation is covered by water. The mean coherence of partially submerged vegetation is 0.89 while the coherence time course mean during non-flooded conditions is only 0.56. Increasing bistatic coherence can be considered as an indicator for flood situations.
Perennial non-water covered areas of reeds and bushes (class 3, fig. 2.3.6c) show no significant variance of the coherence in the frequently flood affected period from 2011-11-30 to 2012-03-08. For the following non-flooded period, the coherence and backscatter of class 2 shows similar characteristics as class 3. This underlines the similarity of the samples of the two classes and confirms the impact of the inundation in the first period. By comparing the classes 2 and 3 in the non-flooded period, the backscatter has a smaller variance than the coherence.
The user's and producer's accuracies is 99.7% and 97.9% for open water and 66.3% and 85.6% for flooded vegetation within the Wabash River test site by combining amplitude information and bistatic coherence data.

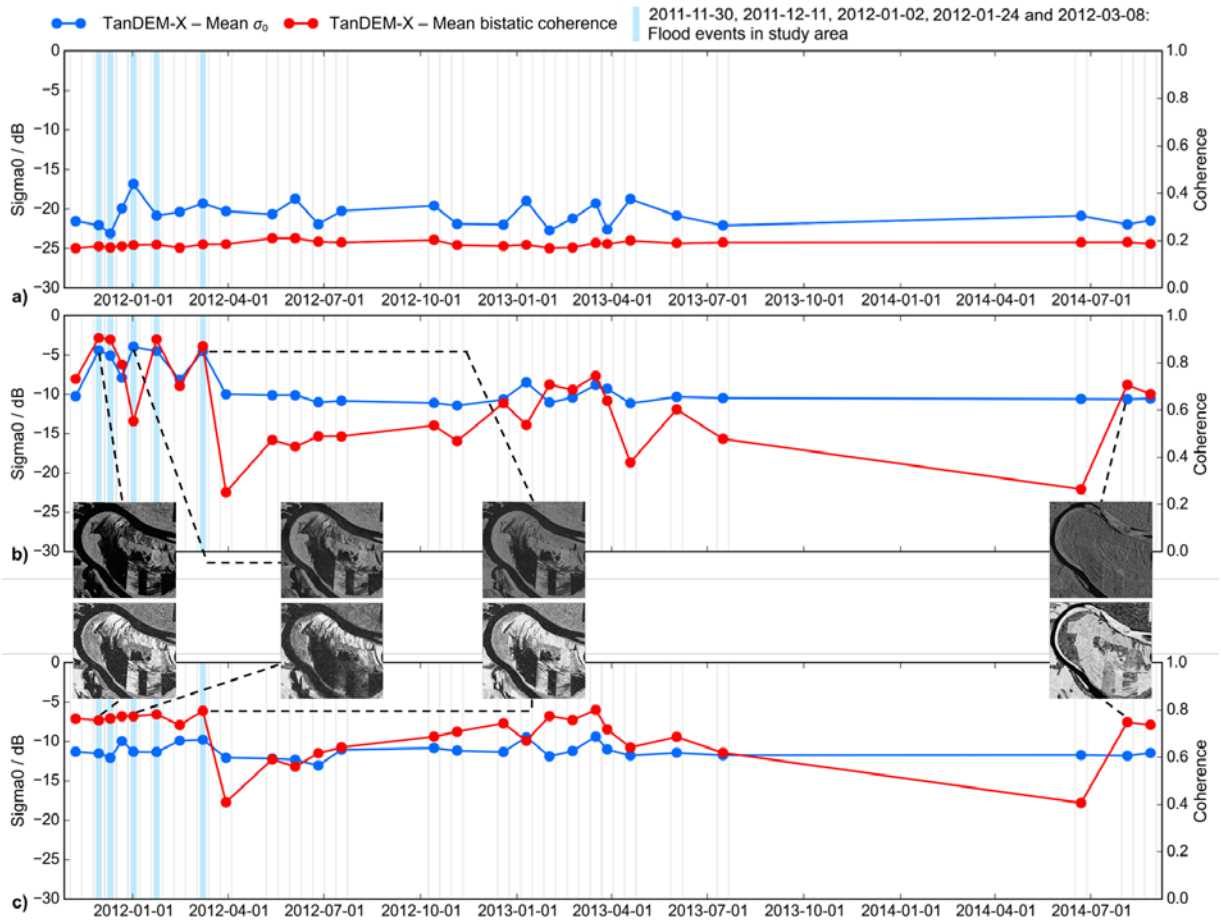

Figure 2.3.6: Time course and selected chips of σ_0 and bistatic coherence for for a) class 1: permanent water, b) class 2: reeds/bushes, flooded, and c) class 3: reeds/bushes, non-flooded (Source: Martinis et al. 2015).

Conclusion

Due to the relatively low sensibility of the bistatic coherence to water surface roughness and its high sensibility to partially submerged vegetation it can be synergistically used with amplitude data for an optimised detection of flood surfaces.

References

1. Engman, E.T. Applications of microwave remote sensing of soil moisture for water resources and agriculture. Remote Sensing of Environment, 35, 213-226.
2. LAU - State office Saxony-Anhalt for environment protection, 2011: Management plan fort the FFH-area „Saale-, Elster-, Luppe-Aue between Merseburg and Halle. URL *http://www.lau.sachsen-anhalt.de/fileadmin/Bibliothek/Politik_und_Verwaltung/MLU/LAU/Naturschutz/Natura2000/Managementplanung/Dateien/Saale-Elster-Luppe-Aue-zw-Mers-u-Hal_ges.pdf* (accessed on 19 March 2015).
3. LHW - State office for flood control and water management Saxony-Anhalt. January 2011 flood report, 2011: URL: *http://www.hochwasservorhersage.sachsen-anhalt.de/dokumente/hochwasserberichte/jan_2011/abschlussbericht_2011.pdf* (accessed on 19 March 2015).
4. LHW - State office for flood control and water management Saxony-Anhalt, 2013: June 2013 flood report in Saxony-Anhalt. Emergence, course, management and statistical placement 2013. URL: *http://www.lhw.sachsen-anhalt.de/fileadmin/Bibliothek/Politik_und_Verwaltung/Landesbetriebe/LHW/neu_PDF/4.0/SB_Hochwasserschutz/Hochwasserbericht_2013.pdf* (accessed on 19 March 2015).
5. Martinis, S., Rieke, C., Fissmer, B. 2015: Time series analysis of multi-frequency SAR backscatter and bistatic coherence in the context of flood mapping. Multitemp, Annecy, France, 22-24 July 2015.
6. O'Grady, D., Leblanc, M., Bass, A. 2014: The use of radar satellite data from multiple incidence angles improves surface water mapping. Remote Sensing of Environment, 140, 652-664.

2.3.4 Semi-automated mapping of flooded vegetation using polarimetric Sentinel-1 and ALOS-2 data

Aim of the study described in this section is the development of a semi-automated procedure for mapping of flooded vegetation based on polarimetric Sentinel-1 (S-1) and ALOS-2/PALSAR-2 SAR imagery. Besides the mapping of open water areas, special focus is on the detection of all flooded areas, including especially flooded vegetation. The latter is very difficult to map using single polarised SAR imagery, used by classical flood detection processors. Therefore, we developed an advanced procedure using dual-polarimetric SAR data (S-1), providing much more information about the backscattering properties of the area of interest and a better separation of different land cover types. Furthermore, a fusion of S-1 with dual-pol and quad-pol imagery of ALOS-2/PALSAR-2 enabling an improved mapping of flooded vegetation is presented.

Study site and data

The methodology has been developed and tested on a site at the River Evros, located at the border of Greece and Turkey. There, a long-lasting flood event, started in February 2015, caused widespread flooding of farmland. Subsets of nine Sentinel-1 C-band dual-pol (VV+VH) datasets acquired between February to April 2015 in the IW mode and two ALOS-2/PALSAR-2 L-band scenes, one acquired in dual-pol (HH+HV) and one in quad-pol were analysed. The developed methodology was validated by means of reference information generated by visual interpretation and digitalisation of two pan-sharpened WorldView-2 scenes of 0.5m spatial resolution. Table 2.3.3 provides further details on the used SAR and optical satellite imagery.

Table 2.3.3: SAR data analysed in this case study.

Acquisition date	Sensor*	Mode**	Wavelength	Polarisation	Relative orbit	Pass direction
16.02.2015	S-1	IW	C-band	VV+VH	29	Ascending
01.03.2015	S-1	IW	C-band	VV+VH	36	Descending
11.03.2015	W-2	FullSwath	Optical	-	-	-
12.03.2015	S-1	IW	C-band	VV+VH	29	Ascending
13.03.2015	S-1	IW	C-band	VV+VH	36	Descending
18.03.2015	S-1	IW	C-band	VV+VH	109	Descending
24.03.2015	S-1	IW	C-band	VV+VH	29	Ascending
05.04.2015	S-1	IW	C-band	VV+VH	29	Ascending
17.04.2015	A-2	HS	L-band	HH+HV	2790	Descending
18.04.2015	S-1	IW	C-band	VV+VH	36	Descending
20.04.2015	WV-2	FullSwath	Optical	-	-	-
24.04.2015	S-1	IW	C-band	VV+VH	131	Ascending
24.04.2015	A-2	HS	L-band	HH+HV+VH+VV	810	Ascending

*A-2: ALOS-2/PALSAR-2; S-1: Sentinel-1; WV-2: WorldView-2

**IW: Interferometric Wide swath (20m azimuth and 5m ground range spatial resolution); HS: High Sensitive (6m spatial resolution); WV-2: 0.5m spatial resolution (pan-sharpened).

Method

This section describes the methodology developed for semi-automated mapping of flooded vegetation based on polarimetric SAR imagery. Due to the systematic acquisition of most land areas on the globe, the high revisit time and free availability of Sentinel data, the focus of the developed methodology is the use of Sentinel-1 SAR imagery. Moreover, as for the AOI also ALOS-2 imagery, one dual-pol and one quad-pol imagery, acquired within a very short time difference to S-1 imagery (one day or even from the same date, respectively) was available, the methodology has also been adapted and enhanced to work with (a) only ALOS-2 dual-pol imagery, (b) only ALOS-2 quad-pol imagery, (c) fusion of S-1 and ALOS-2 dual-pol imagery and (d) fusion of S-1 and ALOS-2 quad-pol imagery. Eight different scenarios were developed, analysed and validated (see tab. 2 for details).

The procedure can be divided into four steps (fig. 2.3.7), starting with (I) pre-processing of the SAR imagery, followed by (II) decomposition of the polarimetric SAR data to derive information of the physical scattering mechanism of the ground targets. Next, (III) the decompositions are used as input of an unsupervised classification followed by (IV) a hereon based object-oriented image analysis for further refinement, including neighbouring relationships between open water and flooded vegetation and topographic information (the HAND-EM Layer) as well as masking out urban areas based on the Global Urban Footprint (GUF), as urban area shows similar backscattering characteristics as flooded vegetation.

Table 2.3.4: Developed and tested scenarios. The scenarios I) to IV) are based on only S-1 (H/α dual-pol Wishart), ALOS-2 (H/α dual-pol Wishart), ALOS-2 (H/A/α quad-pol Wishart), or ALOS-2 (Freeman Wishart), respectively. The scenarios V) to VIII) are based on the fusion of S-1 (H/α dual-pol Wishart) with ALOS-2 (H/α dual-pol Wishart), ALOS-2 (H/A/α quad-pol Wishart), ALOS-2 (Freeman Wishart), or ALOS-2 (Yamaguchi helix), respectively.

PolSAR data	S-1 H/α dual-pol Wishart	ALOS-2 H/α dual-pol Wishart	ALOS-2 H/A/α quad-pol Wishart	ALOS-2 Freeman Wishart	ALOS-2 Yamaguchi: Helix scattering*
S-1 H/α dual-pol Wishart	Scenario I)	Scenario V)	Scenario VI)	Scenario VII)	Scenario VIII)
ALOS-2 H/α dual-pol Wishart		Scenario II)			
ALOS-2 H/A/α quad-pol Wishart			Scenario III)		
ALOS-2 Freeman Wishart				Scenario IV)	

* Scenario VIII): The entire initial classification of all classes (open water, dry land and flooded vegetation) is based on only S-1 H/α dual-pol Wishart (i.e., equal to scenario I)). In scenario VIII) only the initial classified flooded vegetation objects are refined by helix scattering. A complete classification as done for the other scenarios would not be possible for only ALOS-2 Yamaguchi helix scattering. Therefore, a ninth scenario based on only ALOS-2 Yamaguchi helix scattering is not applied.

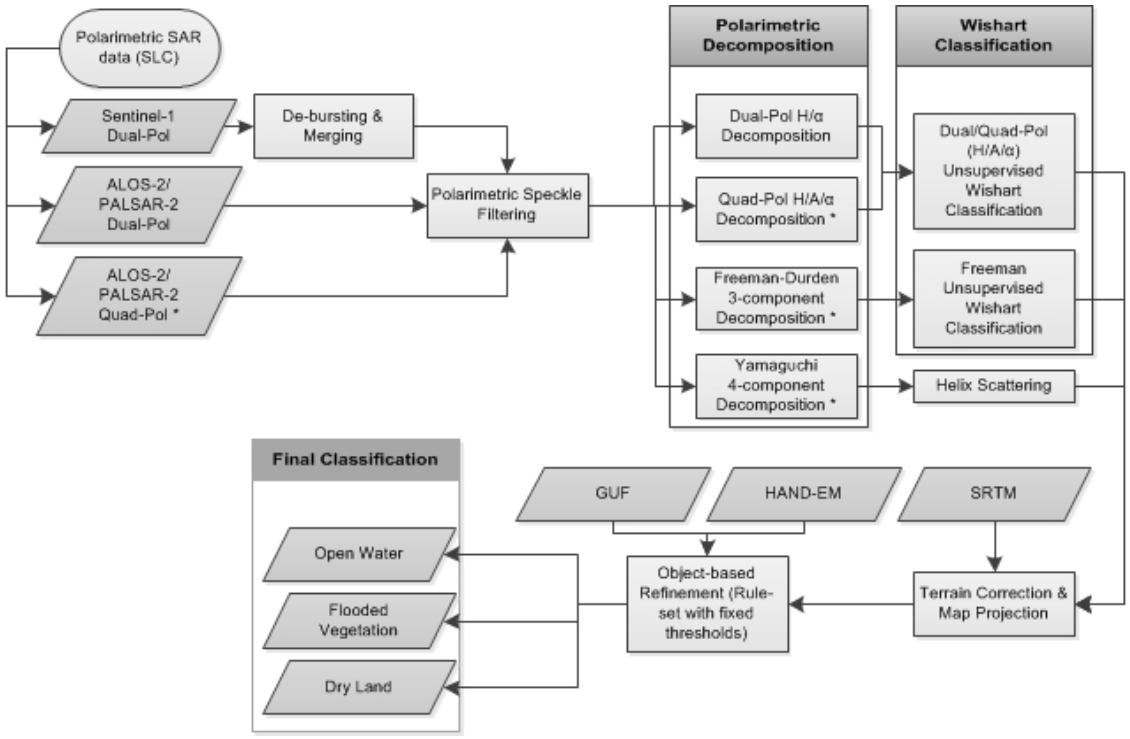

Figure 2.3.7: Flow chart of the semi-automatic procedure for mapping of flooded vegetation and open water areas.

Pre-processing: Sentinel-1-Debursting

The developed methodology is based on polarimetric SAR imagery. To preserve the phase information, which is required for polarimetric decomposition procedures, Single Look Complex (SLC) is the required input data for our procedure. The IW mode is the most common one of Sentinel-1 for monitoring of land areas. Sentinel-1 IW SLC images are acquired using the so-called Terrain Observation by Progressive Scan (TOPSAR) operation (De Zan et al. 2006). Thereby, each product consists of one image per swath per polarisation, i.e. dual-pol IW has 3 swaths with 2 polarisations each. Using the S-1 Toolbox module of ESA's SNAP software, the Sentinel-1 SLC images are debursted and merged to one SLC image per polarisation. This pre-processed imagery is then used as input for the following processing steps.

Polarimetric Speckle Filtering

Visual interpretation and classification of SAR images is strongly complicated by the speckle effect, which is caused by the interference of the coherent reflected SAR waves of many individual scatterers within a resolution cell (assuming a distributed target such as natural environment).

After pre-processing of the SLC SAR images speckle filtering is applied using the refined Lee filter (Lee 1981, Lee et al. 1994). This filter aims to preserve the structure of the image, i.e. the preservation of edges and on the same time the filtering of homogenous area. Moreover, the correlation between the different polarisations is conserved.

Polarimetric Decomposition

Polarimetric SAR data enable an improved classification of the land cover compared to imagery acquired by single polarised SAR sensors. Objects on the ground of different structural and geometric properties show different SAR backscatter at different polarisations. Based on physical assumptions, polarimetric decomposition procedures aim to separate these different backscatter types.

Three different polarimetric decompositions are applied to the SAR data available for this study: entropy/anisotropy/alpha (H/A/α) decomposition proposed by Cloude and Pottier (1997), the Freeman-Durden 3-component decomposition (Freeman and Durden 1998) and the further enhancement of it, the Yamaguchi 4-component decomposition (Yamaguchi et al. 2005).

For the dual-pol SAR imagery (S-1 and ALOS-2) the dual-pol version of the H/α decomposition was applied. The α angle describes the type of backscattering, ranging from very small α values (close to zero) which indicate domination of surface scattering (single bounce scattering), to high α values representing domination of double bounce scattering (e.g., indication of either urban area or tree trunks). α values in between the aforementioned extremes (i.e., ~45°) show domination of volume scattering, caused by multiple scattering inside a volume, e.g., such as the crown of a tree (dense vegetation). The entropy H represents the heterogeneity of the scattering and ranges from 0, which indicates a dominant scatterer such as a corner reflector, to 1, representing a random mixture of scattering mechanisms (e.g., forest areas). For quad-pol data, a third parameter, the anisotropy A enables further investigation of the relationship between the second and third backscattering mechanism in the resolution cell. Further decompositions applied to the quad-pol ALOS-2 imagery are the Freeman-Durden and the Yamaguchi decomposition.

The Freeman-Durden 3-component decomposition is a model-based methodology, which aims to separate the backscattering of the SAR wave into three components: Surface scattering, volume scattering and double bounce scattering. Yamaguchi et al. (2005) further enhanced the model of Freeman-Durden by adding a fourth component, the helix scattering. This scattering type appears in heterogeneous areas, especially in complicated shape areas or man-made structures and disappears for almost all natural distributed scattering areas (Lee and Pottier 2009). In the present case, helix scattering was very dominant in areas of flooded vegetation, which are characterized by complex scattering effects (mixture of double bouncing between the water surface and the tree trunks and multiple scattering inside the crown of the trees and bushes).

Unsupervised Wishart Classification

Next, based on the results of the decompositions explained above, an unsupervised Wishart classification is applied to derive the land cover of the AOI. The Wishart polarimetric classification procedure executes a Maximum Likelihood (ML) statistical segmentation of a polarimetric data set based on the multivariate complex Wishart probability density function. Three different types of Wishart classifications were applied: based on the results of the dual-pol H/α decomposition, quad-pol the H/A/α decomposition and the Freeman-Durden decomposition.

Training

The classification results obtained by the Wishart classification described in the previous section are the results of an unsupervised classification. Therefore, these results have to be manually interpreted and the Wishart classes have to be labelled to meaningful and useful classes. In order to do so, training areas have been generated by visual interpretation and manual digitalisation on an optical VHR WV-2 image acquired one day before the Sentinel-1 SAR image used for the Wishart classification (cf. tab. 2.3.3). Due to a time difference of ~31 hours between the Sentinel-1 and WV-2 data set, stable flood conditions have been ascertained using consecutive SAR and optical satellite acquisitions. No significant change in water level was observable. The training areas were generated for three classes with 50ha per class: (I) Open water, (II) dry land and (III) flooded vegetation.

Improvement by HAND-EM

To improve the accuracy of the proposed methodology for mapping of flooded vegetation, the HAND index is integrated (see section 2.2.3). Based on the HAND index, only areas situated <15m above the drainage network are considered as flood-prone areas. This was realised by calculating a binary exclusion mask (termed “HAND-EM” in the following) to separate flood-prone from non-flood prone areas. Thereby, false classification at elevated areas is prevented.

Improvement by GUF

As both flooded vegetation and urban areas are characterised by strong double bouncing and multiple scattering effects, making the separation of both classes very complicated, additional geospatial-information such as information about urban areas is used to improve the accuracy of the proposed methodology for mapping of flooded vegetation. The Global Urban Footprint (GUF) is derived from the local speckle statistics of TanDEM-X SAR imagery (Esch et al. 2012). The advantage of the GUF is its global availability and consistency. The currently available GUF has a spatial resolution of 75m. A higher spatial resolution (12m) version of the GUF is currently being processed by the German Aerospace Center (DLR).

Improvement by OBIA

After masking out areas where a flood event is highly uncertain (using the HAND-EM) and urban areas (based on the GUF), an object-oriented image analysis procedure is applied for further refinement, including for instance spatial contextual relationships between open water and flooded vegetation as well as a minimum area threshold for open water to be mapped. The developed OBIA ruleset uses fixed thresholds for minimum areas considered and distances between neighbouring classes. Therefore, the ruleset can be applied fully automatic.

Results and discussion

Analysis based on only Sentinel-1 dual-pol imagery

Figure 2.3.8 shows the accuracy values for the different steps of the methodology development. For all steps, the class open water shows with 99% user's accuracy (UA) the highest values. The producer's accuracy (PA) of the class open water is ca. 87.0% and confirms the high accuracy of the methodology for mapping of open water areas even at the first step of its development. The overall accuracy (OA) and the KHAT value range from 86.0% to 90.0% and 0.64 to 0.81, respectively. UA and PA for the class dry land range from 52.0% to 86.0% or 91.0% to 95.0%, respectively. For the class flooded vegetation, UA at the first step of the methodology was with 30.0% very low. First aim of improving our developed procedure was to increase UA of the class flooded vegetation, to guarantee that pixels, which are classified as flooded vegetation, are this land cover class in reality.

Next, the HAND-EM layer was implemented in the procedure. As with the HAND-EM possible false (over) classification of flooded vegetation on higher elevated dry land (mostly forested areas characterised by complex scattering properties) are excluded, the UA of the class flooded vegetation strongly increased to a value of 57.0%. The PA of the class flooded vegetation shows stable values compared to the results without HAND-EM.

In our analysed cases the GUF brought no increase of the accuracy, as the urban areas where either already masked out by HAND-EM due to their higher elevation or masked out by the object-based refinement. However, in general urban area information such as the GUF is useful to decrease false classification in urban area.

Finally, the object-based refinement, described above, is applied, increasing the value of UA for the class flooded vegetation up to 63.0%, while slightly decreasing PA of this class.

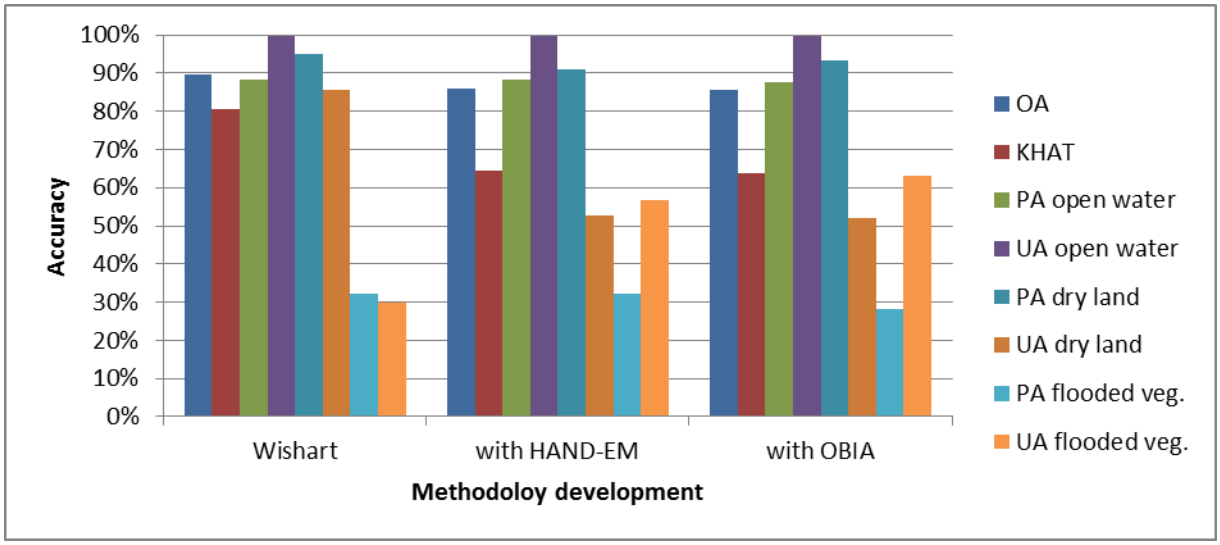

Figure 2.3.8: Accuracy values for the different steps of development. From left to right: Using only the results of the unsupervised Wishart classification ('Wishart'), refinement by HAND-EM and additional refinement of the classification using the OBIA ruleset ('OBIA').

Figure 2.3.9 shows the final result of the semi-automated mapping of open water and flooded vegetation based on polarimetric Sentinel-1 data. The comparison of the VHR optical WV-2 imagery, acquired on 11 March 2015, and the validated classification results based on Sentinel-1 data, acquired on 12 March 2015, confirm the high UA of the class open water. Areas classified as open water are by 99.0% open water in the reference dataset. The red colours show areas where open water is underestimated. These are mainly areas close to dry land and thin channels of water surrounded by dry land. Also in the upper right part of figure 2.3.9, thin lines of vegetation within open water areas can be perceived. However, these red coloured lines are much wider in the classification of the SAR image compared to the vegetation lines in the optical WV-2 scene. Due to geometric distortions such as foreshortening and layover resulting from the side-looking geometry of the sensor, the SAR-derived flood extent is commonly underestimated in these areas.

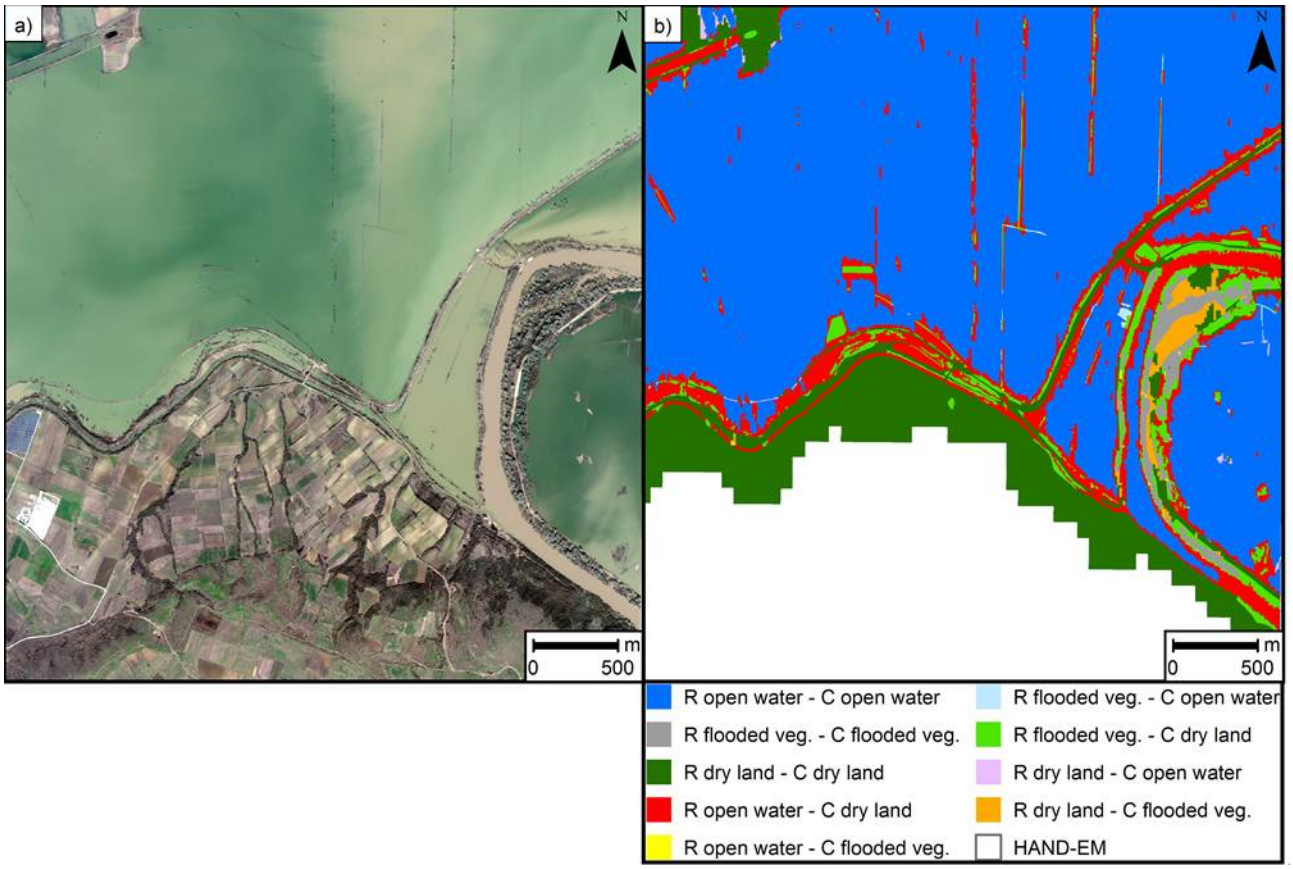

Figure 2.3.9: a) Optical VHR WV-2 acquisition (11 March 2015) used for generation of the validation mask. b) Result of the semi-automated mapping of flooded vegetation based on polarimetric Sentinel-1 data (12 March 2015). R = reference, C = classification result. For instance, dark blue, grey or dark green colors show correct classification of the classes open water, flooded vegetation or dry land, respectively. The other colors show the corresponding false classifications.

Bright green coloured areas showing an underestimation of flooded vegetation and an overestimation of dry land can be found especially around the peninsula in the east of the AOI. Due

to the relatively low penetration depth of C-band compared to longer wavelength such as L-band, the Sentinel-1 imagery is more influenced by the tree canopy in these denser forest areas. Areas of sparse flooded trees are very well detected by the classifier. Here, double bounce effects between open water and the tree trunks are more dominant compared to dry land forest areas. Orange coloured areas show an over-classification of flooded vegetation and a corresponding under-classification of dry land. This effect especially appears inside the peninsula. However, even with very high resolution optical imagery it is sometimes very difficult to distinguish between flooded and dry forest. We set flooded forest in the reference at areas where we could visually see water between the trees. At very dense forest this is sometimes not possible. Therefore, some of the orange coloured areas might even be correct classified.

Fusion of ALOS-2/PALSAR-2 with Sentinel-1 imagery

For two additional AOIs, called AOI 4 and 5, a further accuracy assessment was applied based on reference data derived from a second optical data set (tab. 2.3.3.). One S-1 image, acquired on 18 April 2015, and one ALOS-2 dual-pol scene, acquired on 17 April 2015, covering the same area, were available. As the optical VHR imagery was acquired on 20 April 2015, and a decline of the water level was observed when the SAR intensity imagery and the optical data were compared, a synthetic reference layer was created. This layer was derived by visual interpretation and manual digitalization based on the optical data and then further refined using the SAR intensity information. This procedure enabled the creation of the best possible realistic reference layer. For both aforementioned AOIs, three accuracy assessments have been performed, analysing three scenarios: I), II) and the fusion scenario V) (cf. tab. 2.3.3 and 2.3.4). Regarding the open water class, scenario I) (only S-1) provides higher values for UA (93%), compared to scenario II) (only ALOS-2 dual) with UA open water (68-86%) (fig. 2.3.10). Scenario I) is better suited for mapping open water areas. Contrary to this, higher values for UA and PA of the flooded vegetation class are obtained in scenario II), based on only ALOS-2 dual-pol data (e.g. UA of flooded vegetation of AOI 4 is ca. 32% higher in scenario II) compared to scenario I)). In order to combine the advantages of both sensors, C-band S-1 and L-band ALOS-2, we developed an object-based refinement based on the H/α Wishart classification derived from both SAR scenes. This fusion scenario V) achieves the best results: High accuracy values for the open water class combined with high accuracy values for the flooded vegetation class, as well as for dry land. The latter has very similar UA and PA values as scenario I) (only S-1), since S-1 data is used to differentiate between open water and dry land and ALOS-2 data is used to map flooded vegetation.

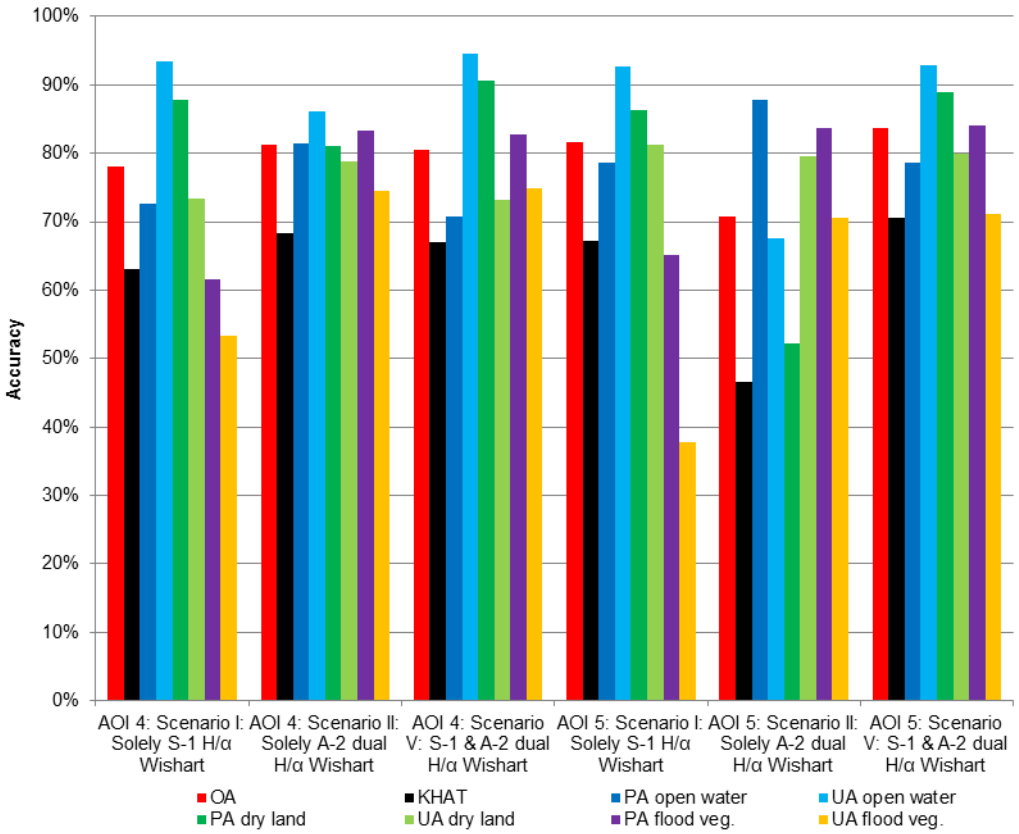

Figure 2.3.10: Accuracy assessment results for the scenarios I) only S-1 dual-pol, II) only ALOS-2 dual-pol and V) fusion of S-1 and ALOS-2 dual-pol. For all aforementioned scenarios the dual-pol H/α Wishart classification was applied. Overall accuracy (OA), user's accuracy (UA), producer's accuracy (PA).

For the two AOIs 4 and 5 also an image pair of an S-1 dual-pol and an ALOS-2 quad-pol scene acquired on the same date (24 April 2015) where available. For the generation of the reference layer the optical VHR imagery acquired on 20 April 2015 was used. To compensate for changes in the water level between the time of acquisition dates, again the SAR intensity information is used to refine and optimize the reference layer to achieve the most realistic one.

For each of the two AOIs six scenarios where computed and validated: I), III), and IV), based on single datasets, and VI), VII), VIII), based on fusion of S-1 and different decomposition / classification results derived from ALOS-2 quad-pol imagery (cf. tab. 2.3.4). The figures 2.3.11 and 2.3.12 show the accuracy values for these six different scenarios at the two AOIs 4 and 5, respectively. In accordance with the descriptions above, scenario I) (only S-1) provides the highest accuracy values for open water when compared to the other scenarios based on only ALOS-2 Freeman or ALOS-2 H/A/α Wishart. Contrary to this, only S-1 also provides the lowest accuracy values for the class flooded vegetation. Scenario VIII) refines the flooded vegetation classification of scenario I) (only S-1) by additionally utilizing the helix component of the 4-component Yamaguchi decomposition derived from ALOS-2 quad-pol imagery (cf. sections 3.3 and 3.8).

Scenario VIII) shows a strong increase of the UA for flooded vegetation, while keeping all other accuracy values stable compared to scenario I). The results of scenarios III) and IV) (cf. Table 2.3.4) show higher UA and PA values for flooded vegetation compared to scenario I). However, these classification based on only ALOS-2 data are characterized by lower UA and PA values for open water compared to the classification only using S-1 imagery (scenario I)). The best result is obtained for scenario VI), fusion of S-1 dual-pol and ALOS-2 quad-pol H/A/α Wishart-classified imagery. This fusion combines the high accuracy values for the open water and dry land classes (derived from the C-band S-1 data) with the high UA and PA values for flooded vegetation (derived from the L-band ALOS-2 imagery). Scenario VII) (fusion of S-1 and ALOS-2 Freeman Wishart) provides even higher UA values for flooded vegetation than scenario VI). However, as PA of flooded vegetation is definitely higher in scenario VI) than in VII), scenario VI) is selected as the fusion scenario with the highest accuracy in general.

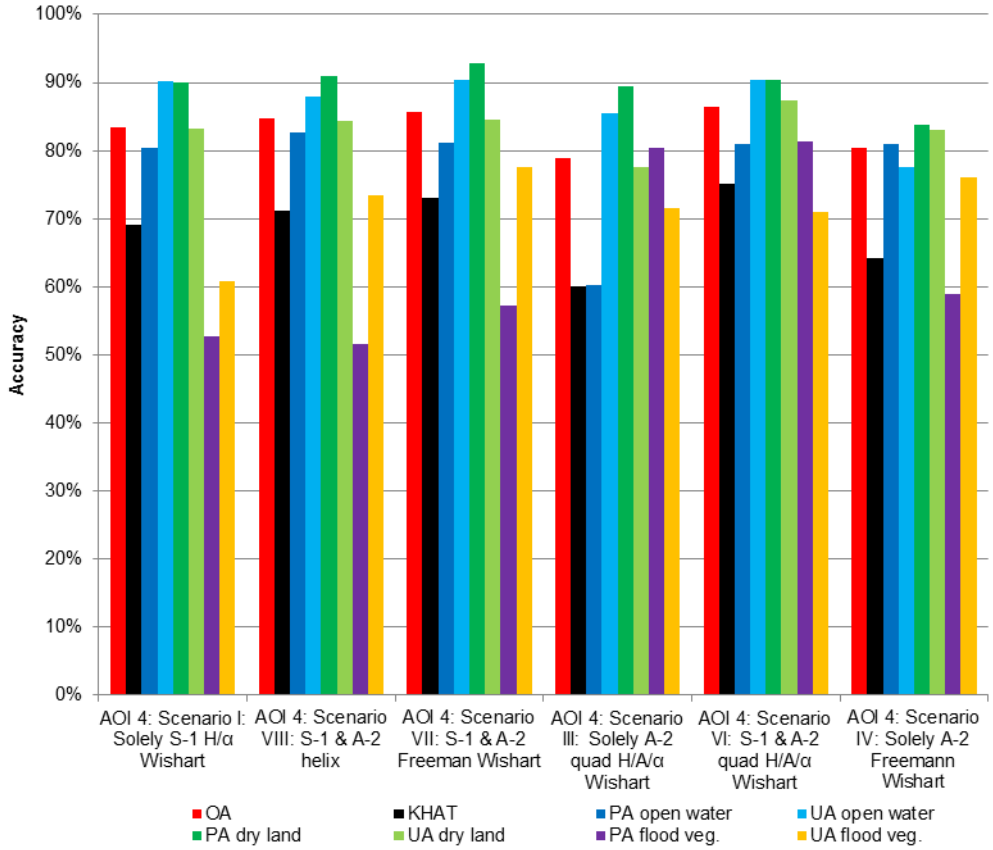

Figure 2.3.11: AOI 4: Accuracy assessment results for the scenarios I) only S-1 dual-pol H/α Wishart, III) only ALOS-2 quad-pol H/A/α Wishart, IV) only ALOS-2 Freeman Wishart, VI) fusion of S-1 dual-pol H/α Wishart and ALOS-2 quad-pol H/A/α Wishart, VII) fusion of S-1 H/α dual-pol Wishart and ALOS-2 Freeman Wishart, VIII) fusion of S-1 H/α dual-pol Wishart and ALOS-2 Yamaguchi helix. Overall accuracy (OA), user's accuracy (UA), producer's accuracy (PA).

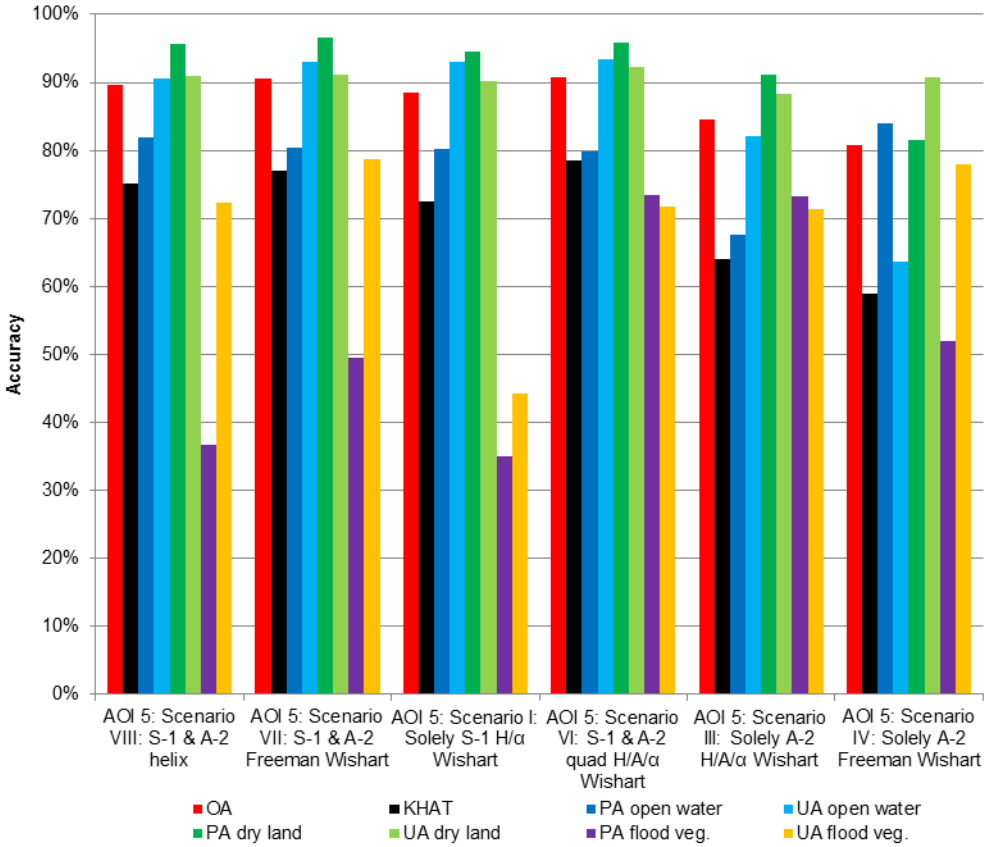

Figure 2.3.12: AOI 5: Accuracy assessment results for the scenarios I) only S-1 dual-pol H/α Wishart, III) only ALOS-2 quad-pol H/A/α Wishart, IV) only ALOS-2 Freeman Wishart, VI) fusion of S-1 dual-pol H/α Wishart and ALOS-2 quad-pol H/A/α Wishart, VII) fusion of S-1 H/α dual-pol Wishart and ALOS-2 Freeman Wishart, VIII) fusion of S-1 H/α dual-pol Wishart and ALOS-2 Yamaguchi helix. Overall accuracy (OA), user's accuracy (UA), producer's accuracy (PA).

Time series analysis based on Sentinel-1 dual-pol imagery

The methodology described above was applied to a time series of nine Sentinel-1 datasets acquired between 16 February and 24 April 2015 (cf. tab. 2.3.3 for details). The flood event showed a high dynamic during this period. Figure 2.3.10 shows the frequency of flooding over nine dates. Thereby, the classes open water and flooded vegetation were combined to the class flooded area. Detailed analysis showed that the small isolated areas being flooded only once or twice (especially located in the eastern part of the area) are false alarms caused by water look-alikes, i.e. wet agricultural fields characterised by similar low backscatter as open water bodies. These false classifications appear only at the Sentinel-1 SAR imagery acquired on 18 and 24 April 2015, not at the other seven acquisitions. One criteria of the methodology for mapping flooded vegetation is that this class always has to be located in the neighbourhood of open water areas and not isolated far away from this class. Detailed analysis of the isolated false classifications mentioned above showed that the percentage of falsely classified flooded vegetation is very low.

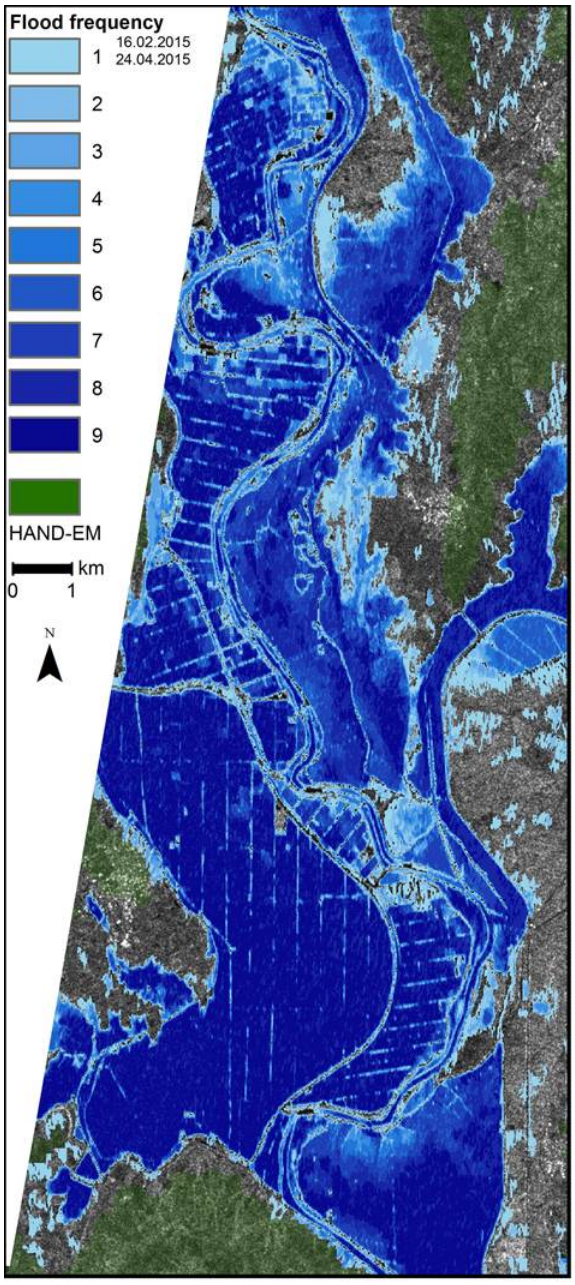

Figure 2.3.10: Flood frequency of the time series of nine Sentinel-1 datasets acquired between 16 February and 24 April 2015 (cf. tab. 2.3.3), ranging from bright blue (flooded at one date) to dark blue (flooded nine times). A Sentinel-1 image (VV) acquired on 12 March 2015 serves as backdrop.

Conclusion

This section presented a semi-automated procedure for mapping of flooded vegetation based on polarimetric Sentinel-1 and ALOS-2/PALSAR-2 imagery. The combination of pixel-based unsupervised Wishart classifications with object-based refinement using class neighbourhood conditions and minimum mapping units enables together with the integration of exclusion layers (HAND-EM and GUF) an semi-automatic detection of flooded areas with high accuracy values.

Thereby, besides the mapping of open water areas, special focus is on the detection of all flooded areas, including especially flooded vegetation.

The developed procedure is based on Sentinel-1 imagery due to its systematic acquisition and free availability. As the C-band dual-polarimetric (VV+VH) Sentinel-1 data is characterised by some limitations regarding the described application, we also analysed the suitability of L-band dual-pol and quad-polarimetric ALOS-2/PALSAR-2 SAR imagery as well as on the fusion of both, Sentinel-1 and ALOS-2 data. Quad-pol SAR imagery enabled the application and investigation of much more polarimetric decompositions enabling in summary a better separation of different land cover types. L-band SAR data shows a higher penetration depth into vegetation and enables therefore a better differentiation of flooded and non-flooded vegetation. The highest accuracies could be obtained by combining dual-pol S-1 H/α Wishart and ALOS-2 H/A/α quad-pol Wishart.

References

1. Cloude, S.R., Pottier, E., 1997: An entropy based classification scheme for land applications of polarimetric SAR. Transactions on Geoscience and Remote Sensing, 35, 68-78.
2. De Zan, F., Monti Guarnieri, A.M., 2006: TOPSAR: Terrain observation by progressive scans. IEEE Transactions on Geoscience and Remote Sensing, 44, 2352-2360.
3. Esch T., Taubenböck H., Roth A., Heldens W., Felbier A., Thiel M., Schmidt M., Müller A., Dech S., 2012: TanDEM-X mission: New perspectives for the inventory and monitoring of global settlement patterns. Journal of Selected Topics in Applied Earth Observation & Remote Sensing, 6, 22.
4. Freeman, A., Durden, S.L., 1998. A three-component scattering model for polarimetric SAR data. IEEE Transactions on Geoscience and Remote Sensing, 36, 963–973.
5. Lee, J.S., 1981: Refined filtering of image noise using local statistics. Computer Vision Graphics and Image Processing, 15, 380-389.
6. Lee, J.S., Jurkevich, I., Dewaele, P., Wambacq, P., Oosterlinck, A., 1994: Speckle filtering of synthetic aperture radar images: A review. Remote Sensing Reviews, 8, 313-340.
7. Lee, J.-S., & Pottier, E., 2009. Polarimetric Radar Imaging—From Basics to Applications.
8. CRC Press: London, UK.
9. Yamaguchi, Y., Moriyama, T., Ishido, M., & Yamada, H., 2005. Four-component scattering 1108 model for polarimetric SAR image decomposition. IEEE Transactions on Geoscience and Remote Sensing, 43, 1699–1706.

2.4 Technical note on flood and flood trace detection in urban areas

2.4.1 State-of-the-art

Flood mapping in urban areas

HR and VHR optical data have a proven track record in monitoring flooding including that of complex scenarios such as (sub-) urban areas (Meinel et al. 2003, Yésou et al. 2012). The working scale must be very precise as too coarse a spatial resolution can lead to the underestimation of flood extent if data resolution is not adapted (Allenbach and Battiston 2007).

Previous studies (Yésou et al. 2012, Huber et al. 2010, Enwright et al. 2012) have already highlighted that an increase in resolution by a factor of two leads to detecting up to 20% additional water. Comparisons have been realised between water bodies detected on Kompsat-2 (1.0m) and WV-2 (0.5m) acquired on the same day (the 7th of March 2010) over the Baie de l'Aiguillon in France, during the Xynthia storm event (fig. 2.4.1).

Kompsat-2 data (1m, 07/03/2010) WorldView-2 data (0.5 m, 07/03/2010) Water extraction

Figure 2.4.1: VHR data acquired during the March 2010 Xynthia flood event (Vendée, France), in light blue: water extracted on the Kompsat-2 image, in dark blue: water extracted on the WV-2 image (Yésou et al. 2012).

With 0.5m resolution data, nearly 20% additional water is detected compared to the 1.0m resolution data. The WV-2 image shows less confusion between water and shadows, vegetation and submerged vegetation (Yésou et al. 2012). Other studies, at lower resolutions, confirmed this phenomenon (Huber et al. 2010, Enwright et al. 2012).

Urban areas are complex environments where water body detection is often hampered. With optical HR or VHR data, significant building shadows related to the narrow streets can disturb automatic water detection. This is exacerbated when a flood crisis image is taken at a high incident angle which can sometimes make it impossible to see road/ground surfaces between buildings.

Flood trace detection in urban areas

For the detection of moisture and flood traces, the contribution of SWIR wavelengths is remarkable. Without SWIR, areas previously affected by floods have similar spectral signatures as non-affected areas and, hence, it is difficult to delineate a flood's extent. When a sensor has a SWIR band, this distinction can be made easier (fig. 2.4.2).

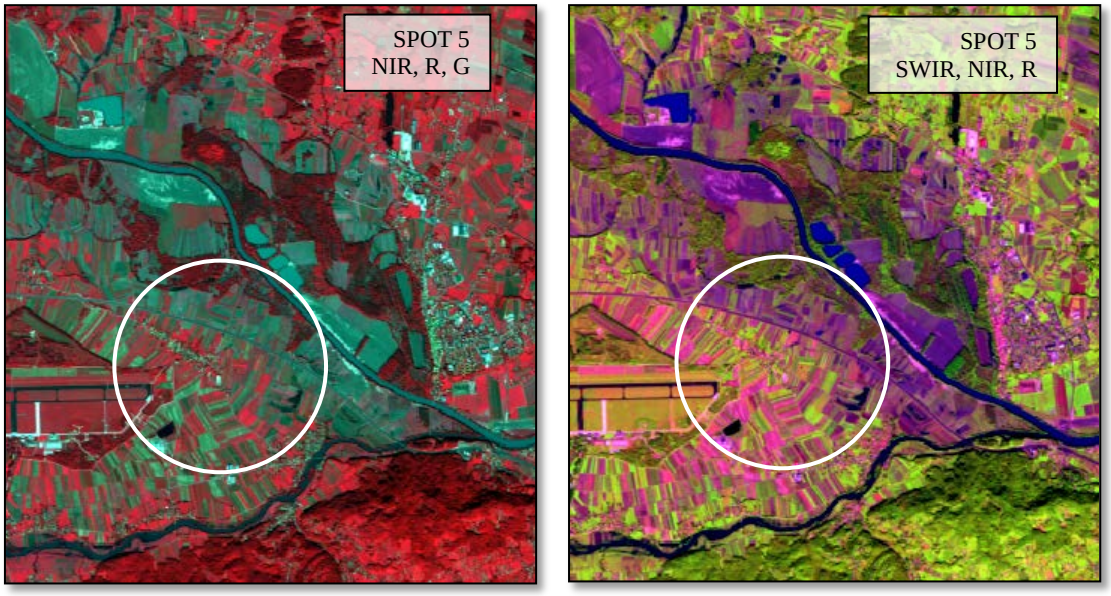

Figure 2.4.2: Contribution of SWIR band to flood trace detection. SPOT-5 acquired on 2010-09-23 in the frame of the GMES SAFER project over Croatia. Processing by SERTIT 2010.

Moreover, flash floods are even more difficult to observe because these floods peak and abate extremely rapidly after a rainfall event lasting only a couple of hours. In this case, flood trace detection makes it possible to deduce the area most affected by a flood. Little literature exists on this complex topic. A lot of studies focused on methodologies to generate flood models in urban areas using DSM. But few exist on the potential of VHR optical imagery to detect mud deposits and flood traces in urban areas when the water has receded (fig. 2.4.3) (Battiston et al. 2012). Moisture can be detected with all kinds of optical images, especially when SWIR channels are available. Hence, when these sensor characteristics are combined, as in the case of WV-3, surface moisture detection should be improved even in urban areas.

A study over the city of Krymsk (Russia), affected by a flash flood in July 2012, demonstrated the potential of SWIR data in moisture detection, but also the synergy between a HR sensor (2.5m) with a SWIR band (SPOT-5) and a VHR sensor (0.7m) without SWIR (Pléiades). Although the results of this work showed the usefulness of infrared and SWIR bands in particular for water and moisture extraction, the automatic extraction of mud traces was not possible. SWIR has no particular capacity to distinguish dry muddy areas giving their similar spectral signatures with those of other mineral surfaces. In this last case, VHR data are most appropriate bringing more accuracy and providing a more precise and complete delineation of muddy areas (Huber et al. 2013).

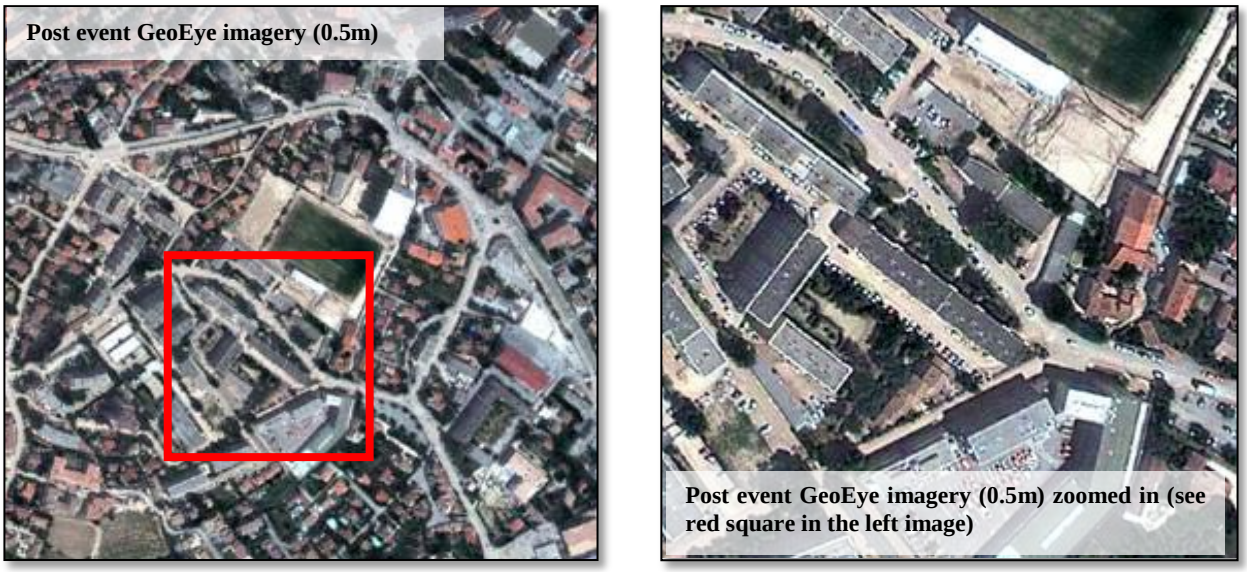

Figure 2.4.3: GeoEye image (0.5m) acquired a week after the flash floods that affected Draguignan (Var, France) in June 2010, showing a high quantity of mud deposition left by the floods (© GeoEye 2010. All rights reserved. Processing SERTIT 2010).

More recently, SERTIT worked with the CCR (French Reinsurance Company) after a flood event in the Southern part of France in October 2015. A WV-1 image was acquired over the affected area few hours after the thunderstorms (on 04 October 2015). Some remaining water was still visible in specific neighbourhoods, but also flood traces. With WV-1 imagery, no automatic detection was possible due to the lack of several needful multispectral bands. Thus, the identification of damage, flooding and flood traces was carried out by photo-interpretation (fig. 2.4.4).

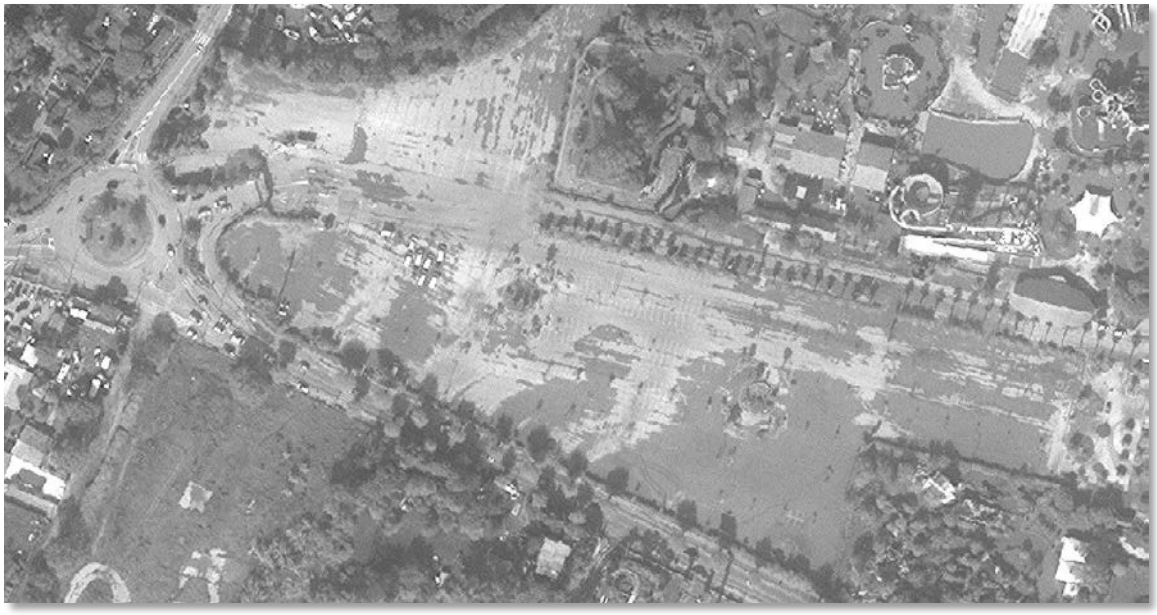

Figure 2.4.4: WV-1 image (0.5 m) acquired the day after flash floods that affected Antibes (Alpes-Maritimes, France) in October 2015, showing moisture and a high quantity of mud deposition left by the floods on the car park (© Digital Globe 2015. Processing SERTIT 2015).

References

1. Allenbach, B., Battiston, S., 2007: La télédétection, une vision détaillée des inondations, un gisement d'informations précieux pour la gestion de l'aléa, Brochure MEDAD, 40 p.
2. Battiston, S., Giraud, H., Dick, D., Bach, H., Fellah, K., 2012: Parametric flood insurance products development. Note on technical feasibility in urban areas, ESA Value Added Element, 34p.
3. Enwright, N., Jones, W., Garber, A., Keller, M., 2012: Analysis of the impact of spatial resolution on land/water classification using High Resolution aerial imagery. International Journal of Remote Sensing, x, 12p.
4. Huber, C., Lai, X., Uribe, C., Huang, S., Marié, T., Chen, X., Andréoli, R., Li, J., Yésou, H., 2010: Influence of spatial resolution on water bodies detection and relationship between water extent and water level, case of Poyang Lake (P.R. China), Proceedings of Living Planet Symposium, 27 juin - 2 juillet 2010, Bergen, ESA SP 686, 9p.
5. Huber, C., Battiston, S., Yésou, H., Tinel, C., Laurens, A., Studer, M., 2013: Synergy of VHR Pléiades data and SWIR spectral bands for flood detection and impact assessment in urban areas: case of Krymsk, Russian Federation, in July 2012, IGARSS, Melbourne, Australia, July 2013, 4p.
6. Meinel, G., Schumacher, U., Hennersdorf, J., 2003: GIS technical evaluation of the flood disaster in summer 2002 with respect of Dresden on basis of remote sensing, laser scanner and measurement data, ISPRS, Remote Sens. Spatial Inf. Sc., 34, 104-111.
7. Yésou, H., Studer, M., Huber, C., de Fraipont, P., 2012: Retour d’expérience suite à la tempête Xynthia, Rapport final - Convention MEDDTL – Université de Strasbourg 2100593016, 12.

2.4.2 Optical HR and VHR based flood detection in urban areas

Methodologies for flood detection in urban areas

The most basic method to extract water bodies uses thresholds on spectral bands in order to "split" histograms in two parts: water and non-water, with good results not often being easy to obtain. This method can be improved by using indexes derived from optical satellite bands to investigate the extraction of water surfaces. The most popular are the Normalised Difference Vegetation Index (NVDI) and the Normalised Difference Water Index (NDWI) which both need near infrared spectral bands and the NDWI requiring a SWIR channel. These indexes have demonstrated their efficiency in water discrimination and detection (Rouse 1973, Gao 1996) when used as inputs to a thresholding procedure. Other indexes were developed to improve water detection (or were adapted to other sensor types and spectral bands) such as the modified NDWI, the McFeeters' NDWI or the Water Ratio Index (WRI) (tab. 2.4.1). The thresholding of a combination of channels and indexes is often necessary.

Table 2.4.1: Main water indexes (B: blue, G: green, R: red, NIR: near infrared, SWIR: shortwave infrared).

Index		Equation
NDVI	*Normalised Difference Vegetation Index*	NIR-R / NIR+R
NDWI	*Normalised Difference Water Index*	NIR-SWIR / NIR+SWIR
Modified NDWI	*Modified Normalised Difference Water Index*	G-SWIR / G+SWIR
McFeeters' NDWI		G-NIR / G+NIR
NDWI adapted		B-NIR / B+NIR
WRI	*Water Ratio Index*	G+R / NIR+SWIR

With HR imagery thresholding methods are well adapted for water mapping with simple, double or more thresholds, and also supervised or non-supervised classifications. But with VHR imagery, pixel based methods get more complicated due to high image detail especially in urban areas. Also, the spectral characteristics and patterns of urban objects are sometimes so similar that they cannot be separated using only spectral information. Since the arrival of VHR sensors (IKONOS launched in 1999), the interest greatly increased in incorporating textural and geometrical information (Blaschke and Strobl 2001). Object-based classification methods generating objects through a multi-resolution segmentation process not only take spectral information into account but also other parameters such as texture, geometry or context of each feature during the classification step. This methodology seems to be very attractive and seems more adapted than pixel-based ones for VHR classification data in urban areas (Blaschke 2003).

In the frame of this project, namely the development of robust, transferable, fast and accurate methods to significantly enhance rapid mapping techniques, object-based classification in an urban environment is not always well adapted because this type of classification can be time consuming, This particularly applies for the segmentation step (not the segmentation procedure, but the time

required by the operator to find the best segmentation scales). So, in a rapid mapping context, it is important to explore how to reduce segmentation time and/or to explore other methods such as pixel-based image segmentation and classification by K-means, SVMs or Markov Random fields, which can be useful for detecting floods in particular using high spatial resolution images (Grizonnet and Inglada 2010).

Test sites for flood detection in urban areas

Several floods occurred in Central Europe in June 2013 due to heavy rainfalls. Both the Elbe and Danube basins were affected and more particularly cities like Budapest (Hungary), Prague (Czech Republic), Vienna (Austria), Passau and Dresden (Germany). In the frame of a partnership between SERTIT, ESA and the principal players in the (re-) insurance industry (e.g. Swiss Re, Allianz SE, PERILS AG), Airbus DS provided satellite data in a rush mode to evaluate the potential usage of space imagery within the insurance industry for flood impact assessment.

Within the ASAPTERRA project, it is planned to use Pléiades 1A data acquired over the city of Dresden and two SPOT-6 data acquired over the Northern area of Budapest during this flood event which has been graciously donated by Airbus DS.

Flooding in Dresden - Germany (June 2013)

The Pléiades 1A data was acquired on the 05 June 2013 (fig. 2.4.5) over Dresden in Germany. The spatial resolution of the data is 2.4m resampled to 2.0m for the multispectral (MS) channels and 0.7m resampled to 0.5m for the panchromatic (PAN) channel. The imagery were delivered as requested in bundle format, separate MS and PAN images.

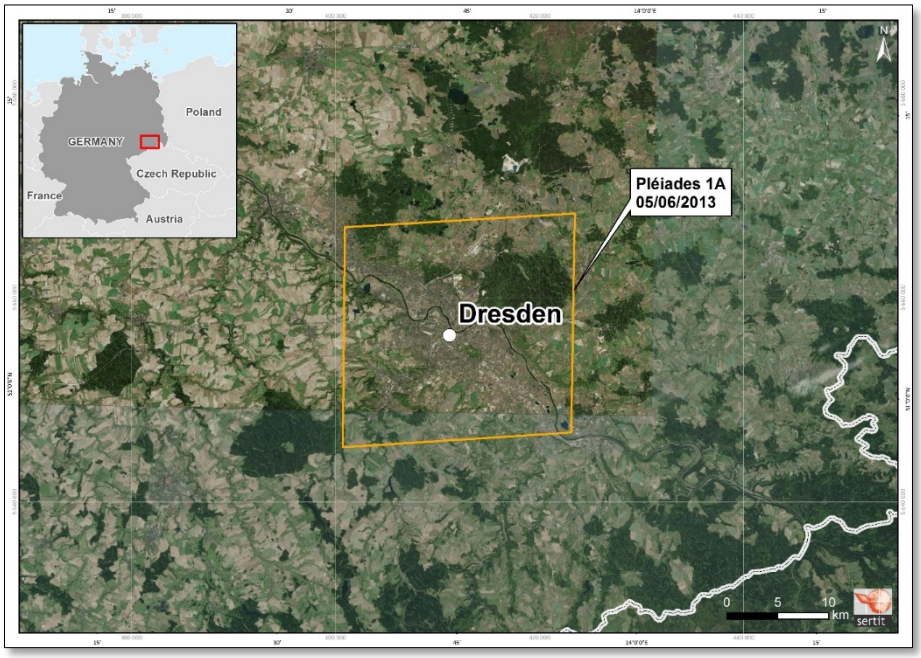

Figure 2.4.5: Footprint of Pléiades 1A data acquired on 2013-06-05 over Dresden, Germany.

In this data, some neighbourhoods along the Elbe River are flooded (fig. 2.4.6). This data was chosen because the spectral signature of water is disturbed by turbidity.

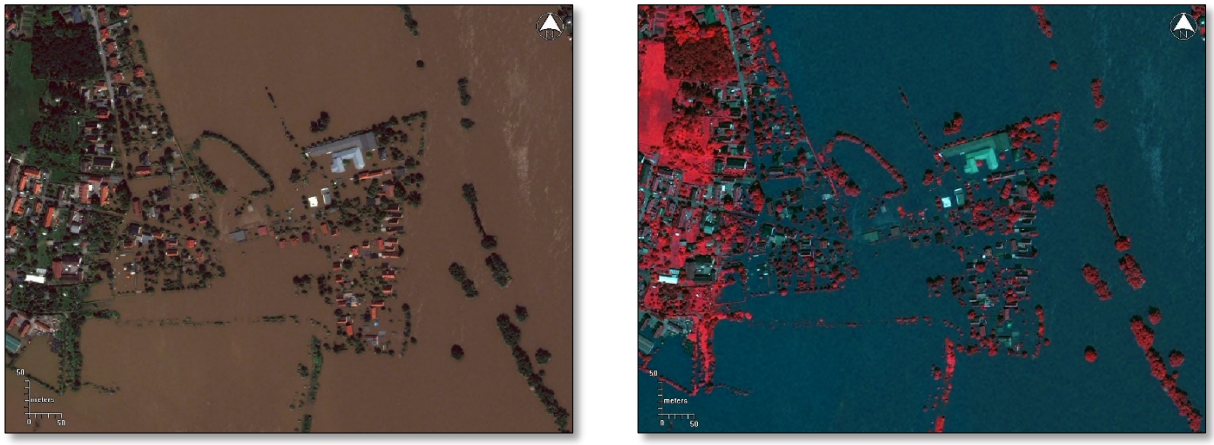

Natural colour composite (B, G, R) *False colour composite (NIR, R, G)*

Figure 2.4.6: Subset of Pléiades 1A MS data over Dresden acquired on the 2013-06-05.

Flooding to the North of Budapest – Hungary / Slovakia (June 2013):

Two SPOT-6 data were acquired on 08 June 2013 over the Danube River, in the Northern area of the city of Budapest, along the border between Hungary and Slovakia (fig. 2.4.7). The data were delivered already pansharpened with MS and PAN merged. Therefore, the resolution of these SPOT-6 data is 1.5m.

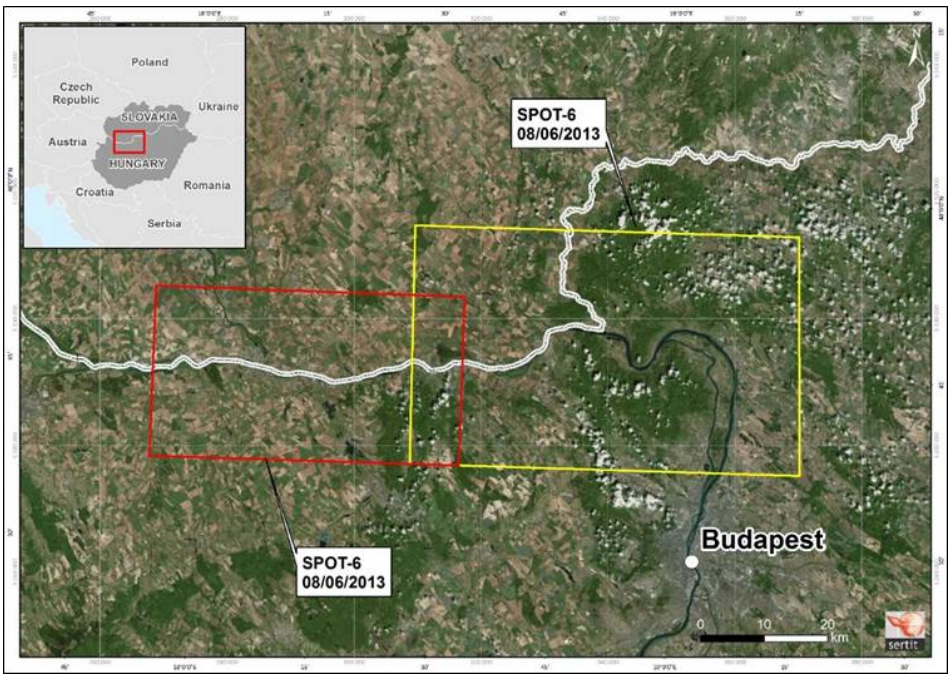

Figure 2.4.7: Location of the SPOT-6 data acquired over the Danube River (Hungary and

Slovakia).

In these data, the radiometric characteristics of water are not uniform. Over a large area the water bodies seem to carry a lot of sediment as water appears very bright on both natural colour and false colour composites (fig. 2.4.8).

Natural colour composite (B, G, R)

False colour composite (NIR, R, G)

Natural colour composite (B, G, R)

False colour composite (NIR, R, G)

Figure 2.4.8: Subset of SPOT-6 data over an area to the north of Budapest acquired on 2013-06-08.

Test sites for flood trace detection in urban areas

In July 2012, torrential rains battered the southern Russian Krasnodar region and more particularly the city of Krymsk. A Pléiades 1A scene was acquired over this region in the frame of the International Charter “Space and Major Disasters” to be analysed in a rapid mapping mode by SERTIT. Due to persistent cloud cover, the Pléiades data were acquired on 16 July 2012 over Krymsk, 10 days after the flood event (fig. 2.4.9). The Pléiades data were ordered in bundle mode, hence MS (2. m) and PAN (0.5m) channels are delivered in separate image files.

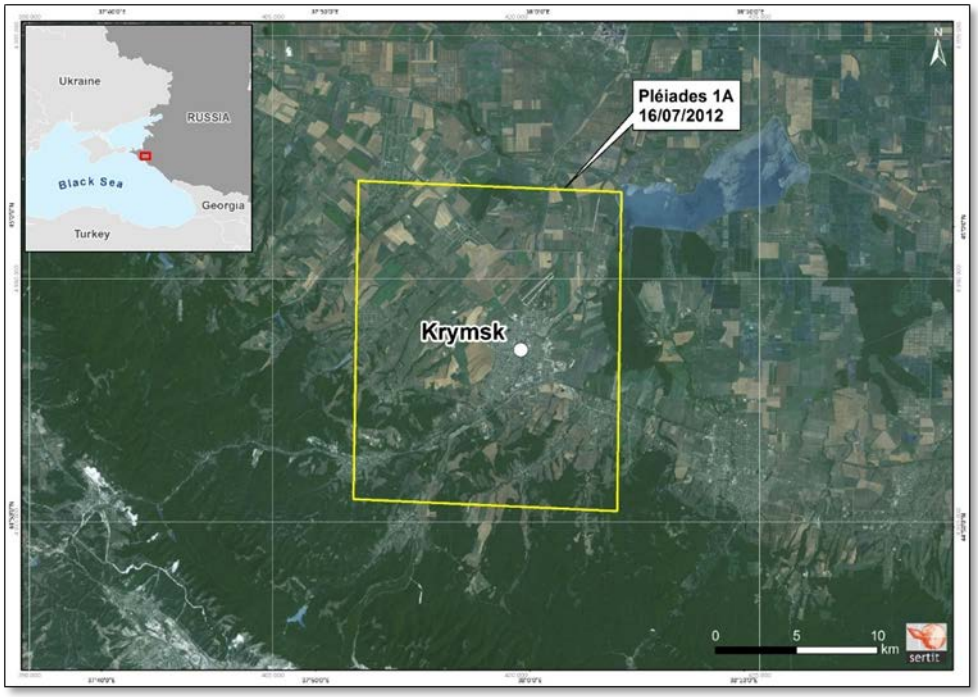

Figure 2.4.9: Location of the Pléiades 1A data acquired over the city of Krymsk (Russia).

No floodwaters are visible anymore on this satellite data, but flood traces can be detected in the urban area in the streets and in the stadium (fig. 2.4.10).

Natural colour composite (B, G, R) *False colour composite (NIR, R, G)*

Figure 2.4.10: Subset of Pléiades 1A MS data over Krymsk acquired on 2012-07-16.

In the frame of the Charter, flood traces were detected by visual interpretation. The aim of ASAPTERRA in this work package is the development of an automatic or semi-automatic method to detect these dry or wet mud deposits in urban areas.

Results concerning water detection in urban areas

The work was started with the Pléiades 1A image acquired over Dresden, using only the multispectral data (resampled to 2.0m). For reasons of timing, the work started on a cloud-free subset of the whole image (fig. 2.4.11). Otherwise, the subset is representative of the general landscape of the scene. Its size is roughly 4 x 2km.

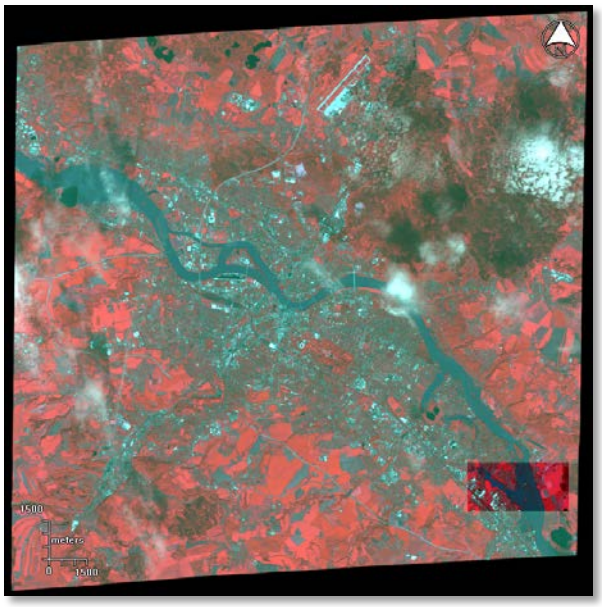

Figure 2.4.11: Pléiades 1A data over Dresden, Germany, highlighting the chosen subset.

The first step was to prepare a reference water layer in to order to validate water extraction tests. This reference layer was derived from the crisis water layer produced during the rush activation. At the time it was produced by a region growing method in Photoshop followed by photo-interpretative validation. For this study the layer was further corrected and reshaped by visual interpretation to obtain a very precise floodwater layer as reference (fig. 2.4.12).

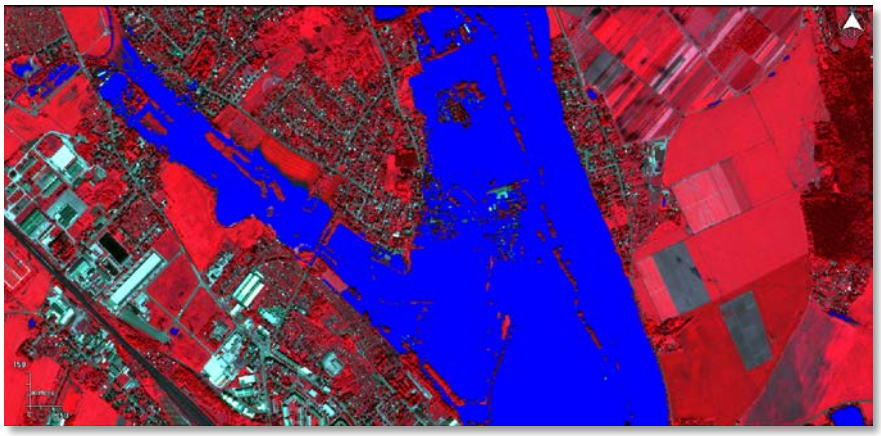

Figure 2.4.12: Floodwater reference layer derived from Pléiades 1A data acquired over Dresden on the 2013-06-05 using Photoshop and photo-interpretation methods.

Two tests were performed in ASAPTERRA: firstly, water extraction using “classical methods” i.e. thresholding, then a second with the OTB implemented SVM classification algorithms, using different input parameters.

Threshold methods using the NIR band and indexes

A first try was to test a double thresholding on the Pléiades 1A MS subset using the NIR band and the NDVI. Results show that to detect all water bodies and reduce underestimation in certain areas a lot of non-water pixels are included in the water layer (i.e. roofs and streets) (fig. 2.4.13).

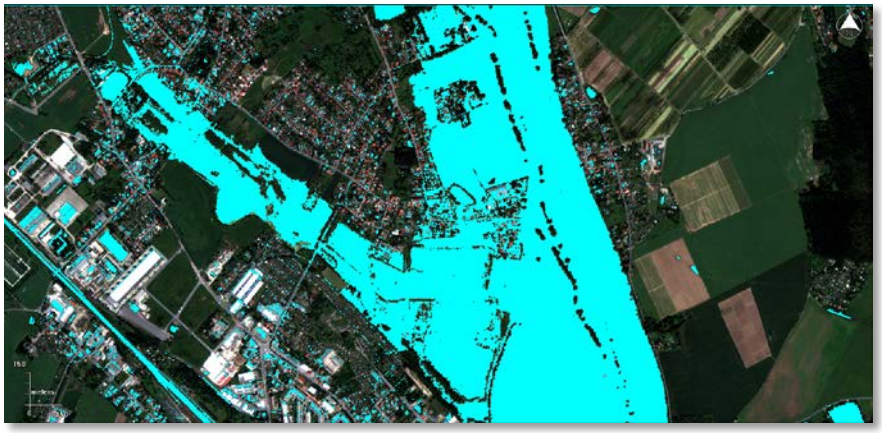

Figure 2.4.13: Water detection with a simple thresholding process (NIR and NDVI) from Pléiades 1A MS data acquired over Dresden on 2013-06-05.

A comparison with the reference water (fig. 2.4.14) indicates that 93.0% of the water is detected with the threshold method, and 7.0% of reference water is missing. These 7.0% correspond to the water bodies’ borders. But more than 12.0% of global water is overestimated. Confusions appear between water and urban objects.

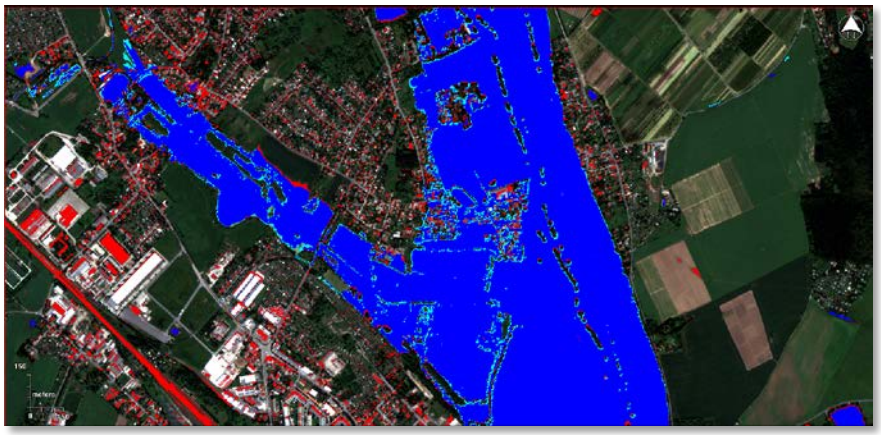

Figure 2.4.14: Comparison between results derived for water detection using a traditional threshold method (NIR and NDVI) and a reference water layer. In blue: common water with the reference layer, in light blue: missed water and in red: overestimate water.

On the same Pléiades 1A MS subset, two other tests have been performed combining the NIR band with the NDWI adapted or the Mc Feeters' NDWI. Results show a good proportion of common water extraction with the three thresholds. Comparing results using the NDWI adapted index there is higher omission errors (11.1%) than with the NDVI. These omission errors correspond to the water bodies' edges (tab. 2.4.2). Whereas, with the Mc Feeters' NDWI, results are nearly the same.

Table 2.4.2: Comparison between results obtained with threshold methods and reference water layer.

Double thresholding	Common water with the reference layer	Omission error of water	Commission error of water
NIR and NDVI	93.6%	6.4%	12.8%
NIR and NDWI adapted	88.9%	11.1%	2.3%
NIR and McFeeters' NDWI	90.4%	9.6%	3.0%

These first tests confirm that this "classical" method detects large parts of the water bodies, but due to over-estimation, a lot of manual cleaning work will be necessary. This result is not optimal for the aim of this work package because we wanted to avoid as much as possible this recoding step.

SVM classification with OTB

The second test was realised with OTB using the SVM algorithm (the SVM algorithm is explained in section 2.1.3). Before starting the process, this supervised method requires samples. We chose to classify the image in two classes: Water and non-water. 14 water and 57 non-water samples have been collected. The "non-water" class contains bare soils, artificial surfaces (buildings, streets), vegetation and shadows.

OTB was accessed through the QGIS software that supports all of OTB's algorithms. As in the section 2.1.3, tests between ANN and SVM classification methods show that the linear kernel is the most efficient one for the SVM method. Therefore, it was decided to choose it without testing the others (RBF and polynomial), but adjusted only the ratio between training and validation (i.e. if the ratio is 0.7 it means that 70% of the samples will be used for the validation step).

Results are quite good (fig. 2.4.15). At a first look, it appears that less confusion with the other landscape elements is observed. The comparison with the reference water layer confirms this observation. As for the thresholding method, a large part of the water area is well detected with the SVM classification (91.9 to 92.5%) (tab. 2.4.3). There are omissions of 7.5 to 8.1%. These missing pixels correspond also to the borders of the water bodies. Concerning commission errors, and in part contrary to the previous SVM test, false detections are reduced to only 2.3 to 3.0% of the pixels. This seems to be a promising method to further develop.

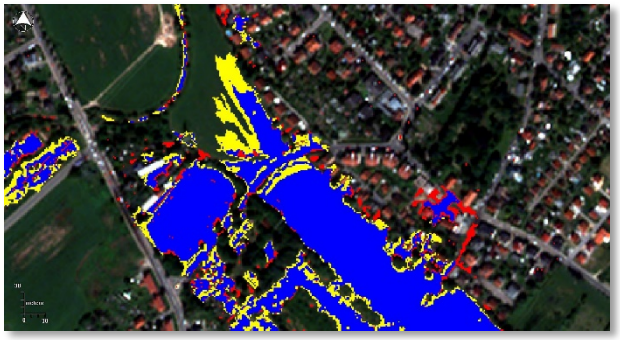

Kernel : Linear ; ratio training / validation : 0.3

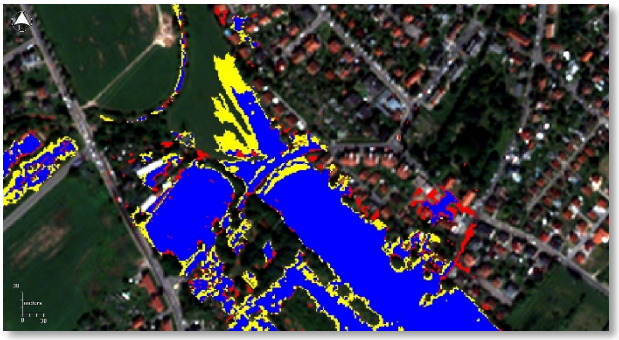

Kernel : Linear ; ratio training / validation : 0.5

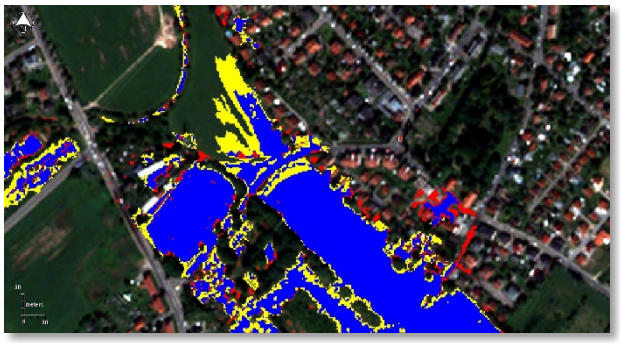

Kernel : Linear ; ratio training / validation : 0.7

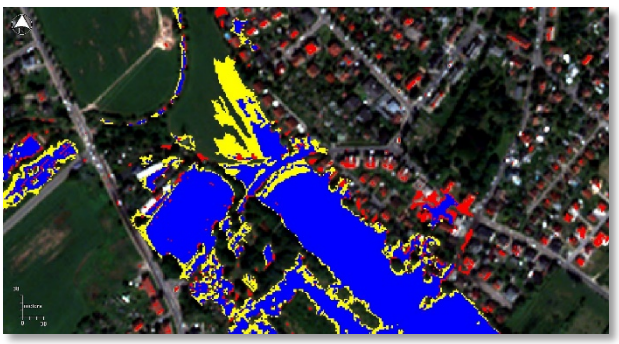

Kernel : Linear ; ratio training / validation : 0.9

Figure 2.4.15: Comparison between water detection using the SVM algorithm and reference water layer. In blue: common water with the reference layer, in yellow: missing water and in red: overestimation of the water extent.

Table 2.4.3: Comparison between results obtained with SVM classification methods and reference water layer.

SVM linear kernel	Common water with the reference layer	Omission error of water	Commission error of water
Ratio train. / valid. : 0.3	92.5%	7.5%	2.6%
Ratio train. / valid. : 0.5	92.3%	7.7%	2.5%
Ratio train. / valid. : 0.7	92.1%	7.9%	2.3%
Ratio train. / valid. : 0.9	91.9%	8.1%	3.0%

Texture analysis

A texture analysis can improve a classification, especially on VHR imagery and when objects have similar spectral signatures. In the case of floods in urban areas, water is often turbid and can have similar colours as e.g. bare soils. The texture measures used in this chapter were derived from the second-order statistics of grey-level co-occurrence matrix (GLCM), which indicates the probability that values of each pair of pixels co-occur in a given direction and at certain distance in the image. The calculations of texture statistics were based on a moving window around each pixel and the statistics were then attributed to each centre pixel (Haralick et al. 1973; Feng et al. 2015). The study by Feng et al. (2015) recommended the use of a 5 x 5 moving window to yield the highest accuracy.

We generated these textural indexes with the ITT ENVI software. We choose four texture measures among several options as regards to their applicability in urban areas (Puissant et al. 2005): homogeneity, dissimilarity, entropy and the angular second moment (fig. 2.4.16).

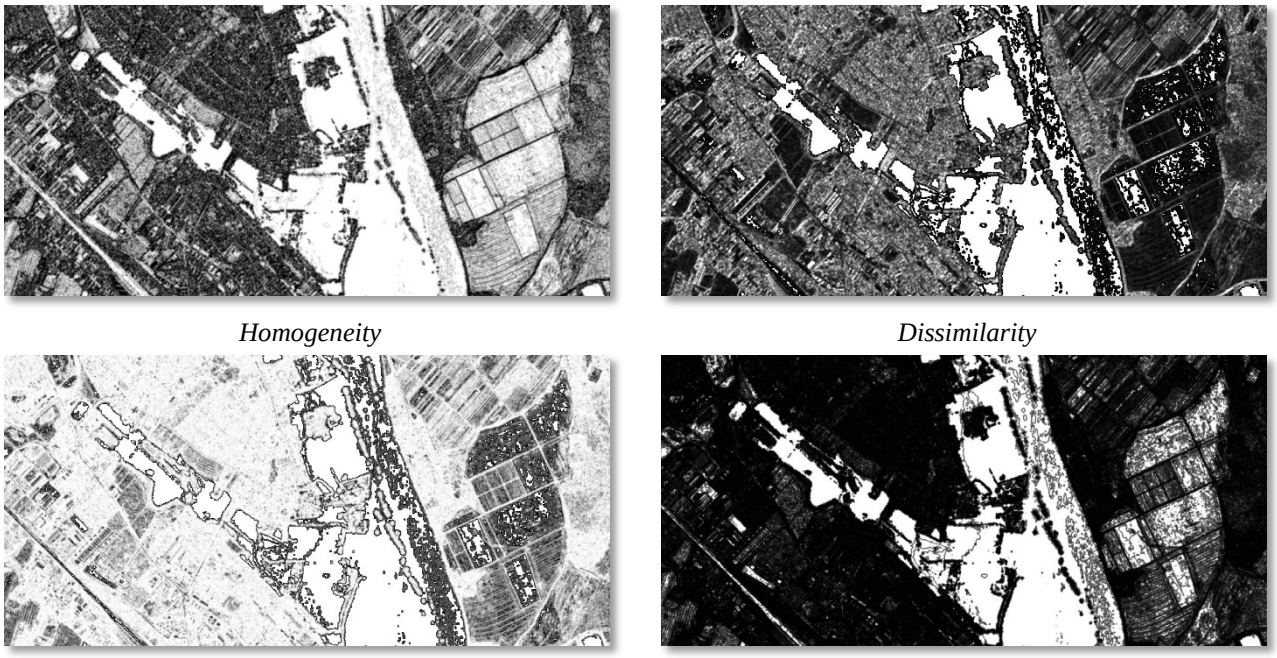

Homogeneity *Dissimilarity*

Entropy *Angular Second Moment*

Figure 2.4.16: Co-occurrence-based texture measures used for classification tests.

As the aim is to improve a classification only based on spectral bands, these four texture measures were added, band per band, to the initial image. Double thresholding and SVM classification methods were tested again.

Combining thresholds on the NIR band and a texture measure did not give as good results as expected (tab. 2.4.4.). In fact, results are worse than using only the NIR band and the NDVI. Less common water is detected with the texture measures, but the commission error is reduced.

Table 2.4.4: Comparison between results obtained with double thresholding methods and reference water layer.

Double thresholding	Common water with the reference layer	Omission error of water	Commission error of water
NIR and homogeneity	89.2%	10.8%	6.6%
NIR and dissimilarity	85.3%	14.7%	6.1%
NIR and entropy	89.6%	10.4%	6.9%
NIR and angular second moment	82.2%	17.8%	2.7%

The same approach was taken with the SVM classification. The linear kernel was chosen, with a ratio between training and validation set at 0.7. Tests using the four spectral bands and texture

measures were performed. Here also, results are not as expected. The addition of one or all texture measures did not improve significantly the classification (tab. 2.4.5).

Table 2.4.5: Comparison of results obtained with SVM classifications and reference water layer.

SVM linear kernel	Common water with the reference layer	Missed water	Commission water
Spectral bands + Homogeneity	91.4%	8.6%	2.0%
Spectral bands + Dissimilarity	91.8%	8.2%	2.2%
Spectral bands + Entropy	92.2%	7.8%	2.3%
Spectral bands + Angular second moment	91.9%	8.1%	2.2%
Spectral bands + all texture measures	91.2%	8.8%	2.2%

It seems that the method that obtains the highest amount of common water with the reference layer is a double threshold using the NIR band and the NDVI (93.6% of common water). Unfortunately, this method generates more than 12.0% commission error, which leads to manual corrections. With the SVM algorithm, the part of common water detection varies between 91.9 and 92.5%. This is lower than with the previous method but the omission and commission errors are significantly reduced. Hence, the SVM algorithm is for now the best option and merits deeper exploration.

Results summary

Machine learning techniques, notably SVMs, were tested in order to classify open water within complex urban areas trying to minimise classification and post-classification operator intervention. This particular work focuses on the most promising techniques arising from the optical rural mapping. At present the mapping of water (especially flood waters) in urban areas is very time consuming and complex. This was especially noticed during the Elbe and Danube floods of 2013.

Results over Dresden, Germany, orient the development work towards the use of SVM methodologies using Pléiades imagery and insuring very high thematic accuracy. Overall accuracies and KHAT values ranged between 97–98% and 0.97–0.98, respectively. The results have been evaluated in the context of rapid mapping with a focus on simplicity, robustness, and speed of procedure execution and are deemed satisfactory.

This procedure has been chosen for deployment within rapid mapping when mapping spectrally complex floodwater bodies.

References

1. Blaschke, T., 2003: Object-based contextual image classification built on image segmentation, Advances in Techniques for Analysis of Remotely Sensed Data, 2003 IEEE Workshop on, Issue Date: 27-28 Oct. 2003, 17p.
2. Blaschke, T., Strobl, J., 2001: What's wrong with pixels? Some recent developments interfacing remote sensing and GIS. GIS – Zeitschrift für Geoinformationssysteme 14 (6), 6p.

3. Feng, Q., Liu, J., Gong, J., 2015: Urban Flood Mapping Based on Unmanned Aerial Vehicle Remote Sensing and Random Forest Classifier—A Case of Yuyao, China. Water, ISSN 2073-4441, 31/03/2015, 19p.
4. Gao, B.C., 1996: NDWI - A Normalized Difference Water Index for Remote Sensing of Vegetation Liquid Water From Space, Remote Sens. Environ. 58:257-266 (1996) ©Elsevier Science Inc., 1996, 10p.
5. Grizonnet, M., Inglada, J., 2010: Monteverdi – Remote Sensing Software from Educational to operational context, Remote Sensing for Science, Education and Natural and Cultural Heritage, 749-755.
6. Grisonnet, M., Michel, J., 2013: Monteverdi 2.0 - Remote sensing software for Pleiades images analysis, EARSeL, 2013, 10p.
7. Haralick, R.M., Dinstein, I., Shanmugam, K., 1973: Textural features for image classification, IEEE Trans. Syst. Man Cybern. 1973, 3, 610–621, 11p.
8. Puissant, A., Hirsch, J., Weber, C., 2005: The utility of texture analysis to improve per-pixel classification for high to very high spatial resolution imagery, International Journal of Remote Sensing, Vol. 26, No. 4, 20 February 2005, 733-745, 13p.
9. Rouse, J.W., Haas, R.H., Schell, J.A., Deering, D.W, 1973: Monitoring Vegetation Systems in the Great Plains with ERTS (Earth Resources Technology Satellite), Proceedings of Third Earth Resources Technology Satellite Symposium, Greenbelt, ON, Canada, 10–14 December 1973, Volume SP-351, 17p.

2.4.3 Results concerning flood trace detection in urban areas

As exposed in the state-of-the-art (section 2.4.1), flood traces are not easy to detect. Two types of flood traces can be distinguished: moisture (wet traces) and mud deposits (often already dry). The study carried out over Krymsk (Russia) quoted in section 2.4.1 (Huber et al., 2013) already demonstrated the complexity of flood traces detection. A comparison between the potential of a SPOT-5 image, with a SWIR band but at a resolution of 2.5m, and a Pléiades image (no SWIR band, but a resolution of 0.7m) was performed over the same area. The comparison shows that mud deposits observed on the SPOT-5 imagery are included in the extension of mud observed in the Pléiades image; there were only 2.0% of commission pixels. But with Pléiades imagery three times more affected areas could be detected than with the SPOT-5 imagery (fig. 2.4.17).

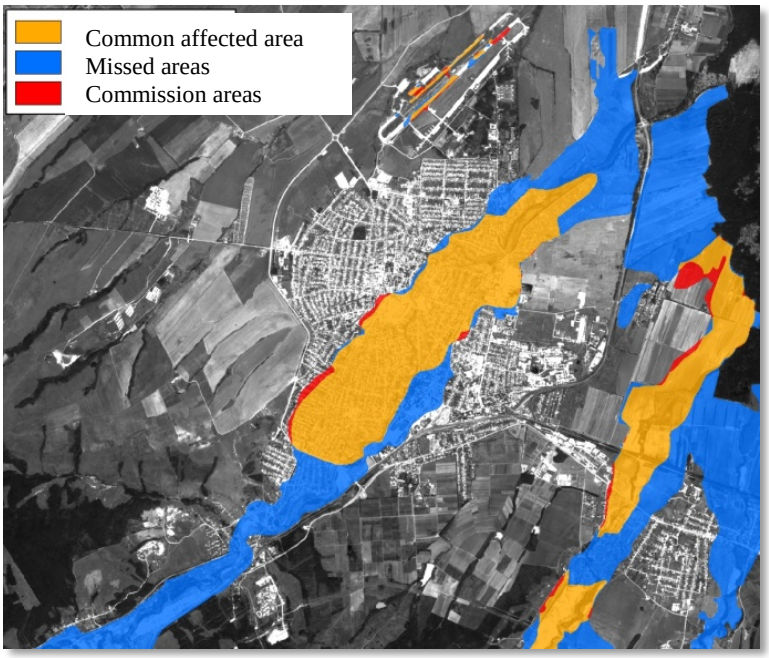

Figure 2.4.17: Mud deposits observed on SPOT-5 compared to mud extension observed on Pléiades imagery.

This comparison confirms that the SWIR band does not bring enough information to detect mud depositions, but the resolution is probably the main factor influencing the capability of their detection.

Concerning moisture, the same comparison was performed and results are opposite: only 19.0% of moisture detected by SPOT-5 is observed in the Pléiades imagery, and more than 80.0% of moisture detected on SPOT-5 is missing in Pléiades data. Moreover, with Pléiades, there occur large parts of false alarms (59.0% of commission pixels of mud) compared with SPOT-5 (fig. 2.4.18). These false detections are mainly due to the lack of a SWIR band in Pléiades data.

Hence, moisture detection is very dependent on a SWIR band, on the contrary, mud deposits detection required VHR but only visible bands are sufficient. The aim of this study over Krymsk

was to highlight the potential of each sensor and their synergy, but it did not contribute to improved detection and extraction methodologies. Extractions were carried with traditional methods (thresholds) and thematic layers obtained were corrected by visual interpretation before analysis. It was decided to drop work on this topic for the second year of ASAPTERRA.

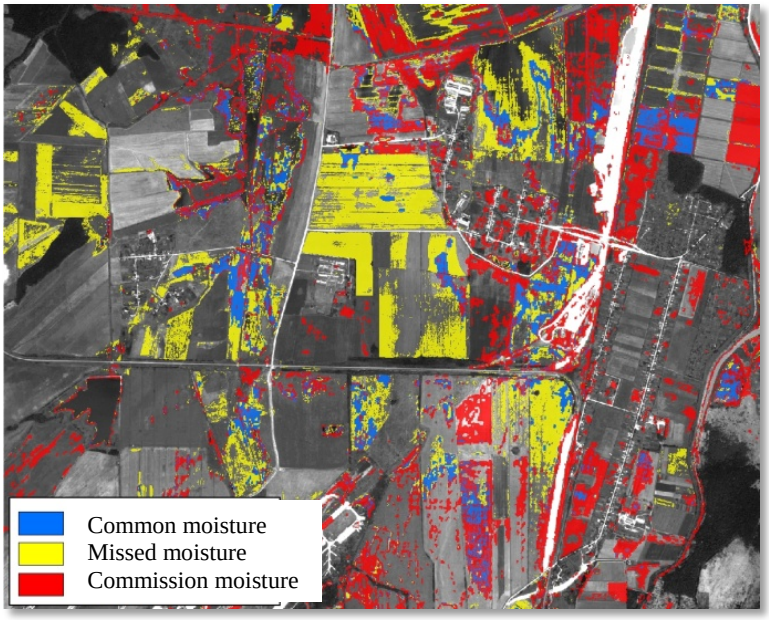

Figure 2.4.18: Comparison between soil moisture observed by Pléiades and SPOT-5 imagery.

2.5 Technical note on landslide detection

2.5.1 Optical data-based landslide detection in rural areas

2.5.1.1 State-of-the-art

A landslide is a movement of rock, earth, or debris down a sloped section of land. Landslides are caused by rain, earthquakes, volcanoes, or other factors that make the slope unstable. Near populated areas, landslides present major hazards to people and property (National Geographic). Remote sensing techniques represent a powerful tool for landslide detection.

This state-of-the-art inspired by Scaioni et al. (2014) giving a complete overview of achievements and perspectives about remote sensing for landslide detection.

The first studies started with low spatial resolution sensors, in the order of 10-30 m (e.g., Landsat, SPOT-1-4). Then, from IKONOS to Pléiades, HR and VHR optical sensors were used, characterised by more, new beneficial properties in terms of spatial resolution, number of multispectral bands, acquisition frequency, image quality, global coverage, and stereo mode (Santurri et al. 2010). Some papers have been published in recent years on the visual or analytical interpretation of satellite images, mainly based on HR/VHR data (Tsai et al. 2010). A comparison of landslide inventories obtained from aerial photos and satellite images showed that the new data sources can provide similar results even in areas where landslides have left only faint signs (Fiorucci et al. 2010).

Actually, in the literature, the visual interpretation of optical imagery has proved to be particularly useful for mapping landslides, because after an event the boundaries between depletion, transport, deposition areas and the unaffected landscape are usually distinguishable. Nevertheless, delineating the boundaries of deep-seated and large complex slope movements is a very hard task, even for fresh slope failures, with the boundary between the stable terrain and the failed mass frequently transitional. Furthermore, the older the landslide, the more indistinct become the borders. This is due to different causes: local adjustments of the landslide, new slope failures, earth filling, erosion, and land cover changes with colonising vegetation (Malabud et al. 2004, Guzetti et al. 2012). The main drawbacks of photo-interpretation are the uncertainty of outputs, the subjectivity, the time loss and the strict dependency on human expertise.

Recently, many developments have been made with the aim to automate landslide detection. The first algorithms tested for classification were pixel-based: they consider the spectral information associated to each pixel independently of the neighbourhood. As stated by Martha et al. (2010), considering the resolution of EO data and the typical size and distribution of landslides, pixel-based methods may be error prone. Therefore, in the latest studies there was an increasing interest in considering the spatial context of every pixel that led to the development of algorithms for object-based landslide delineation (Blaschke 2010). Semi-automatic algorithms for EO imagery classification treat landslides as objects composed of pixels instead of uncorrelated cells. The size of aggregations can be different, even variable within the same method as proposed by Lu et al. (2011). In Stumpf et al. (2014) a region-based active learning algorithm, which belongs to

supervised classification techniques, was performed on multi-temporal very high resolution optical images to recognize large scale shallow landslides. Automated processing and the visual analysis of RapidEye data, combined with field reconnaissance and historical records, have been exploited to detect and characterise 250 landslides in Southern Kyrgyzstan (Golovko et al. 2014).

In this work package SERTIT aims to detect landscape changes caused by landslides focussing on 2D change detection procedures but also exploring if it is possible to detect and measure volumetric changes. This small part could combine radar and optical methodologies to model 3D changes.

References

1. Scaiono, M., Longoni, L., Melillo, V., Papini, M., 2014: Remote Sensing for Landslide Investigations: An Overview of Recent Achievements and Perspectives, Remote Sensing, 6, 9600-9652.
2. Santurri, L. Carlà, R., Fiorucci, F., Aiazzi, B., Baronti, S., Cardinali, M., Mondini, A., 2010: Assessment of very high resolution satellite data techniques for landslide recognition. Int. Arch. Photogramm. Remote Sens. Spat. Inf. Sci, 38/B7, 492-496.
3. Tsai, F., Hwang, J.-H., Chen, L.-C., Lin T.-H., 2010: Post-disaster assessment of landslides in southern Taiwan after 2009 Typhoon Morakot using remote sensing and spatial analysis. Nat. Hazard. Earth. Syst., 10, 2179-2190.
4. Fiorucci, F., Cardinali, M., Carlà, R., Rossi, M., Mondini, A.C., Santurri, L., Ardizzone, F., Guzetti, F., 2011: Seasonal landslide mapping and estimation of landslide mobilization rates using aerial and satellite images. Geomorphology, 129, 59-70.
5. Malabud, B.D., Turcotte, D.L., Guzzetti, F., Reichenbach, P., 2004: Landslide inventories and their statistical properties. Earth Surf. Processes, 29, 687-711.
6. Guzetti, F., Mondini, A.C., Cardinali, M., Fiorucci, F., Sanatngelo, M., Chang, K.-T., 2012: Landslide inventory maps: New tools for an old problem, Earth Sci. Rev., 112, 42-66.
7. Blaschke, T., 2010: Object based image analysis for remote sensing, ISPRS J. Photogramm. Remote Sens., 65, 2-16.
8. Martha, T.R., Kerle, N., Jetten, V., van Westen, C., Vinod Kumar, K., 2010: Characterising spectral, spatial and morphometric properties of landslides for semi-automatic detection using object-oriented methods, Geomorphology, 116, 24-36.
9. Stumpf, A., Lachiche, N., Malet, J.P., Kerle, N., Puissant, A., 2014: Active learning in the spatial domain for remote sensing classification, IEEE Trans. Geosci. Remote Sens., 52, 2492-2507.
10. Lu, P., Stumpf, A., Kerle, N., Casagli, N., 2011: Object-oriented change detection for landslide rapid mapping, IEEE Geosci. Remote Sens. Lett., 8, 701-705.

2.5.1.2 Automatic extraction of landslides

An automatic change detection based landslide processing chain has been elaborated within ASAPTERRA. Given the lack of possible recent test sites the processing chain has been developed using two large scale events in Nepal and Japan observed by optical satellite imagery.

Test site #1: Nepal Earthquake, 2015

An earthquake in Nepal with a magnitude of 7.9M, 10 km depth, occurred in April 2015 with at least one consequent aftershock of 7.1M, 10 km depth. The epicentre was located between the capital Kathmandu and the city of Pokhara, and was also felt in northern parts of India and in Tibet. Extensive damage to buildings and injuries has been reported. The study case is focused on Gumda area, North of Kathmandu, where huge landslides occurred.

Test site #2: Japan Earthquakes, 2016

The 2016 Japan Earthquakes are a series of earthquakes, including a magnitude 7.3 main-shock which struck on April 16 beneath Kumamoto City, Kumamoto Prefecture in the Kyushu Region, at a depth of about 10 km, and a foreshock earthquake with a magnitude 6.5 on April 14 at a depth of ~ 11 km. The two earthquakes killed at least 49 people and injured about 3,000 others in total. More than 44,000 people were evacuated from their homes due to the disaster. Strong shocks combined with heavy rain made high sloping ground unstable and vulnerable to landslides (fig. 2.5.1).

Kumamoto Prefecture lies at the southern end of the Japan Median Tectonic Line, where a system of active faults fork in two directions at the Beppu-Haneyama Fault Zone. Specifically, the series of quakes ruptured the 81 km-long Hinagu Fault and the 64 km-long Futagawa Fault to its north, as well as lesser but discernible interaction with the farther flung Beppu-Haneyama Fault Zone. A 27 km section of the Futagawa Fault Zone slid 3.5 m. The earthquakes occurred along the Beppu–Shimabara graben, with epicentres moving from west to east over time as illustrated in the figure 2.5.2.

Figure 2.5.1: Impressive landslides caused by the earthquakes ©Reuters-kyodo.

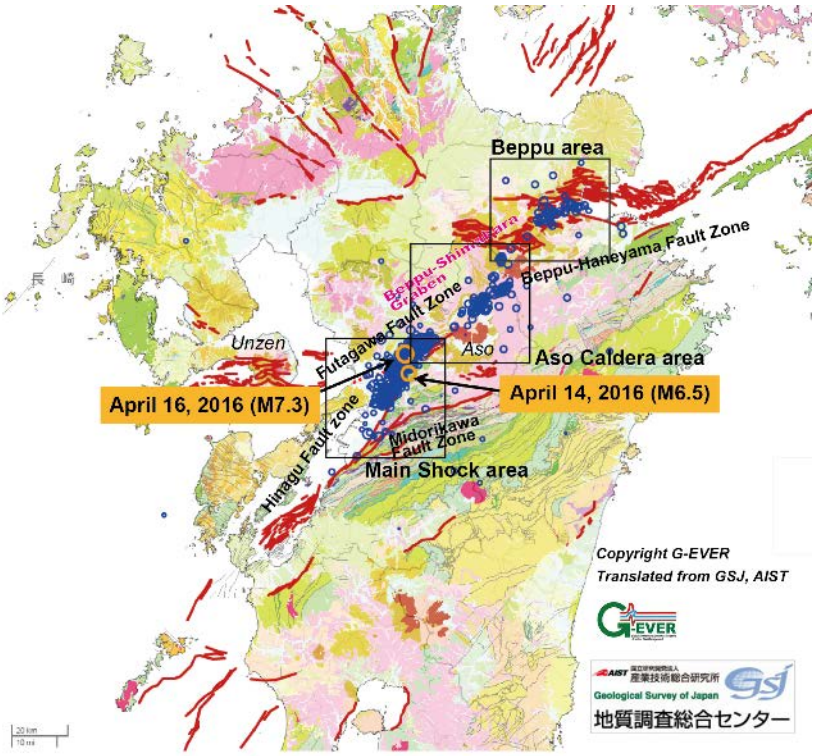

Figure 2.5.1: Orange circles denote epicentres of two major earthquakes, blue circles are aftershocks and other smaller earthquakes. Size of the circles is proportional to the magnitude of the earthquakes. Red lines show traces of active faults in this area.

Data set

The data used for these case studies in Nepal and Japan are listed in the table below (tab. 2.5.1):

Table 2.5.1: Satellite reference and crisis image details.

Test site	Image	Sensor	Acquisition date	Resolution (m)
Nepal	Reference	SPOT-7	12/03/2015	1.5
	Crisis	SPOT-6	02/05/2015	1.5
Japan	Reference	Landsat-8	20/03/2016	15
	Crisis	Landsat-8	23/05/2016	15
	Reference	Sentinel-2	03/03/2016	10
	Crisis	Sentinel-2	10/08/2016	10

Nepal

SPOT-6 and SPOT-7 images were acquired and processed in the framework of the Copernicus EMS Rapid Mapping contract EMSR125. An important aspect to highlight is that both satellites are identical making processing and interpretation easier. The map presented hereafter was produced in

this context (rush mode) after a photo-interpretation work and shows landslide delineation in Gumda area.

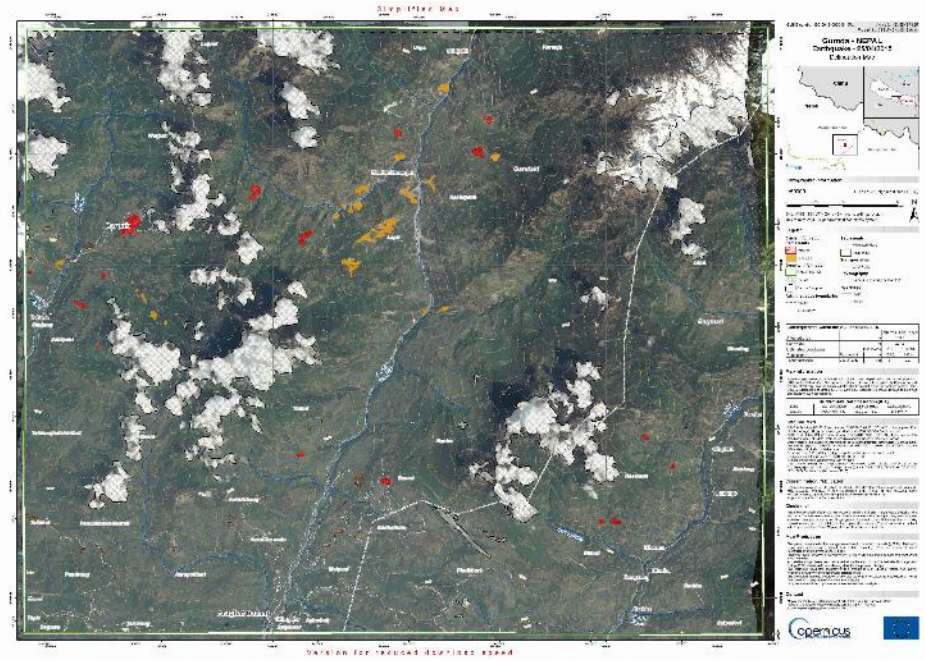

Figure 2.5.3: Copernicus EMS delineation map showing detected landslides in orange (and the affected settlements in red).

Japan

Systematic acquisitions of Landsat-8 and Sentinel-2 data permit to have free optical data over Kyushu Island. A pre/post disaster couple of images were selected and downloaded. They were processed independently from each sensor to keep optimal co-registration between pre and post images. Unfortunately the first crisis Sentinel-2 image available with acceptable cloud coverage was acquired almost four months after the disaster and some landslides could have been cleaned up, especially along infrastructure and in urban areas.

Landslides detection methodology

Given the goals to save time in rush mode production and to be as automatic as possible, a pixel-based approach is chosen. The methodology, which is not novel, relies on a basic principle which is the sudden disappearance of vegetation where a landslide occurs. A change detection between both images, reference (fig. 2.5.3) and crisis (fig. 2.5.4), would highlight this vegetation disappearance. Figures 2.5.5 and 2.5.6 show results of NDVI computed on both images. The large beige-grey area on the crisis NDVI reveals an absence of vegetation and can be characterised as a landslide thanks to the change detection using the reference data.

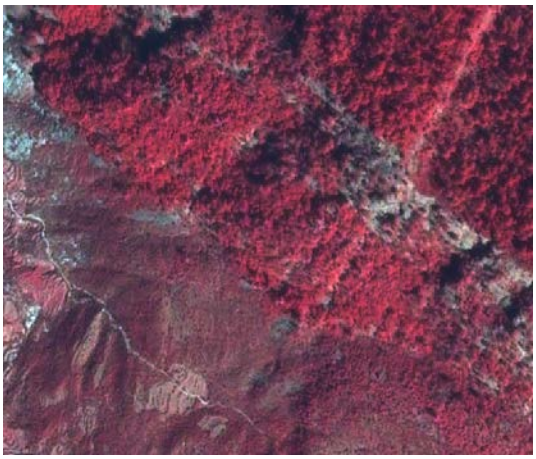

Figure 2.5.4: SPOT-7 reference image, pre-landslide

Figure 2.5.5: SPOT-6 crisis image, post-landslide

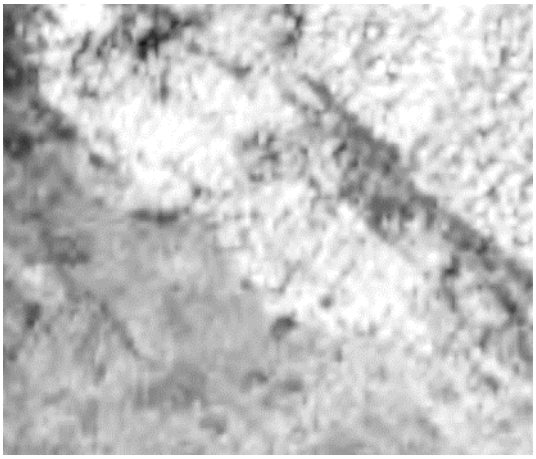

Figure 2.5.6: reference NDVI

Figure 2.5.7: crisis NDVI

A threshold is applied on the result on NDVI difference computation (fig. 2.5.6). As the index used is normalised in theory the threshold should not have to change with a different set of data, on condition that there is vegetation in the reference image. This is important because the methodology has been built regarding the reproducibility of the process.

Complementary processing presented hereafter in the table 2.5.2 are necessary depending on the data acquisition parameters and are appended to the workflow in order to enhance the extraction either to detect missing landslides or to reduce false detection.

Table 2.5.2: Post-processing details

Error	Reason	Additional process	Specific conditions	Comments
Omission	Landslides not detected because of shadowed areas in reference image (low NDVI value)	Shadow index computed on the reference image, and specific NDVI multi-thresholds applied on shadowed areas	- VHR data - Low sun elevation - Steep relief (Himalaya)	Additional processing unnecessary on HR data
Commission	Detection of shadowed areas in the crisis image	Shadow index computed on the crisis image, post-processing to remove landslide detection within shadowed areas	- VHR data - Low sun elevation - Steep relief	Additional process unnecessary on HR data
	Detection of cropland vegetation in reference image and bare soils in the crisis data	Slope computed on SRTM DEM, post-processing removing 'landslide detection' within flat areas	- HR data (10-15m)	This process can be applied on VHR data only if a better DEM than SRTM is available because a lot of true detection would disappear due to the resolution of 90m.

Figure 2.5.8 shows how the specific process on shadowed areas fills parts of landslides not detected in the under-estimated preliminary results obtained via a single index threshold.

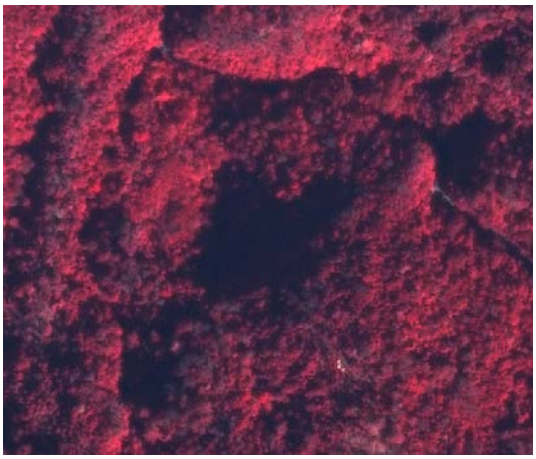

a) SPOT 7 reference image

b) SPOT 6 crisis image

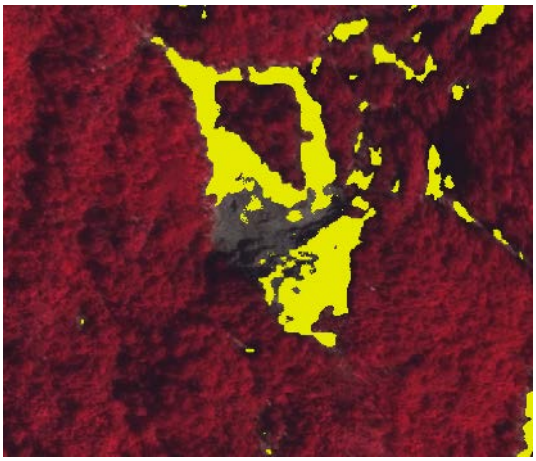

c) Landslide detection by a single threshold on pre/post disaster NDVI differences

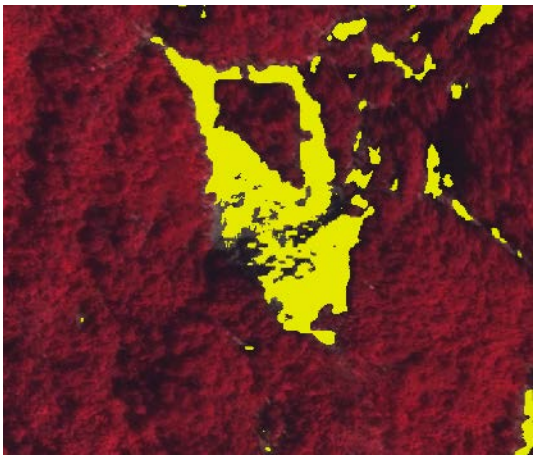

d) Landslide detection using two thresholds on NDVI pre/post disaster indexes depending on the presences of reference image shadows

Figure 2.5.8: Added detection of landslides in shadowed parts of reference image.

Figure 2.5.9 shows how the post-processing using slope information removes false alarms within flat areas linked to the change detection of vegetation disappearing within land parcels between the images.

a) Landsat 8 crisis image

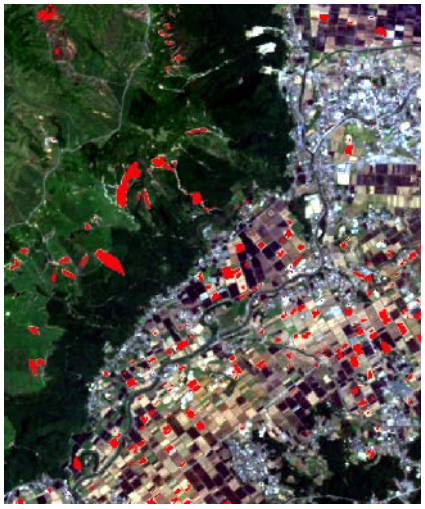

b) Landslide detection by a single threshold on pre/post disaster NDVI differences (red)

c) Landslide detection after false detection removal by a post-process using slope information (red)

Figure 2.5.9: Removal of crops detection by post-processing.

The workflow applied on the two test sites is based on the same change detection method but complementary processes adapted to the data in input are appended in order to enhance the results as already indicated in table 2.5.2. Moreover the geometric correction phase is unnecessary in the

case of data delivered or downloaded already co-registered. Therefore, the landslide detection workflow has different options depending of the data and the area processed (resolution, relief, and season). One workflow per test site is established:

- firstly to process VHR data which could include shadowed areas in both reference and crisis image,
- secondly to process HR data and specifically images acquired by Landsat-8 and Sentinel-2 sensors which offer systematic acquisitions and data free access (fig. 2.5.10). Figure 2.5.11 shows the results of the processing chain applied on Landsat-8 images.

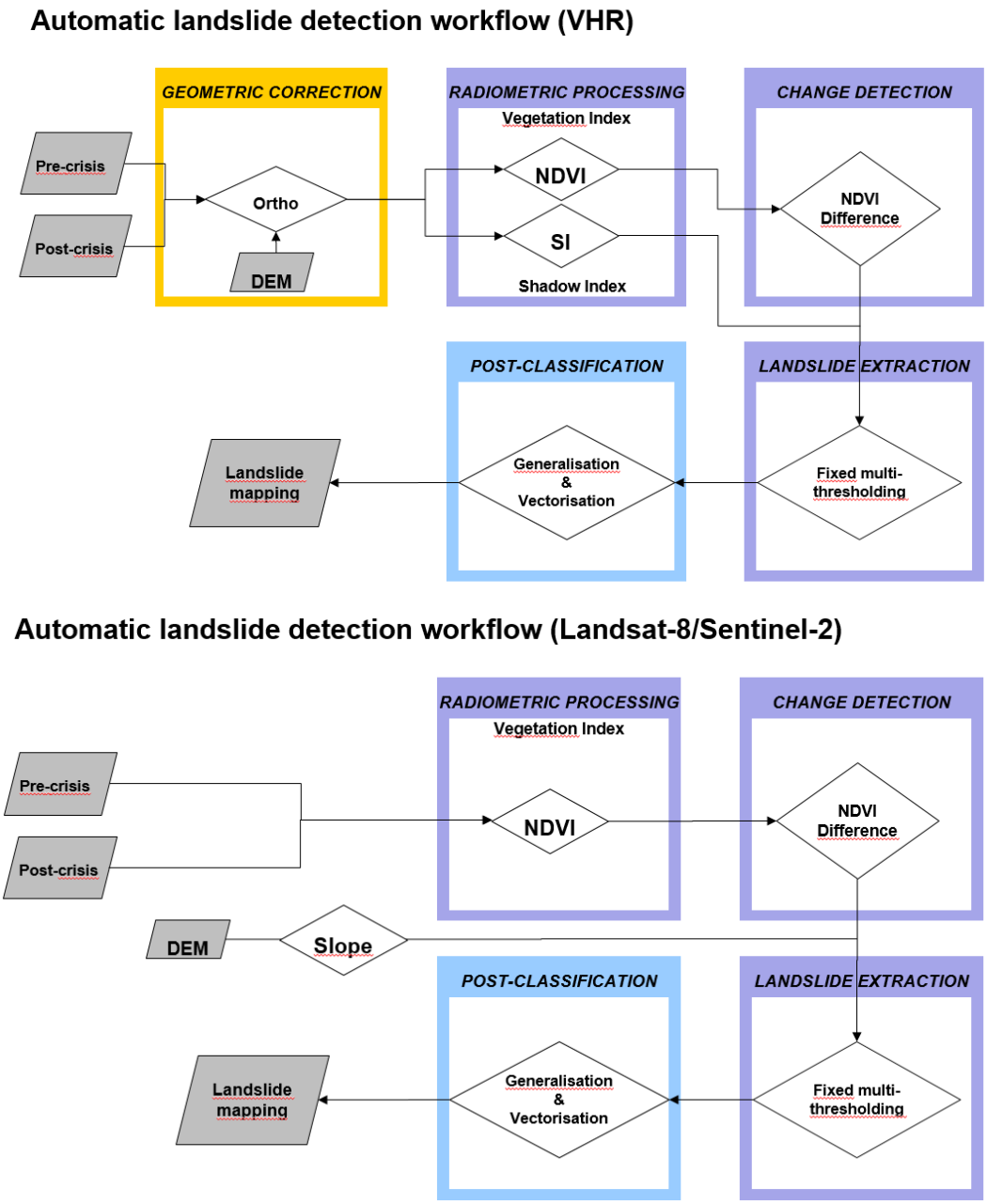

Figure 2.5.10: Automatic landslide detection workflows.

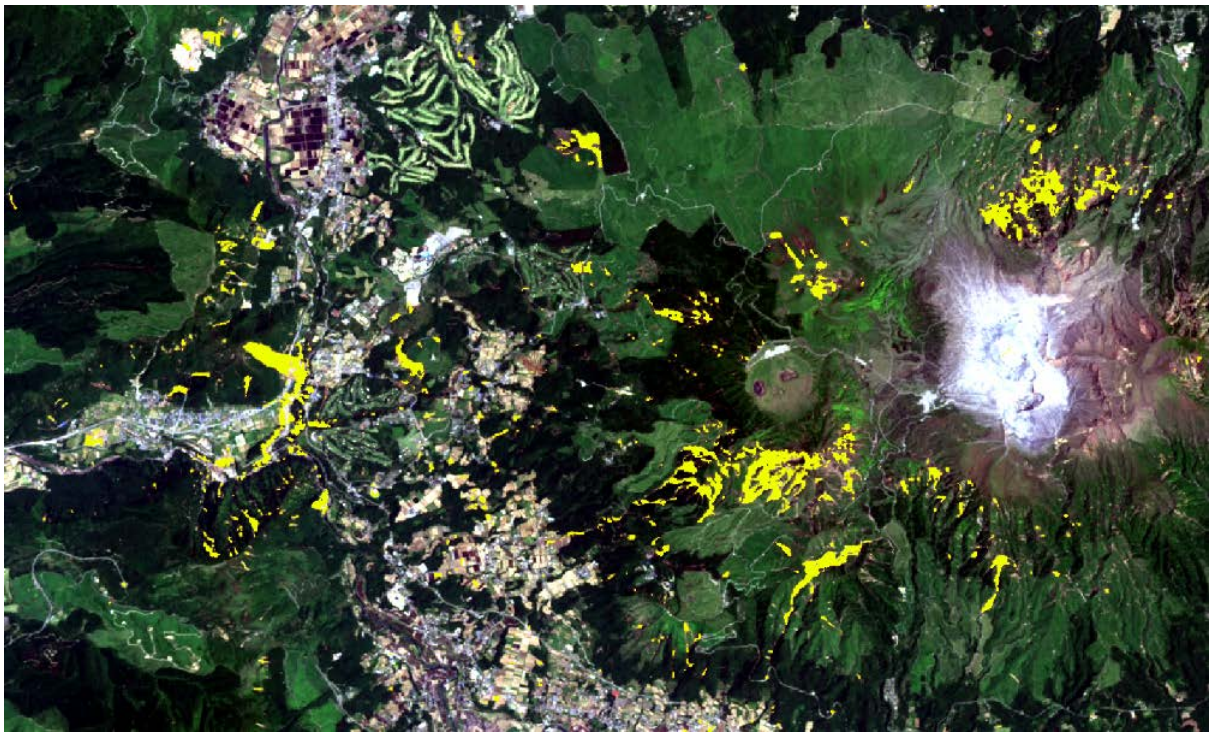

Figure 2.5.11: Automatic landslide detection in yellow, output of the workflow applied on Landsat-8 data.

2.5.1.3 Results summary and perspectives

Process chain implementation

The development of a fast and transferable landslide detection procedure by applying change detection methods between a pre- and post-event optical dataset has been successful. The method is implemented in OTB as a macro script and in SPRINGBOX to enhance the speed of execution with the objective being to create a robust, exhaustive method producing an intermediary landslide layer for further validation. SPRINGBOX is a guided user interface (GUI) developed by CNES and allowing to call tools from extern libraries such as OTB or GDAL with parameters. Using this GUI makes it easier to disseminate the developed tool in a production environment especially for people not comfortable with script languages. Figure 2.5.12 shows how the process chain looks like within the SPRINGBOX interface.

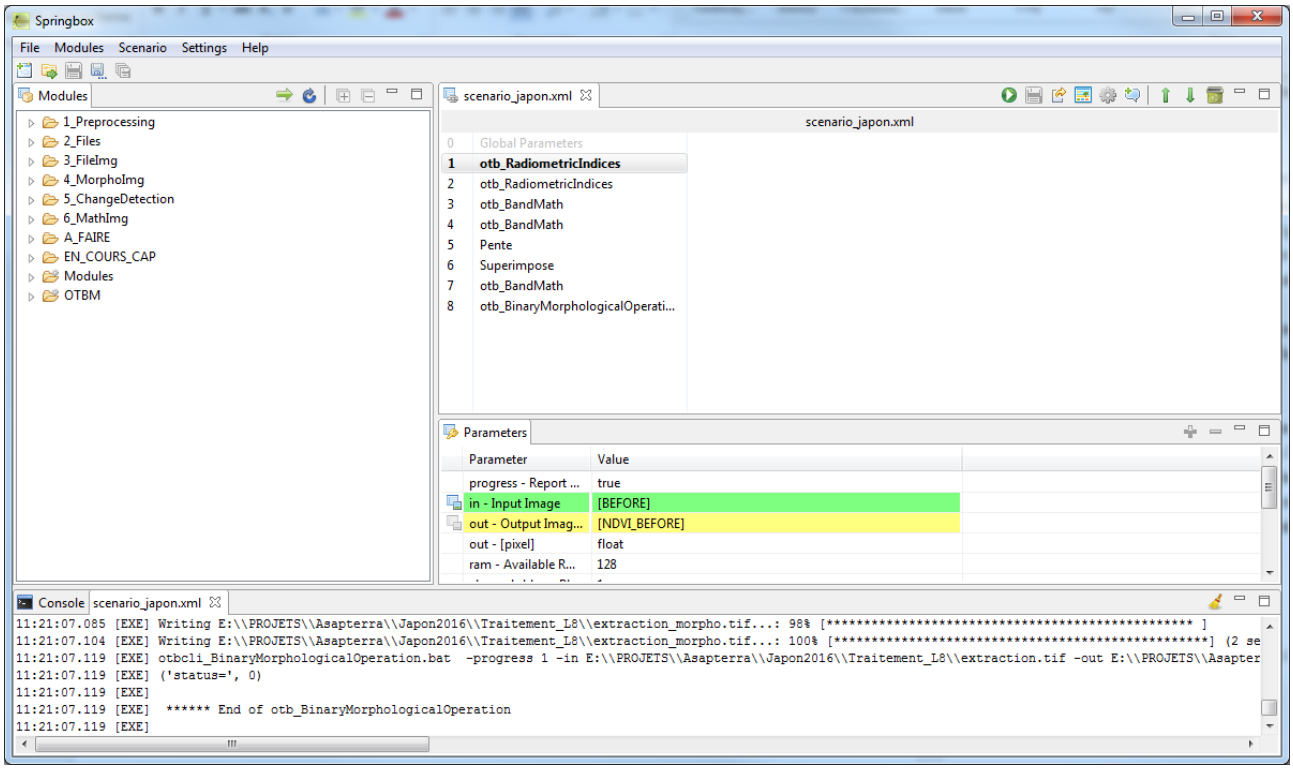

Figure 2.5.12: Automatic landslides detection chain within SPRINGBOX interface

The landslide detection procedure has been applied over a Nepal site close to Gumda, North of Kathmandu and over a Japan site in Kyushu Island. Based on a change detection method using NDVI differences, the workflow includes optional complementary processes to run in some specific cases (shadowed areas within VHR data, commission in flat areas) in order to enhance the results.

Results validation and analysis

Table 2.5.3: Results validation

Test site	Data	User accuracy (%)	Producer accuracy (%)	Automatic process timing	Timing of obvious false detection removal	Clouds perturbation
Nepal	Spot 6/7	75	81	20 min	15 min	Yes
Japan	Landsat-8	94	72	9 min	-	No
Japan	Sentinel-2	76	84	28 min	5 min	Yes

Over Nepal user's and producer's accuracies of 75 % and 81%,% respectively, were obtained from results in output from a process including 20min of fully automatic processing and 15min of validation by photointerpretation to reject obvious false detection (clouds, shadows). Statistics are computed using as validation a landslide layer built by photointerpretation of SPOT6/7 images.

Over the Japanese test site, a VHR image acquired the 16th of April 2016 available through the Google Satellite WMS layer has been used for validation.

Curiously the higher the resolution is the less accurate is landslide detection. Several reasons can explain those results:

- Co-registration between pre and post event images over Nepal is not as good as Landsat-8 and Sentinel-2 couples. Of course Himalaya Mountains present an extreme relief but in general co-registration problems are avoided or at least reduced working on Landsat-8 and Sentinel-2 images couples delivered already co-registered;
- Shadowed areas observed in VHR images make more complex the landslides detection process, especially in the Himalaya Mountains;
- Results obtained from Sentinel-2 images are not as accurate as we could expect and should be more accurate than Landsat-8, but the crisis Sentinel-2 image is very cloudy and indeed more complex to process. Moreover the acquisition date is almost 4 months after the disaster and the image used for validation, work has already been done to clean up affected areas.

Conclusion and perspectives

A generic process chain to map landslides has been set up based on a change detection method which gave good results in three study cases. Meanwhile complementary post-processing is necessary either to detect missing landslides in shadowed areas which are could not be negligible in very high resolution imagery, or to remove false detection in flat areas.

Results are very good, especially when acquisitions conditions are optimal (no geometry problems, cloud free) in the case of Landsat-8 data processing. Moreover the lower the resolution is, the faster is the calculation timing (less than 10min for 15m resolution data).

Sentinel-2 images are very promising to map landslides and could give better results than Landsat-8 thanks to the 10m resolution data without pan-sharpening but the dataset available is not optimal. Actually the crisis image is very cloudy and has been acquired too late. No other sooner post-event acquisition is exploitable and no other Sentinel-2 dataset cover large landslides at this moment to perform an advanced test. This could be interesting in a near future to exploit the coverage, the high frequency acquisitions and the 10m resolution within emergency mapping operations.

2.5.2 SAR-based landslide detection in rural areas

2.5.2.1 State-of-the-art

Rapid damage mapping after natural disasters, such as landslides, is crucial, i.e. to detect the affected area, including grade and type of damage. Thereby, SAR remote sensing plays an important role, as with its day-and-night availability and almost complete weather independency, SAR imagery for a dedicated area of interest is in most cases earlier available after landslide triggering events such as heavy rainfalls than the first useful (cloud-free) optical imagery (Christophe et al. 2010). Moreover, contrary to optical sensors being more sensitive to the chemical structure of the ground targets, the larger wavelength of SAR sensors enables the investigation of the physical characteristics of the objects on the ground, i.e., SAR is sensitive to the surface roughness, its moisture content and for geometric structures, whereas the last aspect is very critical for damage assessment (Arciniegas et al. 2007).

Plank (2014) provides a comprehensive review on rapid damage assessment using multi-temporal SAR, emphasizing especially the opportunities provided by the Sentinel-1 mission.

Within the ASAPTERRA project the focus is on the development of methods for post-failure landslide detection, especially the detection of shallow landslides of unconsolidated rock (e.g. debris slide, debris flows, debris spread, etc.).

According to Yonezawa et al. (2012) and Joyce et al. (2014), a single-temporal post-event SAR imagery is not useful for landslide detection, as the backscatter signal cannot be associated with the mixed features in a landslide such as exposed soils and fallen vegetation. The SAR backscatter is influenced by the dielectric parameters and roughness of the surface. In case of a landslide these parameters change in an unpredictable way due to complexity and variability of the environment. This statement of Joyce et al. (2014) is especially true for single polarised SAR imagery, as polarimetric SAR imagery enables more detailed land cover classification and assuming the availability of pre-event land cover information, also the detection of changes due to e.g. landslides (Czuchlewski et al. 2003).

In general two different approaches can be distinguished: (I) SAR data-based change detection, requiring the availability of pre- and post-event SAR imagery, and (II) polarimetric SAR (PolSAR) data-based landslide detection, enabling landslide detection based on only post-event SAR imagery.

The multi-temporal approach (I) requires the pre-disaster image or image pair to be recorded shortly before the landslide event and the post-disaster image shortly after the event. Thereby, the temporal baseline between all acquisitions should be as small as possible to decrease the influence of changes (e.g. temporal de-correlation) not caused by the landslide itself. All three images have to be acquired at the same imaging geometry (i.e., same pass direction (ascending/descending), relative orbit, imaging mode, incidence angle and SAR wavelength) (Plank 2014).

Three different kinds of change detection procedures can be distinguished:

a) Pre-classification change detection based on the amplitude of the SAR image

b) Pre-classification change detection based on the interferometric coherence
c) Post-classification change detection based on classification results derived from PolSAR imagery (described in detail below)

Assuming the availability of one useful pre-event SAR acquisition (see prerequisites above), approach (a) – change detection based on the SAR amplitude – can be applied. Thereby, the change (e.g. a landslide) between the pre- and the post-event image can be detected by e.g. image differencing or image ratioing (Lu et al. 2004).

Joyce et al. (2014) states that approach (b) – change detection based on the interferometric coherence – provides in general more accurate results than approach (a). However, the interferometric based change detection requires the availability of three SAR images: a pair of pre-event SAR data and at least one post event SAR acquisition (see prerequisites above). Two coherence maps are generated: One using the two pre-event images and one between the second pre-event image (shortly acquired before the event) and the post-event acquisition (Plank 2014). The difference between the two coherence maps is calculated. This double-differencing approach removes coherence variability due to temporal changes (vegetation and land cover) and emphasizes changes that are uncommon to both coherence maps, such as landslides (Joyce et al. 2014). Christophe et al. (2010) used a time-series of L-band ALOS PALSAR imagery for interferometric coherence based landslide detection.

A similar approach is reported by Kawamura et al. (2011) who detected landslides after the 2009 Sumatra Earthquake, Indonesia, based on post-event TerraSAR-X imagery. The interferometric coherence was used to distinguish between forest areas (low coherence values) and possible landslides characterised by bare soil areas (high coherence values).

Friedl and Hölbling (2015) developed a post-event landslide detection methodology based on single-pair SAR interferograms and coherence imagery using an object-based image analysis (OBIA) approach.

Simons et al. (2015) and Yun et al. (2015) report a rapid imaging and analysis procedure for damage assessment after natural hazards, such as landslides, based on the interferometric coherence.

Polarimetric SAR imagery (PolSAR) enables an improved classification of the land cover compared to single polarised SAR data (Calbe et al. 2014). Objects on the ground characterised by different structures and geometries show different backscatter characteristics at different SAR polarisations. Based on physical assumptions, polarimetric decomposition procedures aim to separate these different backscatter types. Especially in warm and humid regions, slopes are mostly covered by vegetation (e.g. forest), which characterises as volume scatter of the SAR signal. Contrary to this, a landslide is characterised by bare soil, a surface scatterer. Consequently, after a landslide event the surface component of the SAR backscatter increases while the volume component decreases (Rodriguez et al. 2002, Czuchlewski et al. 2003, Shibayama and Yamaguchi 2014).

However, landslides are very complex features. For instance fallen vegetation within the landslide area increases the volume component and decreases the surface component of the SAR backscatter, making the differentiation of landslides and the surrounding vegetated areas more difficult (Joyce et al. 2014). Moreover, the type of backscattering strongly depends on the SAR wavelength. The longer the wavelength, the stronger is the penetration of the SAR signal into vegetated areas. X-band at wavelength λ = 3.1cm is mostly backscattered at the top of the canopy, while the longer L-band SAR waves (λ = 23.5cm) penetrate the canopy and interact with the tree trunks and the ground (Bamler and Hartl 1998). For instance, Dabbiru et al. (2013) compared the results of dual-pol X-band (TerraSAR-X) and dual-pol L-band (UAVSAR) analysis and reported more accurate results when using the longer wavelength. Also Shimada et al. (2014) reported much better results when using L-band compared to X-band. Nevertheless, Li et al. (2014) reported good results for landslide detection after the 2008 Wenchuan Earthquake, China, using airborne VHR full-pol X-band SAR imagery.

The most often used polarimetric decomposition approaches for landslide detection reported in the literature are:

a) The eigenvalue and eigenvector based Entropy/Anisotropy/Alpha ($H/A/\alpha$) decomposition proposed by Cloude and Pottier (1997): The α angle, ranging from 0° to 90°, describes the type of backscattering. Very small α values indicate domination of surface scattering, high α values represent domination of double bounce scattering (caused by either urban area or tree trunks) and α values at around 45° show domination of volume scattering (e.g. vegetation). The entropy H, representing the heterogeneity of the scattering, ranges from 0, indicating a pure target (e.g., a dominant scatterer such as a corner reflector) to 1, representing a random mixture of scattering mechanisms (e.g., forest). The anisotropy A enables the investigation of the relationship between the second and third dominant backscattering mechanism.
b) The model-based 3-component Freeman-Durden decomposition (Freeman and Durden 1998): This decomposition derives for each resolution cell the power of the three different scattering types: surface, double-bounce and volume scattering.
c) The model-based 4-component Yamaguchi decomposition (Yamaguchi et al. 2005): A further development of the 3 component Freeman-Durden decomposition providing an additional backscattering type: Helix.

Full (quad) polarimetric SAR data provides much more information than dual-polarimetric imagery. Therefore, most studies reported in the literature are based on full-pol data. For dual-pol SAR imagery only the decomposition (a) – $H/A/\alpha$ – can be used (Plank et al. 2014).

Czuchlewski et al. (2003) and Yonezawa et al. (2012) found low α and H values for landslide and high α and H values for forested areas, confirming the increase of surface and decrease of volume scattering after a landslide event (of a formerly forested area). The anisotropy A did not provide useful information for landslide detection. The $H/A/\alpha$-based decomposition and the hereon based unsupervised Wishart classification (Lee et al. 1999) enabled the differentiation of landslides from

forests, water, snow, etc., but did not perform well when differentiating between landslides and farmland. Therefore, Czuchlewski et al. 2003, Yonezawa et al. (2012) and Shibayama and Yamaguchi (2014) suggest the use of pre-event land cover information and DEM data (to exclude moderate slopes where landslides rarely happen) to reduce errors of commission. If this ancillary data is available, landslide detection based on only post-event PolSAR data is much more accurate.

Meng et al. (2014) reported good results for landslide detection in the Three-Gorges Area, China, using the unsupervised Wishart classification based on the Freeman-Durden 3-component decomposition (using RADARSAT-2 full-pol data).

Watanabe et al. (2012), Yamaguchi (2012) and Shibayama and Yamaguchi (2013, 2014) demonstrated accurate landslide detection by full pol ALOS-PALSAR (L-band) pre- and post-event imagery using the Yamaguchi 4-component decomposition.

Besides these most often used decompositions mentioned above, also other parameters are reported in literature for landslide detection. For instance Czuchlewski et al. (2003) used the Radar Vegetation Index (RVI) developed by Kim and Van Zyl (2002) for quad-pol data and developed an adapted RVI useful for co-cross-dual-pol data (HH/HV). High RVI values indicate forest, low RVI values landslide area.

Furuta and Sawada (2013) used pre- and post-event dual and quad-polarimetric ALOS-PALSAR imagery for landslide detection in vegetated areas by computing the difference of the phase coherences between the co-co-pol channels (HH and VV) of the two acquisitions.

Plank et al. (2015) reported first results of a new landslide detection methodology developed within the ASAPTERRA project (see section 2.5.2.2 for more details).

References

1. Arciniegas, G.A., Bijker, W., Kerle, N. and Tolpekin, V.A., 2007: Coherence- and amplitude-based analysis of seismogenic damage in Bam, Iran, using ENVISAT ASAR data. IEEE Transactions on Geoscience and Remote Sensing, 45, 1571-1581.
2. Bamler, R. and Hartl, P., 1998: Synthetic aperture radar interferometry. Inverse Problems, 14, 1-54.
3. Calbe, J.W., Kovacs, J.M., Shang, J. and Jiao, X., 2014: Multi-Temporal Polarimetric RADARSAT-2 for Land Cover Monitoring in Northeastern Ontario, Canada. Remote Sensing, 6, 2372-2392.
4. Christophe, E., Chai, A.S., Yin, T. and Kwoh, L.K., 2010: 2009 Earthquakes in Sumatra: The Use of L-band Interferometry in a SAR-Hostile Environment. In Proceedings of the IEEE IGARSS, Honolulu, HI, USA, 25–30 July 2010, 1202-1205.
5. Cloude, S.R. and Pottier, E, 1997: An entropy based classification scheme for land applications of polarimetric SAR. IEEE Transactions on Geoscience and Remote Sensing, 35, 68-78.
6. Czuchlewski, K.R., Weissel, J.K. and Kin, Y., 2003: Polarimetric synthetic aperture radar study of the Tsaoling landslide generated by the 1999 Chi-Chi earthquake, Taiwan. Journal of Geophysical Research, 108(F1), 10 pp.

7. Dabbiru, L., Aanstoos, J.V., Hasan, K., Younna, N.H., Li, W., 2013: Landslide Detection on Earthen Levees with X-band and L-band Radar Data. In IEEE Applied Imagery Pattern Recognition Workshop Sensing for Control and Augmentation (AIPR), 5 p.
8. Freeman, A. and Durden, S.L., 1998: A three-component scattering model for polarimetric SAR data. IEEE Transactions on Geoscience and Remote Sensing, 36, 963-973.
9. Friedl, B. and Hölbling, D., 2015: Using SAR Interferograms and Coherence Images for Object-Based Delineation of Unstable Slopes. Fringe 2015, 23.-27. March 2015, Frascati, Italy.
10. Furuta, R. and Sawade, K., 2013: Case Study of Landslides Recognition using Dual/Quad Polarisation data of ALOS/PALSAR. In Proceedings of the Asia-Pacific Conference on Synthetic Aperture Radar (APSAR), 481-484.
11. Joyce, K.E., Samsonov, S.V., Levick, S.R., Engelbrecht, J. and Belliss, S., 2014: Mapping and monitoring geological hazards using optical, LiDAR, and synthetic aperture RADAR image data. Natural Hazards, 73, 137-163.
12. Kim, Y. and van Zyl, J., 2002: Comparison of forest estimation techniques using SAR data. In IEEE 2001 International Geoscience Remote Sensing Symposium, vol. 3, 1395-1397.
13. Kawamura, M., Tsujino, K., Tsujiko, Y. and Tanjung, J., 2011: Detection Method of Slope Failures Due to the 2009 Sumatra Earthquake by Using TerraSAR-X Images. In Proceedings of the IEEE IGARSS, Vancouver, BC, Canada, 24–29 July 2011, 4292-4295.
14. Li, N., Wand, R., Deng, Y., Liu, Y., Wang, C., Balz, T. and Li, B., 2014: Polarimetric Response of Landslides at X-Band Following the Wenchuan Earthquake. IEEE Geoscience and Remote Sensing Letters, 11(10), 1722-1726.
15. Lee, J.S., Grunes, M.R., Ainswort, T.L., Du, L.J., Schuler, D.L. and Cloude, S.R., 1999: Unsupervised classification using polarimetric decomposition and the complex Wishart classifier. IEEE Transactions on Geoscience and Remote Sensing 37, 2249-2258.
16. Lu, D., Mausel, P., Brondízio, E. and Moran, E., 2004: Change detection techniques. International Journal of Remote Sensing, 25(12), 2365-2401.
17. Meng, Y., Lan, H. and Ping, B., 2014: Landslide deformation monitoring and location identification with polarimetric SAR in Three Gorges regions. In Proceedings of the IEEE IGARSS, Québec, Canada, 13–18 July 2014, 418-421.
18. Plank, S., 2014: Rapid Damage Assessment by Means of Multi-Temporal SAR — A Comprehensive Review and Outlook to Sentinel-1. Remote Sensing, 6, 4870-4906.
19. Plank, S., Mager, A. and Schoepfer, E., 2014: Monitoring of Oil Exploitation Infrastructure by Combining Unsupervised Pixel-Based Classification of Polarimetric SAR and Object-Based Image Analysis. Remote Sensing, 6, 11977-12004.
20. Plank, S., Hölbling, D., Eisank, C., Friedl, B., Martinis, S. and Twele, A., 2015: Comparing object-based landslide detection methods based on polarimetric SAR and optical satellite imagery – a case study in Taiwan. 7th International Workshop on Science and Applications of SAR Polarimetry and Polarimetric Interferometry, POLinSAR 2015, 27.-30. Jan. 2015, Frascati, Italiy, 5 p.
21. Rodriguez, K.M., Weissel, L.K. and Kim, Y., 2002: Classification of Landslide Surfaces Using Fully Polarimetric SAR: Examples from Taiwan. In Proceedings of the IGARSS, Toronto, Canada, 24–28 June 2002, 2918-2920.
22. Shibayama, T. and Yamaguchi, Y., 2013: An application of polarimetric radar analysis on geophysical phenomena. In Proceedings of the IEEE IGARSS, Melbourne, Australia, 21–26 July 2013, 3191-3194.

23. Shibayama, T. and Yamaguchi, Y., 2014: A landslide detection based on the change of scattering power components between multi-temporal PolSAR data. In Proceedings of the IEEE IGARSS, Québec, Canada, 13–18 July 2014, 2734-2737.
24. Shimada, M., Watanabe, M., Motooka, T., Ohki, M. and Wada, Y., 2014: PALSAR-2 and Pi-SAR-L2 – Multi frequency Polarimetric Sensitivity on Disaster. In Proceeding of the EUSAR 2014, 93-94.
25. Simons, M., Owen, S., Hua, H., Yun, S.-H., Agram, P., Sacco, G.F., Webb, F., Rosen, P., Lundgren, P., Fielding, E.J., Manipon, G., Moore, A., Liu, Z., Milillo, P., Riel, B.V., Milillo, G., Cruz, J., Polet, J. and Samsonov, S., 2015: Using SAR and GPS for Hazard Management and Response: Progress and Examples from the Advanced Rapid Imaging and Analysis (ARIA) Project. Fringe 2015, 23.-27. March 2015, Frascati, Italy.
26. Wanatabe, M, Yonezawa, C., Iisaka, J. and Sato, M, 2012: ALOS/PALSAR full polarimetric observations of the Iwate–Miyagi Nairiku earthquake of 2008. International Journal of Remote Sensing, 33(4), 1234-1245.
27. Yamaguchi, Y., Yajima, Y. and Yamada, H., 2005: Four-component scattering model for polarimetric SAR image decomposition. IEEE Transactions on Geoscience Remote Sensing, 43, 1699-1706.
28. Yamaguchi, Y., 2012: Disaster Monitoring by Fully Polarimetric SAR Data Acquired With ALOS-PALSAR. Proceedings of the IEEE, 100(10), 2851-2860.
29. Yonezawa, C., Watanabe, M. and Saito, G., 2012: Polarimetric Decomposition Analysis of ALOS PALSAR Observation Data before and after a Landslide Event. Remote Sensing, 4, 2314-2328.
30. Yun, S.-H., Milillo, P., Simons, M., Owen, S., Webb, F., Fielding, E.J., Hua, H., Milillo, G., Coletta, A., Rosen and P., Dini, L., 2015: Interferometric Coherence for Rapid Disaster Response. Fringe 2015, 23.-27. March 2015, Frascati, Italy.

2.5.2.2 Texture analysis based landslide detection using polarimetric SAR – a case study in Taiwan

Introduction

First results of a new landslide detection methodology developed within the ASAPTERRA project have been published in Plank et al. (2015). This section gives a summary of the methodology and first results focusing on the SAR-based landslide detection procedure.

Objective of the study is the development of an object-based landslide detection procedure based on polarimetric SAR data applied to a test site in southern Taiwan. Object-based image analysis (OBIA) supports the integration of different datasets (e.g. SAR data, DEMs, etc.) and offers an efficient framework for the semi-automated analysis of complex natural features such as landslides, e.g. by its ability to consider spectral, spatial as well as contextual properties.

Study site and data

The approx. 25km² large study site is located around the Baolai village, Huaguoshan catchment, southern Taiwan. The landslides within the study area are mainly triggered by heavy rainfalls, which are brought along by typhoons, especially during summer season. The detection of the

landslides is based on a dual-polarimetric (HH/HV) TerraSAR-X SM imagery, acquired on 8 November 2010 (fig. 2.5.8). Additionally, a digital elevation model (DEM) with 5m spatial resolution, which was compiled from ortho-photos taken in 2003 and 2004, and therefrom derived products (e.g. slope) were used as ancillary data.

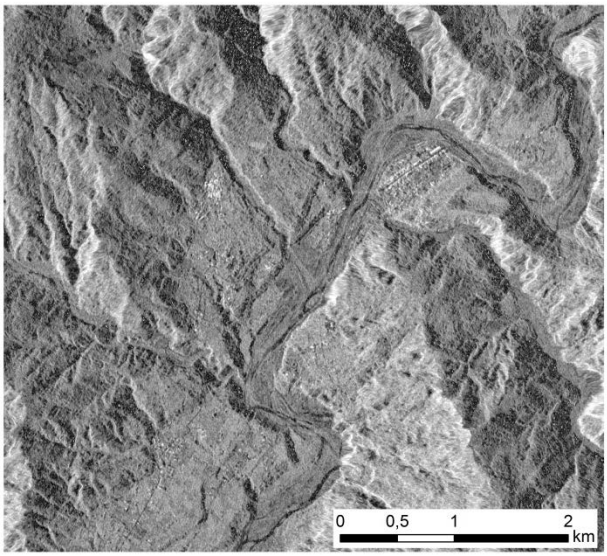

Figure 2.5.8: The calibrated HH channel of the TerraSAR-X imagery of the study area.

Method

The presented PolSAR-based landslide detection methodology makes use of the different backscattering signals of the land cover classes to be distinguished. I.e., in the cross-polarised channel (HV) forest and other vegetated areas are characterised by a much higher backscatter than bare soil, assumed as an indication for the occurrence of mass-movements and debris/sediment transport and deposition areas.

Procedure of the PolSAR-based landslide detection: First, speckle filtering of the PolSAR data using the refined Lee filter is applied. Then, after radiometric calibration (σ^0), the intensity information of both polarisation channels (HH and HV) is geocoded. Next, a newly developed OBIA procedure, making use of the different backscattering behaviour of forest as compared to bare soil (mass-movement indicator), is used to derive the features we are interested in from the PolSAR imagery (i.e. landslides, debris flows and river bed). An important indicator is the newly developed Normalised Difference Standard Deviation (NDSD) of the calibrated intensities of both polarimetric channels, HH and HV. Thereby, the OBIA procedure considers (a) the higher variation of the backscattering intensities in forest areas and (b) the relatively higher backscattering of vegetated areas in the cross-polarised channel compared to bare soil areas. To differentiate landslides and debris flows from the river bed (all features are characterised by the same polarimetric backscattering properties), slope information derived from a high resolution DEM is used (fig. 2.5.9).

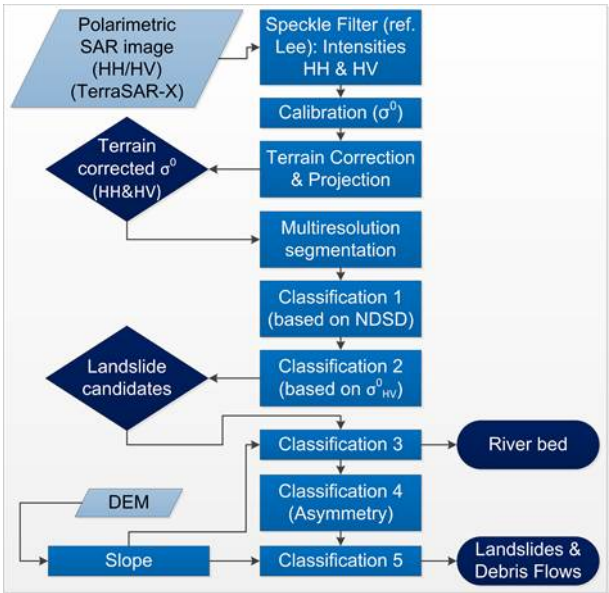

Figure 2.5.9: Workflow of the landslide detection procedure based on dual-pol SAR and DEM data.

Results and discussion

As reference for validation a dataset of landslides, debris flows and river beds produced through manual digitisation, performed by a local expert is used (fig. 2.5.10). The classification results were compared to the reference data to assess the spatial overlaps. Corresponding user's (UA) and producer's accuracy (PA) values were calculated.

Fig. 2.5.11 shows the results of the PolSAR based landslide detection procedure. Compared to the reference dataset, the methodology achieves a UA and PA of 60.3% and 27.9% for the landslides and debris flows combined, and 99.5% and 96.0% for the river bed, respectively. When focusing only on the detection of debris flows, its PA increases to 45.0% (while the UA remains stable).

The main challenges for the SAR based landslide detection methodology are the spatial distortions of SAR images caused by its 'range-azimuth' imaging geometry. Especially in foreshortening and layover areas, the detection of landslides and debris flows is complicated due to the strong backscatter of the SAR signal. Nevertheless, the result of the novel object-based method based on PolSAR data reveals a certain potential for landslide detection, especially for rapid assessment of affected areas after landslide triggering events.

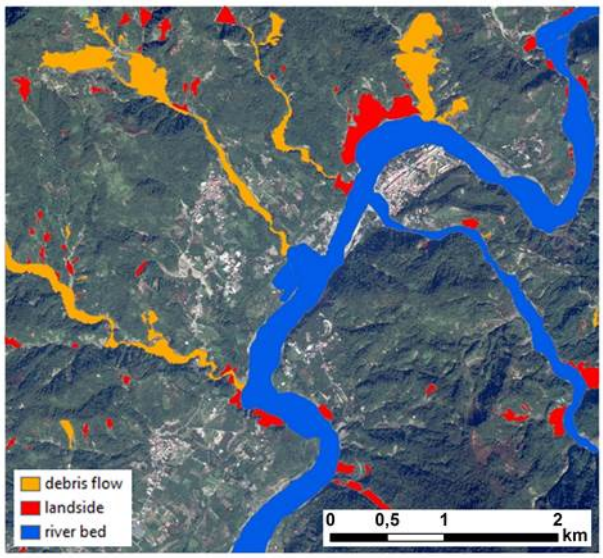

Figure 2.5.10: Reference (derived by manual digitisation by a local expert). Background QuickBird imagery (acquired 28 November 2010).

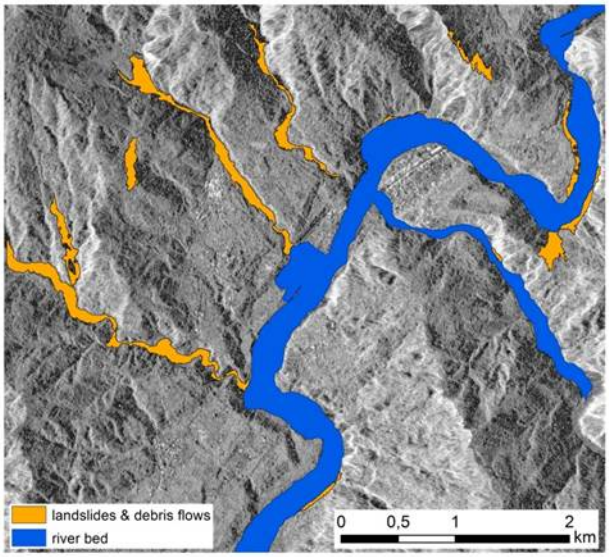

Figure 2.5.11: Result of the semi-automated OBIA method for landslide detection.

References

1) Plank, S., Hölbling, D., Eisank, C., Friedl, B., Martinis, S. and Twele, A., 2015: Comparing object-based landslide detection methods based on polarimetric SAR and optical satellite imagery – a case study in Taiwan. 7th International Workshop on Science and Applications of SAR Polarimetry and Polarimetric Interferometry, POLinSAR 2015, 27.-30. Jan. 2015, Frascati, Italiy, 5 p.

2.5.2.3 Entropy based landslide mapping by means of VHR post-event polarimetric SAR data

Introduction

This chapter presents a fast and transferable procedure for rapid mapping of landslides, with the advantage of requiring only post-event polarimetric SAR imagery supported by pre-event freely available and systematically acquired optical imagery of Landsat-8 or Sentinel-2. The methodology was successfully tested at two landslides of different characteristics: a rotational landslide at the Yeager Airport near Charleston, West Virginia, USA and a mining waste landslide event, which occurred on 1 April 2015 near Bolshaya Talda, Kemerovo Oblast, Russia.

Very High Resolution (VHR) archive SAR imagery recorded shortly before a landslide event is commonly not available. Modern VHR SAR missions such as TerraSAR-X, COSMO-SkyMed or RADARSAT-2 do not systematically cover the entire world. Each acquisition has to be programmed manually. Furthermore, due to limited disk space on board the satellites and especially due to limited downlink transmission rates, these sensors are not able to provide worldwide coverage within a short time period – i.e., no archive image recorded shortly before the event. Therefore, a methodology for rapid landslide mapping based on post-event polarimetric SAR data supported by pre-event freely available and systematically acquired optical imagery of Landsat-8 or Sentinel-2 was developed. A detailed description of the methodology and the results is presented in Plank et al. (2016)

Study sites and data

a) The Yeager Airport landslide, Charleston, West Virginia, USA

Since June 2013 movements at a slope nearby the Yeager Airport, 5km east of downtown Charleston in West Virginia, USA, were noticed. In the following time, the deformation increased. On 12 March 2015, the slope failed (fig. 2.5.12). A secondary failure of the slope occurred on 13th April 2015 (for details see: AGU landslide blog, http://blogs.agu.org/landslideblog/).

The available SAR data are two post-event TerraSAR-X HighResolution SpotLight (HS) dual-pol (HH/VV) imagery, acquired on 25 March 2015 (after the first slope failure) and on 16 April 2015 (after the second slope failure). In addition, one pre-event Landsat-8 imagery is available, acquired on 15 January 2015.

Figure 2.5.12: Left: Prefailure image of the Yeager Airport (STGEC). Right: After the first failure of the slope at the Yeager Airport (Charleston Daily Mail).

b) Mining waste landslide near Bolshaya Talda, Kemerovo Oblast, Russia

On 1 April 2015, a huge mining waste landslide occurred near Bolshaya Talda, Kemerovo Oblast, Russia. Two post-event TerraSAR-X HS dual-pol (HH/VV) SAR imagery acquired on 26 April and 7 August 2015 as well as one pre-event optical Landsat-8 image acquired on 14 September 2014 were available for the analysis.

Methodology

Assuming land cover changes due to the landslide event, i.e. destruction and removal of the vegetation cover (cf. fig. 2.5.13) the first step of our object-oriented procedure is the pre-selection of formerly vegetated areas based on the NDVI of freely available pre-event optical imagery (e.g. Landsat-8 or Sentinel-2). Next, after polarimetric speckle filtering using the edge-preserving refined Lee filter, the entropy/ alpha (H/α) decomposition is applied to the post-event polarimetric SAR image to detect, within the pre-selected areas, regions characterised by low entropy values, i.e. an evidence of bare soil or rock (landslide material). Then, assuming a certain minimum slope value as a necessary requirement for a landslide event, the landslide detection map is refined accordingly. As the Yeager Airport landslide took place on an artificial slope, which was constructed in the year 2007, the Shuttle Radar Topography Mission (SRTM) DEM from the year 2000 is too old and could not be used for the slope analysis at this site. Therefore, we used a bi-static TanDEM-X dataset acquired on 02 April 2014 to generate via SAR interferometric (InSAR) analysis an up-to-date DEM of 12 m spatial resolution. Therefore, a more accurate measurement of the pre-failure slope was obtained.

Analysis of optical imagery (Landsat, as well as GoogleEarth) showed that the second study site, i.e., the mining waste landslide in Russia, is a very dynamic area with lots of changes that occurred after the last TanDEM-X acquisition on 23 August 2012 over this area. Therefore, neither the SRTM DEM nor a TanDEM-X DEM could be used for slope analysis in this area.

Finally, to decrease the number of false classifications, all detected landslides smaller than a minimum mapping unit (MMU) of 30 m x 30 m are excluded.

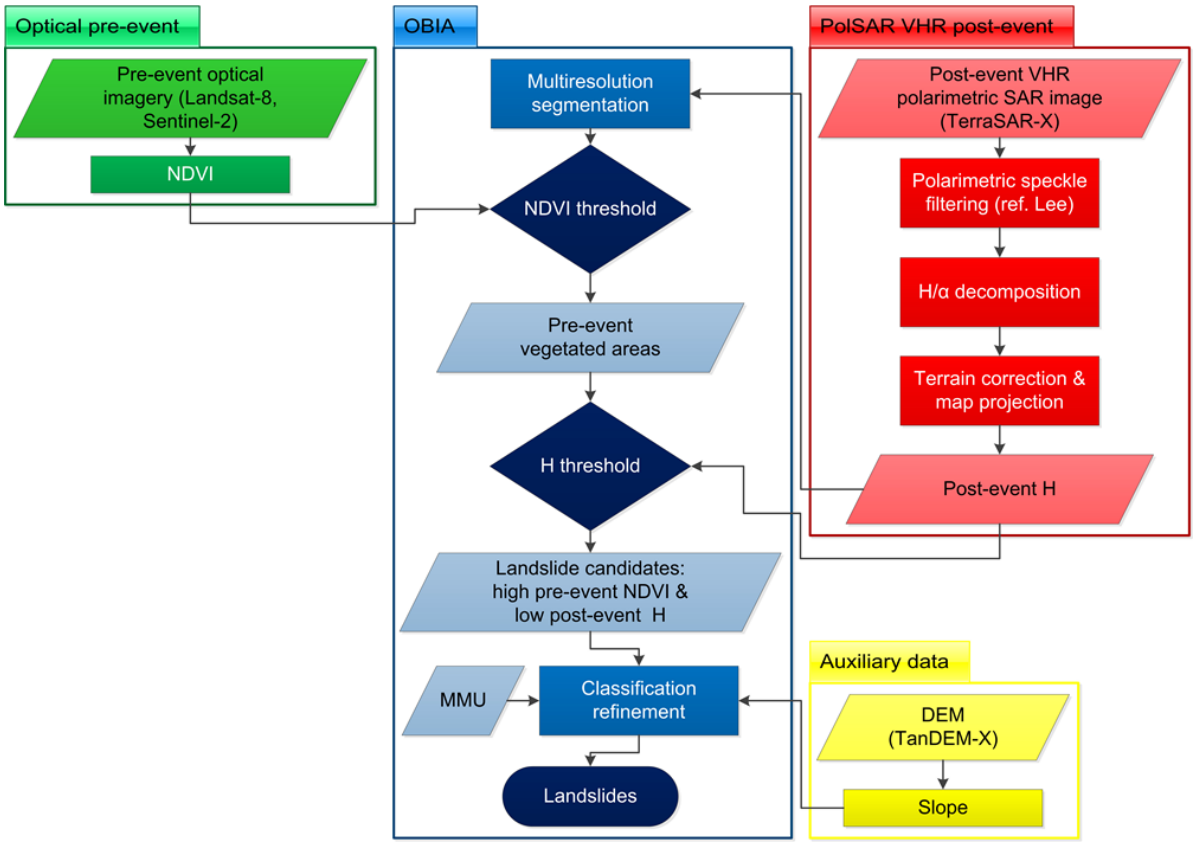

Figure 2.5.13: Workflow of the landslide detection procedure based on post-event polarimetric SAR and pre-event optical imagery.

Results and discussion

a) The Yeager Airport landslide, Charleston, West Virginia, USA

Figures 2.5.14 and 2.5.15 show the results of the developed landslide detection procedure based on pre-event optical Landsat-8 imagery and post-event polarimetric VHR SAR applied to TerraSAR-X imagery acquired on 25 March 2015 (after the first failure of the slope) and 16 April 2015 (after the second slope failure). Image in the background is the corresponding speckle filtered SAR image. Figures 2.5.14 and 2.5.15 show that the landslide is very well detected by the classification. In the SAR image acquired on 25 March 2015 one can also see a small false over classification in the western part of the image. At the SAR image acquired after the second slope failure the landslide detection procedure was able to detect the main part of the landslide. However, the scarp area of the landslide is not detected. Here, the second slope failure extended the scarp area of the landslide. At this very steep part, geometric distortions such as layover and foreshortening occur, changing the SAR backscattering values, which influence the landslide detection procedure.

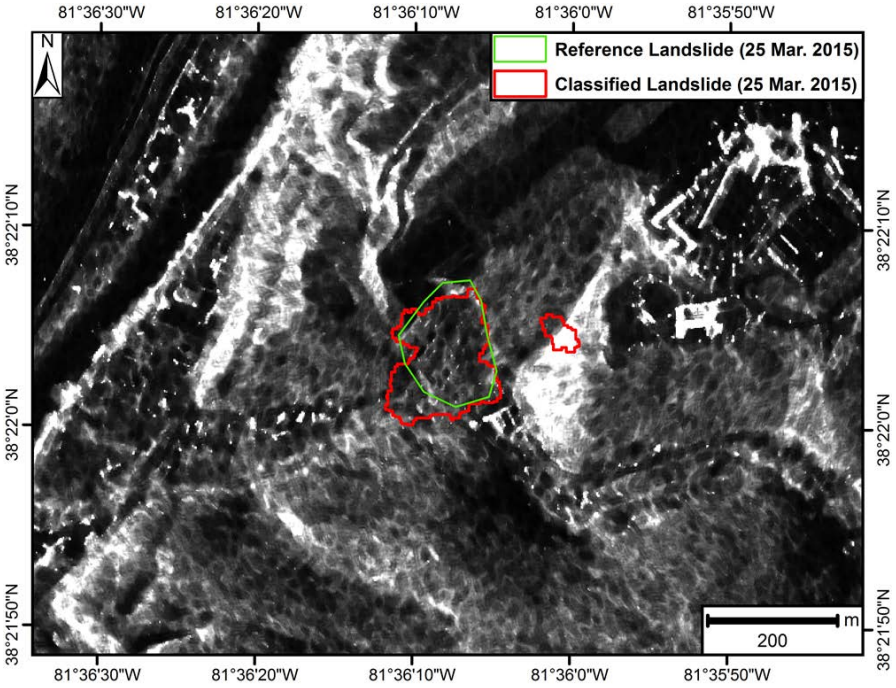

Figure 2.5.14: Result (red) of the landslide detection procedure at Yeager Airport based on post-event dual-pol TerraSAR-X (acquired on 25/03/2015; red) and pre-event Landsat-8 (15/01/2015) data. The green polygon marks the reference landslide derived by manual digitalisation.

Table 2.5.2 shows the accuracy values of the methodology applied to the Yeager Airport landslide at the two stages of the landslide event. The classification results are compared to a polygon of the landslide derived by visual interpretation of the SAR image and manual digitalisation. The overall accuracy (OA) as well as the values of the UA and PA of the class remaining are with 99.9% very high. This is due to a two class problem, i.e. landslide and remaining (areas not affected by landslides), with the percentage area of the latter being much higher than the percentage area coverage of landslide. Consequently, the interesting parameters of the accuracy assessment are the values of the UA and PA of the class landslides.

The good match between landslide classification result and the reference data shown in figure 2.5.14 for the SAR image acquired after the first slope failure is reflected by the high values of UA and PA of the landslide class with ca. 67.4% and 87.0%, respectively (cf. tab. 2.5.2). Contrary to this, classification results of the data acquired after the second slope failure show definitely lower values for OA and UA of the landslide class. The KHAT coefficient of the two SAR acquisitions shows a similar behaviour.

Table 2.5.2: Classification accuracies for the Yeager Airport landslide (12/03/2015 & 13/04/2015).

Date	OA	PA landslide	UA landslide	PA remaining	UA remaining	KHAT
25/03/2015	99.9%	87.0%	67.4%	99.9%	100.0.%	0.759
16/04/2015	99.9%	64.3%	66.9%	99.9%	99.9%	0.655

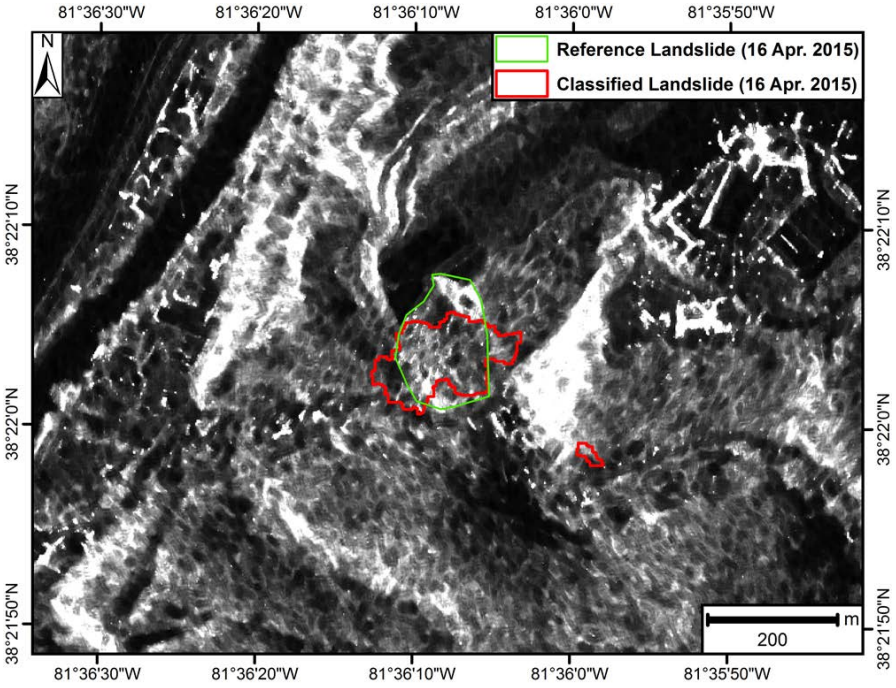

Figure 2.5.15: Result (red) of the landslide detection procedure at Yeager Airport based on post-event dual-pol TerraSAR-X (acquired on 16/04/2015; red) and pre-event Landsat-8 (15/01/2015) imagery. The green polygon marks the reference landslide derived by manual digitalisation.

b) Mining waste landslide near Bolshaya Talda, Kemerovo Oblast, Russia

Figure 2.5.16 shows a false colour composite pre-event Landsat-8 imagery acquired on 14 September 2014 of the mining waste site near Bolshaya Talda, Kemerovo Oblast, Russia.

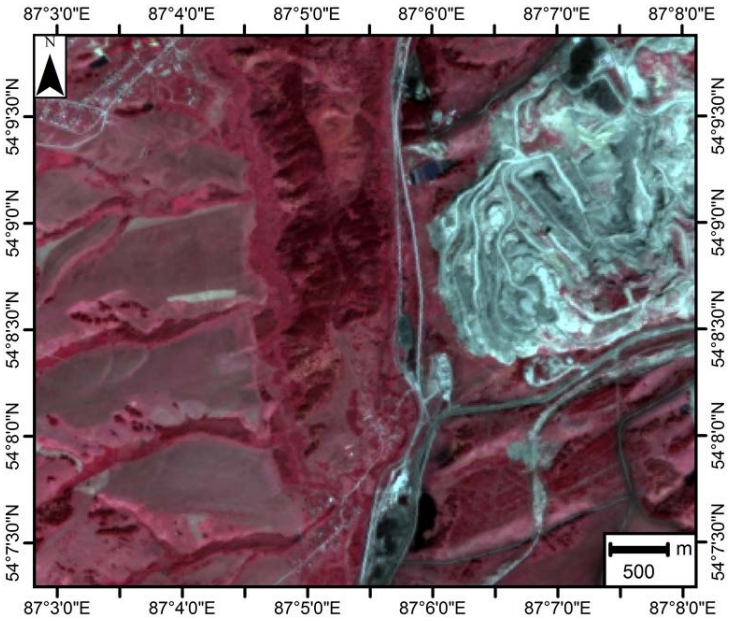

Figure 2.5.16: Landsat-8 pre-event imagery (14 September 2014) of the Russian mining waste site (NIR/Red/Green). The mining area (cyan) is free of vegetation.

The figures 2.5.17 and 2.5.18 show the corresponding classification results of the developed landslide detection procedure as well as the reference data derived by visual interpretation of the SAR image and manual digitalisation. Figures 2.5.17 and 2.5.18 clearly show that the developed methodology is only able to detect parts of the landslide. UA values of the class landslides are with ca. 90.0% very high, i.e. most of the classification results are correct. However, the low PA values (class landslides) show that only ca. 50.0% of the real landslide area was detected (tab. 2.5.3). The reason for this is that the methodology assumes that the landslide area was covered by vegetation before the landslide event. However, this is only true for the area at the foot of the landslide, where the landslide ran over an area outside of the mining waste area (formerly vegetated area) (landslide movement from east to west). The mining waste area itself is free of vegetation and shows therefore low NDVI values in the pre-event optical imagery (fig. 2.5.16). Therefore, the developed methodology is not able to detect the part of the landslide which occurred inside the mining waste area. Furthermore, also the entropy alone would only detect the entire mining waste area and not only the landslide area, as the entire mining waste area is characterised by low entropy, i.e. the area is free of vegetation (bare soil). When considering only the area outside of the original mining site as affected landslide area, the PA of the landslide class increases to 83%–90%, while the UA of the landslide class slightly decreases.

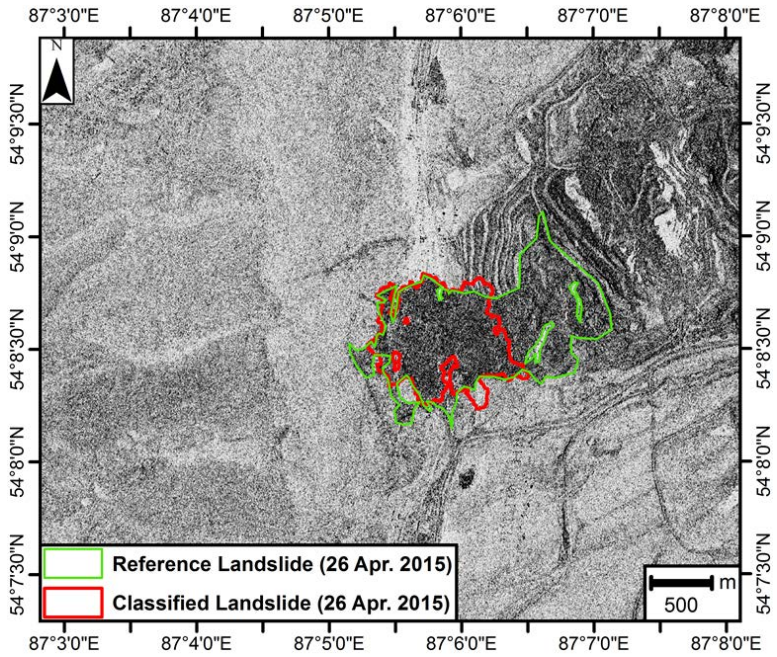

Figure 2.5.17: Red: Result of the landslide detection procedure at the Russian mining waste site based on post-event dual-pol TerraSAR-X (acquired on 26 April 2015) and pre-event optical Landsat-8 (14 September 2014) imagery. Green: Reference derived by manual digitalisation.

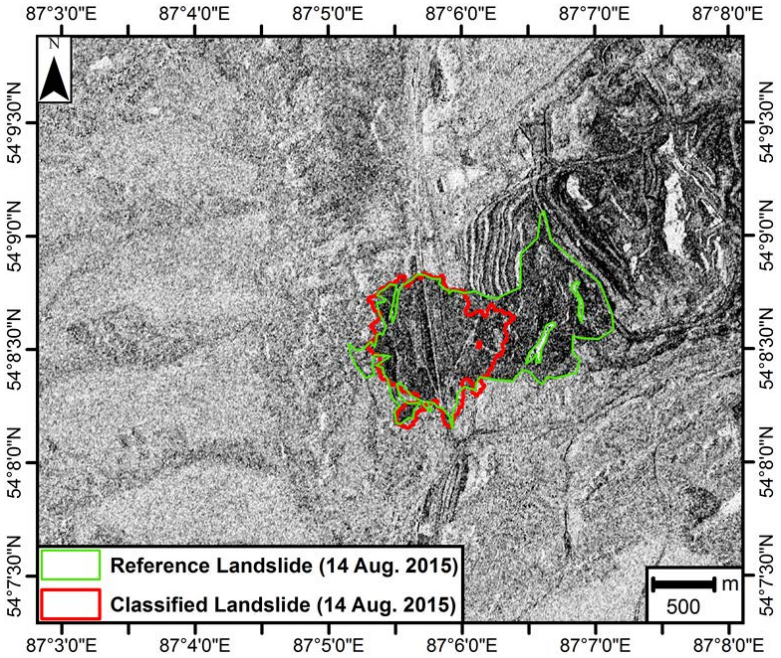

Figure 2.5.18: Red: Result of the landslide detection procedure at the Yeager Airport based on post-event dual-pol TerraSAR-X (acquired on 16/04/2015) and pre-event optical Landsat-8 (14/09/2014) imagery. Green: Reference derived by manual digitalisation.

The developed landslide detection methodology based on post-event polarimetric VHR SAR imagery showed promising accuracy values. However, the limitation of this methodology is that only landslides at slopes previously covered by vegetation can be detected.
The methodology and the results obtained are described in detail in Plank et al. (2016).

Table 2.5.3: Classification accuracies for the Russian mining waster landslide (01 April 2015). Lower two rows *: Only landslide material outside the original mining site is treated as a landslide.

Date	OA	PA landslide	UA landslide	PA remaining	UA remaining	KHAT
26/04/2015	96.8%	48.2%	89.6%	99. 7%	97.0%	0.612
14/08/2015	96.8%	49.7%	90.0%	99. 7%	97.0%	0.625
26/04/2015*	98.8%*	83.1%*	76.4%*	99.3%*	99.5%*	0.790*
14/08/2015*	99.1%*	90.0%*	81.6%*	99.4%*	99.7%*	0.850*

References

Plank, S., Twele, A., Martinis, S., 2016: Landslide Mapping in Vegetated Areas Using Change Detection Based on Optical and Polarimetric SAR Data. Remote Sensing, 8, 307.

2.5.2.4 Further concepts and results on landslide detection-based SAR imagery

Further developments and tests of new landslide detection procedures based on SAR imagery have been undertaken. Besides the two landslides described below, further test sites are currently analysed. Moreover, during the project we plan to react on actual large landslides events. An important information source about landslide events is the AGU Landslide Blog by Prof. Dave Petley (http://blogs.agu.org/landslideblog/).

a) The Domkar Monastery landslide in Qinghai, eastern Tibet

On 02 November 2014, a large rotational landslide at the Domkar Monastery (Qinghai, Tibet) occurred. According to Petley (AGU landslide blog, http://blogs.agu.org/landslideblog/), the landslide material appears to be loess. The available SAR data for the analysis of this landslide is a pre- and post-event image pair of Sentinel-1 IW data acquired on 17 October 2014 and 11 November 2014, respectively.

First, the pre- and post-event Sentinel-1 data were co-registered using ESA's Sentinel-1 Toolbox (S-1 TBX). Then, the co-registered data stack was terrain corrected based on a SRTM DEM using the Range-Doppler algorithm implemented in the S-1 TBX and projected to the corresponding UTM zone. Next, an automatic change detection procedure is applied to detect the landslide.

Fig. 2.5.19 shows first results of this change detection. Green colours represent stable (unchanged) areas. White coloured areas are affected by layover due to the steep terrain. The dark green line in the lower half of the image is a river. Red colours indicate an increase of the SAR backscatter in the post-event imagery compared to the pre-event acquisition. The landslide area is characterised by a strong increase of the SAR backscatter due to the chaotic structure of the landslide material. The black line marks the boundary of the landslide. The white and red dots in the west half of the study area is built up area (north of the river).

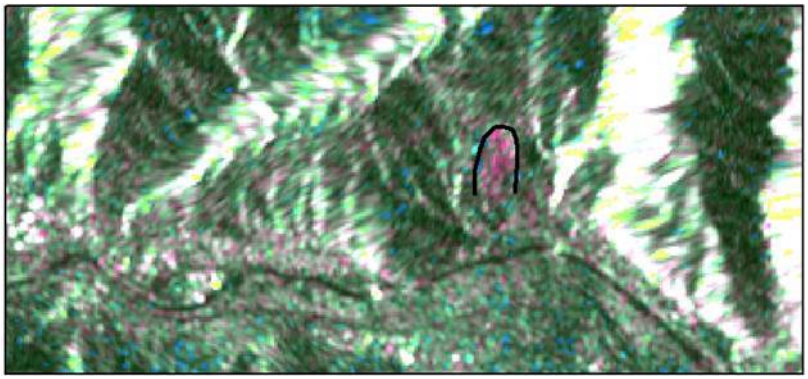

Figure 2.5.19: Landslide at Domkar Monastery (Qinghai, Tibet), detected by automatic change detection using pre- and post-event Sentinel-1 data. The black line marks the boundary of the landslide.

b) The Landslides triggered by the 2015 Nepal Earthquake

The great Earthquake in Nepal on 25 April 2015 (Magnitude 7.8), followed by hundreds of aftershocks and a second big event on 12 May 2015 (Magnitude 7.3) triggered many landslides. First analysis have been undertaken at a site at the city of Machhakholagon, located in the valley of Budhi Gandaki river, ca. 75 NW of Nepal's capital Kathmandu. At this site also landslide detection based on optical imagery has been done (cf. section 2.5.1).

The analysis is based on a data stack of Sentinel-1 SAR imagery. Two pre-event images acquired on 05 and 17 April 2015 as well as one post-event image acquired on 23 May 2015. After co-registration of all three images to a common master (05 April 2015) using the InSAR optimised co-registration of ESA's SNAP software (S-1 Toolbox module), two coherence pairs were computed:

- Pre-event image pair: 05 and 17 April 2015
- Co-event image pair: 05 April 2015 and 23 May 2015

The coherence has been calculated using different window sizes ranging from 2 (azimuth) times 8 (range) up to 4 (azimuth) times 16 (range).

The coherence ranges from 0 to 1 and is a measure of the phase stability of the SAR signal. The principle of the coherence based change detection is that the interferometric signal strongly de-correlates (low coherence) due to changes on the ground in the time between the SAR acquisitions, such as a landslide event. The coherences of the pre-event and the co-event image pairs were compared for different land cover classes. The land cover was derived by visual interpretation and manual digitalisation of optical SPOT imagery acquired before (12 March 2015) and after the event (02 May 2015). However, the coherence values or the differences of the pre-event coherence and the co-event coherence, respectively, showed no significant difference between the landslides and other land cover classes (tab. 2.5.4).

At this case study, the coherence based change detection could not be successfully applied for landslide detection. This is due to several reasons. First, the areas were the landslides occurred were previously covered by dense vegetation (forest). Vegetated areas show strong de-correlation within a short time due to movements induced by wind. Therefore, also the pre-event coherence at these areas is very low. Consequently, landslides do not stand out in their coherence difference values compared to the surrounding forest areas. Second, the spatial resolution of Sentinel-1 is too rough to detect thin landslides. Moreover, the coherence has to be estimated over several windows, further decreasing the spatial resolution. For instance even within the urban area low coherence values can be observed (also in the pre-event coherence). Urban area in this region is characterised by sparse settlement structures with lots of trees and other vegetation between the single buildings. At the rough spatial resolution of the SAR sensor Sentinel-1 these urban area are very similar to vegetated areas. Third, due to the steep valley sides, geometric distortion (layover and foreshortening) occurred on one side of the valley, preventing further analysis at this part of the valley.

Table 2.5.4: Pre-event and co-event coherence values for different land cover classes

Mean coherence	Farmland	Forest	Grassland	Landslide	Plain land	Shrubland	Urban area
Pre-event	0.41	0.35	0.40	0.34	0.38	0.39	0.33
Co-event	0.32	0.32	0.32	0.32	0.32	0.32	0.25
Difference	0.09	0.03	0.08	0.02	0.06	0.07	0.08

Beside the coherence based change detection described above, also polarimetric Sentinel-1 data has been analysed. However, as polarimetric Sentinel-1 imagery of the landslide affected area in Nepal was only available after the event, our analysis was only possible using post-event data (acquired on 28 April 2015).

After polarimetric speckle filtering using the refined Lee filter, the entropy/anisotropy/alpha decomposition was applied to the dual-pol Sentinel-1 post-event image. Moreover, an unsupervised Wishart classification based on the results of the decomposition was executed. Next, the results of this classification as well as the results of each decomposition parameter were compared with the land cover classification described above. This reference data is based on visual interpretation of pre- and post-event optical SPOT imagery and manual digitalisation.

Unfortunately, landslides could not be separated from the surrounding land cover classes based on the polarimetric signal. This is due to following reasons. First, the area of interest is characterised by a high topographic relief. The Wishart classification is in this case more influenced by the different SAR backscattering of layover and foreshortening areas compared to slopes leaning away from the SAR sensor, as by different land cover classes such as forests and bare soil (landslide areas). Second, the relatively rough resolution of Sentinel-1 prevents the detection of thinner landslides (many landslides of the area of interest have a width smaller than the pixel size of terrain corrected Sentinel-1 imagery). Moreover, computation of the decomposition parameters requires spatial averaging over several pixels, further decreasing the spatial resolution of the imagery and increasing the limit of detectable landslides. Third, Sentinel-1 acquires only dual-pol data, which provides only limited information about the ground's backscattering properties compared to quad-pol data of e.g. RADARSAT-2 or ALOS-2/PALSAR-2. Quad-pol would enable the application of much more polarimetric decomposition, such as the Yamaguchi 4-component decomposition, enabling more detailed separation of the backscattering signal into surface, double bounce and volume scattering.

2.6 Technical note on optical data-based burnt area mapping

2.6.1 State-of-the-art

Fire forest management occurs during three phases: prevention and risk management before the fire, crisis management during the fire and damage assessment and rehabilitation after the fire. Remote sensing can contribute largely to damage assessment and is an alternative to field surveys, GPS techniques and aerial photography. It reduces the cost and the time necessary to assess damages and can provide long-term monitoring with data covering large areas and from different spectral bands. Automatically extracting burnt areas is one of the main issues of damage assessment and it encounters recurrent problems. Indeed, projects are based on various data, from different environmental conditions and from different satellites with specific spectral and spatial resolutions and it causes some difficulties in the elaboration of an automatic and reusable burnt scar extraction procedure. The burnt land is often mixed up with urban and arable areas with shadows caused by terrain or clouds adding to the complexity. Noticing the difference between slightly burnt and unburnt vegetation is also a difficulty. Several techniques which are widely used as a basis for burnt areas detection algorithms are treated below.

2.6.1.1 Techniques

Vegetation indices are the most frequently used indices in burnt areas detection and are based on the spectral analysis of the burnt areas. Generally, the index calculations require at least two spectral bands. The NDVI (Normalised Difference Vegetation Index) (Rouse et al. 1973) is less influenced by illumination condition, field slope and satellite acquisition angle and is used to estimate vegetation density. The SAVI (Soil Adjusted Vegetation Index) (Huete 1988), the MSAVI (Modified Soil Adjusted Vegetation Index) (Qi et al. 1994) and the TSAVI (Transformed Soil Adjusted Vegetation Index") have shown a better sensitivity in the case of sparse vegetation. The GEMI (Global Environmental Monitoring Index) (Pinty and Verstraete 1992) is less affected by atmospheric variations and is more relevant than NDVI to detect burnt areas (Pereira 1999). The BAI (Burnt Area Index) (Chuvieco et al. 2002) is specially defined to detect burnt areas. The previous indices are part of bi-spectral space visible/NIR whereas the following indices are in the bi-spectral space NIR/SWIR. The NDII (Normalised Difference Infrared Index) (Kaufman and Remer 1994) and NBR (Normalised Burn Ratio) (Garcia and Caselles 1991, Key and Benson 1999) are normalised differences between reflectance registered in NIR and SWIR. By analogy with the NDVI, the NDII and the NBR are defined by replacing the Red band with the SWIR band. Finally, the CSI (Char Soil Index) (Smith et al. 2005) is defined as the simple ratio between NIR and SWIR reflectance. Harris et al. (2011), evaluate the performance of 19 spectral indices for assessing fire severity.

Principal component analysis (PCA), conceived by Pearson (1901), is “a statistical technique that linearly transforms an original set of variables into a substantially smaller set of uncorrelated variables that represents most of the information in the original set of variables” (Dunteman 1989). PCA is often used in remote sensing as a process before a classification: Fung and LeDrew (1987), Pereira (1992), Martín et al. (1994), Siljeström and Moreno (1995) used the PCA for change detection on multi-temporal data composed of pre- and post-fire images. In contrast, Hudak and Brockett (2004) used the PCA on a single image before using the parallelepiped algorithm to classify.

When a classification is processed, it often happens that pixels are non-classified or wrongly classified. The problems encountered are due to different objects with a close reflectance or are due to mixed pixels. The mixed pixels are a consequence of limitations in spatial resolution of the data and the heterogeneity of features on the ground. The mixture spectra are often generated when the pixel covers more than on land-cover class (Lu et al. 2002). Linear Spectral Mixture Analysis (LSMA) assumes that the spectrum measured by a sensor is a linear combination of the spectra of all components within the pixel (Ustin et al. 1993, Roberts et al. 1998). Caetano et al. (1994, 1996) show that LSMA is successful for burnt vegetation mapping because the classification is based on the abundance of burnt vegetation within the area covered by the pixel. This explains why SMA seems more appropriate for burnt vegetation mapping, than those techniques that identify burnt areas by their low biomass content, e.g. NDVI. These create confusion between burnt areas and bare soil, areas with low vegetation cover or even clear cut areas in multi-temporal studies. Rogan and Franklin (2001) and Quintano et al. (2006) used a decision tree classifier and a region growing algorithm. The LSMA gives lower results compared to neural network classifier.

2.6.1.2 Burnt area detection algorithms

In the literature, two types of algorithms for automatic or semi-automatic detection burnt areas are opposed: multi-temporal methods and uni-temporal methods. The first ones use change detection techniques between pre- and post-fire data or analyse the variation of vegetation indices from time series data. The second ones work only with a single crisis image. Multi-temporal methods present the advantage to reduce the confusion between burnt areas and other areas which present similar spectral characteristics. However, they require several images and supplementary processing (registration and geometric, radiometric and atmospheric corrections) (Henry 2008).

Several methods are based on a two phase methodology: the first one to detect the most likely burnt areas and the second one to improve the burnt area mapping by analysing the neighbours of previously detected pixels.

Logistic regression analysis

The logistic regression models have demonstrated to be an effective technique to identify burnt area core pixels. These discrimination models are based on original bands and on spectral indices

(Bastarrika et al. 2007). Whereas an iterative criterion decision method used by Bastarrika et al. (2011) determines seed pixels for burnt area mapping. Fraser et al. (2002), propose to use a logistic regression algorithm based on a probability calculation in function of NDVI and NDII indices between pre- and post-fire images.

Supervised and unsupervised classifications

The methods based on supervised or un-supervised classification standard algorithms mainly identify burnt pixels and non-burnt pixels from samples. Stroppiana et al. (2002) use a classification tree whereas Gitas et al. (2004) developed an object-based classification model using spectral as well as contextual object information to obtain a burnt area map. Cao et al. (2009) and Zammit (2008) proposed an approach based on SVMs, a supervised classification technique that has higher accuracy and better generalisation ability than traditional classifiers. In order to take into account the spatial information provided by the crisis SPOT-5 image, the One-Class SVM algorithm is used as a region-growing technique, thereby decreasing false positives and improving the boundaries of burnt areas. Moreover, the samples of burnt areas required for the training step of the SVM are automatically selected from the image histogram.

Multi-thresholding approaches

Several methods are based on the analysis of the variation of vegetation indices in multi-temporal data, which includes the threshold of the previous indices. The most difficult part in thresholding is to find a global threshold, applicable for different data (various areas, periods and type of image). A threshold has to be precise in order not to overestimate or underestimate the burnt area. Several studies combine the spectral indices and channels to extract the burnt areas (Kasischke et al. 1993, Barbosa et al. 1999, Pereira 1999, Roy et al. 1999, Chuvieco et al. 2002, Chuvieco et al. 2008). Giglio et al. (2009) elaborate an algorithm which applies dynamic thresholds to composite imagery generated from a burn-sensitive vegetation index and a measure of temporal texture. Cumulative active fire maps are used to guide the selection of burnt and unburnt training samples. Fraser et al. (2000) worked on a technique for burnt area mapping named HANDS, Hotspot and NDVI Differencing Synergy. It combines hotspot detection and multi-temporal NDVI differencing. Hotspots are used to dynamically train an NDVI difference threshold for separating scars. NDVI differencing is used to remove falsely detected hotspots and to fill in patches within individual burns that were not detected as hotspots. Garcia et al. (2014) worked on NDVI time series data to elaborate a two-step process. The differences between pre and post images allow the identification of burnt seed pixels, and then fire scars for each potential wildfire are delimited using an extension algorithm from the seed pixels.

Kontoes et al. (2009) evaluate and compare two burnt area detection algorithms: the first one uses a fixed thresholding method from a set of specifically combined image enhancements, whereas the

second one is a decision tree classification approach based on a wide range of biophysical parameters. The two methods reach high detection capability rates ranging from 80.0 to 91.0%.

References

1. Barbosa, P. M., Grégoire, J. M., Pereira, J. M. C. (1999). An algorithm for extracting burnt areas from time series of AVHRR GAC data applied at a continental scale. Remote Sensing of Environment, 69(3), 253-263.
2. Bastarrika, A., Chuvieco, E., Martín, M. P. (2007). Automatic discrimination of core burn scars using logistic regression models. Towards an operational use of remote sensing in forest fire management, 195.
3. Bastarrika, A., Chuvieco, E., Martín, M. P. (2011). Mapping burnt areas from Landsat TM/ETM+ data with a two-phase algorithm: Balancing omission and commission errors. Remote Sensing of Environment, 115(4), 1003-1012.
4. Caetano, M.S., Mertes, L.A.K. Pereira, J.M.C., (1994). Using Spectral Mixture Analysis for Fire Severity Mapping, 2nd Int.Conf. Forest Fire Research, Coimbra, 667-677.
5. Caetano, M.S., Mertes, L., Cadete, L. Pereira, J.M.C. (1996), Assessment of AVHRR data for characterising burnt areas and post-fire vegetation recovery., EARSeL Advances in Remote Sensing, 4, 124-134.
6. Cao, X., Chen, J., Matsushita, B., Imura, H., Wang, L. (2009). An automatic method for burn scar mapping using support vector machines. International Journal of Remote Sensing, 30(3), 577-594.
7. Chuvieco, E., Martin, M. P., & Palacios, A. (2002). Assessment of different spectral indices in the red-near-infrared spectral domain for burnt land discrimination. International Journal of Remote Sensing, 23(23), 5103-5110.
8. Chuvieco, E., Englefield, P., Trishchenko, A. P., Luo, Y. (2008). Generation of long time series of burn area maps of the boreal forest from NOAA-AVHRR composite data. Remote Sensing of Environment, 112(5), 2381–2396.
9. Dunteman. G.H, (1989), Principal components analysis (No. 69). Sage.
10. Fraser, R. H., Li, Z., Cihlar, J. (2000). Hotspot and NDVI differencing synergy (HANDS): A new technique for burnt area mapping over boreal forest. Remote Sensing of Environment, 74(3), 362-376.
11. Fraser, R. H., Fernandes, R., and Latifovic, R. (2002). Multi-temporal burnt area mapping using logistic regression analysis and change metrics. In IEEE International Geoscience And Remote Sensing Symposium (IGARSS), Toronto, Canada.
12. Fung, T., LeDrew, E. (1987). Application of principal components analysis to change detection. Photogrammetric engineering and remote sensing, 53(12), 1649-1658.
13. García, M. A., Alloza, J. A., Mayor, Á. G., Bautista, S., and Rodríguez, F. (2014). Detection and mapping of burnt areas from time series of MODIS-derived NDVI data in a Mediterranean region. Central European Journal of Geosciences, 6(1), 112-120.
14. Giglio, L., Loboda, T., Roy, D. P., Quayle, B., and Justice, C. O. (2009). An active-fire based burnt area mapping algorithm for the MODIS sensor. Remote Sensing of Environment, 113(2), 408-420.
15. Gitas, I. Z., Mitri, G. H., and Ventura, G. (2004). Object-based image classification for burnt area mapping of Creus Cape, Spain, using NOAA-AVHRR imagery. Remote Sensing of Environment, 92(3), 409-413.

16. Harris, S., Veraverbeke, S., Hook, S. (2011). Evaluating spectral indices for assessing fire severity in chaparral ecosystems (Southern California) using MODIS/ASTER (MASTER) airborne simulator data. Remote Sensing, 3(11), 2403-2419.
17. Henry, M. C. (2008). Comparison of single-and multi-date Landsat data for mapping wildfire scars in Ocala National Forest, Florida. Photogrammetric Engineering & Remote Sensing, 74(7), 881-891.
18. Hudak, A. T., Brockett, B. H. (2004). Mapping fire scars in a southern African savannah using Landsat imagery. International Journal of Remote Sensing, 25(16), 3231-3243.
19. Huete, A. R. (1988). A soil-adjusted vegetation index (SAVI). Remote sensing of environment, 25(3), 295-309.
20. Kaufman, Y. J., Remer, L. A. (1994). Detection of forests using mid-IR reflectance: an application for aerosol studies. Geoscience and Remote Sensing, IEEE Transactions on, 32(3), 672-683.
21. Kasischke, E. S., French, N. H., Harrell, P., Christensen, N. L., Ustin, S. L., and Barry, D. (1993). Monitoring of wildfires in boreal forests using large area AVHRR NDVI composite image data. Remote Sensing of Environment, 45(1), 61-71.
22. Key, C. H., and Benson, N. C. (1999). Measuring and remote sensing of burn severity: the CBI and NBR. Poster abstract. In L. F. Neuenschwander and K. C. Ryan (Eds.), Proceedings Joint Fire Science Conference and Workshop, Vol. II, Boise, ID, 15-17 June 1999. University of Idaho and International Association of Wildland Fire. 284 pp.
23. Kontoes, C. C., Poilve, H., Florsch, G., Keramitsoglou, I., and Paralikidis, S. (2009). A comparative analysis of a fixed thresholding vs. a classification tree approach for operational burn scar detection and mapping. International Journal of Applied Earth Observation and Geoinformation, 11(5), 299-316.
24. Garcia, M. L., Caselles, V. (1991). Mapping burns and natural reforestation using Thematic Mapper data. Geocarto International, 6(1), 31-37.
25. Lu, D., Batistella, M., and Moran, E. (2002). Linear spectral mixture analysis of TM data for land-use and land-cover classification in Rondonia, Brazilian Amazon. International archives of photogrammetry remote sensing and spatial information sciences, 34(4), 557-562.
26. Martín, M. P., Viedma, O., Chuvieco, E. (1994). High versus low resolution satellite images to estimate burnt areas in large forest fires. In Second International Conference on Forest Fire Research, Coimbra, Portugal (Vol. 2, pp. 653-663).
27. Pereira, J. M. (1992). Burnt area mapping with conventional and selective principal component analysis. Finisterra: Revista portuguesa de geografia, 27(53), 63-78.
28. Pereira, J. M. (1999). A comparative evaluation of NOAA/AVHRR vegetation indexes for burnt surface detection and mapping. Geoscience and Remote Sensing, IEEE Transactions on, 37(1), 217-226.
29. Pinty, B., Verstraete, M. M. (1992). GEMI: a non-linear index to monitor global vegetation from satellites. Vegetatio, 101(1), 15-20.
30. Qi, J., Chehbouni, A., Huete, A. R., Kerr, Y. H., Sorooshian, S. (1994). A modified soil adjusted vegetation index. Remote sensing of environment, 48(2), 119-126.
31. Quintano, C., Fernandez-Manso, A., Fernandez-Manso, O., Shimabukuro, Y. E. (2006). Mapping burnt areas in mediterranean countries using spectral mixture analysis from a uni-temporal perspective. International Journal of Remote Sensing, 27(4):645–662.
32. Roberts, D. A., Batista, G., Pereira, J., Waller, E., Nelson, B. (1998). Change identification using multitemporal spectral mixture analysis: Applications in eastern Amazonia.

33. Rogan, J., Franklin, J. (2001). Mapping burn severity in southern California using spectral mixture analysis. In Geoscience and Remote Sensing Symposium, 2001. IGARSS'01. IEEE 2001 International (Vol. 4, pp. 1681-1683). IEEE.
34. Rouse Jr, J., Haas, R. H., Schell, J. A., Deering, D. W. (1973). Monitoring vegetation systems in the Great Plains with ERTS. NASA special publication, 351, 309.
35. Roy, DP, Giglio, L, Kendall, JD, Justice, C. O. (1999). Multi-temporal active-fire based burn scar detection algorithm. International journal of remote sensing, 20(5), 1031-1038.
36. Siljeström Ribed, P., Moreno López, A. (1995). Monitoring burnt areas by principal components analysis of multi-temporal TM data. International Journal of Remote Sensing, 16(9), 1577-1587.
37. Smith, A. M., Wooster, M. J., Drake, N. A., Dipotso, F. M., Falkowski, M. J., Hudak, A. T. (2005). Testing the potential of multi-spectral remote sensing for retrospectively estimating fire severity in African Savannahs. Remote Sensing of Environment, 97(1), 92-115.
38. Stroppiana, D., Grégoire, J. M., Pereira, J. M. (2002). The use of SPOT VEGETATION data in a classification tree approach for burnt area mapping in Australian savanna. International journal of remote sensing, 24(10), 2131-2151.
39. Ustin, S. L., Smith, M. O., Adams, J. B. (1993). Remote sensing of ecological processes: A strategy for developing and testing ecological models using spectral mixture analysis. Scaling physiological processes: Leaf to globe, 339-357.
40. Zammit, O. (2008). Détection de zones brûlées après un feu de forêt à partir d'une seule image satellitaire SPOT 5 par techniques SVM, PhD thesis, Université Nice Sophia Antipolis.

2.6.2 (Semi-)automatic extraction of burnt areas

The main aim of this work package is the improvement of strategies for the (semi-) automatic extraction of burnt areas from Pléiades-1A/1B and Sentinel-2 type data including considering complementary hotspot detection.

In the following section, initial results over two test sites, one in Australia and one on the Réunion Island, are presented using object oriented processing and near-automatic processing in OTB respectively. The Réunion Island work is being further validated at present.

2.6.2.1 Fire mapping in Bullsbrook, Australia

A devastating fire occurred in Bullsbrook, Australia, from 09 January until 12 January 2015, and destroyed approx. 7000 ha of land and damaged two derelict homes and five sheds. Figure 2.6.2 shows the location of Bullsbrook, and a false colour composite of a Landsat-8 scene acquired on 20/01/2015.

This image has also been used to derive the burnt area extent. Therefore, an object-based semi-automatic approach has been applied. As a first processing step, image segmentation, mainly using the colour information of the NIR and MIR, was performed with the eCognition Developer software. The second step applied was the classification of the burnt area, based on the following spectral indices:

$$MSAVI = \frac{2\rho_{NIR} + 1 - \sqrt{(2\rho_{NIR} + 1)^2 - 8(\rho_{NIR} - \rho_{RED})}}{2}$$

$$NDSWIR = \frac{\rho_{NIR} - \rho_{SWIR}}{\rho_{NIR} + \rho_{SWIR}}$$

$$BAI = \frac{1}{(0.1 - \rho_{RED})^2 + (0.06 - \rho_{NIR})^2}$$

Where: $\rho_{RED}, \rho_{NIR}, \rho_{SWIR}$ = *red*, near and middle infrared band, respectively.

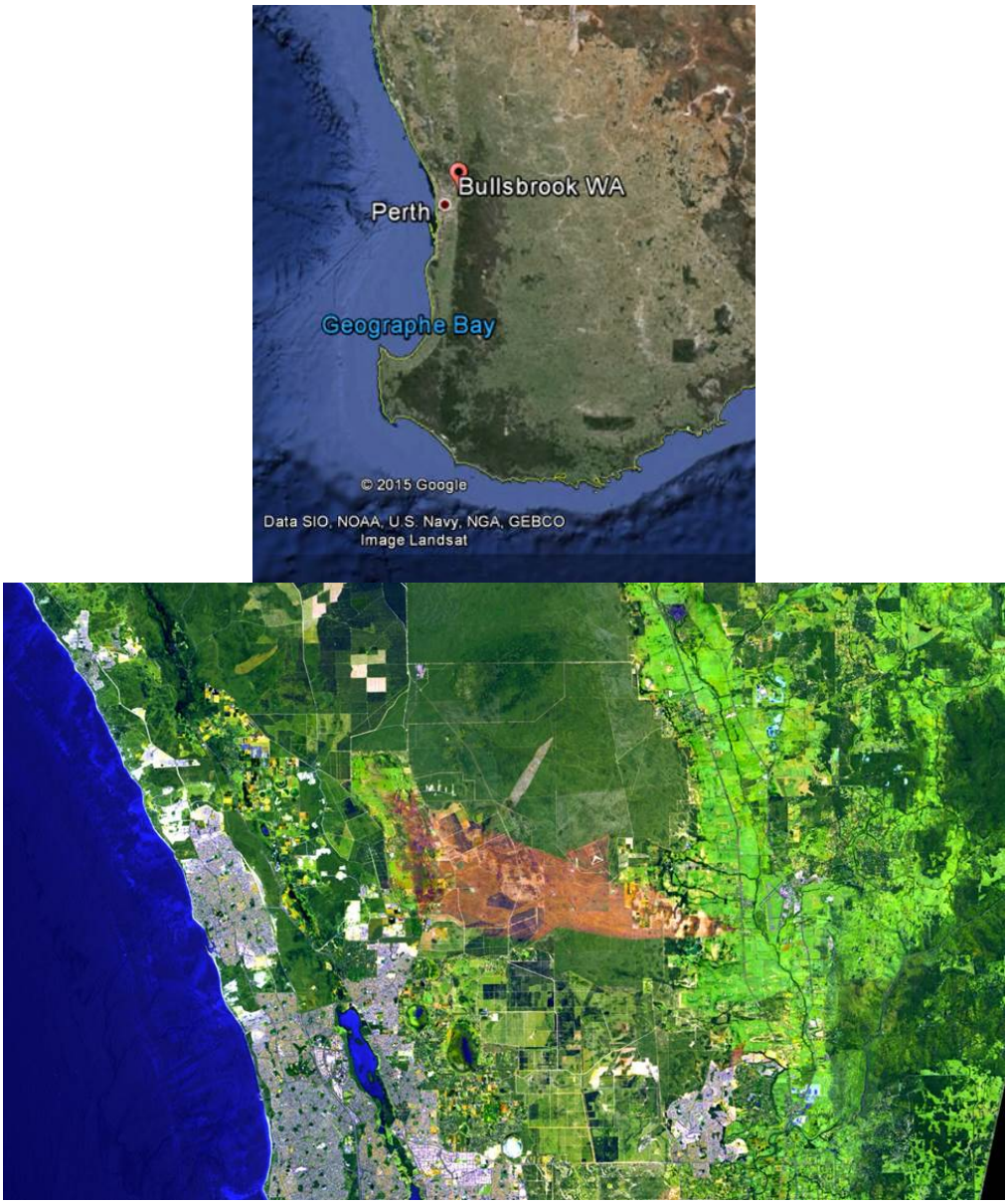

Figure 2.6.2: Location of Bullsbrook, and visualsation of the burnt area using a Landsat-8 false colour composite (combination red=MIR, green=NIR, blue=green).

To avoid misclassifications, the first step of the classification was the exclusion of most unburnt parts of the image. The unaffected areas were classified during a fuzzy classification using the indices MSAVI (Modified Soil Adjusted Vegetation Index) and NDSWIR (Normalised Differenced Shortwave Infrared). Finally, the burnt area was classified by means of a fuzzy classification approach containing the MSAVI, BAI (Burnt Area Index) and NDSWIR. All applied classification steps were threshold based. The different threshold values were determined by a literature review and visually by an iterative approach, whereas the graphical user interface simplified the adjustment to different investigation areas. Figure 2.6.3 shows the burnt area (false colour image, combination:

red=middle infrared, green=near infrared, blue=green) and the extracted burnt area extent (in yellow). In order to map the burnt area as accurate as possible, a visual refinement was performed.

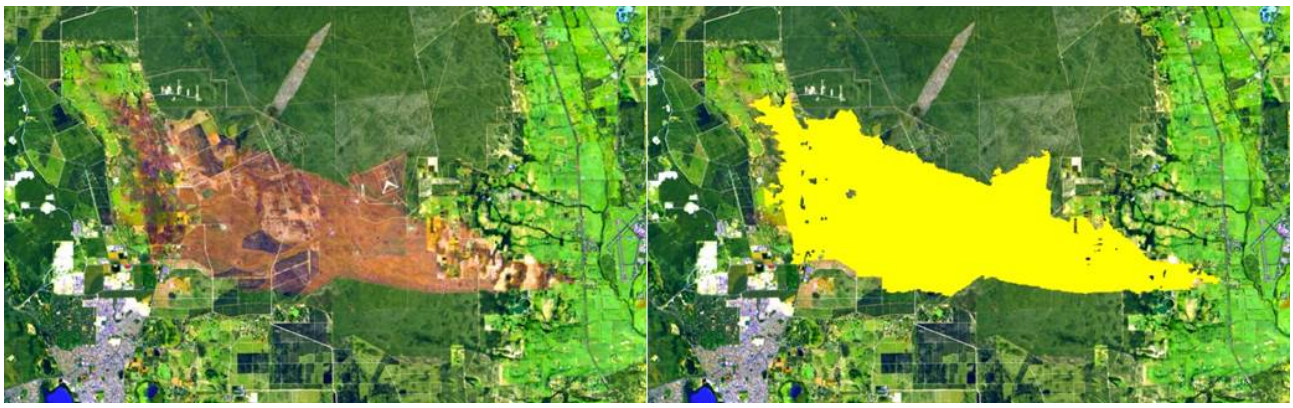

Figure 2.6.3: Comparison of the burnt area (false colour image, combination red=middle infrared, green=near infrared, blue=green) and the extracted burnt area, shown in yellow.

2.6.2.2 Fire mapping without a SWIR channel over Reunion Island, France

End October until early November 2011, in the SAFER rapid mapping framework, SERTIT followed over a 6-days period the evolution of forest fires onthe Maido slopes, Réunion Island, in the hearth of a National Park, with one satellite image acquisition per day and map production in NRT. According to the prefecture report, the fire burnt > 2600 ha. This work was carried out by manually digitising a burnt area and is used as a reference for this project's work where the intention was to investigate how far the procedure can be automatized. The burnt area mapping was validated by an Office National des Forêts (ONF) field campaign.

Establishing an automatic method for the extraction of burnt areas in a context of rapid mapping imposes many constraints. The extraction is based on a comparison of pre- and post-fire images and needs therefore reference and crisis images. These images can be from different sensors with different characteristics. The elaborated method should work with all images and should be compatible with the spectral characteristics.

The calculation of band ratios or specialised fires and vegetation indices is the most frequently used method. The state of the art highlights the NDVI, BAI, NDII and NBR indices which are more relevant for burnt areas extraction. Nevertheless, the NDII and NBR indices require the SWIR component, which is not often measured by present sensors (currently measured by Landsat) but its availability is going to greatly increase with the arrival of Sentinel 2A and 2B. On the contrary, the NIR component is measured by all the sensors and the NDVI index can always be calculated.

In the event that the type of fire is known, a pre-fire LULC classification could be useful to target the burnt areas. Such a classification is sometimes not available, so it can only be considered as an optional data to help to extract the burnt areas.

In the context of rapid mapping, the (semi-) automatic method for burnt area extraction has to be executed in a simple manner and quickly by everyone. The choice of parameters is generally the hardest task for the applications user, so the number of parameters has to be minimised.

Data

A set of satellite images acquired over the Réunion Island site include a SPOT 5 reference image and three crisis images, whose details are summarized in the table below (table 2.6.1). These images are used to illustrate the method which is developed in this section. The burnt area extent, considered as a reference, has been manually digitalised. The Corine Land Cover classification can be used as an optional LULC classification input.

Table 2.6.1: Reference and crisis images details.

Image	Sensor	Acquisition date	Resolution	Spectral characteristics [µm]
Reference	SPOT-5	30/05/2011	10 m	G : 0.50 - 0.59 R : 0.61 - 0.68 NIR : 0.78 - 0.89 MIR : 1.58 - 1.75
Crisis	SPOT-4	12/12/2011	10 m	
	RapidEye	27/10/2011	6.5 m	B : 0.44 - 0.51 G : 0.52 - 0.59 R : 0.63 - 0.685 RE : 0.69 - 0.73 NIR : 0.76 - 0.85
	RapidEye	29/10/2011	6.5 m	

Processing tools

In order to automatise the burnt areas extraction, an existing OTB tool was used and SERTIT developed its own module. OTB is “an open-source C++ library for remote sensing image processing, distributed under the CeCILL-v2 license. It has been initiated and funded by the CNES in the frame of a program named ORFEO to prepare, accompany and promote the use and the exploitation of the images derived from Pléiades satellites. OTB aims to enable the state-of-the-art processing of large images even on limited resource laptops, and is shipped with a set of extensible ready-to-use tools for classic remote sensing tasks (https://www.orfeo-toolbox.org/).
The advantage of using OTB is that a script can be written to automatically process all the tools in one stroke (time saving). Users just have to define paths of images or other files.

Initial method for burnt area detection

The multi-temporal method elaborated during this study for burnt areas extraction relies on change detection between pre-fire and post-fire situation and focuses specially on the comparison of the NDVI at these two dates. In the future the method will also aim to classify the fire areas according

to their degree of severity. The method is now broken down into four steps and detailed below with the Maido fire used to illustrate the results:

- Subset creation, resampling and co-registration
- Radiometric calculation of indices
- Deriving cloud and vegetation masks plus NDVI difference
- Deriving the fire mask

Step 1 - Subset creation, resampling and co-registration

A subset of the reference and crisis images is extracted in order to reduce the area to process and to speed up the time of processing. The two images are then resampled to the same resolution and co-registered so that the two images are easily superimposed (fig. 2.6.4).

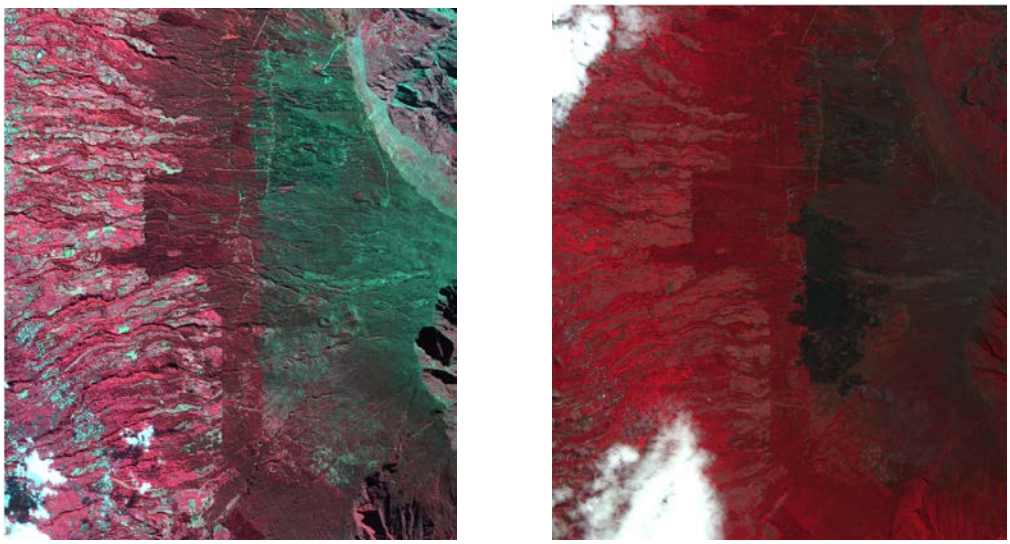

Figure 2.6.4: Left: SPOT-5 reference image (30/05/2011); right: RapidEye crisis image (27/10/2011).

Step 2 - Radiometric calculation of indices

First of all, the adopted strategy for burnt area extraction is to remove the areas that are for sure not burnt. Such obvious areas are clouds, healthy vegetation and water. To extract them, radiometric indices are calculated before masking them in step 3.

The NDVI is calculated from the NIR and the Red bands, according to the following formula:

$$NDVI = \frac{NIR - R}{NIR + R}$$

By definition the NDVI values are stretched between -1 and 1and qualify the density of vegetation response present in the scene. The normalization by the sum of the two bands reduces the

illumination effects. The negative values correspond to surfaces other than canopies (such as water, clouds, etc.). For bare soil, the NDVI has values close to 0 whereas areas containing a dense vegetation canopy will tend to positive values.

The *Shadow Index* (SI) is defined from the Red and the Green bands (Rikimaru and Miyatake, 1997):

$$SI = \sqrt{(Max(G) - G).(Max(R) - R)}$$

The SI stretches the values according to the darkness degree of the objects and highlights the clouds which are the brightest objects in the image.

The *Normalized Difference Water Index* (NDWI) defined by (McFeeters, 1996) needs Green and NIR components and is expressed as followed:

$$NDWI = \frac{G - NIR}{G + NIR}$$

This index is designed to (1) maximise the reflectance of water by using green wavelengths; (2) minimise the low reflectance of NIR by water features; and (3) take advantage of the high reflectance of NIR by vegetation and soil features. As a result, water features have positive values and thus are enhanced, while vegetation and soil usually have zero or negative values (McFeeters 1996). The use of this index is a little bit tricky because the burnt areas don't have a high reflectance in the NIR bands and therefore they are classed with the water features according the zero threshold. The separation between the water features and the burnt areas can be considered by a criterion of features size.

Step 3 – Deriving cloud and vegetation masks plus NDVI difference
The clouds mask results from the thresholding of the shadow index image using the OTSU Threshold (fig. 2.6.5) whereas the vegetation mask results from NDVI thresholding.

Cloud mask - OTSU filter
The OTSU filter creates a binary image that separates an image into foreground and background components. The OTSU method assumes that the image contains two classes of pixels following bi-modal histogram (foreground pixels and background pixels), it then calculates the optimum threshold separating the two classes so that their intra-class variance is minimal (Nobuyuki Otsu, 1979). The original OTSU method performs one thresholding but a multi OTSU method has been developed to proceed to a multi-level thresholding.

Within ASAPTERRA the automatic OTSU filter was implemented in OTB using the *itkOtsuMutipleThresholdsImageFilter* from the ITK[1] library.

Healthy vegetation mask and water mask - NDVI and NDWI thresholding

At the same time, an automatic thresholding to extract on one hand the healthy vegetation and on the other hand the water features was performed.

To optimise thresholding, the filter named *itkBinaryThresholdImageFilter* from ITK in OTB was implemented instead of using a BandMath tool.

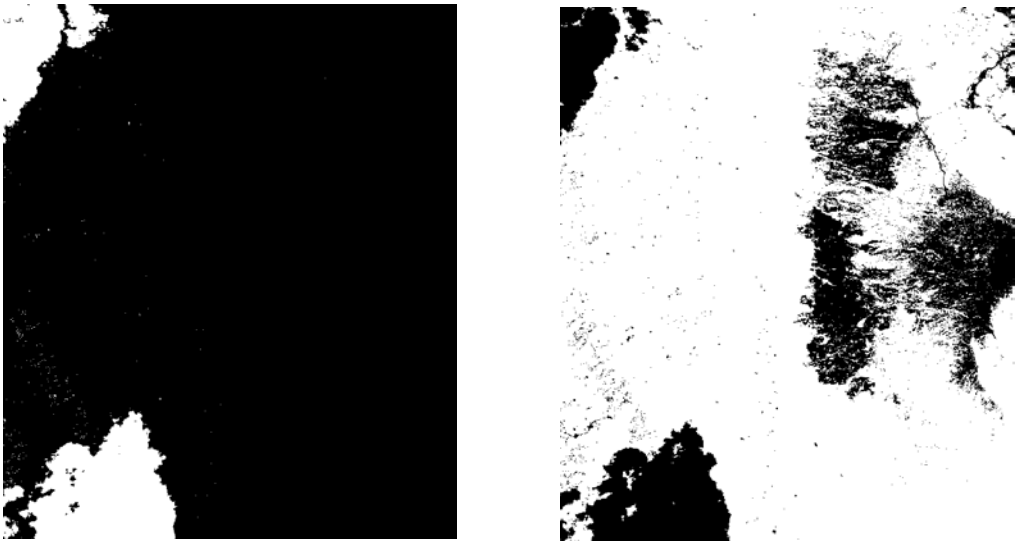

Figure 2.6.5: Cloud mask (left) and healthy vegetation mask (right) with the clouds and healthy vegetation in white.

NDVI difference with normalisation

This part of the process relies in part on the study of Fraser et al. (2000) who worked on a technique for burnt area mapping named HANDS, Hotspot and NDVI Differencing Synergy. It combines hotspot detection and multi-temporal NDVI differencing.

The comparison of the NDVI consists in subtracting pre-fire and post-fire NDVI composites. A simple difference is not suggested because the NDVI composites vary widely annually and seasonally. To face these variations, a normalisation of the post-fire NDVI composite to the pre-fire NDVI composite is required:

$$NDVI_{norm\,(i,j,post)} = NDVI_{(i,j,post)} - (NDVI_{mean\,(post)} - NDVI_{mean\,(pre)})$$

[1] ITK : Insight Segmentation and Registration Toolkit

where $NDVI_{norm}$ is the NDVI normalised composite value, i, j the pixel number and $NDVI_{mean}$ the mean NDVI composite value.

Further the NDVI difference is calculated by subtracting the pre-fire NDVI composite from the post NDVI normalised composite:

$$NDVI_{diff(i,j)} = NDVI_{norm\,(i,j,post)} - (NDVI_{\,(i,j,pre)})$$

where $NDVI_{diff}$ is the NDVI difference (fig. 2.6.6).

Step 4 – Derivation of the fire mask

NDVI difference thresholding

After the NDVI difference is calculated, a suitable threshold has to be established to separate burnt pixels. Vegetation in burnt areas (post-fire situation) is less healthy than in the pre-fire case. This implies that burnt pixels are expected to have a negative NDVI difference value. Therefore, we considered the NDVI difference threshold as zero.

The following extraction conditions must be met for pixels to be classed as burnt area pixels:

1. $NDVI_{diff(i,j)} < 0$ (in figure 2.6.6 values < 0 are in white whereas values > 0 are in black)
2. clouds mask = 0 (no cloud)
3. vegetation mask = 0 (bare soil, mineral areas, burnt areas)

A regularisation process is then applied to improve the fire mask results by creating more homogeneous areas which are easier to handle (fig. 2.6.6).

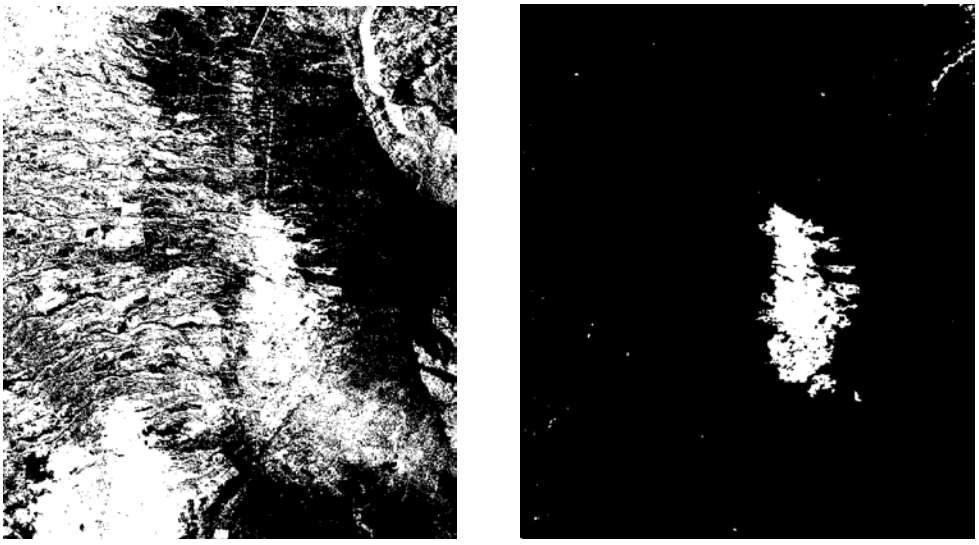

Figure 2.6.6: NDVI difference mask and overall fire mask.

2.6.2.3 Fire mapping with a SWIR channel over Andalusia, Spain

Work was accomplished on a Sentinel-2 oriented burn scar mapping method incorporating a SWIR channel using Landsat-8 and Sentinel-2 data in a multi-temporal workflow for mapping forest fires in Spain. On the 9th of July 2015 the Copernicus EMS Rapid Mapping was triggered for fires in the areas of Lujar and Quesada, Andalusia, Spain:

- On July 5th 2015 at 14:00 a forest fire began in the municipality of Quesada in Jaén province. The fire then spread to neighbouring municipalities such as Larva and Huesa.
- On July 8th 2015 at 10 am, a second forest fire began in the area of Lujar in Granada province. The fire affected other municipalities like Rubite, Gualchos-Castell de Ferro, Órgiva, and Motril. Both fires were active at the moment of the activation.

The Spanish Authorised User triggered the Copernicus EMS to cover these AOIs becoming the activation EMSR127. ICube-SERTIT worked on the activation, using photo-interpretation for the fire delineation and impact grading layers, as is custom in EMS. On this test site SERTIT has decided to concentrate its demonstration activities on the Quesada area in Andalusia although the Lujar area could be used as a back-up.
An interesting aspect of choosing this site is the existence of:

- the burn scars and fire damage severity mapping produced in EMSR127 using VHR data,
- HR Landsat-8 coverage before and after,
- an early winter HR Sentinel-2 coverage (tab. 2.6.2).

Table 2.6.2: Test site associating Landsat-8, Sentinel and ancillary sources over Andalusia, Spain.

Data		**Methods to be tested**
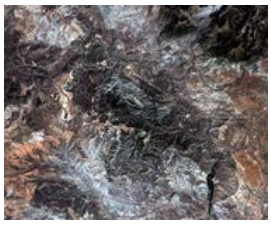	Landsat-8 *30/06/2015*	Reference for burnt scar mapping
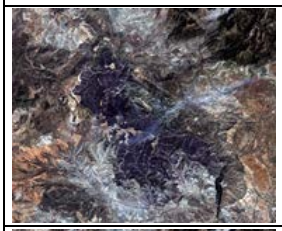	Landsat-8 *16/07/2015*	Burn scar mapping, but cloudy
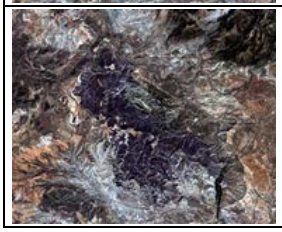	Landsat-8 *01/08/2015*	Burn scar mapping

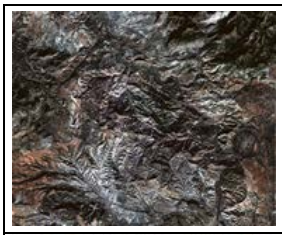	Sentinel-2 06/12/2015 (recovery data)	Soil erosion susceptibility index
	EMS RM fire mapping (SPOT-6 13/07/2015)	Comparative and/or validation data

The multi-sensor database illustrated above enables a comparison to be performed concerning extraction results from EO data at different resolutions and using different techniques (highly automatic image processing results versus photo-interpretation results). The Landsat-8 data which has many spectral similarities to Sentinel-2 will be used to simulate Sentinel-2 data. Of course Landsat-8 has a lower spatial resolution at 30 m instead of Sentinel-2's 10-20 m. In comparison, for validation manually extracted fire delineation products from the VHR data was considered as reference. The workflow has been adapted to incorporate Landsat-8 data and the Normalised Burn Ratio (fig. 2.6.7). The NBR index highlights burned areas using NIR and SWIR wavelengths.

$$NBR = \frac{NIR - SWIR}{NIR + SWIR}$$

NBR was originally developed for use with Landsat TM and ETM+ bands 4 and 7, but it works with any multispectral sensor with a NIR band between 0.76-0.9 µm and a SWIR band between 2.08-2.35 µm. These bands are available on Sentinel-2 at 10 m and 20 m respectively. It is proposed to use the differenced NBR to highlight burn scars using pre and post fire event imagery.

$$\mathrm{dNBR} = \mathrm{NBR}_{(\mathrm{post})} - \mathrm{NBR}_{(\mathrm{pre})})$$

with initial results being presented in figure 2.6.8. The post-classification processing will be enhanced in the coming weeks before the demonstration phase.

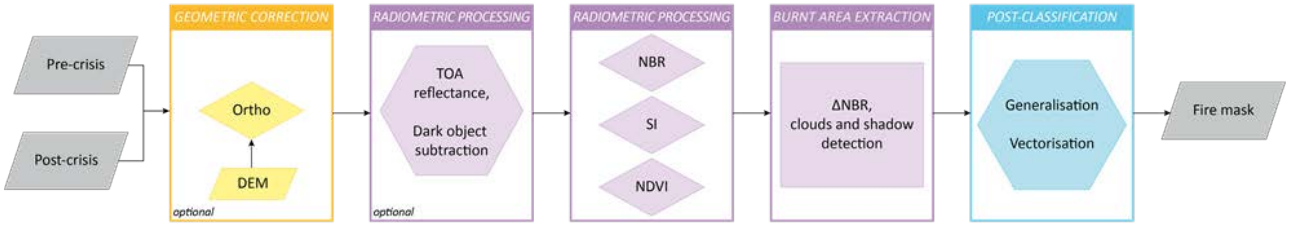

Figure 2.6.7: Adapted SWIR integrated workflow for burn scar mapping.

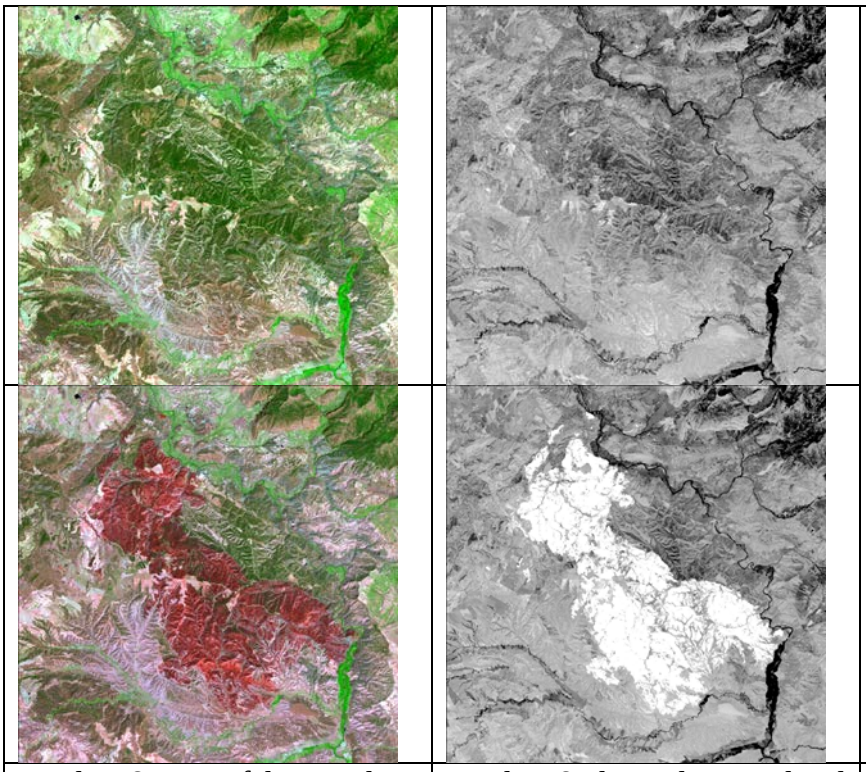

Landsat-8 in false colour composite (7,5,4) for the 30/06/2015 (top) and 01/08/2015 (bottom)	Landsat-8 derived normalised burn ratio for the 30/06/2015 (top) and 01/08/2015 (bottom)	Initial burnt scar mask superimposed on Landsat-8 data 01/08/2015

Figure 2.6.8: Initial burn scar extraction from Landsat-8 data taken before and after a Quesada, Spain fire which was accomplished during Copernicus EMS Rapid EMSR127.

2.6.2.4 Results summary and perspectives

The development of a fast and transferable burnt area mapping procedure by applying change detection methods between optical data taken pre- and post-event is successful. The method is implemented in OTB as a macro script combining algorithms to form a coherent workflow to enhance the speed of execution. Work has concentrated until now on methods not using a SWIR channel. At present, the objective is to create a robust exhaustive method that produces an intermediary burnt area layer, for further manual validation, taking into account imagery that has a SWIR and does not have a SWIR channel.

The Réunion Island's Maido Massif fire event site has been used in burnt area mapping where a large fire occurred in November 2011. During the event photo-interpretation was used to ascertain burnt area extents. Semi-automatic methods are tested that eliminate clouds, cloud shadows, water, and post fire vegetation. The method incorporates the NDVI, Shadow Index, and Normalised Difference Water Index plus pre-/post-event NDVI change detection to produce a fire mask. The method's ergonomics, thematic quality and timeliness have been investigated.

Validation of SPOT4 derived burnt area detection has been carried out with respect to a validated photo-interpreted reference fire extent over the Reunion Island test site. The results are as follows: 92.7% correctly classified pixels, 5.2% omission (94.8% producer accuracy) and 2.1% commission (97.9% user accuracy).

The initial method does not incorporate a SWIR band and needs work on post classification procedures to clean the resulting burnt area mapping layer but is a built-in all-in-one scripted method. At present the normalised burn ratio (NBR) is being incorporated into the model for imagery containing SWIR bands (focussed on 2.20μm) such as Landsat-8 and of course Sentinel-2.

This workflow has now been thoroughly tested and used in rapid mapping environments. Due to the interesting results and rapidly of execution SERTIT has baptised the workflow as BURNOUT. This same workflow (fig. 2.6.7) is used in the fire demonstrators in Chapter 3.

2.7 Technical note on SAR change detection-based burnt areas mapping

2.7.1 State-of-the-art

Forest fires do not only pose an urgent threat to land and life but also contribute to erosion, land degradation, and cause long-term damage to vegetation and soil moisture. Furthermore, the large amounts of smoke emitted from fires impact air quality and affect global warming due to rising trace gas emissions (Beringer et al. 2003, Chuvieco 2009). Despite their significant hazardous characteristics and increasing trend in quality and intensity, wild fires are poorly understood (JRC 2013). Therefore, a comprehensive monitoring and mapping of burnt areas is necessary. A fast and accurate detection of these areas is indispensable both for on-site help and for an assessment of the aftermath. As forest fires often affect large areas, where accessibility is frequently limited, remote sensing can contribute to pre-, active-, and post- disaster mapping in a fast, cost-effective and objective manner with an almost global coverage (Pereira et al. 1999).

Optical data are commonly being used for forest fire mapping in a rush mode due to their sensitivity in the near and mid-infrared bands to fire effects and their straightforward and intuitive interpretability (see chapter 2.6). Nevertheless, optical data availability can be limited by weather conditions, direct fire effects such as smoke plumes or haze, and illumination. The integration of SAR data can overcome these shortcomings and thus offer a high repeat frequency in data acquisitions, since they are able to collect data regardless of weather conditions and illumination. Unfortunately, SAR images contain radar inherent weaknesses as foreshortening, layover or radar shadow. However, SAR fire mapping has a long history, and has shown various promising results. Despite the preliminary investigations of the potential of SAR data for burnt area mapping, the obtained results are often site-specific and not directly comparable. Thus, no consolidated methodology is available. Nevertheless, all methods used for burnt area mapping are based on different change detection techniques, as it was not feasible to detect a burn scar using a post-disaster scene only.

The measured SAR signal is a complex combination of different sources and provides information about vegetation, geometrical (e.g. morphology, roughness), and dielectric properties of the surface and subsurface structure of the observed scene. The occurrence of a fire will most likely change the physical and structural characteristics of the vegetated landscape, thus producing significant variations of its electromagnetic response. When a fire damages vegetation, the contribution to the total backscattering pertinent to volumetric scattering (taking place within the vegetation layer) decreases, making the contribution related to the scattering from the soil more prominent (Ulaby 1982). Indeed, the physical modifications in the vegetation layer depend on pre-fire vegetation characteristics, fire intensity and weather conditions at the time of fire occurrence (Bernhard et al. 2014, Tanase et al. 2010a, 2010c). The post-fire radar signal is strongly affected by soil roughness, and variations in soil moisture, depending on the weather and the soil drainage conditions (Ulaby 1982, Voronovich 1994), which lead to an increase or decrease of the backscatter signal (see tab. 2.7.1).

Dependency on local topography and polarisation has also been observed and linked to the change in the predominant scattering mechanisms (Bernhard et al. 2011, Bourgeau-Chavez et al. 1994, Gimeno 2004a, 2004b), Luckman 1998, Tanase et al. 2010a, 2010c, Van Zyl 1993).
Moreover, different SAR wavelengths interact distinct with vegetation and soil. Since X-band microwaves cannot penetrate as deeply into vegetation cover as C-, L- or P-band wavelengths, the incident beam is mainly influenced by canopy surface scattering (Tanase et al. 2010b), and the attenuation through the forest canopy depends on stand density, canopy architecture (like crown closure, crown shape) and the incidence angle of the sensor (Hoekmann et al. 1987). Therefore, it is of utmost importance, to compare the reaction of different SAR wavelengths over a burnt area.

Table 2.7.1: Change of backscatter signal in different regions.

Satellite	Band	Polarisation	Author	Region	Change of backscatter signal
ERS 1&2	C	VV	Siegert and Rücker 2000	Tropical forest	decrease
			Gimeno et al. 2004b	European Mediterranean	increase
			Ranson et al. 2001	Boreal forest	increase
			Kasischke et al. 1992	Boreal forest	increase
			Bourgeau-Chavez et al. 1995	Boreal forest	increase
			Jenkins et al. 2014	Alaskan Tundra	increase
			Karszenbaum et al. 2003	Argentina	increase
RADARSAT-2	C	HH	Gimeno & Ayanz 2004a	European Mediterranean	increase
			Ranson et al. 2001	Boreal forest	marginally
			French et al. 1999	Boreal forest	increase
JERS-1	L	HH	Nakayama and Siegert 2001	Tropical forest	decrease
			Ranson et al. 2001	Boreal forest	marginally
TOPSAR (airborne)	L & P	VV, HH, VH, HV	Menges et al. 2004	Australia	increase / decrease
TerraSAR-X	X	HH, HV	Tanase et al. 2010a	European Mediterranean	increase (HH) decrease (HV)
		HH, VV	Bernhard et al. 2011/2014	European Mediterranean	increase

In addition to this, studies for burn severity estimation, burnt area mapping, fire damage assessment and vegetation recovery using polarimetric target decomposition matrices or amplitude images with

X-, C-, and L- band showed promising results (Goodenough et al. 2011, Minchella et al. 2009, Tanase et al. 2010a, 2010b, 2010c, 2011, 2014).

A synergistic use of optical and SAR data for burnz area mapping has been addressed only in a few works (Bernhard 2011, 2014, Bourgeau-Chavez 1997, French et al. 1999, Stroppiana et al. 2015).

Studies on deriving fire perimeters with SAR data have been performed in nearly every part of the world. In boreal regions, various studies have highlighted a general increase in SAR backscattering over burnt areas, as a consequence of exposed rough surface and increased soil moisture, mainly due to decreased surface albedo, permafrost melting and lowered evapotranspiration (Bourgeau-Chavez et al. 1995, 1997, 2002, French et al. 1996, Jenkins et al. 2014, Kasischke et al. 1992, 1994, 1997, Liew et al. 2002, Ranson et al. 2001). The impact of different forest types on burnt area detection has been studied for tropical rain forests (Nakayama and Siegert 2001, Siegert and Hoffmann 2000, Siegert and Rücker 2000), wetlands (marshes and forest mix) (Karszenbaum et al. 2003), moorlands (Millin-Chalabi et al. 2014), or savanna woodlands (Menges et al. 2004). These studies found evidence for a change in backscatter signal between burnt and unburnt areas, mainly influenced by soil moisture and the exposure of a rough ground surface. Several studies were undertaken in the European Mediterranean semi-arid environment, where precipitation during the fire season is rare, and the lack of rain reduces backscatter variability due to changes in soil moisture (Tanase et al. 2010a). Promising results could be achieved using C-band SAR data for burnt area detection in Central Portugal (Gimeno et al. 2003, Gimeno et al. 2004a, b). The burnt areas were distinguishable regardless of rainfall, although the wet season showed higher backscatter values than the dry season. Tanase et al. (2010a, 2010b, 2010c) confirmed the utility of X-, C-, and L- band data for fire severity assessment in dry and wet environmental conditions. Moreover, Bernhard et al. (2011, 2014) approved the detection capabilities of X-band SAR data for burnt area mapping and investigated differences in the backscatter signal dependent on pre-fire vegetation and weather conditions. L-band ALOS PALSAR (Advanced Land Observing Satellite Phased Array L-band SAR) images on Greece (Polychronaki et al. 2013) and Sardinia (Mari et al. 2012), and C-band images on pine canopies (Kalogirou et al. 2014) have also been used for burnt area detection.

References

1. Beringer, J., Hutley, L.B., Tapper, N.J., Coutts, A., Kerley, A., Grandy, A.P., 2003: Fire impacts on surface heat, moisture and carbon fluxes from a tropical savanna in northern Australia. International Journal of Wildland fire, 12, 333-340.
2. Bernhard, E., Twele, A., Gähler, M., 2011: Rapid Mapping of Forest Fires in the European Mediterranean Region – a Change Detection Approach Using X-Band SAR Data. Photogrammetrie, Fernerkundung, Geoinformation (PFG), 4, 261-270.
3. Bernhard, E., Twele, A., Martinis, S., 2014: The effect of vegetation type and density on X-band SAR backscatter after forest fires. Photogrammetrie, Fernerkundung, Geoinformation (PFG), 4, 275-285.
4. Bourgeau-Chavez, L.., Kasischke, E., French, F., Szeto, H., Kherkher, C., 1994: Using ERS-1 SAR imagery to monitor variations in burn severity in an Alaskan fire-disturbed boreal

forest ecosystem. Proceedings of the 1994 Surface and Atmospheric Remote Sensing Technologies, Data Analysis and Interpretation, International Geoscience and Remote Sensing Symposium, Pasadena, CA, USA, 8-12 August 1994, 1, 243-245.

5. Bourgeau-Chavez, L., Kasischke, E., Brunzell, S., Muss, J., Tukman, M., 2002: Mapping fire scars in global boreal forests using imaging radar data. International Journal of Remote Sensing, 23, 20, 4211-4234.
6. Bourgeau-Chavez, L., Harrell, P., Kasischke E., French, N., 1997: The detection and mapping of Alaskan wildfires using a spaceborne imaging radar system. International Journal of Remote Sensing, 18, 355-373.
7. Bourgeau-Chavez, L., Kasischke, E., French, N., 1995: The detection and interpretation of Alaskan fire-disturbed boreal forest ecosystems using ERS-1 SAR imagery. IEEE Geoscience and Remote Sensing Symposium, 2, 1246-1248.
8. Chuvieco, E., 2009. *Global impacts of fire.* In: Chuvieco, E. (Ed.): Earth observation of wildland fires in Mediterranean ecosystems, Springer, pp. 1-11.
9. French, N., Kasischke, E., Bourgeau-chavez, L., Harrell, P., 1996: Sensitivity of ERS-1 SAR to variations in soil water in fire-disturbed boreal forest ecosystems. International Journal of Remote Sensing, 17, 3037-3053.
10. French, N., Bourgeau-Chavez, L., Wang, Y., Kasischke, E., 1999: Initial observations of Radarsat imagery at fire-disturbed sites in interior Alaska. Remote Sensing of Environment, 68, 89-94
11. Gimeno, M., San-Miguel Ayanz, M., Liberta, G., 2003: Fire scar detection in central Portugal using RADARSAT-1 and ERS-2 SAR data. IEEE International Geoscience and Remote Sensing Symposium, I-VII: 2491-2493.
12. Gimeno, M., Ayanz, J., 2004(a): Evaluation of Radarsat-1 data for identification of burnt areas in southern Europe. Remote Sensing of Environment, 104,: 346–359.
13. Gimeno, M., San-Miguel-Ayanz, J., Schmuck, G., 2004(b): Identification of burnt areas in Mediterranean forest environments from ERS-2 SAR time series. International Journal of Remote Sensing, 25, 4873–4888.
14. Goodenough, D.G., Chen, H., Richardson, A., Cloude, S., Hong, W., Li, Y., 2011: Mapping fire scars using Radarsat-2 polarimetric SAR data, Canadian Journal for Remote Sensing, 37, 500-509.
15. Hoekmann, D., 1987: Measurements of the Backscatter and Attenuation Properties of Forest Stands at X-, C- and L-Band. – Remote Sensing of Environment, 23, 397-416.
16. Jenkins, L., Bourgeau-Chavez, L., French, N., Loboda, T., Thelen, B., 2014: Development of Methods for detection and Monitoring of Fire Disturbance in the Alaskan Tundra Using a Two-Decade Long Record of Synthetic Aperture Radar Satellite Images, Remote Sensing, 6, 6347-6364.
17. Joint Research Centre, 2013: Forest Fires in Europe, Middle East and North Africa 2012, JRC technical report, URL: http://forest.jrc.ec.europa.eu/media/cms_page_media/9/FireReport2012_Final_2pdf_2.pdf (accessed 19 August 2014).
18. Kalogirou, V., Ferrazzoli, P., Della Vecchia, A., Foumelis, M., 2014: On the SAR backscatter of burned forests: a model-based study in C-Band, over burned pine canopies. IEEE Transactions on Geoscience and Remote Sensing, 52, 6205-6215.
19. Karszenbaum, H., Tiffenberg, J., Grings, F., Marinez, J., Kandus, P., Pratolongo, P., 2003: A SAR time series analysis toolbox for extracting fire affected areas in wetlands. IEEE Geoscience and Remote Sensing Symposium, IGARSS 2003, 6, 4107-4109.

20. Kasischke, E.S., Bourgeau-Chavez, L.L., French, N.H.F., 1994: Observations of variations in ERS-1 SAR image intensity associated with forest fires in Alaska. IEEE Transaction on Geoscience and Remote Sensing, 32, 206-210.
21. Kasischke, E., Bourgeau-Chavez L., French N., Harrell P., Christensen N., 1992: Initial observations on using SAR to monitor wildfire scars in boreal forests. International Journal of Remote Sensing, 13, 3495-3501.
22. Kasischke, E.S., French, N.H.F., Bourgeau-Chavez, L.L., 1997: Monitoring of the effects of fire in North American boreal forests using ERS SAR imagery. In: Proceedings of the Third ERS Symposium on Space at the Service of Our Environment, Florence, Italy, 17-21 March 1997, 363-368.
23. Liew, S.C., Kwoh, L.K., Padmanabahn, K., Lim, O.K., Lim, H., 2002: Delineating land/forest fire burnt scars in global boreal forests using imaging radar data. International Journal of Remote Sensing, 23, 4211-4234.
24. Luckman, A.J., 1998: The effects of topography on mechanism of radar backscatter from coniferous forest and upland pasture. IEEE Trans. Geosci. Remote Sens., 35, 1830-1834.
25. Mari, N., Laneve, G., Cadau, E., Porcasi, X., 2012: Fire Damage Assessment in Sardinia: the use of ALOS/PALSAR data for post fire effects management. European Journal of Remote Sensing, 45, 233-241.
26. Menges, C., Bartolo, R., Bell, D., Hill, G., 2004: The effect of savanna fires on SAR backscatter in northern Australia. International Journal of Remote Sensing, 25, 3857-4871.
27. Millin-Chalabi, G., McMorrow, J., Agnew, C., 2014: Detecting a moorland wildfire scar in the Peak District, using synthetic aperture radar from ERS-2 and ENVISAT ASAR. International Journal of Remote Sensing, 35, 1, 54-69.
28. Minchella, A., del Frate, F., Capogna, F., Anselmi, S., Manes, F., 2009: Use of multitemporal SAR data for monitoring vegetation recovery of Mediterranean burned areas. Remote Sensing of Environment, 113, 588-597.
29. Nakayama, M., Siegert, F., 2001: Comparative study on C and L band SAR for fire scar monitoring. 22nd Asian conference on remote sensing 5-9 Nov. 2001, Singapore.
30. Pereira, J., Sá A., Sousa, A., Silva, J., Santos, T., Carreiras, J., 1999: Spectral characterisation and discrimination of burnt areas. In: Chuvieco, E. (Ed.): Remote Sensing of large wildfires in the European Mediterranean basin, 123-138.
31. Polychronaki, A., Gitas, I.Z., Veraverbeke, S., Debien, A., 2013: Evaluation of ALOS PALSAR imagery for burned area mapping in Greece using object-based classification. Remote Sensing, 5, 5680-5701.
32. Ranson, K., Kovacs, K, Sun, G., Kharuk, V., 2001. Fire scar detection using JERS, ERS and Radarsat data in the Bogucany area, Eastern Siberia, CEOS-SAR01-073.
33. Siegert, F., Rücker, G., 2000: Use of multitemporal ERS-2 SAR images for identification of burned scars in south-east Asian tropical rainforest. International Journal of Remote Sensing, 21 (4), 831–837.
34. Siegert, R., Hoffmann A.A., 2000: The 1998 Forest Fires in East Kalimantan (Indonesia): A quantitative evaluation using high resolution, multitemporal ERS-2 SAR images and NOAA-AVHRR Hotspot data. Remote Sensing of Environment, 72, 64-77.
35. Stroppiana, D., Azar, R., Caló, F., Pepe, A., Imperatore, P., Boschetti, M., Silva, J., Brivio, P., Lanari, R., 2015: Integration of optical and SAR data for burned area mapping in Mediterranean Regions, Remote Sensing, 7, 1320-1345.
36. Tanase, M., Pérez-Cabello F., Riva J., Santoro, M., 2010a: TerraSAR-X data for burn severity evaluation in Mediterranean forests on sloped terrain. IEEE Transactions on Geoscience and Remote Sensing, 48 (2), 917–929.

37. Tanase, M., Santoro, M., Wegmüller, U., de la Riva, J., Pérez-Cabello, F., 2010b: Properties of X-, C- and L-band repeat-pass interferometric SAR coherence in Mediterranean pine forests affected by fires. Remote Sensing of Environment, 114, 2182-2194.
38. Tanase, M., Santoro, M., de la Riva, J., Pérez-Cabello, F., Toan, T., 2010c: Sensitivity of X-, C-, and L-Band SAR Backscatter to Burn Severity in Mediterranean Pine Forests. IEEE Transaction geoscience and remote sensing, 48 (10), 3663-3675.
39. Tanase, M., de la Riva, J., Santoro, M., Pèrez-Cabello, F., Kasischke, E., 2011: Sensitivity of SAR data to post-fire forest regrowth in Mediterranean and boreal forests. Remote Sensing of Environment, 115, 2075-2085.
40. Tanase, M.A., Santoro, M., Aponte, C., de la Riva, J., 2014: Polarimetric properties of burned forest areas at C- and L-band, IEEE Journal of selected topics in applied earth obeservations and remote sensing, 7 (1), 267-276.
41. Ulaby, R.T., Moore, R.K., Fung, A.K., 1982: Microwave Remote Sensing, Addison-Wesley: Reading, MA, USA, 1982.
42. Van Zyl, J.J., 1993: The effect of topography on radar scattering from vegetated areas. IEEE Trans Geosci. Remote Sens., 31, 153-160.
43. Voronovich, A.G., 1994: Wave Scattering from Rough Surfaces, Springer Series on Wave Phenomena, Springer, New York, NY, USA.

2.7.2 SAR change detection based burnt area mapping using X-band coherence images

Different forest fires which occurred in the European Mediterranean between 2009 and 2012 have been evaluated. First, an extensive research of usable data for coherence calculation was accomplished. Table 2.7.2 lists all analysed data sets.

Table 2.7.2: Summary of used X-band images for coherence calculation.

Satellite	Date	Fire condition	Polarisation	Modus	Region
TerraSAR-X	13/12/2007 09/08/2009	Pre-fire Post-fire	HH	Stripmap	La Palma
TerraSAR-X	08/03/2009 31/08/2009	Pre-fire Post-fire	HH	Stripmap	Grammatico
TerraSAR-X	13/05/2008 29/08/2009	Pre-fire Post-fire	VV	Stripmap	Grammatico
TerraSAR-X	20/12/2011 31/12/2011	Pre-fire Post-fire	HH	Stripmap	Torres-del-Paine
TerraSAR-X	12/04/2012 09/07/2012	Pre-fire Post-fire	HH	Stripmap	Andilla

The calculation of coherence on the basis of one pre- and one post-disaster image was performed using the SARscape software. Afterwards, all images have been further processed to data containing image objects, using the eCognition Developer software. An evaluation and comparison of segments inside and outside of the burnt area was accomplished. The reference burnt area has been derived by analysing optical images (SPOT-5: La Palma and Grammatico, Worldview-2: Andilla, RapidEye: Torres-del-Paine).
Concerning the study site Torres-del-Paine, the mean and standard deviation of the coherence of burnt and unburnt areas has been evaluated. Table 2.7.3 shows the obtained results.

Table 2.7.1: Results of coherence analysis of Torres-del-Paine.

	mean	standard deviation
burnt	0.2131	0.1186
unburnt	0.2067	0.1100
difference	0.0064	0.0086

The results show only minor differences between burnt and unburnt areas, with a relative high standard deviation. Thus, no significant change between burnt and unburnt areas could be observed. One reason for this could be found in volume scattering X-band microwaves, which lead to high changes in vegetated areas outside the burnt area (maybe caused by storms). Microwaves penetrating deeper into the vegetation and reaching the ground layer, as C-band for example, could obtain significant differences.
Unfortunately, no detailed land use/land cover classification was available for this region. Thus, a more extensive analysis was not feasible.

Figure 2.7.1 shows the pre-event, the post-event, the SAR amplitude difference and the interferometric coherence of the burnt area in Grammatico, Greece. The burnt area is partly visible in the SAR amplitude difference image. However, the coherence provides no information about the burnt area. As detailed land use/land cover data (CORINE) were available for Grammatico, La Palma and Andilla, an extensive analysis could be performed. Thus, the mean and standard deviation with respect to vegetation type have been calculated. Table 2.7.4 lists the obtained results.

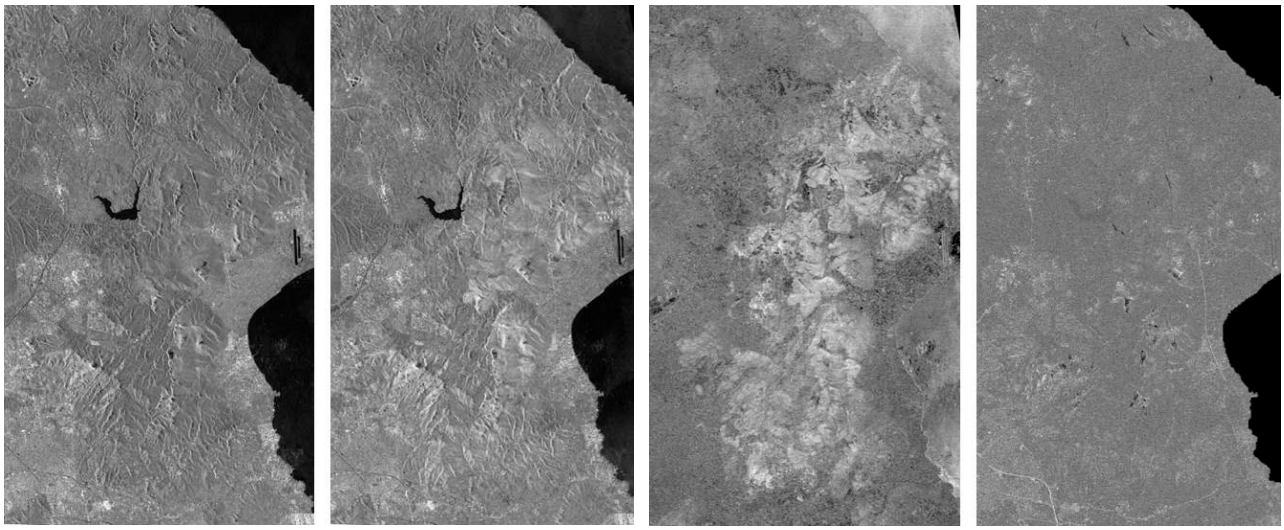

Figure 2.7.1: Burnt area in Grammatico. From left to right: Comparison of the TerraSAR-X pre-disaster scene, the post-disaster scene, the difference image of both and the coherence image.

The analysis showed different results for the three study areas. In Greece and Andilla all burnt areas showed lower values than unburnt areas, whereas higher values could be observed in La Palma. Thus, no consisted trend could be investigated. All change values were quite low (varying between -0.046 and 0.005), with values close to the standard deviation. This indicates that no significant change between burnt and unburnt areas could be observed.

As the acquisition interval of pre- and post- disaster images is between 3 month and > 1.5 years, the obtained results are not satisfying. Phenological differences and various other reasons (e.g. construction projects, deforestation) could lead to high difference values outside the burnt area.

Moreover, the texture parameters of burnt and unburnt objects, with respect to vegetation type, have been evaluated for Grammatico. Several texture parameters included in the eCognition Developer Software, like GLDV contrast, GLDV Ang. 2nd moment, GLDV mean, GLDV entropy, GLCM contrast, GLCM mean, GLCM dissimilarity, GLCM entropy, GLCM correlation and GLCM Ang. 2nd moment have been calculated. The texture parameters are based upon the grey-level co-occurrence matrix after Haralick (GLCM), which is a tabulation of how often different combinations of pixel grey-levels occur in a scene. Another approach to measure texture is to use a grey-level difference vector (GLDV). The GLDV is the sum of the diagonals of the GLCM. It counts the occurrence of references to the neighbor pixels` absolute differences. Both, GLCM and

GLDV are calculated based on the pixels of an object, and are computed for each input layer (eCognition Reference Book, 2014). A more detailed description of GLDV and GLCM can be found in the eCognition Reference Book. As expected due to the high acquisition interval between pre- and post-disaster images, no significant change between the texture parameters of unburnt and burnt objects could be obtained.

Table 2.7.2: Results of coherence analysis in Grammatico, La Palma and Andilla.

Region	CORINE land cover classification	Polarisation	Status	Mean	Stddev.
Grammatico	Complex cultivation patterns	HH	burnt	0.195	0.103
			unburnt	0.200	0.109
			difference	-0.005	-0.006
		VV	burnt	0.198	0.106
			unburnt	0.201	0.108
			difference	-0.003	-0.002
	Land principally occupied by agriculture, with significant areas of natural vegetation	HH	burnt	0.190	0.099
			unburnt	0.193	0.102
			difference	-0.003	-0.003
		VV	burnt	0.194	0.101
			unburnt	0.197	0.104
			difference	-0.003	-0.002
	Coniferous forest	HH	burnt	0.186	0.097
			unburnt	0.187	0.098
			difference	-0.001	-0.001
		VV	burnt	0.188	0.098
			unburnt	0.192	0.101
			difference	-0.004	-0.002
	Natural grasslands	HH	burnt	0.204	0.106
			unburnt	0.240	0.128
			difference	-0.037	-0.022
		VV	burnt	0.218	0.122
			unburnt	0.227	0.122
			difference	-0.009	0.000
	Sclerophyllous vegetation	HH	burnt	0.195	0.102
			unburnt	0.218	0.114
			difference	-0.022	-0.012
		VV	burnt	0.216	0.117
			unburnt	0.240	0.127
			difference	-0.024	-0.010
	Transitional woodland-shrub	HH	burnt	0.193	0.101
			unburnt	0.196	0.103

			difference	-0.003	-0.002
		VV	burnt	0.200	0.107
			unburnt	0.205	0.109
			difference	-0.005	-0.002
La Palma	Vineyards	HH	burnt	0.200	0.104
			unburnt	0.196	0.101
			difference	0.004	0.003
	Pastures		burnt	0.195	0.101
			unburnt	0.195	0.100
			difference	0.000	0.000
	Coniferous forest		burnt	0.201	0.104
			unburnt	0.196	0.101
			difference	0.005	0.003
	Sclerophyllous vegetation		burnt	0.208	0.107
			unburnt	0.206	0.108
			difference	0.002	0.000
Andilla	Vineyards	HH	burnt	0.238	0.123
			unburnt	0.261	0.145
			difference	-0.023	-0.022
	Fruit trees and berry plantations		burnt	0.221	0.118
			unburnt	0.254	0.141
			difference	-0.033	-0.023
	Complex cultivation patterns		burnt	0.229	0.122
			unburnt	0.264	0.145
			difference	-0.035	-0.023
	Land principally occupied by agriculture, with significant areas of natural vegetation		burnt	0.246	0.132
			unburnt	0.275	0.144
			difference	-0.029	-0.011
	Coniferous forest		burnt	0.203	0.106
			unburnt	0.230	0.127
			difference	-0.027	-0.021
	Mixed forest		burnt	0.198	0.102
			unburnt	0.234	0.128
			difference	-0.036	-0.026
	Sclerophyllous vegetation		burnt	0.256	0.133
			unburnt	0.280	0.143
			difference	-0.024	-0.011
	Transitional woodland-shrub		burnt	0.227	0.120
			unburnt	0.273	0.145
			difference	-0.046	-0.025

The work performed shows, that it is important to use pre- and post-disaster data with acquisition intervals as short as possible, with stable weather conditions between the acquisitions, and similar phenological state. A coherence analysis without fulfilling these requirements cannot improve burnt area detection capabilities.

Moreover, using two or more pre-disaster scenes for coherence calculation, or using microwaves of longer wavelength (e.g. C-, L-, or P-band, enabling a higher penetration into the vegetation cover) could also improve fire scar mapping based on phase information (Joyce et al. 2014, Plank 2014, Ulaby 1982).

References

1. eCognition Developer Reference Book, 2014, Trimble Germany GmbH, Munich, Germany.
2. Joyce, K., Samsonov, S., Levick, S., Engelbrecht, J., Belliss, S., 2014: Mapping and monitoring geological hazards using optical, LiDAR, and synthetic aperture RADAR image data, Natural Hazards, 73, 137-163.
3. Plank, S., 2014: Rapid Damage Assessment by Means of Multi-Temporal SAR – A Comprehensive Review and Outlook to Sentinel-1, Remote Sensing, 6, 4870-4906.
4. Ulaby, R.T., Moore, R.K., Fung, A.K., Microwave Remote Sensing, Addison-Wesley: Reading, MA, USA, 1982.

2.7.3 C-band coherence based burnt area mapping using Sentinel-1 SAR imagery

2.7.3.1 Coherence computed within ASAPTERRA

On 13 March 2015 and the following days, a wildfire threatened the city of Valparaiso, Chile. Using this fire event as an example, the usability of C-band SAR interferometry based on a series of Sentinel-1 data was analysed. One pre-event (11 March 2015) and two post-event Sentinel-1 images (04 and 28 April 2015) were used. Burnt area derived by visual interpretation and manual digitalisation of Landsat-8 pre- (01 March 2015) and post-event (02 April 2015) data was used as reference (fig. 2.7.2).

Method

After co-registration of the Sentinel-1 imagery, two coherence datasets were generated. One between the pre- and the first post-event acquisition (named co-event coherence in the following) and one between the two post-event SAR imagery (named post-event coherence in the following). The coherence was estimated by 16 looks in range and 4 looks in azimuth. Then, the difference between the co-event and the post-event coherence was computed and the possible burnt area was classified by thresholding of the coherence difference image (fig. 2.7.2).

Results and discussion

Burnt area is characterised by lower values at the co-event coherence compared to the unburnt area in the surroundings (fig. 2.7.2c). The reason for this is de-correlation caused by strong changes on the ground due to the fire event. Contrary to this, the burnt area cannot be distinguished from the unburnt area when looking at the post-event coherence. The difference between the co-event and the post-event coherence enables the separation of burnt and unburnt area (fig. 2.7.2e, f).

Comparison with reference data obtained from analysis of optical Landsat-8 imagery (fig. 2.7.2.b) gives following accuracy values: overall accuracy 93.1%, KHAT 0.52, burnt area user's and producer's accuracy of 70.5% and 45.9%, respectively.

In spite of the relatively good classification results, one has to notice, that the described procedure is a semi-automatic approach. Thresholding is done manually. Moreover, optical imagery is always required to verify that the change that was classified by the SAR coherence change detection was caused by a fire event.

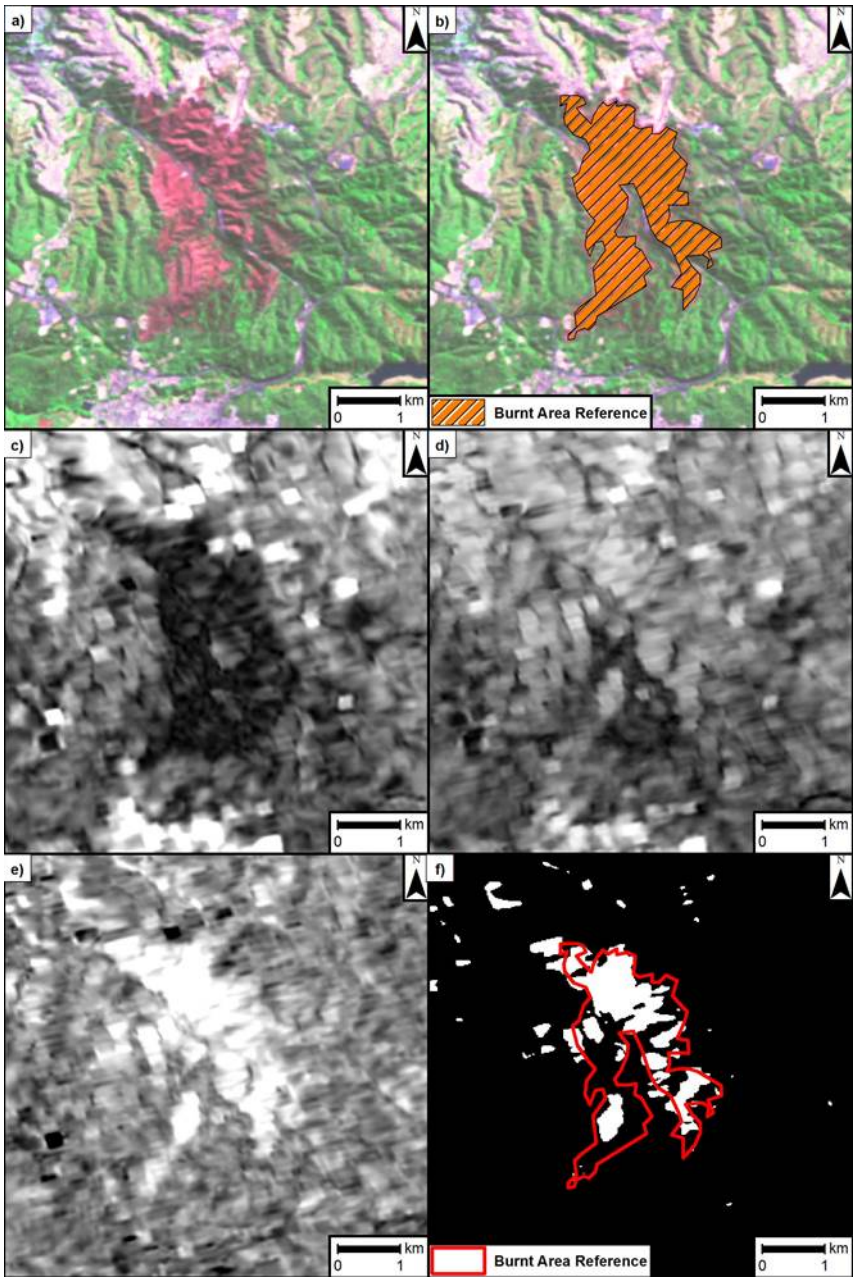

Figure 2.7.2: a) Landsat-8 post event imagery acquired on 02 April 2015 (SWIR/NIR/Green); b) burnt area derived from Landsat-8 post event imagery; c) co-event Sentinel-1 coherence; d) post-event Sentinel-1 coherence; e) difference of co-event and post-event Sentinel-1 coherence; f) classified burnt area (white) based on coherence difference and comparison with reference burnt area (red).

2.7.3.2 Geohazards Exploitation Platform – analysis of the S-1 InSAR Browse service results

This chapter describes the suitability analysis of the Sentinel-1 InSAR Browse Service results for burnt area mapping. This processor is part of ESA's Geohazards Exploitation Platform (GEP). The suitability analysis was performed for three test sites (tab. 2.7.3), for which a series of Sentinel-1

acquisitions and corresponding coherence data computed from consecutive Sentinel-1 data pairs was available. The spatial resolution of the data is 50 m.

Table 2.7.3: Test sites.

Test site	Location	Date of fire	Sentinel-1 data pairs
NW of Marseille, France	Ensues-la-Redonne	15 July 2016	01/07/16 & 13/07/16
	Rognac, Vitrolles	10 August 2016	13/07/16 & 25/07/16 25/07/16 & 06/08/16 06/08/16 & 18/08/16
NW Portugal	Between Porto, Aveiro and Viseu	11-14 August 2016	12/07/16 & 24/07/16 24/07/16 & 05/08/16 05/08/16 & 17/08/16 17/08/16 & 29/08/16 29/08/16 & 10/09/16
N Sardinia, Italy	Borore	4 July 2016	27/05/16 & 08/06/16 08/06/16 & 14/07/16 14/07/16 & 26/07/16

Method

First, a visual analysis of the data provided by the GEP was performed. The amplitude of the Sentinel-1timeseries showed no salience, the burnt area could not be identified. In contrast to this, analysis of the coherence showed a strong decrease of this parameter when comparing the coherence computed from a pre-event pair with the one computed from a co-event pair, including the time of the fire event. After the fire event, the coherence increases again.
Second, to support the visual analysis, several statistics were calculated:

Absolute amplitude difference: $|\Delta_{ampl}| = |ampl(t_1) - ampl(t_2)|$

Absolute coherence difference: $|\Delta_{coh}| = |coh(t_1 \& t_2) - coh(t_2 \& t_3)|$

In accordance to the visual analysis of the single amplitude images, the burnt area could not be identified in the absolute amplitude difference $|\Delta_{ampl}|$. But, the absolute coherence difference $|\Delta_{coh}|$ showed a signature that was suited for further analysis. To further emphasis the influence of a fire event on the Sentinel-1 coherence, following parameter was computed:

Absolute deviation of the coherence to the mean of each single coherence pair i:

$$|\Delta(\mu_{coh})| = |\mu_{coh} - coh_i|$$

With

$$\mu_{coh} = \frac{(coh_1 + coh_2 + \cdots + coh_n)}{n}$$

Thereby, it is important to notice that the coherence pair including the time of the fire event is excluded from the computation of the mean μ_{coh}.

Results and discussion

Figures 2.7.3, 2.7.4 and 2.7.5 show the results for the three test sites described in table 2.7.3. The first row of each figure shows (from left to right): the reference burnt area information derived from optical satellite imagery (Landsat-8 or Pléiades, respectively); a comparison of the Sentinel-1 based classification results with the reference; the final Sentinel-1 based classification result. The second row presents the absolute amplitude difference $|\Delta_{ampl}|$ of consecutive Sentinel-1 data pairs. In the next row the coherence between these data pairs and in row four the absolute coherence difference $|\Delta_{coh}|$ are shown. The last row shows the absolute deviation of the coherence to the mean for each single coherence pair $|\Delta(\mu_{coh})|$.

As described above, at all three test sites it is not possible to identify the burnt area by means of the SAR amplitude or by the difference of consecutive amplitude pairs. At a spatial resolution of 50 m there is no significant change in this C-band SAR amplitude between consecutive Sentinel-1 acquisitions to map the burnt area.

In contrast to this, at two test sites, Marseille and Portugal, the coherence is better suited for the identification of the burnt area. Especially the absolute deviation of the coherence to the mean shows a strong signature. The coherence is highly influenced by changes on the ground in the time between the two SAR acquisitions. High coherence represents stable conditions while low coherence values represent strong changes on the ground. A fire event changes the characteristics of the SAR backscatter at the ground and leads to a decrease of the coherence for the image pair that includes the time of the fire event. The advantage of the absolute deviation of the coherence to the mean $|\Delta(\mu_{coh})|$ compared to the single absolute coherence difference $|\Delta_{coh}|$ is that small changes not related to the fire event are averaged.

The described methodology shows suitable results for burnt area mapping at the test sites Marseille and Portugal. However, at the Sardinia test site, it is very hard to identify the burnt area. This can be explained by the long temporal baseline of 36 days for the Sentinel-1 data pair including the fire event (cf. tab. 2.7.3). The normal temporal baseline between the Sentinel-1 (A) images analysed is 12 days. This is the case for all data pairs of the Portugal and the Marseille test sites. However, as for the Sardinia test site the temporal baseline is three times longer than 12 days, a lot of changes occurred on the ground which are not related to the fire event itself. During these 36 days the temporal baseline decreased over the entire study site, making it impossible to identify the Borore burnt area.

Furthermore, a semi-automated object based classification of the burnt area based on the absolute deviation of the coherence to the mean was performed for the test sites Marseille and Portugal, for which a suitable Sentinel-1 time series (temporal baseline 12 days) was available. The object-based classification procedure consists of empirical thresholding and region growing procedures. Both classification results show a good agreement with the corresponding reference data derived from optical satellite imagery (table 2.7.4).

Table 2.7.4: Accuracy assessment of the classification results based on the absolute deviation of the coherence to the mean.

Test site	Match with reference	Missed alarm	False alarm
NW of Marseille, France (average)	60%	40%	34%
NW of Marseille, France (Ensues-la-Redonne)	42%	58%	3%
NW of Marseille, France (Rognac, Vitrolles)	67%	33%	15%
NNW Portugal	55%	45%	8%
N Sardinia, Italy	Classification not possible	-	-

In conclusion, the Sentinel-1 InSAR Browse Service of ESA's GEP shows some potential for burnt area mapping. The overlap percentages presented in table 2.7.4 demonstrate that the described procedure enable a rough mapping of burnt areas. The minimum size of an area to be detected is ca. 2 ha. In future, the currently relatively low accuracy values could be increased when Sentinel-1B is fully operational, i.e. when the Sentinel-1A and B constellation regularly provides SAR imagery at a 6 days repeat cycle. This would decrease the temporal correlation caused by changes on the ground, which are not related to the fire event itself. Therefore, the consequences of a fire event, i.e. a burnt scar, would more stand out in the coherence imagery.
The data analysed in this study has a spatial resolution of 50 m. The original resolution of Sentinel-1 data is 20 m. It is assumed that this higher spatial resolution would enable a better use of the SAR amplitude.

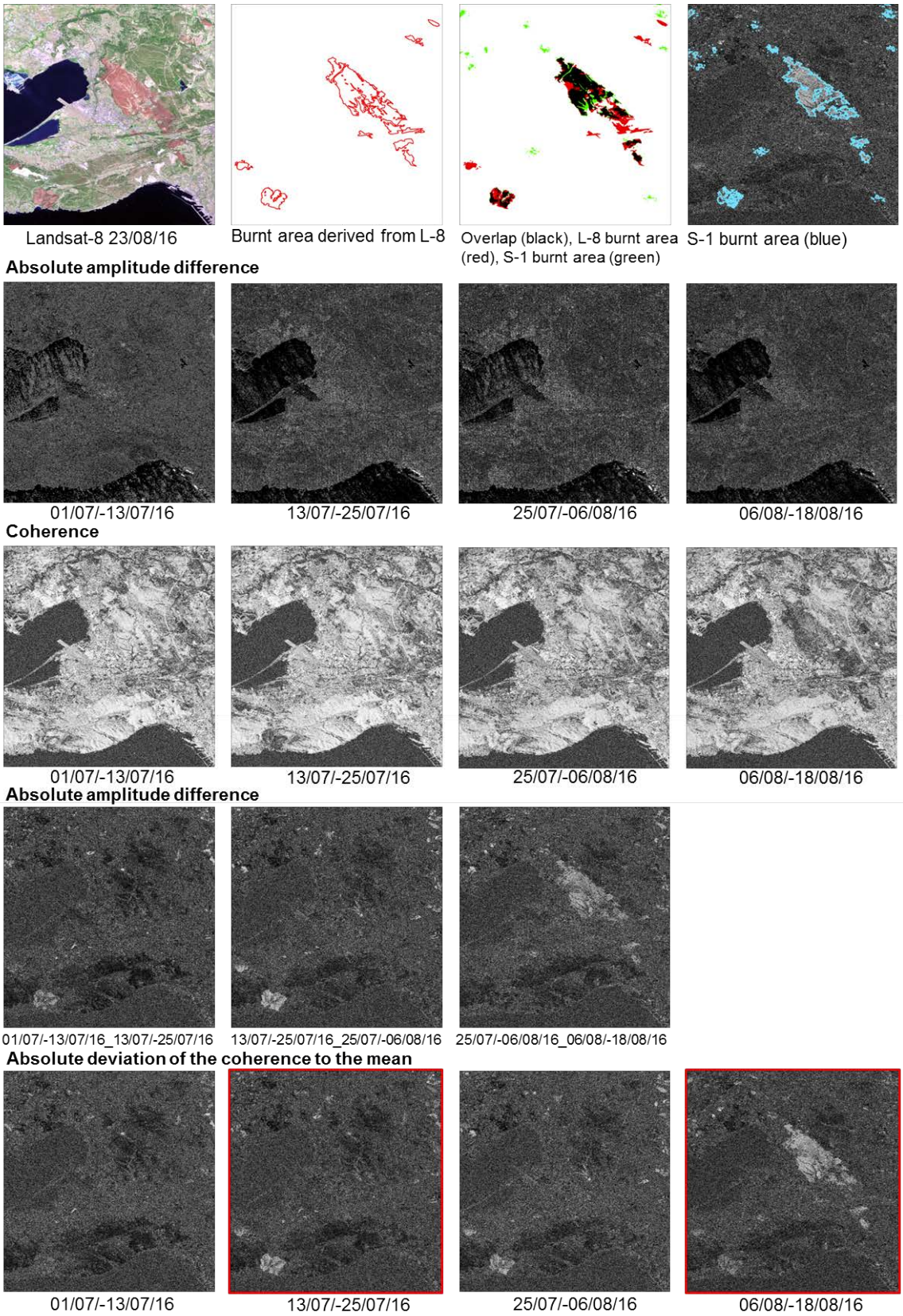

Figure 2.7.3: Results of the Marseille, France, test site.

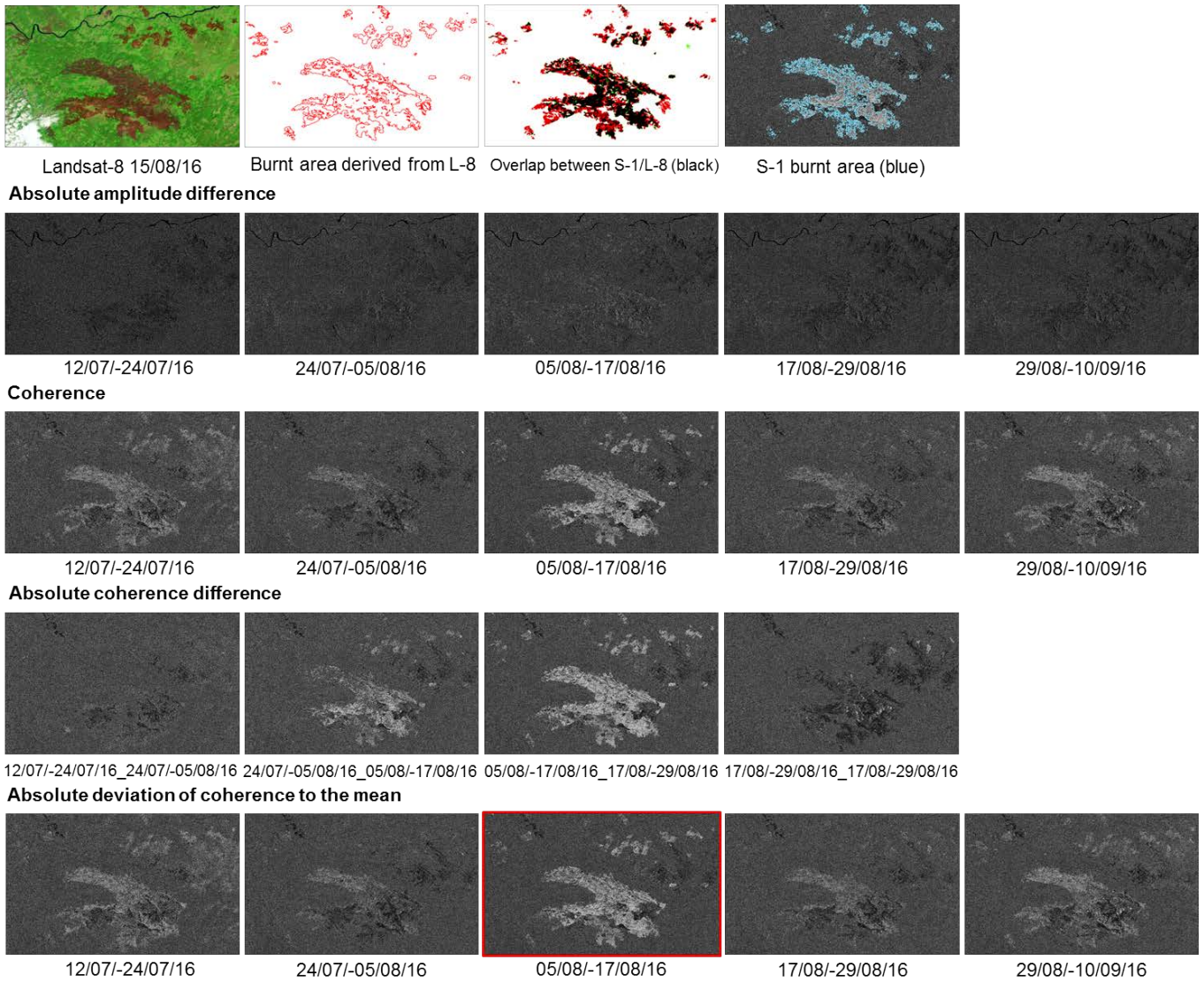

Figure 2.7.4: Results of the Portugal test site.

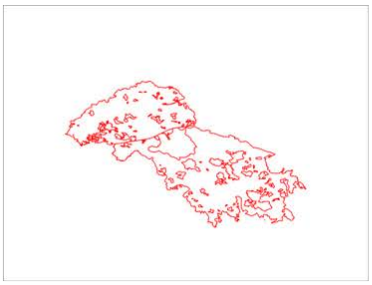

Burnt area derived from Pléiades-1A 16/07/16

Absolute amplitude difference

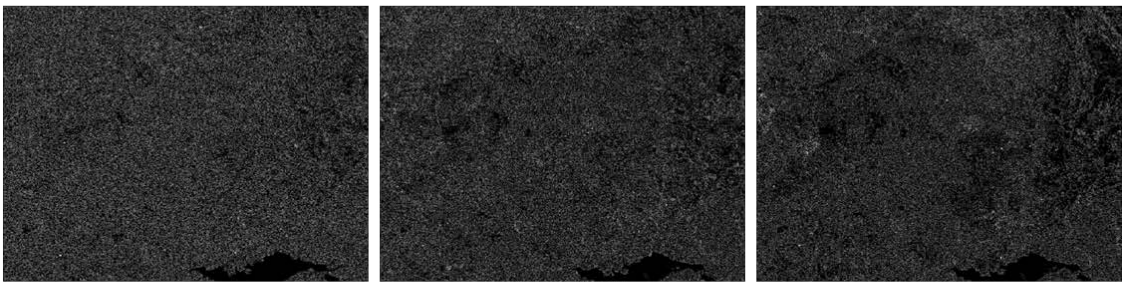

27/05/-08/06/16 08/06/-14/07/16 14/07/-26/07/16

Coherence

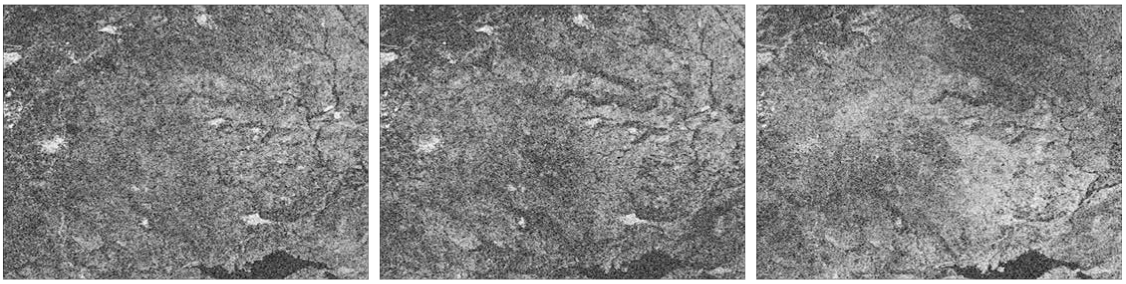

27/05/-08/06/16 08/06/-14/07/16 14/07/-26/07/16

Absolute coherence difference

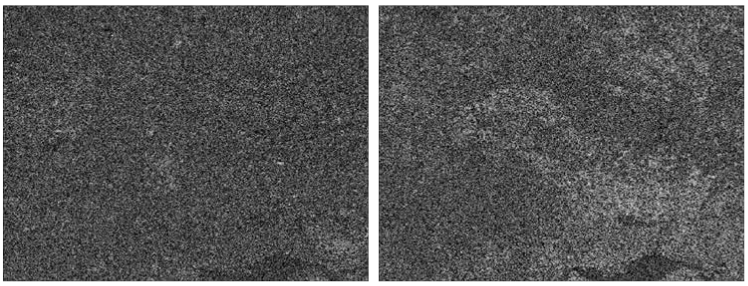

27/05/-08/06/16_08/06/-14/07/16 08/06/-14/07/16_14/07/-26/07/16

Absolute deviation of coherence to the mean

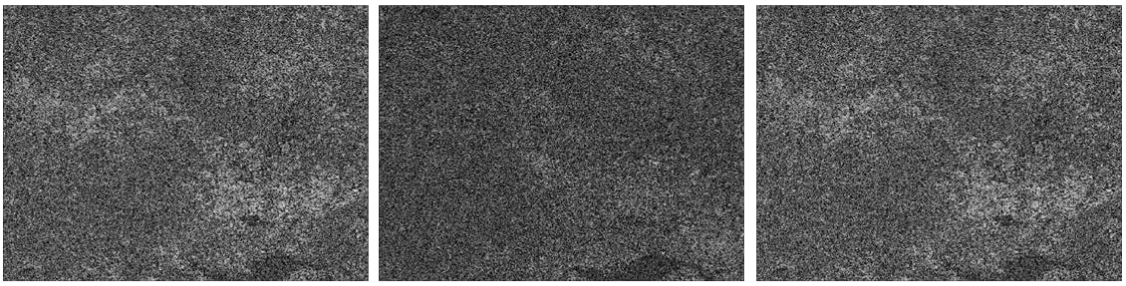

27/05/-08/06/16 08/06/-14/07/16 14/07/-26/07/16

Figure 2.7.5: Results of the Borore, Sardinia, Italy, test site.

2.7.4 SAR change detection based burnt area mapping using Sentinel-1 amplitude images

A devastating fire took place in Bullsbrook, Australia from 09 January until 12 January 2015, and destroyed approximately 7000 ha of land. More information about the fire and how the optical reference layer has been produced can be found in section 2.6.1.

Not only optical data, but also C-band SAR data (Sentinel-1) have been used to map the burnt area. An image pair consisting of pre-disaster (acquired on 24 November 2014) and post-disaster (acquired on 11/01/2015) data has been used for the analysis. No precipitation took place between these two acquisition dates. A detailed pre-processing took place, including radiometric calibration and terrain correction (using the Range-Doppler algorithm implemented in ESA's Sentinel-1 Toolbox). The analysis of the burnt area was performed using a semi-automated, object-based change detection algorithm suited for rapid mapping activities. The algorithm is based on SAR change detection techniques (difference, ratio, normalised change index) in conjunction with a fuzzy classification approach and post-classification refinement. The method is described in more detail in Bernhard et al. (2011). Figure 2.7.2a shows the difference image of Sentinel-1 pre- and post-disaster data. The burnt area is clearly visible in dark grey (high difference values between pre- and post-disaster images), whereas unchanged areas of the scene appear in bright grey. The extracted burnt area extent by the SAR data is highlighted in figure 2.7.2b.

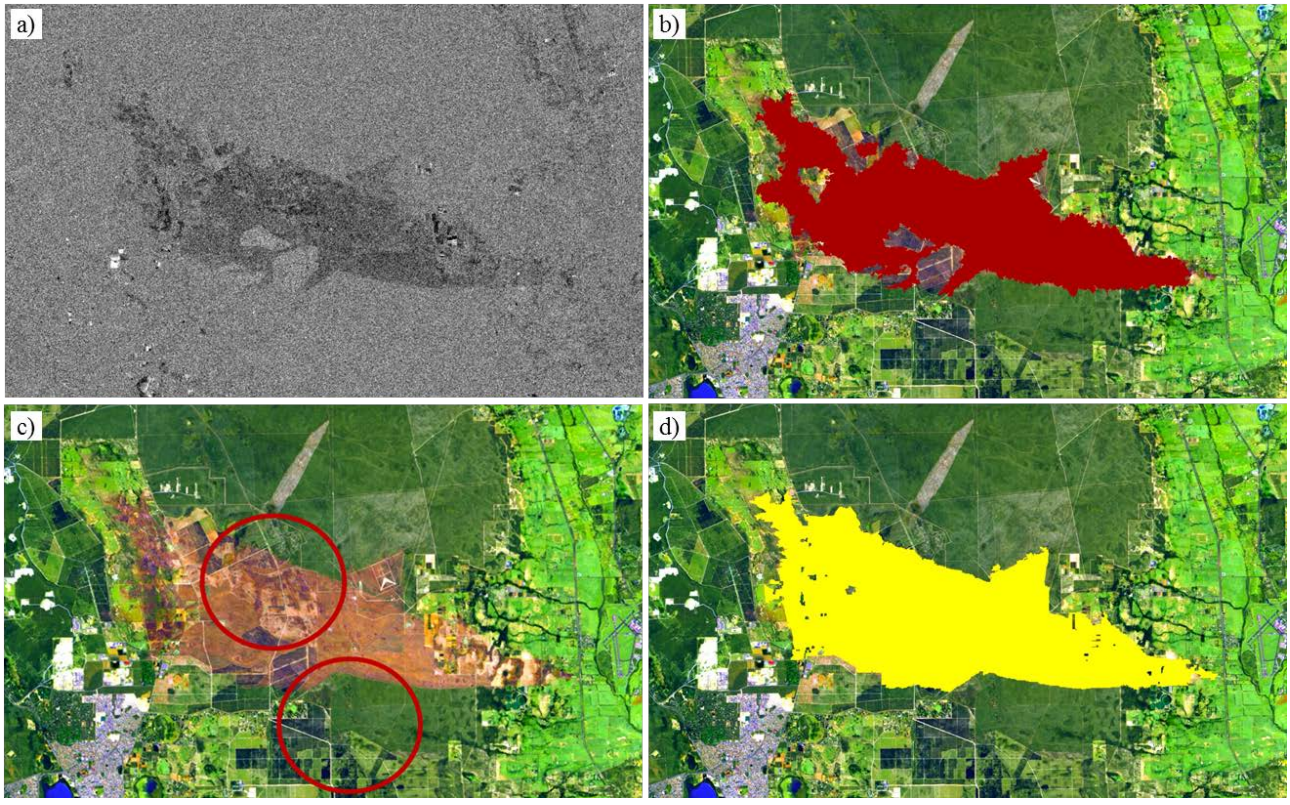

Figure 2.7.2: Comparison of the difference image of Sentinel-1 pre- and post-disaster data (a), the classification result of the SAR method (b), the burnt area shown by a Landsat-8 false colour composite (red=MIR, green=NIR, blue=green) (c), and the classification result of the optical method (d).

A Landsat-8 false colour composite (combination: red=MIR, green=NIR, blue=green) acquired on 20/01/2015 saves as backdrop. The classified SAR burnt area follows more or less the difference image, and maps the affected area very well (see comparison between fig. 2.7.2b, c and d). The fire was under control on 11 January 2015, but still burning. Hence, this could explain why some burnt areas visible in the optical image (highlighted with circles in fig. 2.7.2c) could not be detected by the SAR image, as this was acquired on 11 January 2015. Another explanation could be given by different pre-fire vegetation type and density. As shown by Bernhard et al. (2015), pre-fire vegetation cover has an important impact on fire mapping capabilities. Unfortunately, detailed land cover classification was not available for this area. As these areas appear in different shades of brown in figure 2.7.2c, it can be concluded that these areas have been affected by a different fire severity, which is a combination of pre-fire vegetation and fire intensity.

Comparison of the results based on the SAR data with the analysis of the optical reference data gives following accuracy values: overall accuracy 99.6%, KHAT 0.85; burnt area user' and producer's accuracy: 95.4% and 76.1%, respectively.

2.8 Technical note on 3D analysis in burnt area mapping

2.8.1 State-of-the-art - soil erosion vulnerability

Post-fire soil erosion is a major risk to forest habitats given the long term often permanent damage that ensues. As soil regeneration occurs over geological time-scales serious erosion is generally considered irreversible (San-Miguel-Ayanz et al. 2012).

The Mediterranean region is particularly prone to post-fire water erosion due to its climatic and physical factors: topography (often steep) combined with a climate with long dry summer periods which are often interspersed with fire events followed by heavy autumnal downpours (Gitas et al. 2009). A number of candidate soil erosion estimate models have been developed, tested and implemented over the years such as the Universal Soil Loss Equation (USLE) (Wischmeier and Smith 1978), Water Erosion Prediction Project (WEPP) (Laflen et al. 1991), the Morgan–Morgan–Finney (MMF) (Morgan, Morgan & Finney in Morand and Duzant 2008), and European Soil Erosion Model (EUROSEM) (Morgan et al. 1998). They all have their advantages and disadvantages. A large community of soil scientists use and develop the WEPP and Morgan derived models (Jasrotia and Singh 2006, Ustun, 2008) which are adapted to intensive studies looking for accurate models of complex natural processes including erosion and deposition and many factors relating to this. There are also on-line resources to help in implementing these kinds of models (http://milford.nserl.purdue.edu/).

Whereas physical-based models emulate the real in-field processes, unfortunately many parameters related to each process and hence sub-models are required related to hydrology, hydraulics, meteorology and soil mechanics (Bhattarai and Dutta 2006).

The Universal Soil Loss Equation (USLE) is an empirical equation designed for the computation of average soil loss in agricultural fields. This equation was developed for detachment capacity limited erosion in fields with negligible curvature and no deposition and represents soil loss averaged over time and total area. The equation has the following form (Wischmeier and Smith 1978).

$$A = R * K * LS * C * P$$

where A is the average soil loss, R, is the rainfall intensity factor, K is the soil factor, LS is the topographic (length-slope) factor, C is the cover factor and P is the prevention practices factor. Various modifications of this equation are often applied to the estimation of soil loss using GIS (e.g., Warren et al. 1989).

Revised USLE (RUSLE) uses the same empirical principles as USLE however it can include numerous improvements, such as monthly factors, incorporation of the influence of profile convexity/concavity using segmentation of irregular slopes, and improved empirical equations for the computation of LS factor (Foster and Wischmeier 1974).

A large community of soil erosion work uses and investigates how to improve (de Asis and Omasa 2007, Pal and Samanta 2011) and/or implement this set of models with on-line resources being

available aimed at helping to understand how to implement such a model (Mitasova et al.) and from the official website: www.sedlab.olemiss.edu/rusle (Yoder et al. 1995). Many authors suggest that the RUSLE model can be improved such as concerning the *C* factor through integrating a multi-temporal satellite image coverage which takes intra-annual vegetation cover dynamics into account (Schoettker et al. 2012). Generally, remote sensing is used as an input for the *C* factor (LULC, dynamic vegetation cover), less so the *K* soil erodibility factor, and of course remote sensing can be used to derived Digital Elevation Models and can hence provide input to the LS factor.

References about work in this field, supported by the Copernicus (former GMES) program, indicate the involvement of the JRC in soil erosion applications. The RUSLE is mentioned in a 2012 document (San-Miguel-Ayanz 2012) for its use to model water driven soil erosion. In this context EFFIS employs RUSLE at the European scale. In this document the RUSLE is stated to be used in a three stage process that estimates daily total overland flow runoff, sediment transport and long-term average erosion rates. This service will be available on EFFIS in 2014.

The JRC/IES/Land Resource Management Unit/SOIL Action and the Lab of Forest Management and Remote Sensing, School of Agriculture, Forestry and Natural Environment of the Aristotle University of Thessaloniki have been working together within the geoland2 project to develop a soil erosion model called the “G2 model for erosion” that works on a local to regional scale. This model could be called a Revised USLE model as it is founded to a large extent on the USLE. The formula of the G2 erosion model is:

$$E = (R/V) * S * (T/I)$$

Where

- *E*: erosion (t ha-1)
- *R*: rainfall erosivity (original USLE formulas or alternatives developed by G2 or other authors)
- *V*: vegetation retention (developed by G2 using BIOPAR and land use/management databases, e.g. CORINE)
- *S*: soil erodibility (original USLE formulas or modified from USLE by JRC, 2000-5)
- *T*: topographic influence (USLE modifications, 1996 simulation of original USLE conditions)
- *I*: slope intercept (developed by G2 using satellite data corrective to *T* partially analogous to *P* of USLE)

The G2 model uses harmonised standard input data from European and global databases, such as the LUCAS soil database, the European Soil Database (ESDB), the Topsoil Organic Carbon (TOC), BioPar products of geoland2, Image 2006 imagery, CORINE LC, Landsat TM, the ASTER DEM datasets, and other large public datasets. As a data-oriented model, the cartographic scale of a G2 implementation is determined by the spatial resolution of the input data (Panagos 2014).

In drafting the sub-tasks related to task 3.2.7 ‘3D Fire Damage Assessment Map’ SERTIT indicated it would investigate the implementation of the RUSLE model as it seemed both accepted and accessible, ease of implementation within a GIS is also considered, for an entity not having an extensive soil science specialisation. This investigation into the state-of-the-art confirms this position/opinion. Forests and hence forest fires, the main thematic axes of this project, occur mostly on terrain that would not be conducive to net long term soil deposition (mostly river beds); accept through in situ development or wind-blown deposition.

References

1. Bhattarai, R., Dutta, D., 2006: Estimation of Soil Erosion and Sediment Yield Using GIS at Catchment Scale. Springer Science & Business Media B.V.
2. de Asis, A. M., Omasa, K., 2007: Estimation of vegetation parameter for modelling soil erosion using linear Spectral Mixture Analysis of Landsat ETM data. ISPRS Journal of Photogrammetry & Remote Sensing, 62, 309–324.
3. Foster, G.R., Wischmeier, W.H., 1974: Evaluating irregular slopes for soil loss prediction. Transactions of ASAE, 17(1), 305-309.
4. Gitas, I. Z., Douros, K., Minakou, C., Silleos, G. N., Karydas, C. G., 2009: Multi-temporal soil erosion risk assessment in North Chalkidiki using a modified USLE raster model. EARSeL eProceedings 8, 1/2009.
5. Jasrotia, A. S., Singh, R., 2006: Modeling runoff and soil erosion in a catchment area, using the GIS, in the Himalayan region, India. Environmental Geology, 51, 29-37.
6. Laflen, J.M., Lane, L.J., Foster, G.R., 1991: WEPP – a next generation of erosion prediction technology. Journal of Soil Water Conservation, 46(1), 34–38.
7. Mitasova, H., Brown, W.M., Hohmann, M., Warren, S., Using Soil Erosion Modeling for Improved Conservation Planning: A GIS-based Tutorial Geographic Modeling Systems Lab. UIUC, Engineering Research and Development Center, http://www4.ncsu.edu/~hmitaso/gmslab/reports/CerlErosionTutorial/denix/default.htm.
8. Morgan, R.P.C., Quinton, J.N., Smith, R.E., Govers, G., Poesen, J., Auerswald, K., Chisci, G., Torri, D., Styczen, M.E., 1998: The European Soil Erosion Model (EUROSEM): a dynamic approach for predicting sediment transport from fields and small catchments. Earth Surface Processes and Landforms, 23, 527-544.
9. Pal, B., Samanta, S., 2011: Estimation of soil loss using remote sensing and geographic information system techniques (Case study of Kaliaghai River basin, Purba & Paschim Medinipur District, West Bengal, India). Indian Journal of Science and Technology, 4, 10.
10. Panagos, P., Karydas, C.G., Ballabio, C., Gitas, I.Z., 2014: Seasonal monitoring of soil erosion at regional scale: An application of the G2 model in Crete focusing on agricultural land uses. International Journal of Applied Earth Observations and Geoinformation, 27PB, 147-155, DOI:10.1016/j.jag.2013.09.012.
11. San-Miguel-Ayanz, J., Schulte, E., Schmuck, G., Camia, A., Strobl, P., Liberta, G., Giovando, C., Boca, R., Sedano, F., Kempeneers, P., McInerney, D., Withmore, C., Santos de Oliveira, S., Rodrigues, M., Durrant, T., Corti, P., Oehler, F., Vilar, L., Amatulli, G., 2012: Comprehensive Monitoring of Wildfires in Europe: The European Forest Fire Information System (EFFIS). Approaches to Managing Disaster - Assessing Hazards, Emergencies and Disaster Impacts, Prof. John Tiefenbacher (Ed.).

12. Schoettker, B., Searle, R., Schmidt, M., Phinn, S., 2012: High temporal frequency biophysical and structural vegetation information from multiple remote sensing sensors can support modelling of event based hill-slope erosion in Queensland. International Archives of the Photogrammetry, Remote Sensing and Spatial Information Sciences, XXXIX-B8, XXII ISPRS Congress, 25 August – 01 September 2012, Melbourne, Australia
13. Ustun, B., 2008: Soil erosion modelling by using GIS & remote sensing: a case study, Ganos mountain. The International Archives of the Photogrammetry, Remote Sensing and Spatial Information Sciences, XXXVII, Part B7, Beijing.
14. Warren, S.D., Diersing, V.E., Thompson, P.J., Goran, W.D., (1989): An erosion-based land classification system for military installations. Environmental Management, 13, 251-257.
15. Wischmeier, W. H., Smith, D.D., 1978: Predicting rainfall erosion losses—a guide to conservation planning, U.S. Department of Agriculture, Agriculture Handbook No. 537.
16. Yoder, D.C., Foster, G.R., Weesies, G.A., Renard, K.G., McCool, D.K., Lown, J.B.: Evaluation of the RUSLE Soil Erosion Model, http://s1004.okstate.edu/S1004/Regional-Bulletins/Modeling-Bulletin/rusle-yoder-001016.html
17. Yoder, D.C., Lown, J.B., 1995: The future of RUSLE: Inside the new Revised Universal Soil Loss Equation. J. Soil and Water Conserv. 50(5), 484-489.

2.8.2 Indicator of areas vulnerable to soil erosion based on the RUSLE model

SERTIT worked on a spatial modelling method to derive a soil detachment/erosion indicator and will probably base its work on the Universal Soil Loss Equation (USLE) family of models.

Both the standard and modified equations can be properly applied only to areas experiencing net erosion. Depositional areas should be excluded from the study area. The results can also be interpreted as an extreme case with maximum possible spatial extent of erosion.

Using an appropriate soil erosion model, areas at risk can be estimated and can provide information about current erosion, its trends and allow scenario analysis. The integration of existing soil erosion models, field data and data provided by remote sensing technologies, through the use of geographic information systems (GIS), appears to be a lively field of R&D and applications activity. Moreover, higher soil erosion risk can be linked to a number of factors such as steep slopes, climate characteristics, inappropriate land use, land cover patterns (e.g. sparse vegetation) and ecological disasters (e.g. forest fires). The RUSLE soil erosion model is illustrated below in figure 2.8.1.

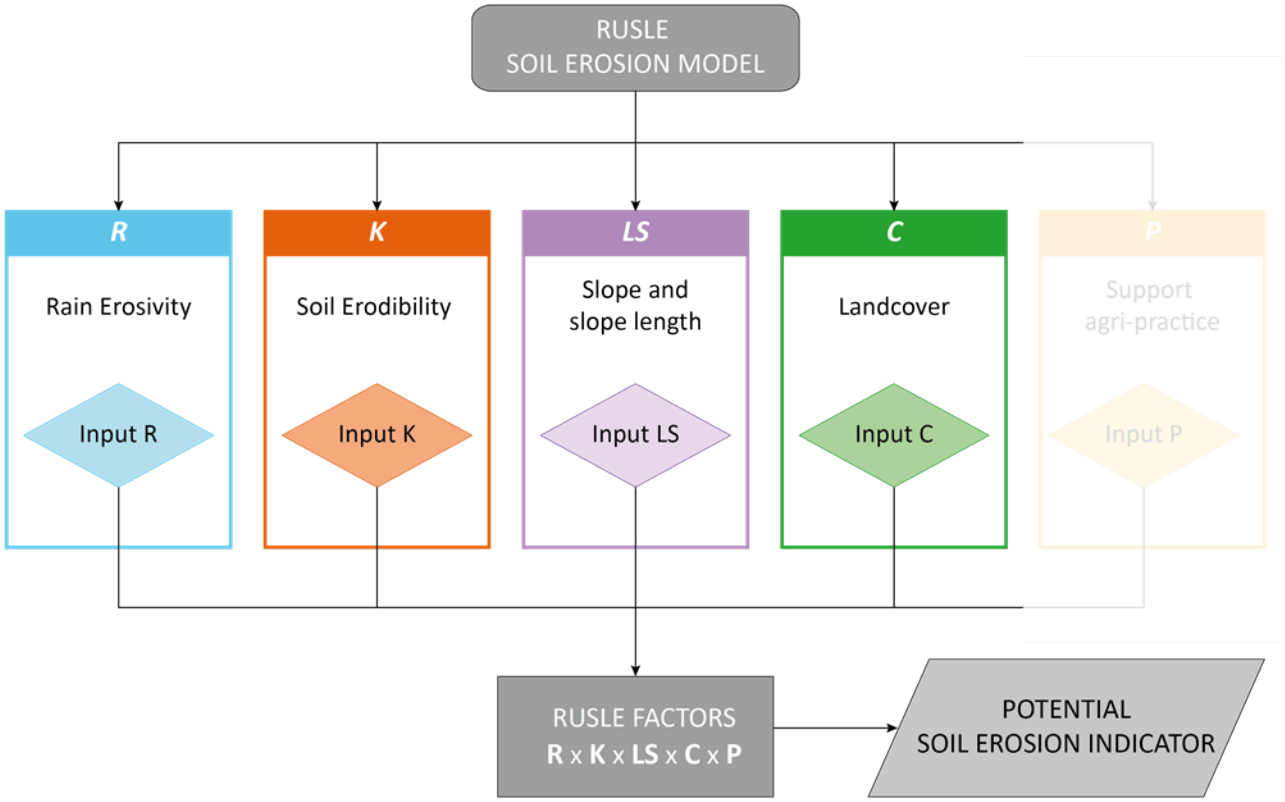

Figure 2.8.1: The RUSLE soil erosion model. Given the lack of information on prevention practices it has been decided to not consider the *P* factor and hence it is illustrated with transparency. The result is named the Soil erosion susceptibility index (SESI).

LS parameter

The *LS* factor has been quite a challenge given the number of different ways it can be calculated depending upon the inputs. Firstly, the influence of the surface topography on erosion process is expressed through the *LS* factor. It combines two features - slope length (*L*) and slope steepness (*S*). The slope length is defined as the horizontal distance from the origin of the overland flow to the point where either the slope gradient decreases enough that deposition begins, or runoff becomes concentrated in a defined channel (Wischmeier and Smith 1978, Renard et al. 1997). When the slope length is measured in meters, the *L* factor is calculated as follows (Wischmeier and Smith 1978):

$$LS = \left(\frac{\lambda}{22.13}\right)^{m}$$

where λ is the slope length, m is the slope length exponent which is taken as 0.5 for steepness of 5% or more, which represents the vast majority of the tests areas.

In Bizuwerk et al. (2008) this equation was modified for GIS applications involving raster data:

$$LS = \left(FA\frac{P}{22.13}\right)^{m}$$

where λ = Flow Accumulation (*FA*) * Pixel size (*P*)

The slope steepness factor (*S*) can be calculated as follows Wischmeier and Smith (1978):

$$S = 0.065 + 0.045S + 0.0065S^2$$

where *S* represents percent slope. Overall, it is then proposed to calculate *LS* in a single index:

$$LS = \left(\frac{\lambda}{22.13}\right)^{m}(0.065 + 0.045s + 0.0065s^2)$$

Or for raster GIS applications:

$$LS = \left(FA\frac{P}{22.13}\right)^{m}(0.065 + 0.045s + 0.0065s^2)$$

Over a Réunion Island test site a DEM derived from a Pléiades stereo-pair that was generalised and resampled to 5m pixel size was used to generate this factor over the AOI using the above equation. In the literature certain land-cover classes often are eliminated from the *LS* calculation as little or no flow accumulation and erosion occurs.

To investigate the effect vegetation land-cover classes might have on the distribution of Flow Accumulation values SERTIT removed vegetated surfaces from the Flow Direction calculation and then applied Flow Accumulation for a pre-fire and a post fire date. In the resulting *LS* calculations quite a difference can be seen as few surfaces are vulnerable to Flow Accumulation in the pre-fire *LS* factor whereas the area is much more susceptible to Flow Accumulation and therefore erosion during the year after the fire (fig. 2.8.2).

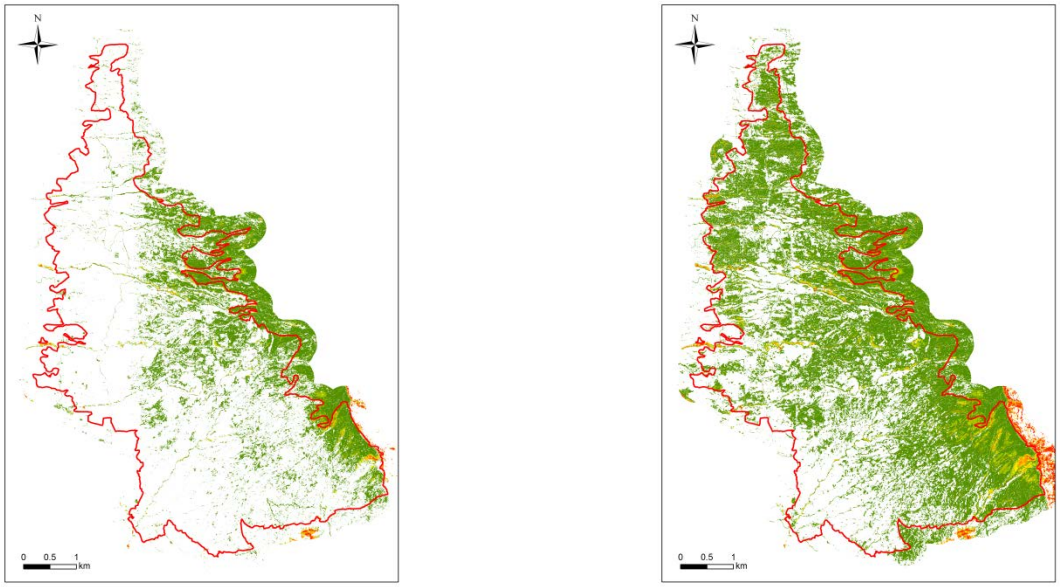

Figure 2.8.2: Pre-fire (left) and post-fire (right) *LS* factors.

C factor

The C parameter is related to the impact of the landcover on soil erosion and is mainly linked to the proportion of vegetation cover. It is defined as the ratio between the erosion induced by a specific landcover type and the erosion of an equivalent bare soil. *C* factor values are related to different parameters (vegetation type, development stage of the vegetation, proportion of vegetation cover) and range between 0 and 1 (0 corresponding to a complete soil cover implying no erosion, and 1 to a bare soil where the erosion is maximum).

As indicated in figure 2.8.1 it is possible to compute the *C* factor from EO satellite imagery from the NDVI, which values are typically comprised between -1 and 1 (vegetation has generally values higher than 0.18). In their study, Gitas et al. (2009) used Landsat 7 data to compute the NDVI. The conversion from NDVI into *C* factor is given thanks to the following expression:

$$C = exp\left(-a\frac{NDVI}{\beta - NDVI}\right)$$

where a = 2 and β = 1 provide satisfying results according to the author, and requires a NDVI ranging in the [0, 1] interval.

Figure 2.8.2 presents an example of the NDVI and the *C* factor derived from a Pléiades image after the fires in the Maido area.

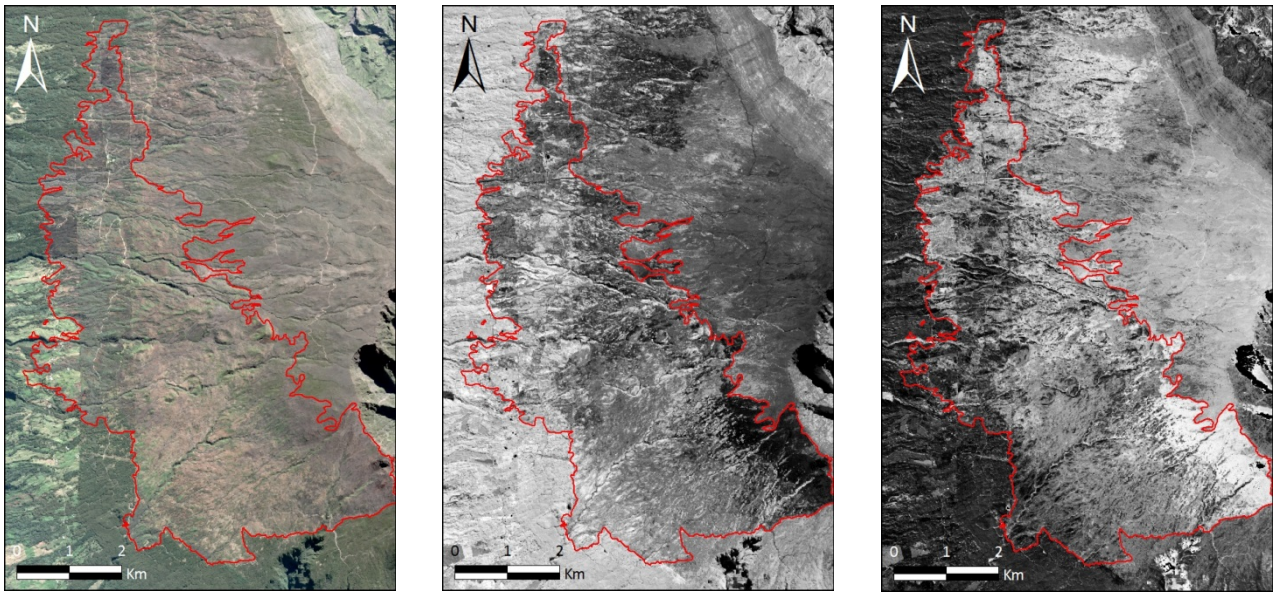

Post-fire Pléiades image (01/07/2012) | NDVI of post-fire Pléiades data | Post-fire *C* factor

Figure 2.8.2: Example of *C* factor generation from a post-fire Pléiades image (01/07/2012).

This method of C-factor is chosen as it is calculated with respect to the vegetation cover at the time of image acquisition and doesn't depend on a LULC classification which may no longer represent vegetation cover, notably due to fires.

R parameter

This parameter is the rainfall erosivity factor (or index). This is the rainfall contribution to the more global erosivity, which represents the capacity of rainfall, wind and runoff to induce erosion, and which can be viewed as an indicator of regional variations in erosion potential. As Morgan (2005) explains in his book entitled "Soil erosion & conservation" soil loss is closely related to rainfall partly through the detaching power of raindrops striking the soil surface and partly through the contribution of rain to runoff. The rainfall erosivity factor is then related to the kinetic energy of the rain and is therefore a function of the intensity and duration of rainstorms.

There are different ways of calculating this factor. For example, Fournier (1960) proposes the ratio p^2/P where p is the highest mean monthly precipitation and P is the mean annual precipitation. To reduce the shortcomings induced in the index by taking into account only precipitation values into one month, a modified Fournier Index (*MFI*) has been introduced by Arnoldus (1980):

$$MFI = \sum_{i=1}^{12} \frac{p_i^2}{P}$$

where p_i is the mean monthly precipitation and P is the mean annual rainfall. In his study, Arnoldus (1980) uses the average of either 8 or 10 years rainfall data to compute the *MFI* index.

Gitas et al. (2009) uses the following equation (similar to the original *MFI*) to derive the *R* factor:

$$\log R = 1.93\ log \sum_{i=1}^{12} \frac{p_i^2}{P} - 1.52$$

The network of meteorological stations is not dense enough over the study area. In order to have a representative *R* factor over the whole region, the solution chosen by Gitas et al. (2009) is to find a relation between precipitation and altitude, for each of the three months analysed. For this site the *R* factor was not calculated.

This method was tried for Réunion Island and Corsican test sites but was dropped when the JRC European Soil Data Centre (ESDAC) published an R-factor covering the whole of Europe at 500m resolution.

_K_ factor

The text hereafter is mostly adapted from Gitas et al. (2009). The *k*-factor (soil erodibility factor) depends on the following combined soil parameters:

- Percentage of silt, very fine sand, clay and organic matter.
- Structure
- Drainage.

Lal and Elliot (1994) proposed the following formula for *k*-erodibility factor calculation:

$$k = 2.8 \cdot 10^{-7} \cdot M^{1.14} (1.2 - a) + 4.3 \cdot 10^{-3} (b - 2) + 3.3(c - 3)$$

where *M* is the size of soil particles (% silt + % very fine sand)·(100 - % clay), *a* is the percentage of organic matter, *b* is the code number defining the soil structure (very fine granular = 1, fine granular = 2, coarse granular = 3, lattice or massive = 4), and *c* is the soil drainage class (fast = 1, fast to moderately fast = 2, moderately fast= 3, moderately fast to slow = 4, slow = 5, very slow = 6). Generally, the above values of the *k* factor are applied on scales of 1:50 000 and 1:10 000 when a soil map is available.

The *k* factor can be approximated from the geological maps if soil maps are unavailable for a study area, with the following steps: where possible the determination of the soil texture class for each type of parent material of the geological map; this procedure was based on soil genesis rules (Buol et al. 2011). Different geological parent material may result in the same or different soil textures. The geological map can then be reclassified into a soil texture map accordingly and then

transformed into *k* values according to the specific soil parameters and domain expertise (tab. 2.8.1).

Table 2.8.1: The *k*-values as they were assigned to soil textural classes derived from the respective parent geologic material

Parent geologic material	**Soil texture***	***k*-values**
Alluvial deposits	SL-L	0.15
Limestone	C or SiC	0.4
Peridotid	CL-C	0.5
Granite	S-SL	0.2
Schists	L	0.7
Gneiss	S or LS or L	0.3
Tertiary deposits	SL-L	0.15

* S: Sandy, L: Loam, Si: Silty, C: Clay

According to the classical evaluation of erodibility andic soils are attributed little vulnerability to water erosion. *K* factor does not suitably characterise susceptibility of andosols to erosion (Wischmeier et al. 1971). Over the Maido site all soils are andic/andosols which easily absorb heavy rainfall (Raunet 1991) and hence the *K* factor is not taken into account over the test site.
This method was tested for Réunion Island and Corsican test sites using geological and soil data but was dropped when the JRC European Soil Data Centre (ESDAC) published a k-factor covering the whole of Europe at 500 m resolution.

Soil erosion indicator

The soil erosion indicator for the Maido site is derived from the *LS* and *C* factors. The results can be seen to take mostly the *LS* factor into account highlighting the main hydrological network and areas of high slope around these. The *C* factor plays a big role in removing vegetated surfaces from areas of higher vulnerability. Consequently, the fire which burnt large areas of vegetation increases the areas at risk especially in areas of higher slope and slope length. Further work will be necessary over Mediterranean sites to see whether a *k* factor and an altitude dependent *R* factor can be integrated.

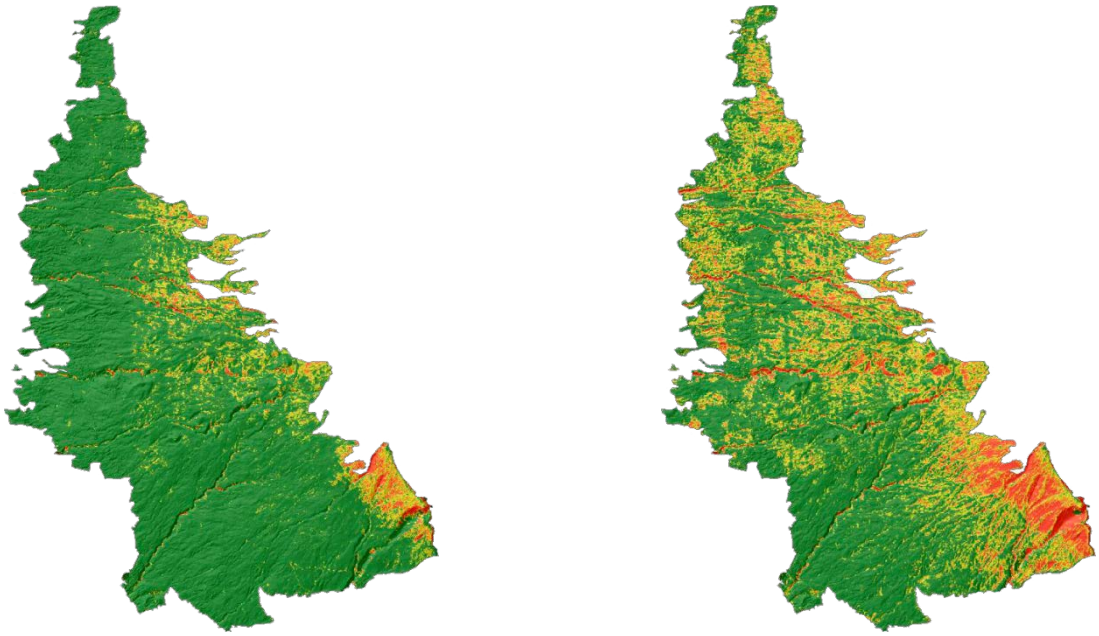

Figure 2.8.4: Pre-fire indicator of vulnerability to soil erosion derived from a Worldview scene of 02/06/2010 and a post-fire indicator of vulnerability to soil erosion derived from a Pléiades image acquired on 05/06/2012.

Results summary and perspectives

The development of a spatial modelling method to derive a soil detachment/erosion indicator based on the Universal Soil Loss Equation (USLE) family of models is at an operational version 1 phase. The method, tested within the FP7 PREFER project, has been implemented in a step-by-step process in ArcGIS modeller. A standardised soil erosion susceptibility index adjusting to the available data is the result.

The method is adapted to and applied to Mediterranean sites integrating more RUSLE factors and the procedure is now automated.

To enhance the capacity to produce interesting products and taking into account satellite and ancillary data availability the chain has:

- migrated from a default status of VHR to HR satellite data products,
- incorporated RUSLE factors elaborated on a European scale in 2014 and 2015 and distributed via the JRC's European Soil Data Centre (ESAC),

enabling the production of Sentinel derived HR products that are easier and faster to produce for major events, to monitor an area's soil erosion vulnerability, slope stabilisation, and vegetation recovery over time, or indeed at the end of the fire season. The industrial and rapid elaboration of DTM's better than SRTM remains an issue. This product is called the Soil Erosion Susceptibility Index (SESI) as SERTIT is not a soil specialist and, hence, would prefer not to mention soil loss per se.

The final objective is to integrate this index into a Risk & Recovery type portfolio and incorporate an updated soil erosion susceptibility index into an offer complementary of Copernicus EFFIS. This is partly achieved.

As already stated, at present the focus is on producing a Sentinel-2 compatible soil erosion vulnerability index adapting to the publication by the JRC's European Soil Data Centre (ESDAC) of RUSLE components covering the fast majority of Europe. The composition and source of RUSLE factors is outlined in a table below (tab. 2.8.2) for an example concerning a summer 2015 fire in Andalusia, Spain. The SESI has also been integrated into the service provided in a Fire demonstrator mentioned in Chapter 3. Normalisation to the JRC RUSLE product needs further improvement and is foreseen in a version to come.

Table 2.8.2 Characteristics of input data for the soil erosion index Sentinel-2 product over an Andalusia, Spain area covering part of an EMS Rapid Mapping activation EMSR127.

Objective: RUSLE Factor or other	**Data source**
AOI and burn scar	Copernicus EMS Rapid Mapping (13/07/2015)
Topographic (LS)	Derived from interpolated SRTM digital elevation model
Landcover (C)	Derived from Sentinel-2 acquired the 06/12/2015
Soil Erodibility (K)	K-Factor (interpolated) JRC's European Soil Data Centre (ESAC) (2014), © European Union
Rain Erosivity (R)	R-Factor (interpolated) JRC's European Soil Data Centre (ESAC) © European Union

A HR 20 m mapping was made concerning a 2009 fire in Corsica, France, using SPOT-4 data to simulate Sentinel-2 data. The results shown in the figure 2.8.5 indicate an increase in soil erosion vulnerability after the fire (24/07/2009) logically over the steepest fire-affected areas.

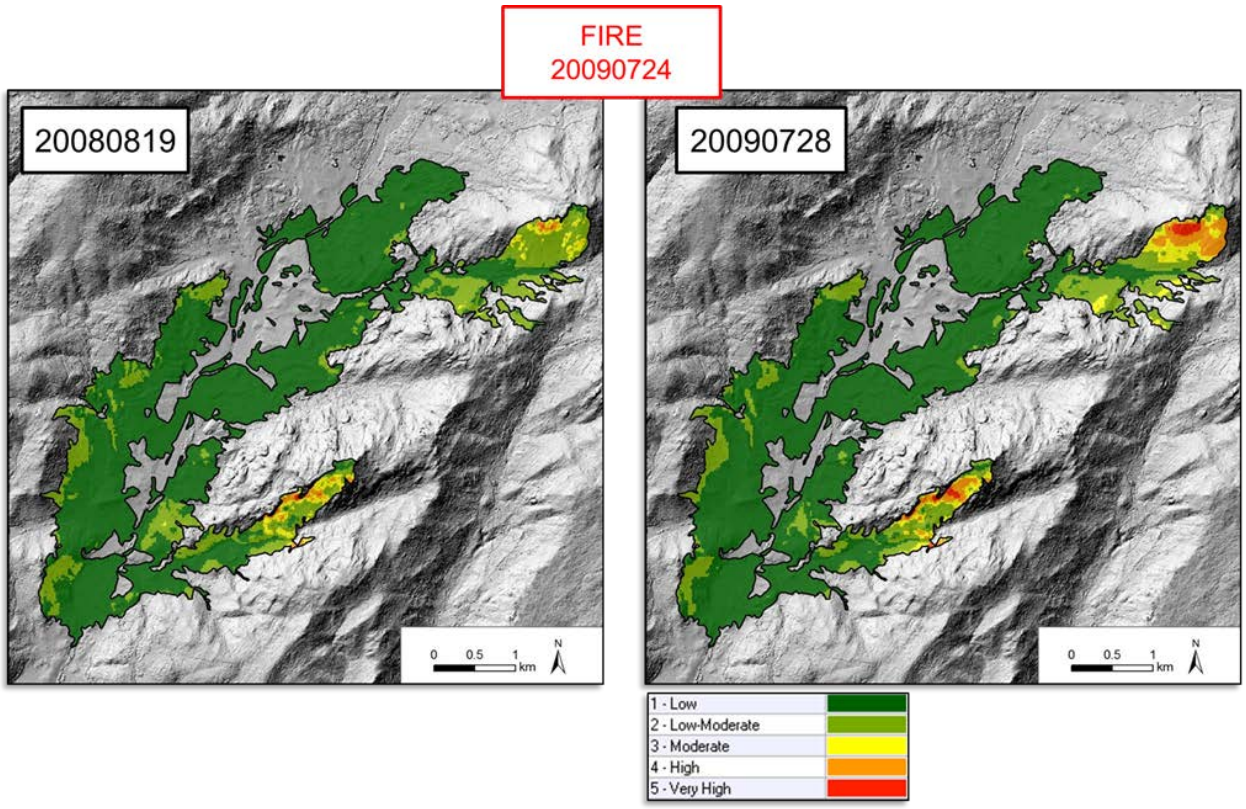

Figure 2.8.5: Pre and post fire soil erosion vulnerability indicator calculated over Sartene, Corsica, France.

As stated before, the method was applied to its first Sentinel-2 image covering the site of an Andalusia, Spain fire which was covered in the Copernicus EMS EMSR127 activation (fig. 2.8.5).

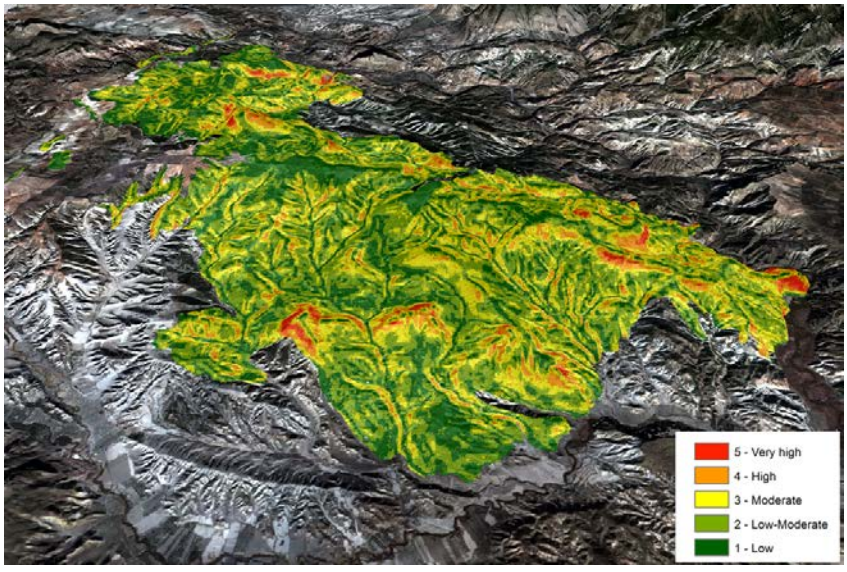

Figure 2.8.5: A 3D view of the Sentinel-2 soil erosion susceptibility index over Quesada, Andalusia, Spain.

Perspectives: The main emphasise in the forthcoming demonstration phase will be in stream-lining the production method to normalise the output with the JRC's RUSLE values and to produce a mapping over a summer 2016 fire with Sentinel-2 data within a rapid mapping context. Within the Demonstrator phase the work described in figure 2.8.1 is named the "Soil Erosion Susceptibility Index (SESI).

Reference

1. Bizuwerk, A., Taddese, G. and Getahun, Y., 2008: Application of GIS for Modeling Soil Loss Rate in Awash Basin, Ethiopia. International Livestock Research Institute, Addis Ababa, Ethiopia.
2. Gitas, I. Z., Douros, K., Minakou, C., Silleos, G. N., Karydas, C. G., 2009: Multi-temporal soil erosion risk assessment in North Chalkidiki using a modified USLE raster model. EARSeL eProceedings 8, 1/2009.
3. Morgan R.P.C., 2005: Soil erosion and conservation. Third edition, © 2005 by Blackwell Science Ltd, a Blackwell Publishing company.
4. Fournier, F. 1960: Climat et érosion: la relation entre l'érosion du sol par l'eau et les précipitations atmosphériques. Presses Universitaires de France, Paris.
5. Arnoldus, H.M.J. 1980: An approximation of the rainfall factor in the Universal Soil Loss Equation. In De Boodt, M. and Gabriels, D. (eds), Assessment of erosion. Wiley, Chichester: 127–32.
6. Buol, SW., Southard, RJ., Graham, RC., McDaniel, PA., 2011: Soil Genesis and Classification. 6th edition (Iowa State University Press, Ames, Iowa, USA) (referenced in Gitas et al. 2009).
7. Raunet, M., 1991: Le Milieu Physique et les sols de l'Ile de la Réunion, Conséquences pour la mise en valeur agricole. Referenced in *Guide des bonnes practiques agricoles à la Réunion, DAAF*.

2.9 Technical note on fire induced volume loss

2.9.1 State-of-the-art - optical extraction of 3D surfaces

Stereoscopy is the science and art that deals with the use of images to produce a 3D visual model with characteristics analogous to that of actual features viewed using true binocular vision (La Prade et al. 1966).

A stereoscopic couple is constituted by two images of the same scene acquired with different view angles, with an overlap. The different between the points of view or positions create a disparity called parallax, used to reconstruct the relief.

If the images are acquired by a plane, the process is called "aerial photogrammetry". Hundreds of images, acquired by a conical geometry camera, are needed to cover a city-sized area. The spatial resolution could be comprised in the range of 5-50cm, but needs potentially significant ad-hoc logistics (aircraft routing).

If the images are acquired via satellite, the process is called "satellite photogrammetry". The images are acquired by a push-broom camera embedded on a satellite. Several systems have been designed to allow multiple acquisitions during a pass: multiple cameras (SPOT-5 HRS, ALOS PRISM), rotation of a mirror (QuickBird), orientation of the satellite (Pléiades-HR, GeoEye).

Since the first experiments of relief reconstruction using the Earth Terrain Camera embedded on SkyLab in 1973/1974 (Toutin 2001), much progress has been made in vectors and instruments, but also in signal processing and interpretation. Nowadays, high and very high resolution images acquired in stereoscopic conditions are becoming easily accessible. We can mention among others SPOT-5 HRS, ALOS PRISM, QuickBird, GeoEye, Ikonos, Worldview, and Pléiades-HR.

The acquisition geometry is generally characterised by the base-to-height (B/H) ratio, which is the distance between the acquisitions divided by the flight height. The B/H ratio therefore expresses the parallax obtained for a height difference of 1m. The longer the base-line (high B/H), the more the perspective rays intersect at a wide angle. This leads to the intersection being precisely defined, but the risk of having hidden parts of the image increases, also the images are very different, this could be an issue if an automatic correlator is used. If the base is short (B/H low), the rays intersect with a small angle and the uncertainly in the attitude of the satellite could have a larger impact on determination Z. However, in this case the images are very similar. This is why a tri-stereo image set is interesting, as this leads to three stereo-pairs, with a corresponding increase in redundancy in the height measurements and a reduction of hidden parts.

Relief reconstruction is firstly carried out by matching of homologous pixels, either through a manual process called stereo-plotting using human perception, or by an automatic process of correlation. The matching is done by analysing similarity between images. Several algorithms have been designed, but the most used are "Mean Sum of Square Difference" or Mean SSD (Wozencraft and Jacobs 1965), Hirshmüller's correlator (Hirshmüller 2007), Energy minimisation (Pierrot-

Deseilligny and Paparoditis 2006). Some others are described in (Brown 1992), and a comparison is presented in (Martin 1995).

A study comparing incidences and *Z* accuracy with several Pléiades-HR images over Melbourne was performed by Bernard et al. (2012) where accuracy is estimated through a set of 200 ground control points (GCP). It is shown that better RMS errors are obtained with wide angle stereo pairs (*B*/*H* = 0.26-0.36, best *Z* RMS = 0.58m) than narrow angle stereo pairs (B/H = 0.18, better Z RMS = 0.78). However, using multi-stereo pairs, better results can be reached (Z RMS = 0.49m with 7 images). These results should be interpreted with caution as the images have been acquired during the flight commissioning of the satellite.

It has been shown, in comparison with a LiDAR dataset, that the altimetric mean bias of a DSM generated using a tri-stereoscopic acquisition can reach 1m, with a standard deviation of <1m (Durand et al. 2013). However, it is also known that the quality of the DSM is closely linked to the land-use/land-cover (LULC); research needs to precise the link between the texture related to the LULC and the correlator performances, especially over forests where texture is particularly complex and variable.

References

1. Bernard M., Decluseau, D., Gabet, L., Nonin, P., 2012: 3D capabilities of Pleiades satellite. International Archives of the Photogrammetry. Remote Sensing and Spatial Information Sciences, 39, B3, 553-557.
2. Brown, L. G., 1992: A survey of image registration techniques. ACM Computing Surveys, 24, 4, pp.325 -376.
3. Durand, A., Michel, J., de Franchis, C., Allenbach, B., Giros, A, 2013: Qualitative assessment of three DSM generation approaches using Pléiades-HR data. Case study: Port-au-Prince, Haiti. 33th EARSeL symposium, 3-6 June 2013.
4. Hirschmüller, H., Scharstein, D., 2007: Evaluation of cost fonctions for stereo matching. IEEEConference on Computer Vision and Pattern Recognition.
5. La Prade, G., 1963: An analytical and experimental study of stereo for radar. Photogrammetric Engineering, 29, 2, 294-300.
6. Martín, M.P., Chuvieco, E., 1995. Cartografía y evaluación superficial de grandes incendios forestales a partir de imágenes de satélite, Ecología., 9, 9-2.
7. Pierrot-Deseilligny, M., Paparoditis, N., 2006: A multiresolution and optimization-based image matching approach: An application to surface reconstruction from SPOT5-HRS stereo imagery. In IAPRS vol XXXVI-1/W41 in ISPRS Workshop On Topographic Mapping From Space (With Special Emphasis on Small Satellites), Ankara, Turkey.
8. Toutin, T., 2001: Elevation modelling from satellite visible and infrared (VIR) data . Int. j. remote sensing, 22, 6, 1097, 1125.
9. Wozencraft, J. M., Jacobs, I. M., 1965: Principle of Communication Engineering. John Wiley and Sons.

2.9.2 Optical data-based extraction of 3D surfaces

3D information extraction from VHR Optical data

3D surface and volume change detection is a strategic development axis for SERTIT and, hence, this work is carried out in the framework of a test-bed, benchmarking process where a number of photogrammetric processing chains are tested and compared over different terrain, at various scales and with a diversity of objects in mind.

At present and in terms of Pléiades (tri-) stereo-pairs, SERTIT now has a much more complete view of the existing range of tools available and of their capacities, advantages and disadvantages. The aim to discern the altimetric precision that can be reached by these DSMs has been attained and the results are quite promising, but are not applicable to all applications. This body of work has led to a number of publications. The PREFER project has led to the testing of these DSM in the forestry domain and in particular 3D fire damage mapping.

DSM generation methodology using Pléiades stereo-pairs

As already mentioned beforehand, before deciding on standard methodology a number of computer packages were tested:

- Openware (Orfeo Toolbox, MicMac),
- Commercial software (Leica Photogrammetry Suite Intergraph, PCI Geomatica)

The tests which were run over a number of zones on different continents led to the conclusion that best DSM generation software is MicMac software, developed by IGN France. Technically it is the best but it does require quite a lot of testing and integration to use it within a DSM processing chain. Within the PREFER project it is the first time it has been applied to forestry applications.

The result of the methodological research has led to the workflow procedure (fig. 2.9.1) outlined in the algorithm chapter. Some semi-automatic cleaning needs to be added to this procedure to eliminate erroneous peaks and troughs.

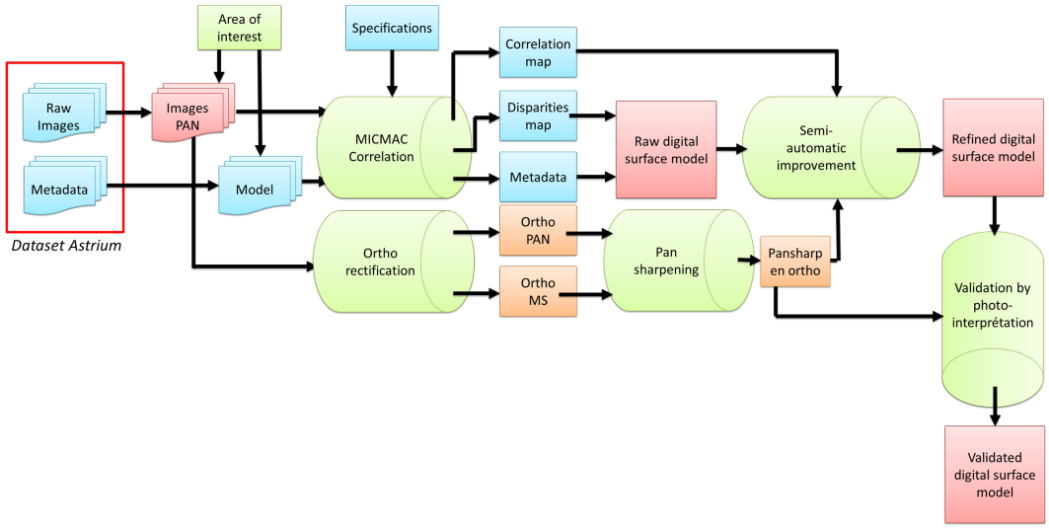

Figure 2.9.1: DSM generation workflow diagram using MicMac.

The methodological test site, which is used to research the best methods to elaborate a DSM for forestry applications, is an area of high relief situated on Réunion Island. This test site was affected by an extensive fire in November 2011 that destroyed 2600 ha of forestry and scrub over a period of one week. SERTIT does not possess a DSM derived before the fire.

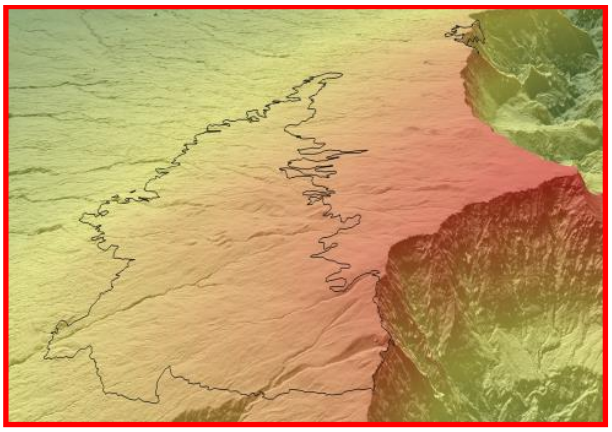

Figure 2.9.2: Extract of the DSM generated over the Réunion Island test site. This section has a strong relief with a height difference of ~2000 m.

The full resolution DSM (fig. 2.9.2 and 2.9.3) has a greatly improved texture when compared to the reference DSM, an IGN digital terrain model, as illustrated in fig. 2.9.2. This is due to the higher resolution but also to the difference between a DSM and a DTM. Individual copses and single trees seem to be visible. Compared to the reference IGN DTM the Pléiades derived DSM lies within an RMS error of 5m which means that it is of high quality with the difference mostly being linked to landcover (trees, bushes and other high features). In an urban environment with less relief this method approached an RMS error of 1m over Port-au-Prince.

Figure 2.9.3: The fire affected area can be clearly seen in the natural colour composite with a dark patch on the lower right (image on left); also DSM is smoothed (image on right) where the trees have been burnt. The central reference DTM is provided for reference.

2.9.3 State-of-the-art – SAR-based extraction of 3D surfaces

Besides the stereoscopy techniques based on optical imagery, there are also possibilities to build 3D surfaces from SAR imagery. Leberl (1990) gives the following definition: “Radargrammetry is the technology of extracting geometric information from radar images”. The first works on radargrammetry started after the Second World War. La Prade (1963) was the first to define the basic principles. Since then it was completed by several developments and led to a large variety of different techniques. Toutin et al. (2000) report four different methods that can be implemented to extract elevation information: clinometry, stereoscopy, interferometry and polarimetry. Like any other technique, each one has its own benefits and drawbacks. By considering the available literature on each particular topic, two methods are clearly preferred, namely stereoscopy (which is often referred to as radargrammetry) and interferometry. They are widespread among the EO community and constitute important research fields while being also very well established techniques for DEM generation.

As it is underlined in their course on radargrammetry (Meric et al. 2009), the use of radar sensors is suitable to overcome the limitations of optical sensors (weather conditions, need for sunlight). As active systems ranging in the microwave part of the electromagnetic spectrum SAR sensors are not very sensitive to atmospheric conditions in acquiring images of the Earth. In his article Ouchi (2013) points out that an increasing number of space-borne SAR platforms have been recently launched since 2006: ALOS PALSAR, RADARSAT-2, TerraSAR-X and TanDEM-X, and Cosmo-SkyMed. Further missions are planned in the coming years (Sentinel Constellation, RADARSAT Constellation Mission). Ouchi et al. (2013) also mention that in comparison with previous SAR satellite sensors the general trends show that these new sensors are capable of acquiring images in a larger number of modes, with finer spatial resolutions and up to four channels of polarisation. As it is the case with optical imagery, the technology embedded on-board of satellites are able to compete against airborne platforms by offering comparable images.

In radargrammetry (a radar stereoscopic method), the concept is basically the same as that used in optical stereoscopy and is well explained in Meric et al. (2009). The methodology relies on the parallax P and the convergence angle $\Delta\theta_V$ indicators (fig. 2.9.4). The parallax is a parameter that is directly connected to point elevation h, and the convergence angle is defined by the intersection of the two lines of sight of the radar. Since the beginning, the biggest challenge consists in finding the maximum correct matching points in both radar images while limiting the number of false matches in order to avoid the distortions in the resulting DEM. Ostrowski (2000) proposed some enhancements to improve the process, like the resampling to quasi-epipolar geometry or automatic screening and editing of matches. In another article studying the potential of RADARSAT-2 high resolution (Ultrafine) mode images for DEM generation, Toutin (2010) examines the influence of different SAR parameters (polarisation, spatial resolution, slant versus ground-range geometry) on the resulting DEM. He concludes that no large difference can be found in the results regardless of the SAR and processing parameters. However some trends are to be noticed: HH achieved better

results than VV, and slant-range geometry provided slightly better results than ground-range geometry.

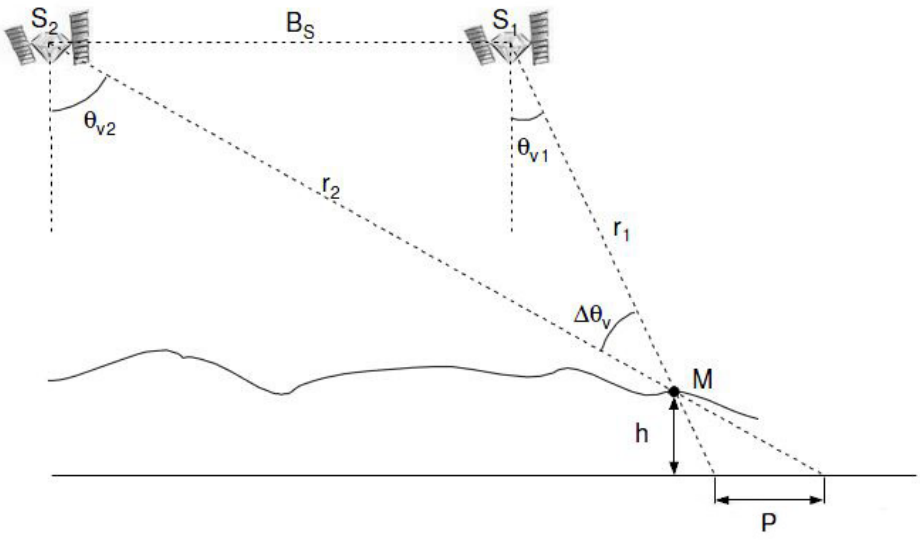

Figure 2.9.4: SAR stereoscopic configuration.

Since the beginning in the 1970s, SAR interferometry or InSAR has been a field that is constantly evolving. One of the first uses of the radar signal phase for topographic mapping by acquiring two images simultaneously appears in 1974 (Graham 1974). At the beginning of the 1980s, the same method was used but this time with images taken from space at different dates. It is also worth mentioning that nearly at the same period it was suggested to take benefit from InSAR developments for measuring ground displacements. The demonstration of this application was only made several years later because of the lack of data available.

Because it deals with a large number of fields (from terrestrial and spatial geodesy, cartography, statistics to signal analysis and processing), this technique has always generated a great interest but is at the same time very complex. Polidori (1997) considers that this need for cooperation between various scientific communities explains why InSAR has not been fully exploited so far. In their book entitled “Imaging with synthetic aperture radar”, Massonnet and Souyris (2008) explain however that InSAR has recently become a fully operational technique thanks to the availability of data from a new generation of space and airborne that came on-line in the last years.

Sefercik and Dana (2011) explain that in comparison with optical stereoscopy, the DEM generation process using InSAR data is not so simple and involves several complicated steps. Moreover the quality of the data sets is one, if not the most crucial point to obtain a DEM with a high quality level. Rodriguez and Martin (1992) offer interesting analyses to understand the origin of the errors induced by the InSAR technique.

The lack of data has been a huge difficulty for a long time. This was almost completely solved thanks to the Shuttle Radar Topography Mission (SRTM) whose goal was to generate a global DEM in either C and X band. It was realised by bringing a specially modified radar system onboard

a space shuttle in February 2000. The usefulness of the SRTM DEM has been widely demonstrated since it has been released. Nevertheless it does not cover the poles and has a grid spacing of 1" (~30 m) in the US territories or 3" (~90m) generally over the rest of the world.
The future global DEM generated by DLR with the twin satellites TerraSAR-X and TanDEM-X relies on the same philosophy, namely acquiring simultaneous interferometric SAR image pairs in order to get a result as accurate as possible. In his paper related to this mission, aiming more particularly at describing the raw DEM generation process, Rossi et al. (2010) specifies that the primary objective is to create a consistent global DEM that follows the high accuracy HRTI-3 standards, shown in the table 2.9.1.

Table 2.9.1: HRTI-3 DEM specifications.

Requirement	**Specification**	**HRTI-3**
Relative vertical accuracy	90% linear point-to-point error over a 1° x 1° cell	2m (slope <20%) 4m (slope >20%)
Absolute vertical accuracy	90% linear error	10m
Relative horizontal accuracy	90% circular error	3m
Horizontal accuracy	90% circular error	10m
Spatial resolution	independent pixels	12m (equator)

Along with the DEM, other information is supplied to assess its quality (height error map, maps of the different artefacts and soil types that can disturb the DEM generation process). A simulation of this DEM and the associated height error map, obtained with two TerraSAR-X images, are presented in figures 2.9.4 and 2.9.5. Thanks to these very valuable data, great improvements are expected for the description of the Earth's topography. In particular, the elevation information in vegetated and forest areas is likely to be enhanced because of the very nature of the acquisition technique. Indeed single-pass acquisitions prevent temporal de-correlation, which is often the main concern as regards vegetation.

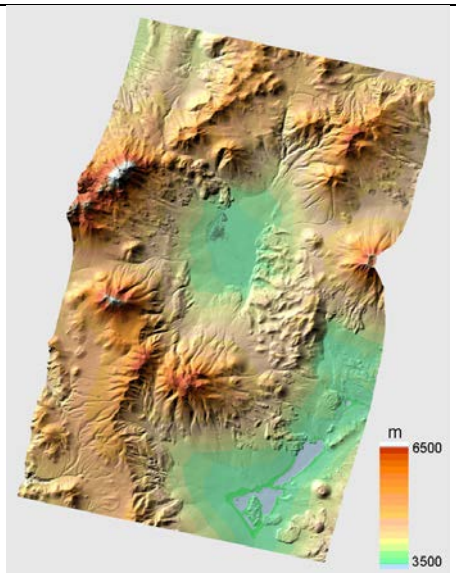

Figure 2.9.4: DEM generated from a TerraSAR-X dual-pass scenario over the Salr de Arizaro region (Argentina).

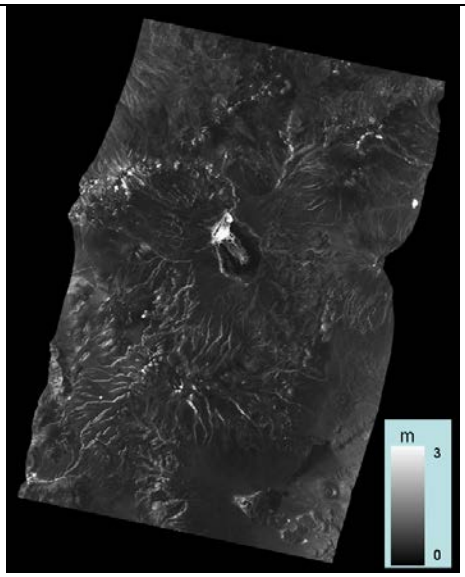

Figure 2.9.5: Height error map corresponding to the DEM shown in figure 2.9.4.

References

1. Graham, L.C., 1974: Synthetic interferometer radar for topographic mapping. Proceedings of the IEEE, 62, 6, 763-768.
2. La Prade, G., 1963: An analytical and experimental study of stereo for radar, Photogrammetric Engineering, 29, 2, 294-300.
3. Leberl, F., 1990: Radargrammetric image processing, Artech House, Norwood, MA.
4. Massonnet, D., Souyris J., 2008: Imaging with synthetic aperture radar, Editions EPFL Press, Lausanne, 177-228/280.
5. Meric, S., Fayard, F., Pottier E., 2009: Radargrammetric SAR Image Processing. Geoscience and Remote Sensing, Pei-Gee Peter Ho InTech.
6. Ostrowski, J.A., Cheng, P., 2000: DEM extraction from stereo SAR satellite imagery. Geoscience and Remote Sensing Symposium, Proceedings IGARSS 2000, 5, 2176-2178.
7. Polidori, L., 1997: Cartographie radar. Editions Gordon and Breach Science Publishers.
8. Rodriguez, E., Martin J., 1992: Theory and design of interferometric synthetic aperture radars. IEEE Proceedings-F, 139, 2, 147-159.
9. Rossi, C., Eineder, M., Fritz, T., Breit, H., 2010: TanDEM-X Mission: Raw DEM Generation. In: Proceedings of 8th European Conference on Synthetic Aperture Radar, EUSAR 2010, Aachen, Germany, 7-10 June 2010 (on CDROM).
10. Sefercik, U.G., Dana, I., 2011: Crucial points of interferometric processing for dem generation using high resolution SAR data. ISPRS Hannover Workshop.
11. Toutin, T., Gray, L., 2000: State-of-the-art of elevation extraction from satellite SAR data. ISPRS Journal of Photogrammetry & Remote Sensing, 5, 1, 13-33.
12. Toutin, T., 2010: Impact of Radarsat-2 SAR Ultrafine-Mode Parameters on Stereo-Radargrammetric DEMs. IEEE Transactions on Geoscience and Remote Sensing, 48, 10, 3816-3823.

2.9.4 DSM generation from TanDEM-X data

In order to test whether SAR interferometry could map changes in canopy height due to fire damage SERTIT decided to use data images provided by the TerraSAR-X (TSX) and TanDEM-X (TDX) satellites. Their close tandem flight formation assuring no temporal decorrelation between the acquisitions, combined with a very high resolution sensor capability offer the possibility to generate DSM with an unprecedented accuracy.

Figure 2.9.6.: Overview of the TanDEM-X interferometric pairs acquired before (17/07/2011, left) and after (21/10/2012, right) the fires on Reunion Island, selected to generate the DSMs.

SERTIT submitted a science proposal to become a TanDEM-X Principal Investigator which was accepted by the DLR. Therefore, SERTIT was able to get and process TanDEM-X CoSSC data in order to obtain a DSM. A couple of TSX /TDX pairs acquired before and after the fires available over the Maido study area on Reunion Island (fig. 2.9.6) was chosen to compute two DSMs from each InSAR pair, necessary for the 3D damage assessment topic. This configuration is ideal for fire event related canopy height change detection. An existing post-fire TSX/TDX dataset was found over the Corsican and Sardinian sites which could enable work over these sites in future.

Methodology (illustration)

The interferometric processing workflow illustrated in figure 2.9.7 is implemented for both InSAR pairs. After importing the raw imagery, a subset of the entire scenes is selected because the burnt area represents only a small part of the image. Given that the data are provided already co-registered the interferogram can be directly generated. The approach chosen here is based on an implicit unwrapping method, meaning that an external DSM is used (here the SRTM). Instead of searching to compute an exact DSM (from an exact interferogram containing all the topographic fringes describing the really observed surface), the external DSM is converted into phase values (within the master image geometry) in order to generate a synthetic interferogram that will be subtracted from the raw interferogram. The resulting interferogram is called a flattened interferogram. To facilitate phase unwrapping it is strongly encouraged to filter this flattened

interferogram, because it greatly reduces the phase noise. Interferograms generated so far only contains fringes with values comprised in the [0, 2π] interval.

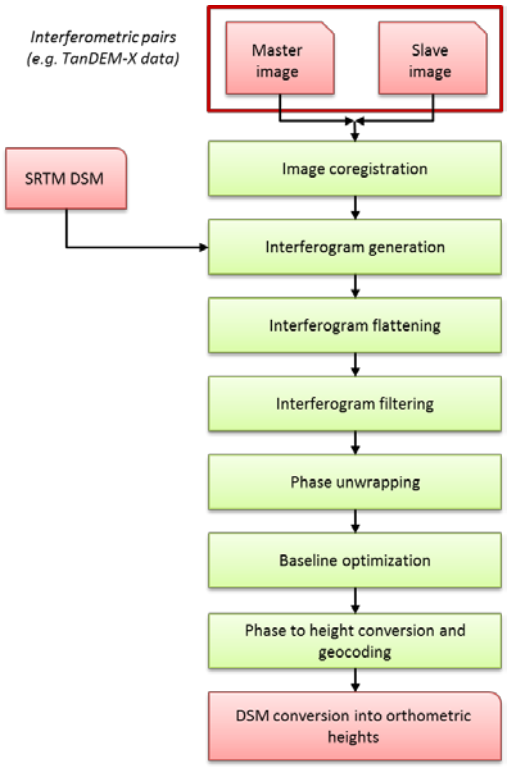

Figure 2.9.7: General interferometric workflow for DSM generation based on TanDEM-X CoSSC data.

It is necessary to add to this value the proper number of cycles omitted in order to "unwrap" the filtered interferogram and to get the real topography. In parallel, the coherence data is computed and gives a measure of the correlation found between the two images for every pixel: the higher the coherence is, the stronger the correlation will be. The decorrelation can be linked to various factors. For instance in the case of multi-pass interferometry, it can be provoked by the variations that occur between the two acquisitions.

Before converting the unwrapped interferogram into height values, it is necessary to optimize the baseline estimation thanks to ground control points. It can be crucial because even a slight error on the orbit parameters can have dramatic effects on the resulting DSM in terms of vertical positioning. A reasonable number of points are taken (~15). To improve the refinement process, it is strongly encouraged to choose points with a high coherence value.

The synthetic interferogram obtained during the flattening process is added to the unwrapped interferogram, and it is then possible to convert the result from the SAR coordinate system into a geographic coordinate system. The resulting DSM values are ellipsoidal heights, and a final step must be done to transform these into ortho-metric heights, which are often referred to as mean sea level values.

3 Demonstration

Five independent trial cases have been conducted at the end of the project with a focus to demonstrate the advanced methods developed within the course of the project within rapid mapping activities by delivering the derived rapid mapping products to the user. The focus was on demonstrating:

- DLR's fully automatic Sentinel-1 Flood Service during two flood related Charter activations in India (CC578) and Australia (CC580).
- SERTIT's optical data-based flood detection workflow implemented in OTB during Charter activation in Australia (CC580) and the activation of Copernicus EMS (EMSRS14).
- SERTIT's fire burn scar mapping tool BURNOUT during a forest fire near Marseille, France, and during an activation of Copernicus EMS on Thassos, Greece (EMSRS10).

3.1 Flood detection

3.1.1 Charter Call 578: Flood in India

DLR's Sentinel-1 Flood Service (see chapter 2.1.2.1) was automatically triggered for Charter Call 578 related to floods across India by detecting a Sentinel-1 scene (04/09/2016, 00:03 UTC) on ESA' Sentinels Scientific Data Hub over the affected areas.

The whole processing duration was 51.4 min for the whole flood processing chain (see workflow in fig. 2.1.3) including data ingestion, pre-processing of the data, computation and adaption of auxiliary data sets, automatic flood mask generation and dissemination of the crisis information via a web client. The flood mask was delivered to the Charter Project Manager from the National Remote Sensing Centre/ISRO.

The automatically generated Sentinel-1 flood mask was compared with a flood mask generated by a semi-automatic object-based flood detection tool (RaMaFlood, Martinis et al. 2009) of DLR/ZKI which requires the interaction of an image interpreter. This tool was developed within the BMBF-funded project SAR-HQ (2007-2010), further developed in the EC-funded project SAFER (2009-2012) and was used for flood mask generation within numerous flood rapid mapping activities of DLR/ZKI.

The processing time for the generation of the water mask with RaMaFlood (incl. 12.5 min pre-processing and 8 min of manual post-processing) was 72 min. The processing time using S-1FS is therefore ~ 30% faster than using RaMaFlood and requires no input of an active image processing specialist. The crisis information can therefore faster be delivered to the user.

Fig. 3.1 shows that most of the flood water extent (2711 km², 81.9%) could be detected by both tools, 519 km² (15.6%) were additionally found using RaMaFlood. These areas are mainly related to bright backscattering water areas towards the near range, which could not be detected by the automatic classifier of S-1FS, but could manually be added by manual post-classification in RaMaFlood. 81 km² (2.4%) of the flood surface have been only detected by S-1FS.

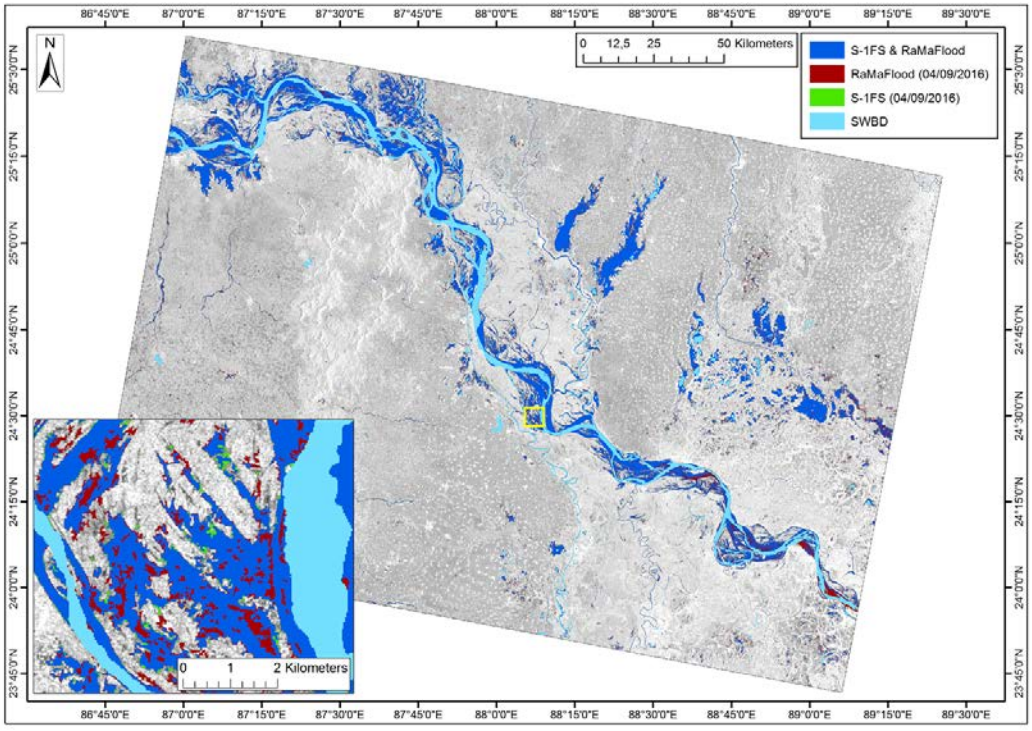

Figure 3.1: Flood classification results derived from Sentinel-1 (04/09/2016) data using S-1FS and RaMaFlood.

The result of S-1FS was further compared to the automatic classification result of DLR's TerraSAR-X Flood Service (TFS) using a TerraSAR-X ScanSAR scence (8.25 m spatial resolution) of 03/09/2016, partly covering the extent of the S-1 scene (figure 3.2).
The results of both processors are quite similar. 977 km² (71.3 %) of the flood surface have been detected by both processors. Deviations result from environmental and system related factors: 189 km² (13.8%) were only detected by TFS mainly resulting from dense clouds which have a similar backscatter as the smooth water as well as due to a slightly higher spatial resolution of the TerraSAR-X data. Presumably a slight increase in water level between the 3rd and 4th of September leads to the effect that ~203 km² (14.8%) were only detected using S-1.

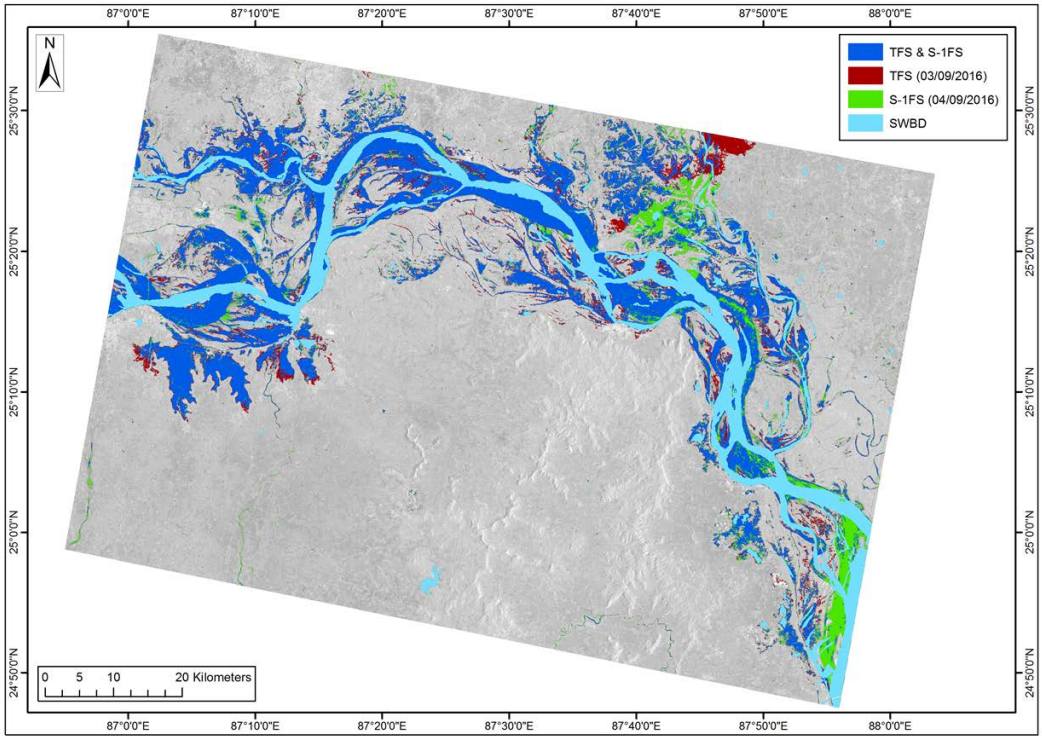

Figure 3.2: Flood classification results derived from Sentinel-1 (04/09/2016) data using S-1FS and TerraSAR-X (03/09/2016) using TFS.

3.1.2 Charter Call 580: Flood in Australia

S-1FS was also automatically triggered for Charter Call 580 related to floods in New South Wales, Australia by detecting a Sentinel-1 scene (27/09/2016, 19:33 UTC) on ESA' Sentinels Scientific Data Hub over the affected areas.

The whole processing duration was 55.5 min for the whole flood processing chain (see workflow in fig. 2.1.3). The flood mask was delivered to the Charter Project Manager from Geoscience Australia.

The automatically generated Sentinel-1 flood mask was compared with a flood mask generated by a RaMaFlood. The processing time for the generation of the water mask with RaMaFlood (incl. 12.5 min pre-processing and 4 min of manual post-classification) lasted 82.5 min. The processing time using S-1FS was therefore ~ 33% faster than using RaMaFlood and requires no input of an active image processing specialist.

Fig. 3.3 shows that most of the flood water extent (466 km², 71.0%) could be detected by both tools, 185 km² (28.2%) were additionally found using RaMaFlood. These areas are mainly related to bright backscattering water areas towards the near range, which could not be detected by the automatic classifier of S-1FS, but could manually be added by manual post-classification in RaMaFlood. 5 km² (0.8%) of the flood surface were only detected by S-1FS.

The automatically derived flood mask was available for delivery 4.5 h after data acquisition. The products have been used by Geoscience Australia for Value Adding (see fig. 3.4 and

https://www.disasterscharter.org/image/journal/article.jpg?img_id=336289&t=1475249187349). A feedback formular from Geoscience Australia about the product is visible in figure 3.5.

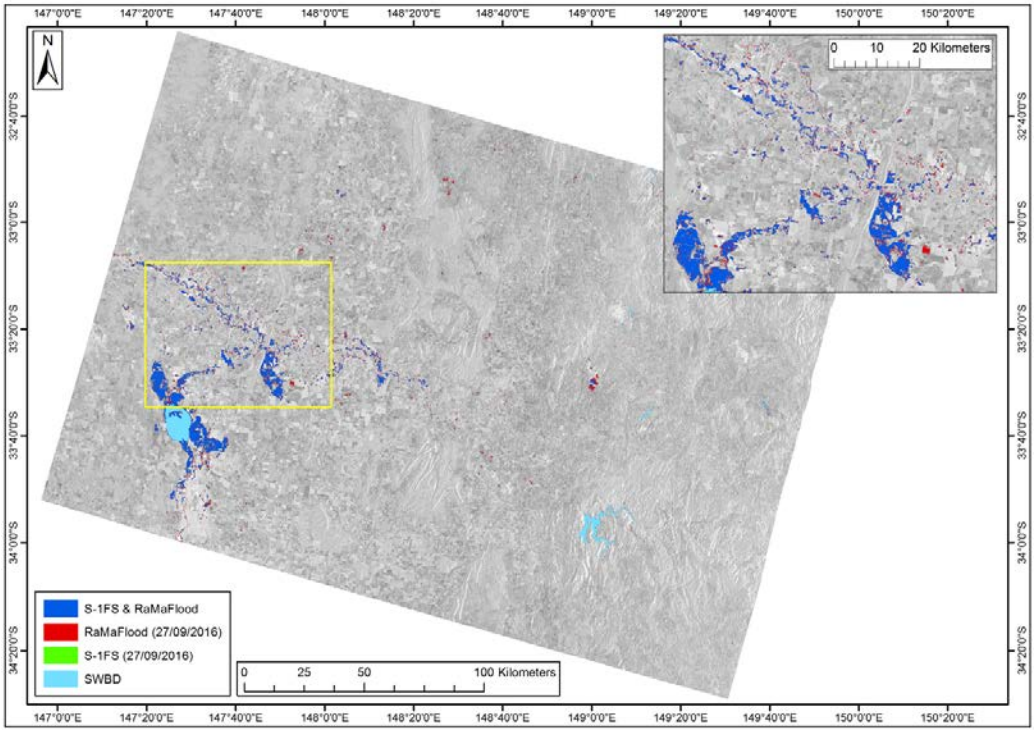

Figure 3.3: Flood classification results derived from Sentinel-1 (27/09/2016) data using S-1FS and RaMaFlood.

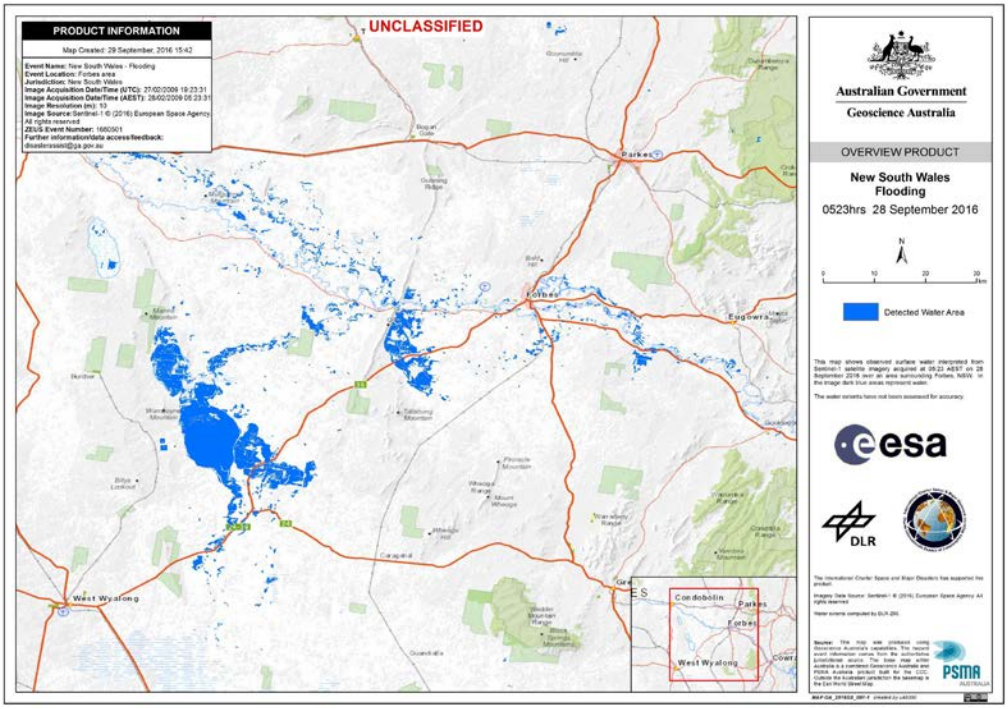

Figure 3.4: Flood classification results derived from Sentinel-1 (27/09/2016) data using S-1FS and RaMaFlood.

Feedback Form - Use of flood masks of DLR's Sentinel-1 Flood Service in Charter Call 580

GENERAL DATA

Activation:	Charter call 580, Floods in Australia
Organisation:	Geoscience Australia
Name:	Müller
First name:	Norman
Role:	Charter Project Manager of Call 580

USE OF PRODUCTS

Have the Sentinel-1 based flood masks been used?	X Yes ☐ No ☐ Partly

For which purpose have the products been used?

The flood masks were used to generate mapping products showing the flood extents over a base, contextual map. The flood masks were also provided to the New South Wales State Emergency Services for use in their own mapping products.

EVALUATION OF PRODUCTS

	Very good	Good	Poor	Unusable
Positional accuracy	X	☐	☐	☐
Thematic accuracy	☐	X	☐	☐
Timeliness of product provision	X	☐	☐	☐

FURTHER COMMENTS

We compared these flood masks with those we derived from RapidEye. While there is less water detected from Sentinel-1, it is clear that this is because of interference from tree canopies in flooded forests and other features that are causing multi-bounce effects for the SAR signal. Some misclassification of muddy areas is also noticeable. The Sentinel-1 flood masks performed better within the urban area of the town of Forbes, where the RapidEye analysis over estimated due to dark roads and building shadows.

Figure 3.5: Feedback form from Geoscience Australia.

3.1.3 Charter Call 580 and EMSR184: Floods in South Eastern Australia

Event description

The 26/09/2016 EC Services/DG ECHO triggered the Copernicus EMS Rapid Mapping team (EMSR184) on behalf of Geoscience Australia to map flooding in the State of New South Wales between Hillston FMP (West) and Gooloogong- Jemalong (East) areas (fig. 3.6). Starting from September 24th, heavy rains have hit the South Eastern part of Australia. Approx. 34,000 km² of the Lachlan river catchment is flooding, with several cities affected, hundreds of people evacuated and 100 properties affected by floodwaters according to the State Emergency Service. The Copernicus EMS service is still monitoring the situation end October 2016.

This event marked the beginning of a wave of recent Charter – EMS collaborations. As an input to Charter Call 580 the CNES acquired Pléiades data over 3 urban areas. Observing that both the Charter and EMS were working for the same AU, the CNES offered the data to EMS for value adding mapping. SERTIT worked on one of the detail maps, the Forbes detail map (fig. 3.7 and 3.8):

http://emergency.copernicus.eu/mapping/system/files/components/EMSR184_09FORBESDETAIL_GRADING_OVERVIEW_v1_100dpi.jpg

http://emergency.copernicus.eu/mapping/system/files/components/EMSR184_08FORBES_DELINEATION_OVERVIEW_v1_200dpi.jpg

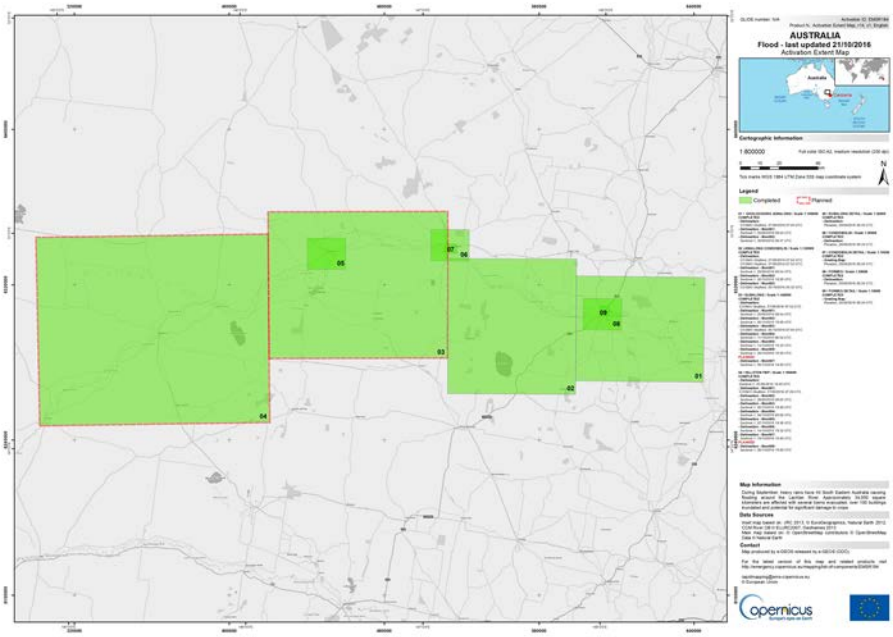

Figure 3.6: Copernicus EMSR184 South Eastern Australia AOI's. The Forbes map is shown as the small green rectangle in the Eastern part of the map within a larger light green rectangle.

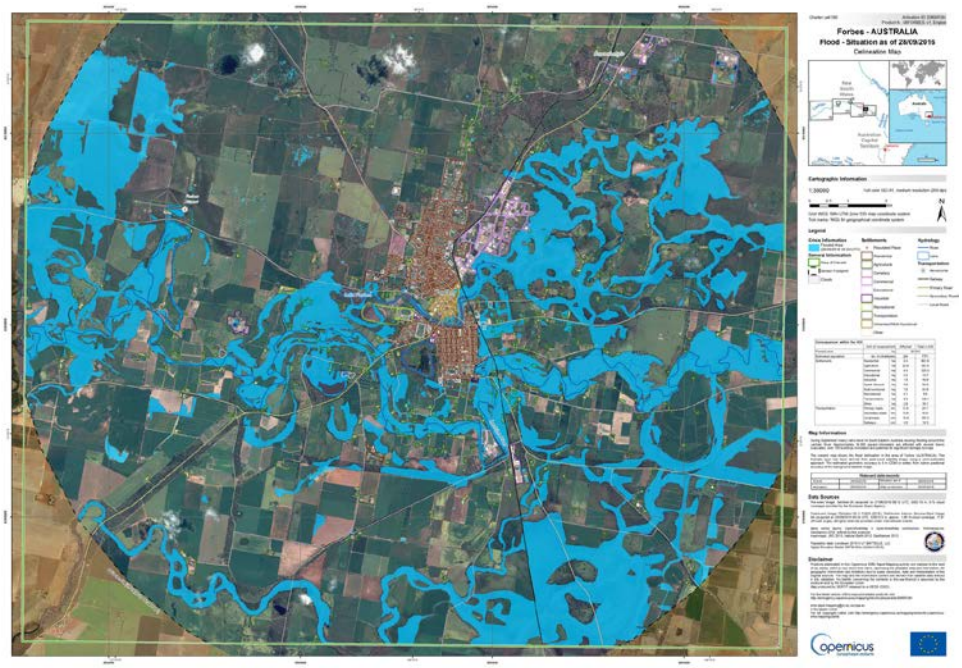

Figure 3.7: Copernicus EMSR184 South Eastern Australia Forbes Map.

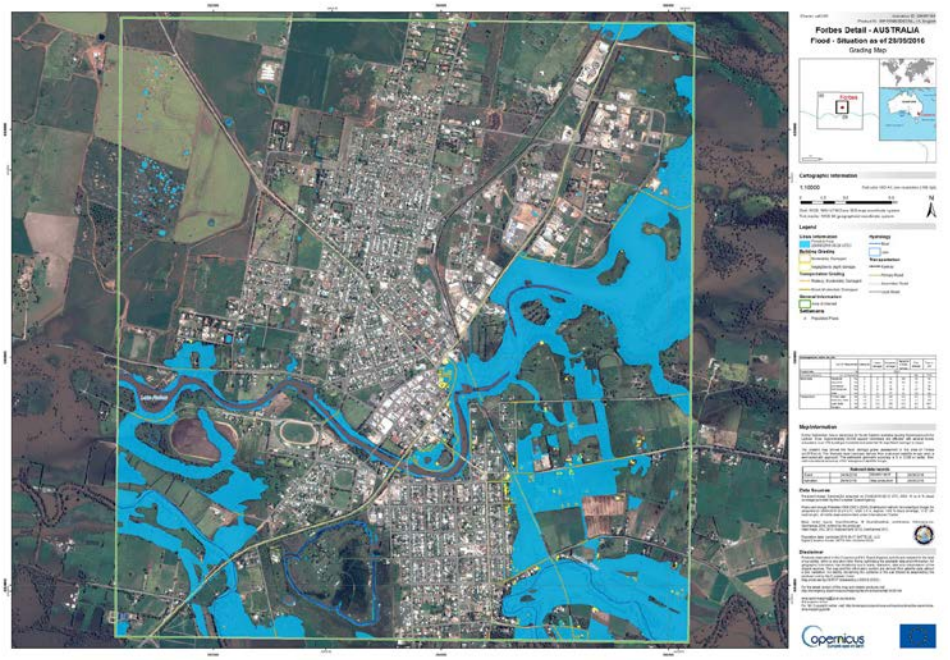

Figure 3.8: Copernicus EMSR184 South Eastern Australia Forbes Detail Map.

Flood extraction

Due to the complexity of extracting this flood extent (highly variable radiometry of water surfaces), SERTIT applied the methodology implemented in the optical rural and urban mapping section of this report (sub-chapters 2.1 and 2.4) namely the SVM-based approahc within OTB. The objective of this work is to drastically reduce manual interpretation and it succeeded. Before delivering the product (fig. 3.7) to Geoscience Australia within EMS the result of this semi-automatic

classification method was post-processed (simplified and smoothed) and thematically validated by an experienced operator.
The overall appreciation sent by mail to the EMS service was “We have found the Copernicus EMS to be of very high quality and very timely. We very much appreciate your efforts.” A formal feedback will arrive whenever the activation ends.

3.2 Fire mapping demonstrators

Two separate demonstrators are carried out to emphasise the operational nature of the BURNOUT workflow/tool that SERTIT has developed. In both cases during rapid mapping events it helped provide a more rapid service. In both demonstrator BURNOUT is used to generate the initial burn scars which are then validated and sent to the users.

3.2.1 EMSR180: Fires on Thassos Island

Event description

On 10/09/2016 between 06:00-07:00 am, four fires started on the island of Thassos (NE Greece) and continued to burn for a third day before EMS triggering. The fires were probably caused by strong lightning activity in the island that was not followed by rain (dry storm). On Saturday, local authorities called for the immediate evacuation of the villages of Prinos, Mikros Prinos, Megalos Prinos and St. Panteleimon. The mayor of the island has reported damaged homes in Mikros and Megalos Prinos and that the fire has also threatened the village of Theologos.

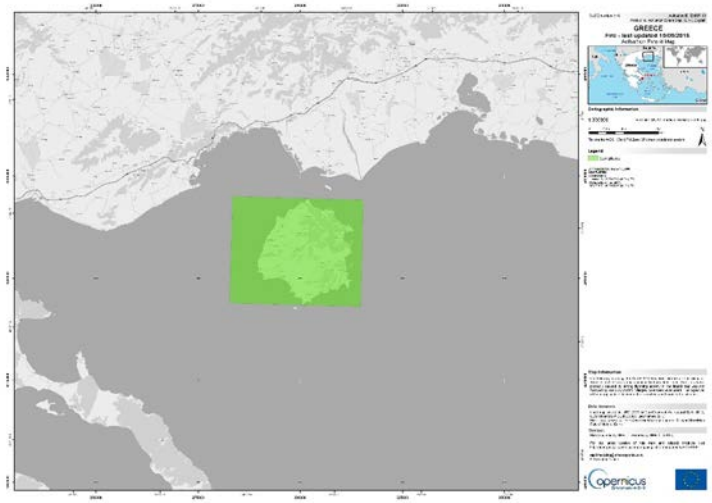

Figure 3.9: Activation Extent Map (AEM).

The General Secretary for Civil Protection has declared the island in a State of Emergency.
According to the Fire Service, 9 aircraft and 6 helicopters were deployed, along with 75 fire engines with 210 fire fighters and a hand crew unit of 53 fire fighters. Nearby municipalities also contributed with 10 water tenders and 3 bulldozers. Finally, the army also offered 40 soldiers.

Copernicus EMS was triggered by the General secretariat for Civil Protection - Directorate for Emergency Planning and Response, Greece on September 12 at 14:36 (UTC), in SL1-mode, in order to provide map products. They asked for the provision of a Delineation and a Delineation Monitoring map over 1 AOI. In total, the activation comprises 2 products.

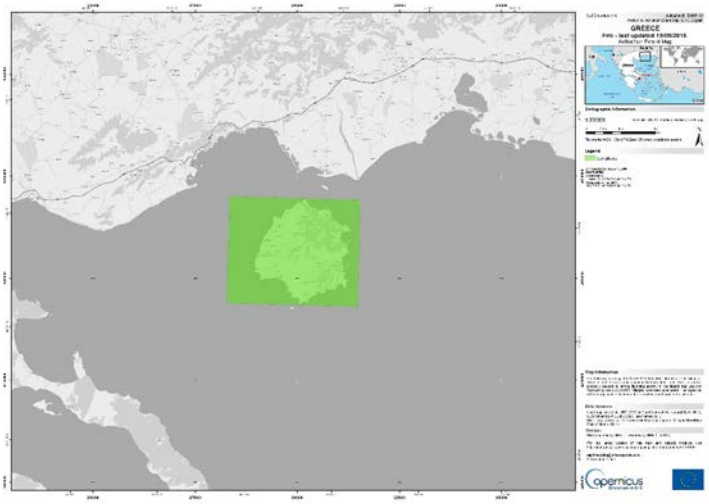

Figure 3.9: Activation Extent Map (AEM)visualises the location of the products.

Burn scar extraction

During this activation the burn scar mapping workflow established in ASAPTERRA, the BURNOUT automatic algorithm, was used to extract burn scars using the Landsat 8 SWIR channels. Then results have been refined by visual interpretation to produce and deliver the final delineation map over Thassos Island (fig. 3.10).

Raw results obtained with BURNOUT and photo-interpreted ones from EMSR180 were compared and hence automatic results obtained from BURNOUT were confronted with a human interpretation; this was taken as a reference. The accuracy evaluation is shown in figure 3.11 and table 3.3 indicating a user accuracy above 95% and a producer accuracy which reaches 90%.

Table 3.2: Crisis data acquired for EMSR180.

Product Type	Sensor Name	Sensor type (optical/radar)	Resolution (m)	Image Acquisition Time (dd/mm/yyyy hh:mm)
Del	Landsat 8	Optical	15	13/09/2016 10:31
Del monit	SPOT 6/7	Optical	1.5	15/09/2016 10:51

Figure 3.10: Delineation Map over Thassos Island (Situation observed on 13/09/2016).

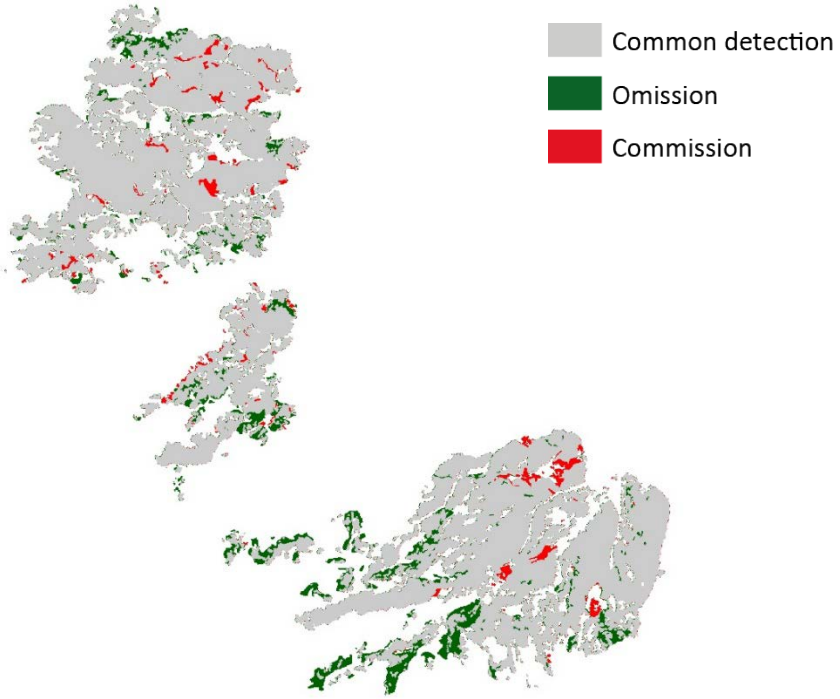

Figure 3.11 Burn scar mapping comparison.

Table 3.3: Confusion matrix.

	Common detection	5803.78	ha
	Commission	253.507	ha
	Omission	664.2	ha

Conclusion

The BURNOUT workflow provides an extremely rapid burn scar mapping that is then validated by visual interpretation before being sent to the user. It is estimated that the gain in time is approximately 4 hours work especially in this large, complex case.

Analyses of the results indicate that the BURNOUT algorithm works very well, exceptions being:

- In terms of omission, sparsely vegetated areas before the fire that are burnt
- And in terms of commission it detects areas that are slightly burnt that the photo-interpreter did not map and also areas that have greatly reduced photo-synthetic activity due to the summer drought.

3.2.2 Fire Demonstrator, Marseille area, France

Event description

During the night of the 10th of August 2016, fires were reported in Rognac commune, located to the north of Marseilles, France. The fires ravaged nearly 2600 hectares of scrubland and pine trees and damaged several buildings, especially in Vitrolles and Les Pennes-Mirabeau. 1800 firefighters and hundreds of policemen and gendarmes, five hundred emergency vehicles, five Canadair, a Tracker, a Dash 8 and two helicopters were mobilized. Thousands of people were affected, hundreds evacuated, and three injured. Aerial and road traffic were severely disrupted, the A7 motorway was closed for several hours. The 12th of August the situation was under control.

The magnitude of the event and the non-solicitation of the European system Copernicus Emergency Management Service (EMS) - Rapid Mapping lead to joint decision of SERTIT and IGN to initiate the actions under the demonstrator "Incendies" the day after the fire started, the 11th of August 2016.

In order to provide the best possible response to the needs of crisis management actors, the French Civil Security (DGSCGC-COGIC) is immediately contacted by SERTIT. The DGSCGC confirms the internal decision to not use the European service Copernicus EMS, without specifying the reason, despite the fact that it closely monitors the event. DGSCGC then expressed interest for this demonstrator.

Figure 3.12: Location of the Vitrolles fire affected area.

Burn scar extraction, severity and soil erosion susceptibility

The images used in this fire demonstrator (tab. 3.4) are listed in the table below. The Sentinel-2 data are used to map the burn scars, fire severity and the soil erosion susceptibility index. Concerning the first two products the Pléiades data were used to refine the results using photo-interpretative methods. Then, the Pléiades stereo-pair were used to produce a high definition DSM to elaborate the RUSLE based Soil Erosion Susceptibility Index. The results are found in table 3.5 below.

Table 3.4: Satellite data.

Data Type	Sensor Name	Sensor type (optical/radar)	Resolution (m)	Image Acquisition Time (dd/mm/yyyy hh:mm)
Crisis data	Pléiades-HR1B stereo	Optical	0.5	13/08/2016 10:48
	Sentinel-2A	Optical	10	13/08/2016 10:30
Reference data	Pléiades-HR1B stereo	Optical	0.5	21/04/2015 10:40
	Sentinel-2A	Optical	10	24/07/2016 10:32

Table 3.5: Burn scar, severity and soil erosion product description and illustration.

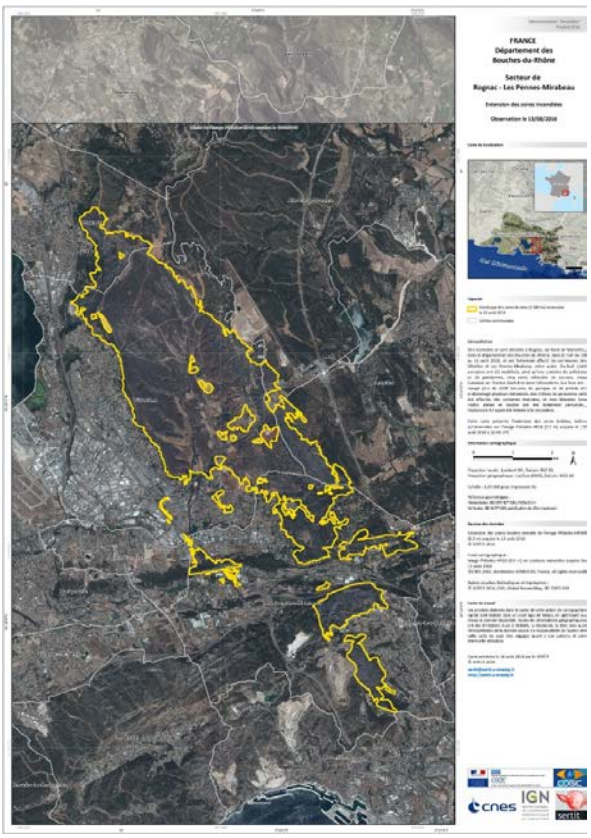

Burn scar extraction

This crisis product presents the extent of burnt areas, obtained firstly by the use of the BURNOUT tool using the pre-post event Sentinel-2 data couple (tab. 3.4). Then the extent of the burnt area was refined by photo-interpretation on the Pléiades-HR1B data acquired the 13/10/2016. The burnt area represents a surface of 2589 ha.

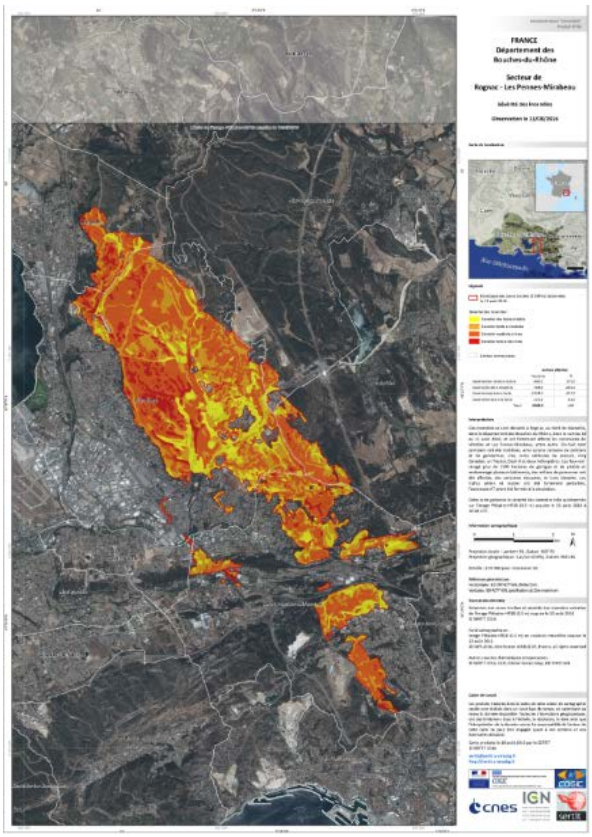

Severity

This product shows the severity of a fire, its intensity of impact. The NBR index is classified after burn scar extraction. This step requires a SWIR channel so Sentinel-2 data were used the results being adapted/interpolated to the Pléiades-HR data (0.5 m) acquired on 13/08/2016 (tab. 3.5). Four severity classes are defined: very low to low, low to moderate, moderate to high, high to very high. The highest severity classes are often located close to urban areas.

Soil erosion susceptibility index

The third post-crisis product shows the soil erosion susceptibility index following the fires (and therefore the risk of landslides), derived from the image-HR1B Pleiades (0.50 m) acquired the 13th of August 2016. Five classes of susceptibility were defined: low, low to moderate, moderate, high, very high. The most important risk is often in sloping areas, especially close to the Rognac and Vitrolles urban areas.

This indicator, calculated from the DSM (Digital Surface Model) obtained from crisis Pléiades data, is a prototype started by SERTIT in the PREFER project (FP7 Copernicus Emergency Management). In ASAPTERRA it has been developed, stream-lined and focussed using available free data sources (Sentinel-2, Landsat 8, and JRC RUSLE parameters) and has been generated during a rapid mapping activation for the first time.

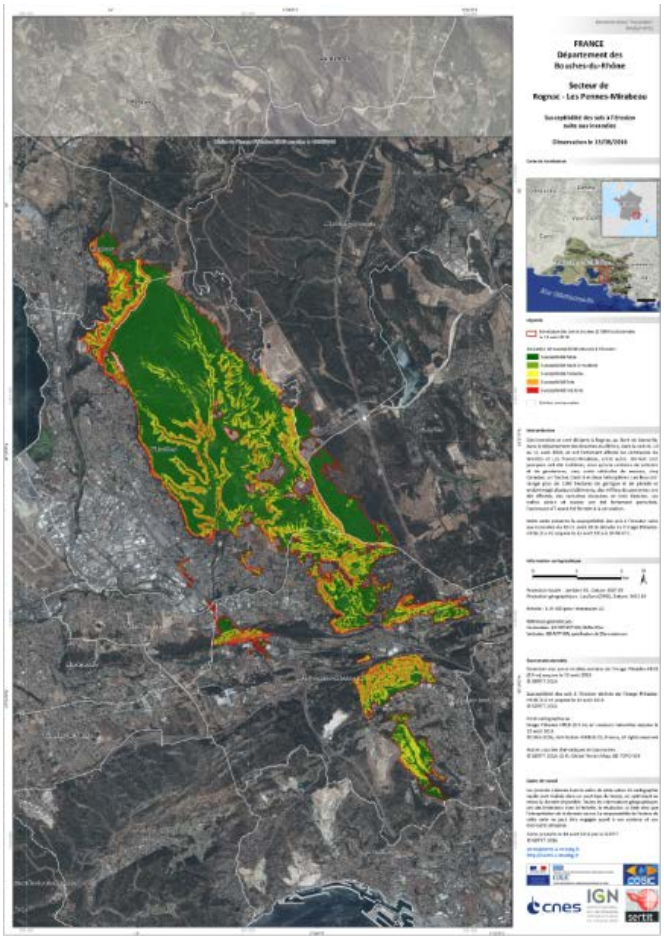

This demonstrator is an opportunity to test the implementation of this indicator obtained from Pléiades data in emergencies, and to confront it with the opinion of new users.

Conclusion

The results of this demonstrator have been well received by the users and there is particular interest in the Soil Erosion Susceptibility Index from the Commune of Vitrolles, France[2]. This product requires further standardisation and validation to become an operational product in the eyes of users. It has definite potential. The user consultation phase is still running.

[2] Oral communication from French Civil Security by phone.

4 Further results

4.1 Surface changes of Villarrica Volcano using Sentinel-1A

A Red Alert has been declared in Chile after the eruption of the Villarrica volcano on 03/03/2015. Over two thousand people were evacuated from Pucon, and another thousand from Panguipulli, two communes close to the volcano. The International Charter Space and Major Disasters has been activated by Chile's risk management authority ONEMI.

Further to the operational support provided by the Charter, ESA and the DLR German Aerospace Center have teamed up to acquire and process Sentinel-1A imagery illustrating changes at the surface of the volcano using a method developed in ASAPTERRA (see chapter 2.1.2.2). This image (see figure 4.1) is a colour composite of the two Sentinel-1 scans from 20 February and 4 March; changes are visually enhanced by a Normalised Change Index (NCI) and some statistical computations. Pink and blue show changes in the radar signal caused by changes in the surface, while areas with no change between the two acquisitions appear grey.

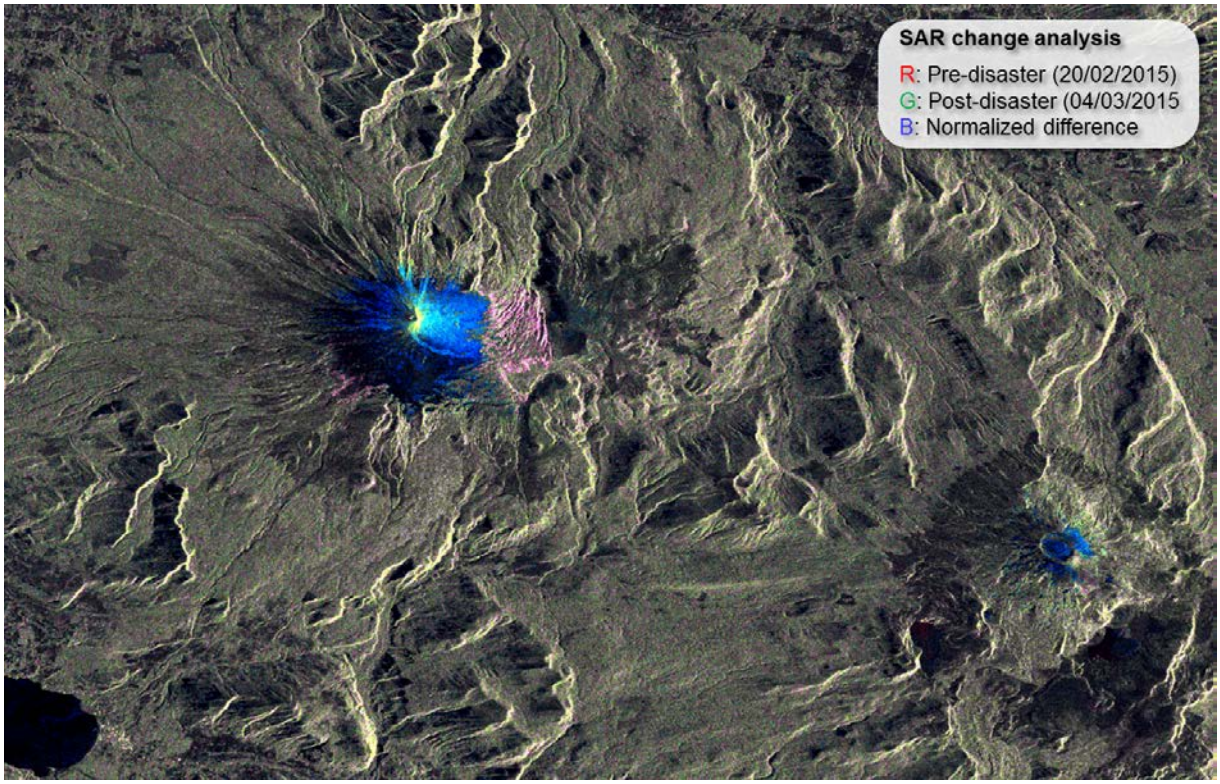

Figure 4.1: Sentinel-1 RGB composite of Villarica Volcano, Chile.

4.2 Earthquake in Central Italy in 2016

On 24/08/2016 an earthquake occurred in the centre of Italy involving a very large territory including several regions (Lazio, Abruzzo, Umbria) and municipalities. After the main shock several others occurred in the areas producing casualties and damages on buildings and infrastructures. The focus of this work was to test the suitability of the Sentinel-1 InSAR Browse Service running at ESA's GEP for detection building damages. The suitability analysis was performed for a test site covering parts of the city of Amatrice, for which a series of Sentinel-1 A/B acquisitions and corresponding coherence data computed from consecutive Sentinel-1 data pairs was available (tab. 4.2.1). The spatial resolution of the data is 50 m.

Table 4.2.1: Sentinel-1 data pairs covering the test site Amatrice.

Test site	Sentinel-1 data pairs
Amatrice, Italy	03/08/16 & 15/08/16 15/08/16 & 21/08/16 21/08/16 & 27/08/16 27/08/16 & 08/09/16

Method

First, a visual analysis of the data was performed based on an AOI covering the mainly damaged part of Amatrice according to the rapid mapping result of the Copernicus Emergency Management Service (figure 4.2.1). The AOI covers 50 pixels (0.125 km²). The amplitude of the Sentinel-1 time series showed no salience, the affected region could not be identified. In contrast to this, the analysis of the coherence showed a strong decrease of this parameter when comparing the coherence computed from a pre-event pair with the one computed from a co-event pair including the time of the earthquake. After the event, the coherence increases again but does not reach the same high coherence values over the AOI compared to the pre-event pairs.

Second, to support the visual analysis, several statistics, the absolute amplitude difference $|\Delta_{ampl}|$, the absolute coherence difference $|\Delta_{coh}|$ and the absolute deviation of the coherence to the mean of each single coherence pair $|\Delta(\mu_{coh})|$, were calculated (see chapter 2.7.3.2 for more details). The results are visualised in fig. 4.2.1 in the 2nd, 3rd, and 4th row, respectively.

Results and discussion

In accordance to the visual analysis of the single amplitude data, the affected area could not be identified using $|\Delta_{ampl}|$.

However, $|\Delta(\mu_{coh})|$ and slightly better $|\Delta_{coh}|$ showed a clear salience to identify the affected area.

To derive parameters for the classification of the data the time series coherence values have been plotted for all 50 pixels of the affected test area in figure 4.2.2. There is a very high coherence for nearly all pixels in the pre-event data pairs (mean ~0.77 for the pair between 03/08/-15/08/2016 and

0.79 for the pair between 15/08/-21/08/2016) and a strong decrease in the coherence values (mean coherence: 0.26) of the co-event pair (21/08/-27/08/2016).
A small area (5 pixels, 0.0125km²) covering a non-affected part of Amatrice (figure 4.2.1) shows a nearly constant coherence over the whole time series (figure 4.2.3).
A semi-automated object based classification of the damaged area based on the pre-event coherence pair (15/08/-21/08/2016) and the absolute coherence difference of the data pairs of 15/08/-21/08/2016 and 21/08/-27/08/2016 was performed. The object-based classification procedure consists of empirical thresholding and region growing procedures. The classification results show a good agreement with the corresponding reference data derived from the Copernicus EMS (figure 4.2.1, first row). An area of 0.102 km² (~82.2%) of the affected AOI could be detected by the classifier.
In conclusion, the Sentinel-1 InSAR Browse Service of ESA's GEP shows some potential for earthquake damage mapping in strongly destroyed areas with a dense urban structure and nearly no vegetation between the buildings. The data analysed in this study has a resolution of 50 m. The original resolution of Sentinel-1 is 20 m. It is assumed that this higher spatial resolution would enable a better use of the SAR amplitude.

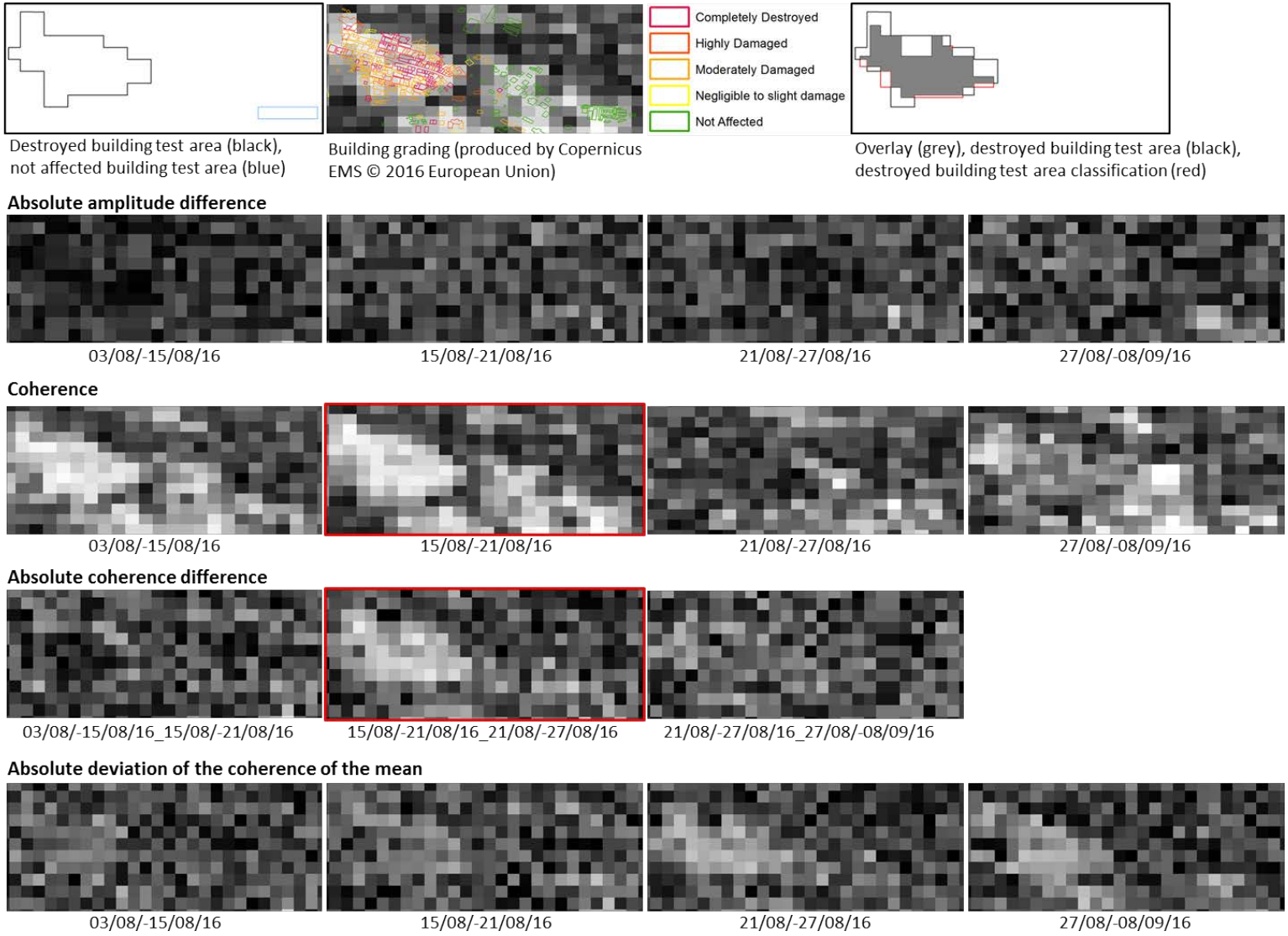

Figure 4.2.1: Results of the Amatrice, Italy, test site. The data surrounded by a red box are used for classification.

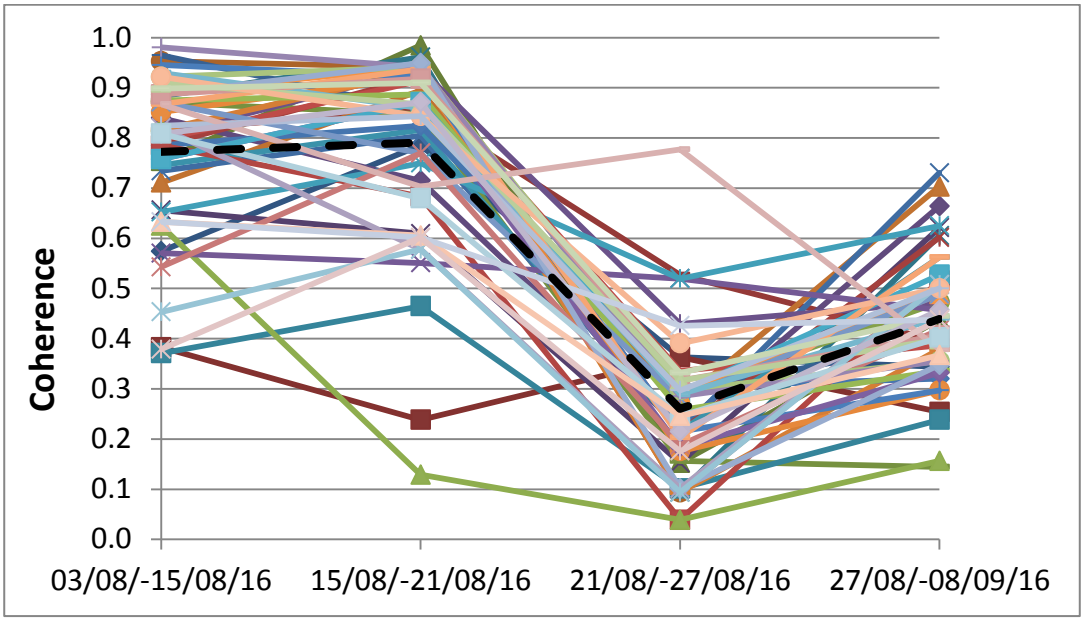

Figure 4.2.2: Time series coherence values for all 50 pixels of the affected test area in Amatrice. The dashed black line corresponds to the mean value.

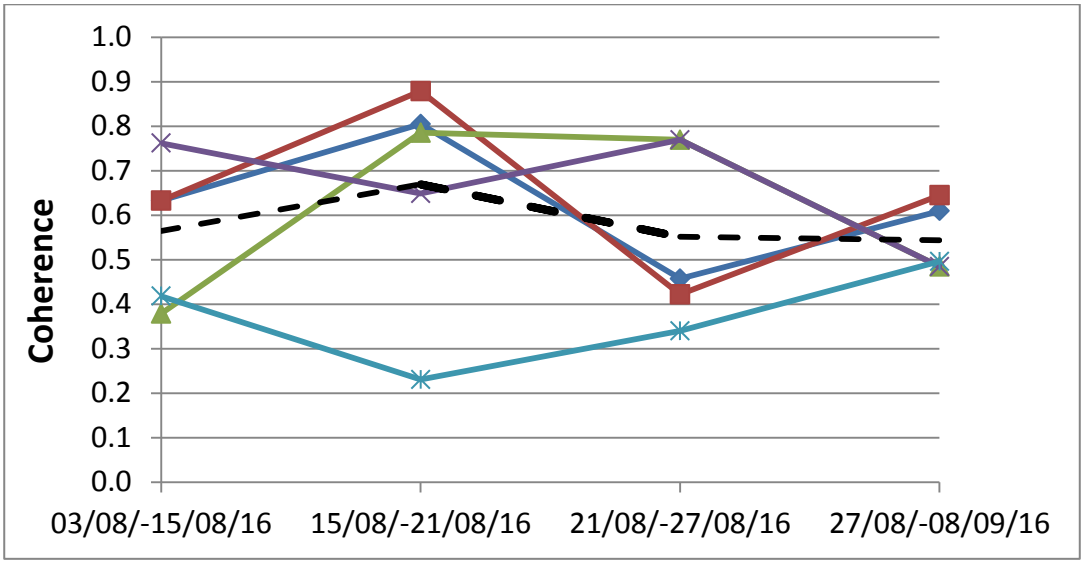

Figure 4.2.3: Time series coherence values for 5 pixels of the non-affected test area in Amatrice. The dashed black line corresponds to the mean value.